1-1-1990

Polymer nematic liquid crystals :: disclination structure and interaction/

Steven D. Hudson
University of Massachusetts Amherst

POLYMER NEMATIC LIQUID CRYSTALS:

DISCLINATION STRUCTURE AND INTERACTION

A Dissertation Presented

by

STEVEN D. HUDSON

Submitted to the Graduate School of the
University of Massachusetts in partial fulfillment
of the requirements for the degree of

DOCTOR OF PHILOSOPHY

September 1990

Polymer Science & Engineering

POLYMER NEMATIC LIQUID CRYSTALS:

DISCLINATION STRUCTURE AND INTERACTION

A Dissertation Presented

by

STEVEN D. HUDSON

Approved as to content and style by:

Edwin L. Thomas, Chairman of Committee

David A. Hoagland, Member

C. Peter Lillya, Member

William J. MacKnight, Department Head
Polymer Science and Engineering

ACKNOWLEDGEMENTS

Life in graduate school has been full! I came a bachelor and am leaving after five short years married with two children. I love Martha, Nicky and Brian.

UMass education has also been good to me. A big thank you is due Prof. Ned Thomas, who does not let his desire for fame inhibit his endeavor to train high quality people. It was great to have the freedom and encouragement to learn and develop in ways that I wouldn't have guessed from the outset. I appreciate his great efforts in helping me develop communication skills. I also appreciate the exposure to other experts which he has afforded. I am fortunate to have worked alongside Prof. Ted Atkins as I started my work.

Even more important, the comradery and stimulation within our group made school worthwhile. I would like to thank especially friends John Reffner and Dave Martin.

I would like to thank Prof. Peter Lillya and Prof. Dave Hoagland for their sharp insight and their involvement on my committee.

There are many other people and organizations which have made my work possible. I am grateful for the faithful financial support of the Materials Research Lab and its director at UMass, Prof. Shaw Hsu. I am indebted to those who have kindly provided the polymer samples: Prof. Q-F. Zhou, Prof. Pradip Bhowmik, Prof. Robert Lenz, Dr. Bill Ward, Dr. Hartmut Fischer, and Prof. Samuel Stupp. I gratefully acknowledge use of the superconducting magnet facility at the Bitter National Magnet Laboratory, Cambridge, MA. I am grateful for the collaboration of Debbie Vezie in opperating the Hitachi S-900 HRSEM at Wright-Patterson Air Force Base, OH. I thank James Fleming for his work developing image processing software.

Finally, I would like to acknowledge the God by whom, through whom and for whom all things exist. I think it's fun to puzzle about His creation.

ABSTRACT

POLYMER NEMATIC LIQUID CRYSTALS:

DISCLINATION STRUCTURE AND INTERACTION

SEPTEMBER 1990

STEVEN D. HUDSON, B.S., CORNELL UNIVERSITY

Ph.D., UNIVERSITY OF MASSACHUSETTS

Directed by: Professor Edwin L.Thomas

Disclinations and inversion walls in the director field of nematic thermotropic liquid crystal polymers (TLCP's) are imaged at high resolution using the lamellar decoration technique of Wood and Thomas. The utility of the lamellar decoration technique has also been greatly extended by using an etch and replication technique to image the director in sections of a bulk sample.

The interaction of disclinations in the presence of an applied magnetic or extensional flow field which tends to align the director is studied. At intermediate field strengths, where the disclination separation is comparable to the characteristic length for director field distortions, pairwise interaction no longer dominates, but clusters of disclinations are observed to form. The applied field suppresses fluctuations of the disclination positions which increase the topological dipole moment of a cluster while enhancing those that preserve zero dipole. The applied field tends to minimize the long range distortional energy which is proportional to the square of the dipole moment. As a result, quadrupolar (Lehmann) clusters of disclinations are commonly observed in either magnetically or extensionally flow aligned samples.

Many-bodied interaction of disclinations in the absence of an applied field is studied via computer simulation, and the results agree favorably with recent experimental work.

The structure of the cores of disclinations has been observed. The core size is on the order of a few molecular lengths, and its structure depends upon polymer architecture. A

rigid polymer splays more within the core of a π wedge disclination, and an excess of chain ends aggregates. A semi-flexible polymer, in contrast, bends more within the core. Hairpins are not thought to be abundant in the semi-flexible TLCP.

The morphology of the TLCP semi-crystalline state has also been examined. It is observed to depend upon the relative primary crystal nucleation and crystal growth rates. The lamellar decoration morphology, where the crystalline lamellae are everywhere perpendicular to the director of the precursor nematic, is favored by rapid nucleation and slow growth. This morphology is unique to TLCP's, but other morphologies are possible. Spherulites have also been grown from the nematic melt. Their growth is favored by slow nucleation and rapid growth.

TABLE OF CONTENTS

LIST OF TABLES

LIST OF FIGURES

CHAPTER 1

INTRODUCTION TO LIQUID CRYSTAL TEXTURES

1.1 Definition and importance of director as elucidated by an application

The macroscopic structure of nematic liquid crystals intrigues both physicist and engineer. The engineer creates novel optical devices and utilizes unusual flow behavior [Windle, 1988]. The physicist enjoys the wealth of structures, topology, instabilities, phase transitions, and defect mediated processes [Kleman, 1989]. In this work I primarily address the physicist. By way of introduction I would like to discuss a most important practical application to motivate and to define terms.

Liquid crystal displays (LCD's) are finding many applications due to their contrast, thickness, and low power consumption [Baur, 1982]. Their structure and operation serve to introduce us to some of the features of liquid crystal physics. Liquid crystal material is placed between two transparent electrodes. The orientation of the rodlike molecules may be manipulated by surface preparation and electric fields. By controlling the orientation of the molecules the optical properties of the display may be controlled.

One of the most popular types of LCD's is the twisted nematic. The term nematic refers to the symmetry of the molecular structure. Rodlike molecules which comprise the nematic phase, are locally aligned with uniaxial symmetry. The direction of orientation is described by a unit vector called the director. In the absence of torques acting on the director, a macroscopic sample is uniformly aligned. Nematic liquid crystals have truly long range orientational order. Variation of the director with position, however, is both of principle interest and very easily obtained.

These rodlike molecules may be small molecules or any of various polymers made from smaller segments. An example of a rodlike molecule, p-methoxybenzylidene-p-butylaniline (MBBA), is shown below.

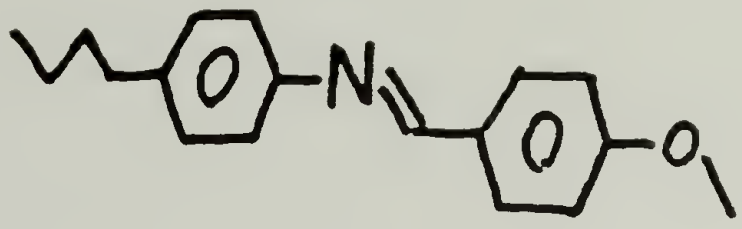

The two aromatic rings linked via the carbon-nitrogen double bond form the rigid unit, while the ends are flexible to promote a fluid phase. There are a myriad of other low molecular weight compounds which form nematic phases, and nearly as many polymer nematics have been synthesized. Rodlike segments may be linked together to make a rigid liquid crystal polymer. Semi-flexible main-chain liquid crystal polymers are prepared by linking small rigid segments (similar to MBBA) end-to-end with segments which permit some flexibility. The rigid segments may also be attached as side groups on a flexible backbone to form a side chain LCP. Side chain LCP's have properties most similar to the low molecular weight materials. In chapter 5, the effect of polymer stiffness on material properties is observed.

The nematic phase may be characterized by a local order parameter measuring the quality of local alignment about the director:

$$s = 3/2 \langle(\mathbf{p}_i \cdot \mathbf{n})^2\rangle - 1/2 \ , \qquad (1.1)$$

where the orientation of each rigid unit, $\mathbf{p}_i$, with respect to the director, $\mathbf{n}$, is averaged. The brackets denote an average over a volume in which the director is uniform. The order parameter is zero in the isotropic phase, and for perfect alignment, s = 1. For typical nematics, s ~ 0.6 - 0.8.

The nematic phase is thermodynamically stable. If the nematic material is heated a first order transition to an isotropic fluid will occur. Upon cooling, the nematic material will transform to at least one of the following: any of several higher ordered liquid crystalline phases, a crystal phase, or a non-equilibrium glassy phase. A material with this thermal behavior is said to be thermotropic. These phase changes may also be effected by adding or removing solvent; such materials are lyotropic.

Returning to the example of the twisted nematic display, the liquid crystal is confined between two parallel surfaces. The surfaces are treated such that the director is parallel to the surfaces, with the director at one surface rotated perpendicular to that on the other. The director rotates smoothly through 90 degrees as shown in figure 1.1(a) [Baur, 1982]. Because the direction of maximum polarizability of the material is coincident with the director, such a cell will readily rotate plane polarized light. This cell is transparent when placed between crossed polars. A mirror is placed behind the cell, and the reflected light makes the area appear white.

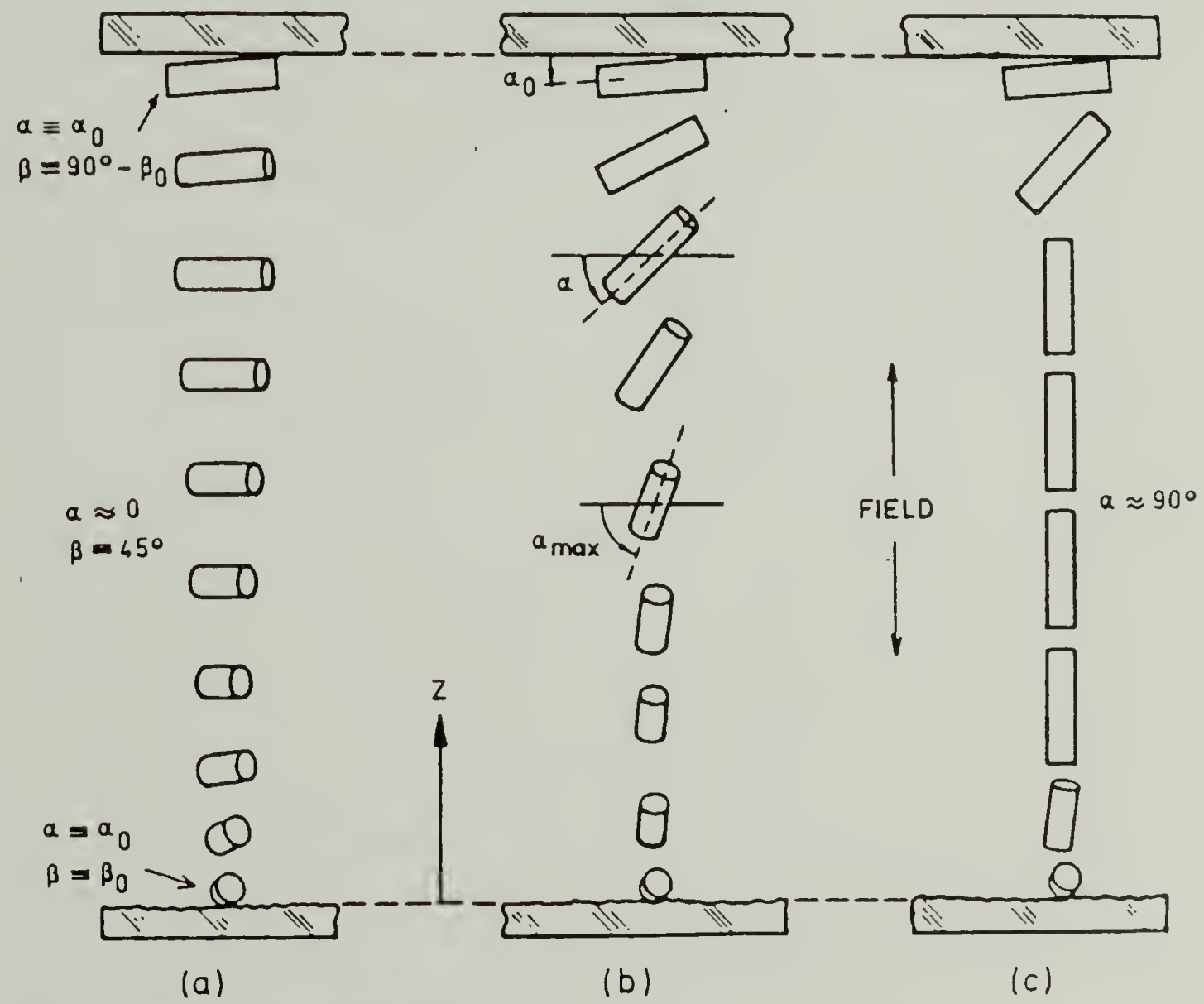

Figure 1.1 Twisted nematic liquid crystal display [Baur, 1982]. The orientation of the director within a pixel is shown for various field strengths. α is the angle of the director with respect to the field and β is the angle with respect to the normal to the paper. (a) No applied field. (b) Intermediate field. (c) Large field. The boundary layer thickness near the surface decreases with field strength.

On the surfaces of a twisted nematic display is an array of transparent electrodes. A pixel of the display is easily made dark with application of an electric field normal to the surfaces. When the field is on, the director aligns along the applied field, as shown in figure 1.1(b). The orientation at the surfaces remains undisturbed, but the boundary layers in which the director rotates towards the field direction become thin as the field strength is increased (see figure 1.1(c)). In this case, the director in the bulk of the film is parallel to the direction of propagation of the light. Because the symmetry of the nematic is uniaxial (i.e. there is no net orientation normal to the director), the cell does not rotate light and is dark. When the field in a pixel is turned off again, the surfaces reestablish the transparent twisted structure.

An important application of polymer liquid crystals is high strength fibers drawn from a liquid crystal solution. The local alignment in the nematic plays a major role in achieving highly aligned fibers. In this case, elongational flow during drawing acts similarly as an electric field to align the director.

Because of the importance the director field has on the material's behavior, our basic understanding of director field features, their origins and interactions, will be reviewed in this introductory chapter.

As we have seen from the example above, the director field is influenced by many factors: material properties, surfaces, applied fields, and flow. Given all of these factors the director field may be determined by minimizing the free energy. The continuum hydrostatic theory of LC's has been developed and explained by Oseen [1933], Frank [1958], Ericksen [1976], and de Gennes [1974]. The theory adequately describes static distortions in LC's. The following brief review follows de Gennes' development.

1.2 Elastic free energy and distortions in the director field

The director, a unit vector field, $\mathbf{n}(\mathbf{r})$, in general varies its direction throughout space. The distortional free energy density per unit volume, g, is a function of $\nabla\mathbf{n}$, and for a nematic

$g=0$ when $\nabla \mathbf{n}=0$, i.e. when the orientation of the director is uniform. We assume that the distortions in the director field are very small on a molecular scale, i.e. $a\nabla \mathbf{n}<<1$ where a is some molecular dimension. Using this assumption, we may expand g in powers of $\nabla \mathbf{n}$.

$$g = f(\nabla \mathbf{n}) + f((\nabla \mathbf{n})^2) + \ldots \qquad (1.2)$$

The free energy density must be independent of coordinate transformations. Because the nematic phase is uniaxial, apolar, and centrosymmetric, g should be invariant to both rotation and inversion operations. This requires g to have no odd powers of $\nabla \mathbf{n}$. To a good approximation, g will contain only $(\nabla \mathbf{n})^2$ terms.

There are only three independent modes of distortion of a liquid crystal--splay, twist, and bend. Each of these three modes will contribute to the energy density. Now let us consider a local coordinate system to illustrate the three terms which exist; see figure 1.2.

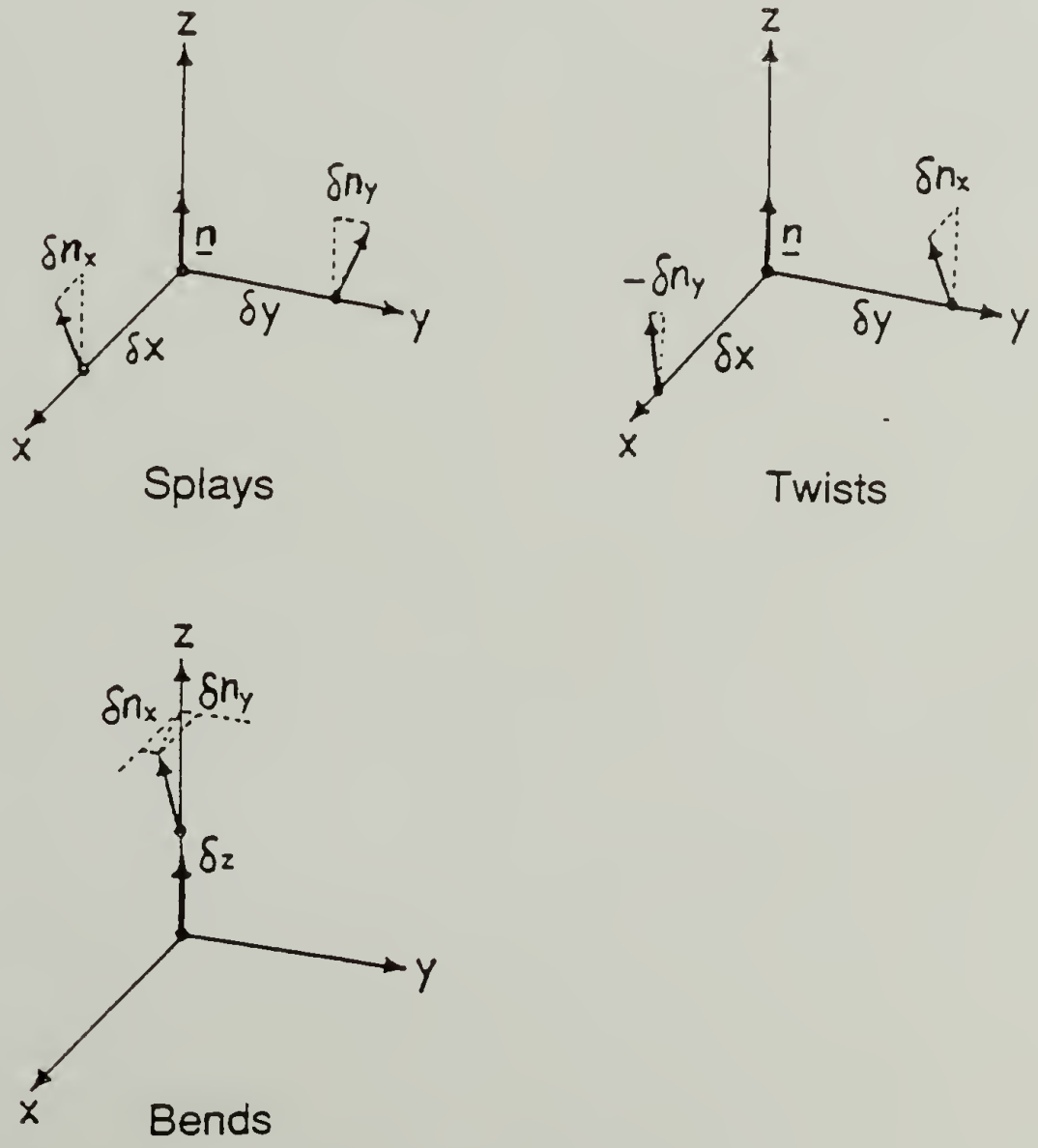

Figure 1.2 Three modes of elastic distortion [Frank, 1958].

The z axis is taken to be coincident with the director. $\nabla\mathbf{n}$ consists of derivatives $\partial n_i/\partial x_j$. Splay is divergence of the director, i.e. when i=j. Twist and bend are described by derivatives where i and j are not equal. Twist is described if x_j is perpendicular to $\mathbf{n}$, and bend is described if x_j is parallel to $\mathbf{n}$. Consequently, twist is the parallel component of the curl of the director, $\mathbf{n}\cdot\nabla\mathbf{x}\mathbf{n}$, while bend is the perpendicular component, $\mathbf{n}\mathbf{x}\nabla\mathbf{x}\mathbf{n}$.

$$\nabla\cdot\mathbf{n} = \partial n_x/\partial x + \partial n_y/\partial y \qquad \text{splay} \qquad (1.3)$$

$$\mathbf{n}\cdot\nabla\mathbf{x}\mathbf{n} = \partial n_y/\partial x - \partial n_x/\partial y \qquad \text{twist}$$

$$\mathbf{n}\mathbf{x}\nabla\mathbf{x}\mathbf{n} = \partial n_x/\partial z + \partial n_y/\partial z \qquad \text{bend}$$

The resulting expression for the free energy density is [Frank, 1958]:

$$g = 1/2\, k_{11}(\nabla\cdot\mathbf{n})^2 + 1/2\, k_{22}(\mathbf{n}\cdot\nabla\mathbf{x}\mathbf{n})^2 + 1/2\, k_{33}(\mathbf{n}\mathbf{x}\nabla\mathbf{x}\mathbf{n})^2 \,, \qquad (1.4)$$

where k_{ii} are elasticity-type coefficients which are a measure of the energetic penalty that the system must pay for each of the three types of distortion.

For typical nematics, these constants are approximately 10^{-6} dynes [Zheng-Min and Kleman, 1984]. The bend and splay constant are approximately equal and the twist constant is typically about half the other two. For convenience of discussion, we now consider the case when all three are equivalent. In this case, the free energy density reduces to:

$$g = 1/2\, k\, (\nabla\mathbf{n})^2. \qquad (1.5)$$

To find the director field, the total free energy is minimized.

Consider first two dimensional director fields. This consideration not only simplifies the present discussion, but it also is describes well our experimental observations of thin films where the director is confined to lie in the plane of the film. In general, the director field is three dimensional, and we will extend our discussion at various points to three dimensions.

In two dimensions the director has the form:

$$\mathbf{n} = \cos\phi\, \mathbf{i} + \sin\phi\, \mathbf{j}, \qquad (1.6)$$

and the director has only one degree of freedom, ϕ. The Euler-Lagrange differential equation which minimizes the total free energy is the Laplacian of ϕ.

$$\nabla^2\phi = 0 \quad . \tag{1.7}$$

The free energy expression which we have so far developed depends only on the gradients of the director field and not on the specific orientation of the director. Because of this, the nematic or molecular field, as it is called, always tends to disperse distortions in the director field. These fluids have truly long range orientational order. In the next section I describe the features of the director field which are a natural consequence of the elastic free energy expression developed in this section.

1.3 Disclinations

1.3.1 Director field of disclinations

Following the development above, the director field, $\phi(\mathbf{r})$, must satisfy the Laplacian. There are no dimensions of length in this differential equation. Therefore, in the absence of any boundary conditions which may impose a length to the problem, the only solution to this equation is

$$\phi = \alpha\,\theta + \beta. \tag{1.8}$$

This solution corresponds to a rotational defect in the director field called a disclination. The constant α is chosen to make the solution single valued. Because $\mathbf{n} = -\mathbf{n}$, this condition leads to the following:

$$\phi(\theta+2\pi) - \phi(\theta) = n\pi \text{ , or} \tag{1.9}$$

$$\alpha 2\pi = n\pi ,$$

where n, the Frank index, may be any integer [Frank, 1958]. $\alpha = n/2 = s$ is called the strength or topological charge of the defect. Sometimes the strength is referred to as $n\pi$. Various strength disclinations are shown in figure 1.3. The strength corresponds to the number of rotations of that the director experiences on a path, called a Frank-Nabarro circuit, that encloses the disclination. In two dimensions, disclinations are singular points. In three dimensions, disclinations are lines along which the director is singular. In the optical microscope, these lines often appear as dark threads because they scatter light.

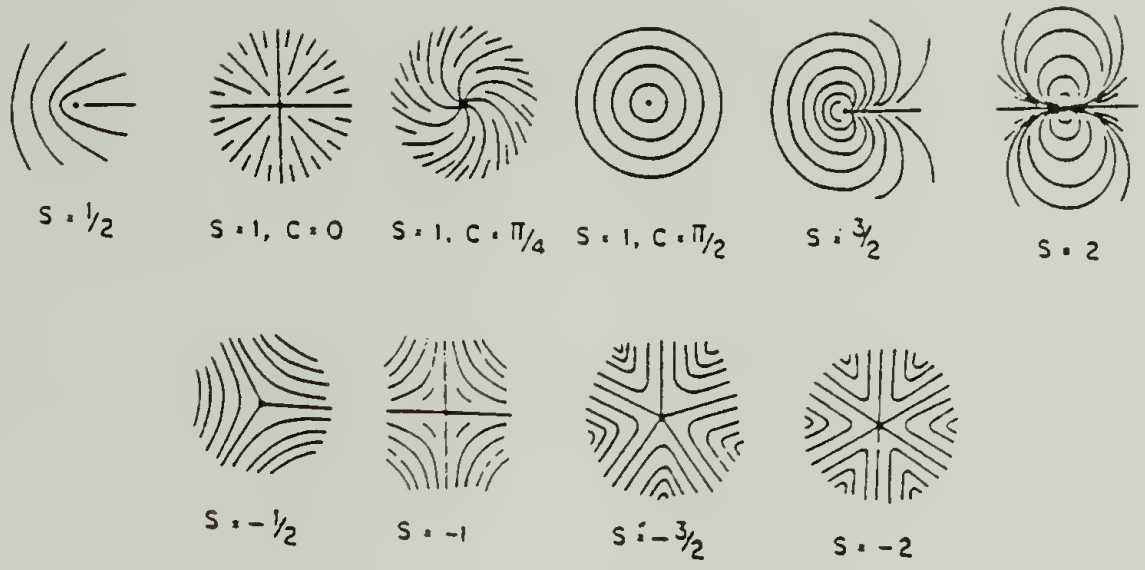

Figure 1.3 Disclination director fields of various strength [Chandrasekhar and Ranganath, 1986]. The integration constant, C, in all cases except for s = 1, simply rotates the figure without distorting it.

These characteristic defects, in fact, give the nematic phase its name. Nematic comes from the Greek word, νεματοσ, meaning thread [Friedel, 1922].

The energy of a disclination is proportional to its length. Because of this, the line has a tension associated with it. In thin films, to minimize the length of disclination lines, disclinations are perpendicular to the film surface. The three dimensional structure appears two dimensional because it is invariant through the thickness of the film.

Because the differential equation for the director field is linear, a sample containing many disclinations is described by superposition of solutions. The director field of an array of disclinations is:

$$\phi = \Sigma\, n_i/2 \tan^{-1}((y-y_i)/(x-x)) + \phi_\infty \ . \qquad (1.10)$$

The director field is determined by disclination types and positions only. The texture may be described by the disclination density or separation which provides an appropriate length scale.

1.3.2 Interaction of disclinations

The free energy of the director field described by equation 1.10 can be calculated using the free energy expression (equation 1.5). Using these two equations it is possible to calculate the interaction between disclinations. Their interaction is directly analogous to two dimensional electrostatics, i.e. parallel infinite charged wires [Nehring and Saupe, 1972]. So like-signed disclinations repel while opposites attract. The force on a disclination due to another is inversely proportional to their separation and along the line of their separation. When two disclinations of equal and opposite strength converge they annihilate one another. I will describe disclination interaction more fully in chapter 4. Note that if the elastic constants are not all equal, the energy of a pair of disclinations will be dependent upon the orientation of the pair with respect to the orientation of the director near the pair [Chandrasekhar and Ranganath, 1986]. In this case, the force on a disclination due to another is not in general along the line of separation.

1.3.3 Topology of disclinations

The topology of different structures may be determined by mapping the director onto an order parameter space [Mermin, 1979]. The order parameter space is all available values of **n**. In two dimensions all possible **n**'s trace a unit circle. Figure 1.4(a) shows a mapping of a contour in real space to a mapping in order parameter space. To characterize the topology of a disclination, the contour in real space is simply a loop enclosing the disclination, as shown in figure 1.4(b). This contour is commonly called a Frank-Nabarro circuit or more generally a Burger's circuit [Harris, 1977]. For any circuit in real space, the corresponding contour in order parameter space may or may not wind around the circle which defines the order parameter space. The number of windings determines the magnitude of the topological charge while the relative direction of the winding determines its sign. The topological charge for a particular defect is independent of the specific real space contour (square, ellipse, etc.)

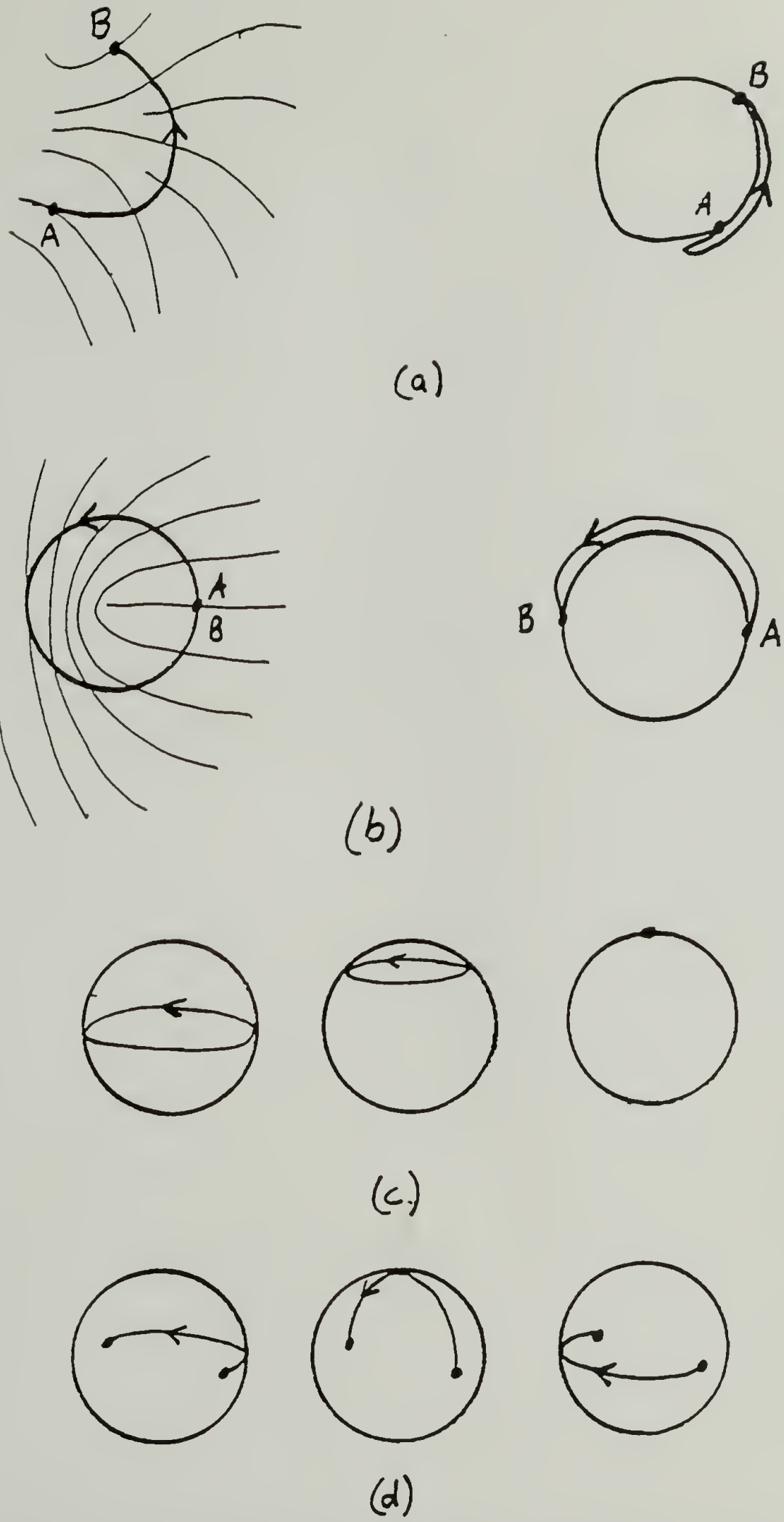

Figure 1.4 Topological characterization of disclinations. (a) A general contour shown in real space on the left with its corresponding order parameter space contour on the right. (b) A Frank-Nabarro circuit characterizing a π disclination. (c) Escape of a 2π disclination in the third dimension. (d) Transformation of a π disclination into a $-\pi$ disclination.

or of the different relative amounts of splay, twist or bend distortions (as will be discussed in chapter 5).

The question of the stability of a structure may be addressed with topological arguments. A more complete analysis includes investigation of the energy as well. To consider whether a structure is topologically stable it is instructive to consider the contour in order parameter space to be an elastic band stretched over a slick surface. The surface is a circle in two dimensions and a sphere in three dimensions. If the band can shrink to a point then the structure is topologically unstable. For a π disclination, the contour ends at diametrically opposite points on the order parameter circle. This contour can not be shrunk to a point. In fact, any disclination (topological charge = $n\pi$) is topologically stable in two dimensions. A contour wound around two times will always be wound around two times.

The number of windings of the order parameter space contour can not be distorted into a contour with a different number of windings. An implication of this is that a single disclination can not simply disappear, for example to the lower energy uniformly oriented state. Because the topological strength is conserved, when two disclinations merge a new topological state is created having a topological strength equal to the sum of the two parent states. Equal and opposite strength disclinations therefore annihilate one another to form a uniformly oriented region.

Each of the disclinations are also energetically stable; however, their energy is proportional to their strength squared. Therefore $\pm\pi$ disclinations are the most likely. Typical optical microscopy observations of thin films of small molecule liquid crystals, approximately 1-10μm thick, show many $\pm\pi$ disclinations but also an inordinate abundance of $\pm 2\pi$ disclinations. As Frank [1958] correctly postulated, this is due to a lower core energy for the $\pm 2\pi$ disclinations. The difference in core energy results from the defects' topology in three dimensions.

In three dimensions, the disclination is no longer a point but a line, and the order parameter space is no longer a circle but a sphere which has profound effects on the stability

and distinction between defects. Defects having an even Frank index are no longer stable. If the contour in order parameter space for a 2π disclination is initially a loop around its equator, as shown in figure 1.4(c) (imagine again an elastic band stretched around a slick ball), the loop may slip upwards and shrink to a point at the pole. A point in order parameter space corresponds to uniform alignment of the director. This process has been termed 'escape in the third dimension' [Meyer, 1972]. This same process can occur with any even index defect. In fact, the $|\pi|$ disclination is the only topologically stable defect [Brinkman and Cladis, 1982].

Even index defects do occur, however, because of certain constraints on the director. Meyer was the first to describe the 'escaped' structure of an even index defect. He considered the case of a 2π disclination along the axis of a capillary tube. The boundary conditions at the tube wall produce a 2π disclination along the tube axis. The director near the core escapes and aligns along the disclination line. Because this non-singular disclination core structure is less energetic, it is sometimes favorable for two odd index disclinations to combine together so that they may share the same less energetic core.

Although $\pm\pi$ defects turn out to be topologically stable in three dimensions, they too are profoundly affected. Any contour of an odd index defect may be reduced to a π disclination. Even a counterclockwise contour of a $-\pi$ disclination may be slipped over to the opposite side of the sphere to create a clockwise contour as shown in figure 1.4(d). Figure 1.5 shows the transformation of a π disclination into a $-\pi$ disclination by the uniform rotation of the director at each point. This process corresponds to slipping the contour to the other side of the sphere. Since disclinations of opposite sign may annihilate one another, a π disclination is its own anti particle! This is another way of saying that the $|2\pi|$ disclination is unstable.

Another way to visualize this property is to see that a $|\pi|$ disclination may appear as a loop, as shown in figure 1.6. Conservation of topological charge dictates that disclinations may only end upon themselves (loops), on other disclinations, or at surfaces. The character

of a disclination changes, however, as the disclination changes its orientation with respect to the axis about which the director rotates. The rotation of the director experienced during a Frank-Nabarro circuit is defined as a vector, Ω, whose orientation defines the axis about which the director has rotated and whose magnitude (nπ) is the amount of rotation. When L and Ω are parallel, the disclination is said to have wedge character. When **L** and Ω are perpendicular, the disclination is said to have twist character [Kleman, 1983]. As a

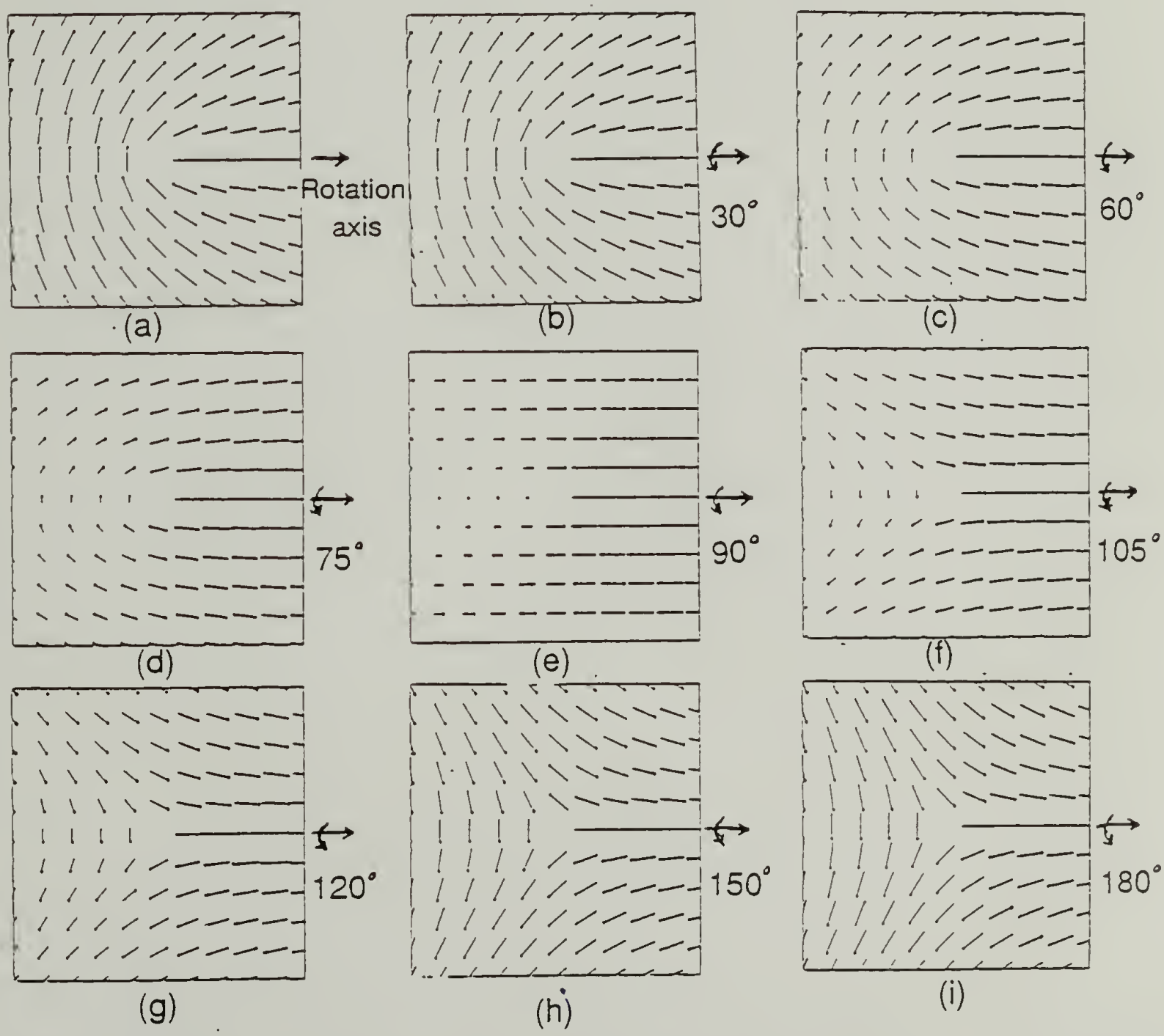

Figure 1.5 All |π| disclinations are topologically equivalent. Although **n** = -**n**, the director is shown as a pin to guide the eye in seeing director rotation. In figures (a) through (i) the director at each point in the fluid is rotated about the axis shown in (a). As the director is rotated the character of the disclination changes. In (a) the disclination is a π wedge, and in (i) it is a -π wedge disclination. When the rotation is 90°, as shown in (e), the disclination has pure twist character.

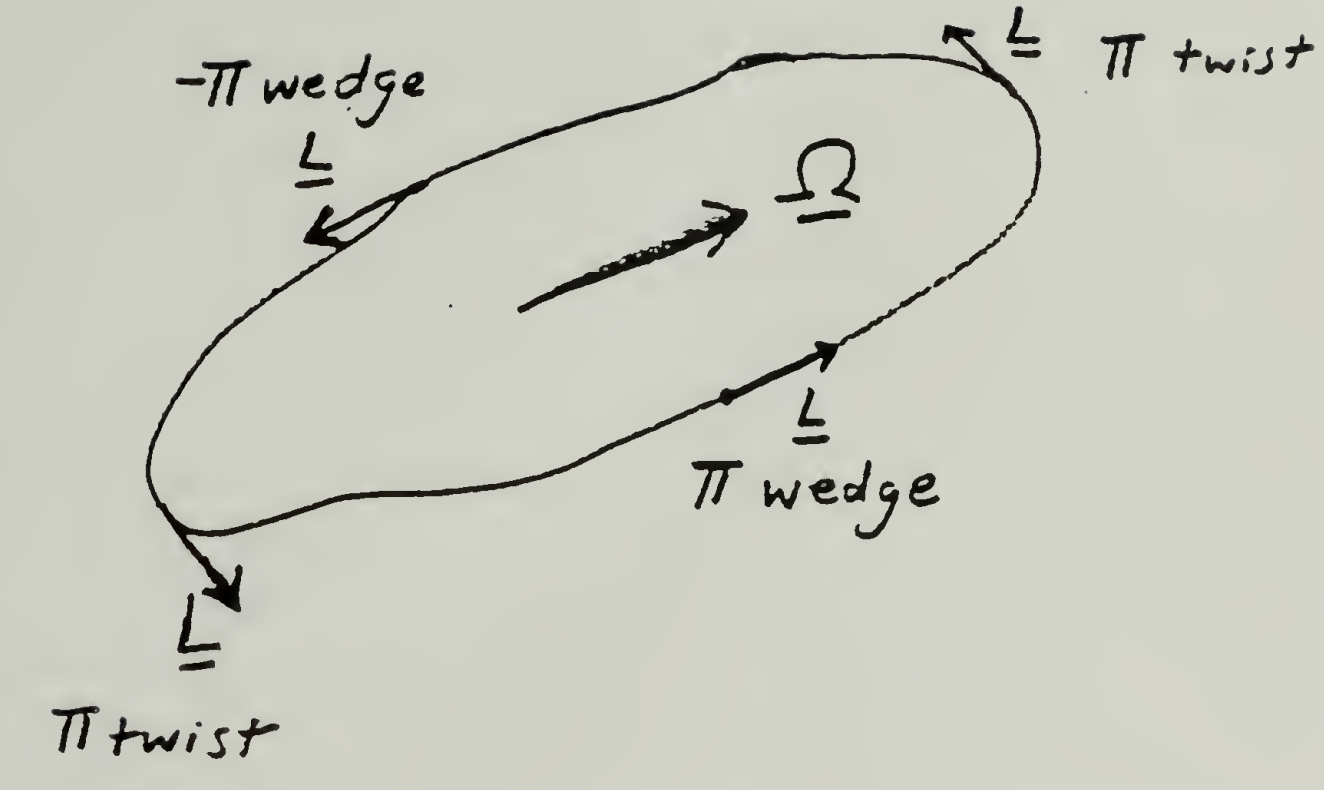

Figure 1.6 A $|\pi|$ disclination loop. The disclination changes its character as it changes its orientation with respect to Ω. Order space maps are shown for different character disclination lines.

disclination loops, the angle between **L** and Ω changes and the character of the disclination continuously changes from a π wedge disclination, through a |π| twist disclination, to a -π wedge disclination.

In the above two sections we have seen that nematic liquid crystals may have a simply described director texture. Characteristic thread-like defects called disclinations result from the nature of the distortional free energy and from the uniaxial symmetry of the nematic phase. In the case of equal elastic constants, the director field is determined by disclination positions only. The texture may be described by the disclination density or separation which provides a convenient length scale.

1.4 Orienting influences

Surfaces, magnetic and electric fields, and flow all may orient the director. Each of these effect the free energy density expression in their own way. In general, the free energy is no longer simply a function of the gradients of the director but also of the director itself.

1.4.1 Surfaces

Only the orientation dependent, or anisotropic, part of the surface tension affects the texture of the sample. The surface tension may be made anisotropic by treating the surface with a surfactant to promote normal boundary conditions or by rubbing the surface to promote tangential boundary conditions with a preferred orientation. The surface tension may be modeled as

$$\gamma = A/2 \sin^2(\phi-\phi_s) \quad . \tag{1.11}$$

where ϕ_s is the preferred orientation at the surface. The free energy density is therefore

$$g = [k(\nabla \mathbf{n})^2 + \delta(z)A\sin^2(\phi-\phi_s)]/2 \quad , \tag{1.12}$$

where the surface is at z = 0. Laplace's equation must still be solved in the volume of the liquid crystal, so the solutions are the similar and distortions are still dispersed. The solutions must however satisfy the new boundary condition. If the boundary conditions are

strong, such that the orientation at the surface is very nearly ϕ_s, the surface introduces an image solution of the disclination [de Gennes, 1974]. Therefore disclinations are repelled from a surface. Figure 1.7 shows a disclination near one and two surfaces.

If, however, the disclination is near enough to the surface that the distortional energy at the surface is strong compared to the surface energy, the disclination is attracted to the surface and is bound. The core of the disclination moves outside the surface entirely. The solution is [Meyer, 1973]:

$$\phi = \phi_s + \tan^{-1}[(z+z_o)/x] \quad , \tag{1.13}$$

where the disclination appears to be at $x = 0$, $z_o = - k/A$. Typical values of z_o would be at least 10nm. Disclinations bound at a surface must overcome an activation barrier to detach. Near the isotropization temperature, the value of z_o and the activation barrier decrease, allowing disclinations to detach.

1.4.2 Electric and magnetic fields

An electric or magnetic field orients liquid crystals due to their anisotropic polarizability or diamagnetic susceptibility. If the anisotropy is positive, an electric field tends to orient the induced dipole which is largest along the molecular axis. A magnetic field behaves similarly because the induced field, which opposes the applied field, is weakest when the molecular axis is parallel to the field. The anisotropy, however, is very weak and only a tiny fraction of the molecules may be aligned in the isotropic state. For very strong applied fields the order parameter may be only 10^{-3}. The nematic phase, however, is easily aligned because of cooperativity. Alignment of one molecule along the field tends to also align its neighbors.

The free energy density for a nematic is

$$g = k/2\,(\nabla \mathbf{n})^2 + 1/2\,\chi_a H^2 \cos^2(\phi-\phi_H) \tag{1.14}$$

$$g = k/2\,(\nabla \mathbf{n})^2 + 1/2\,\Delta\varepsilon E^2 \cos^2(\phi-\phi_E)$$

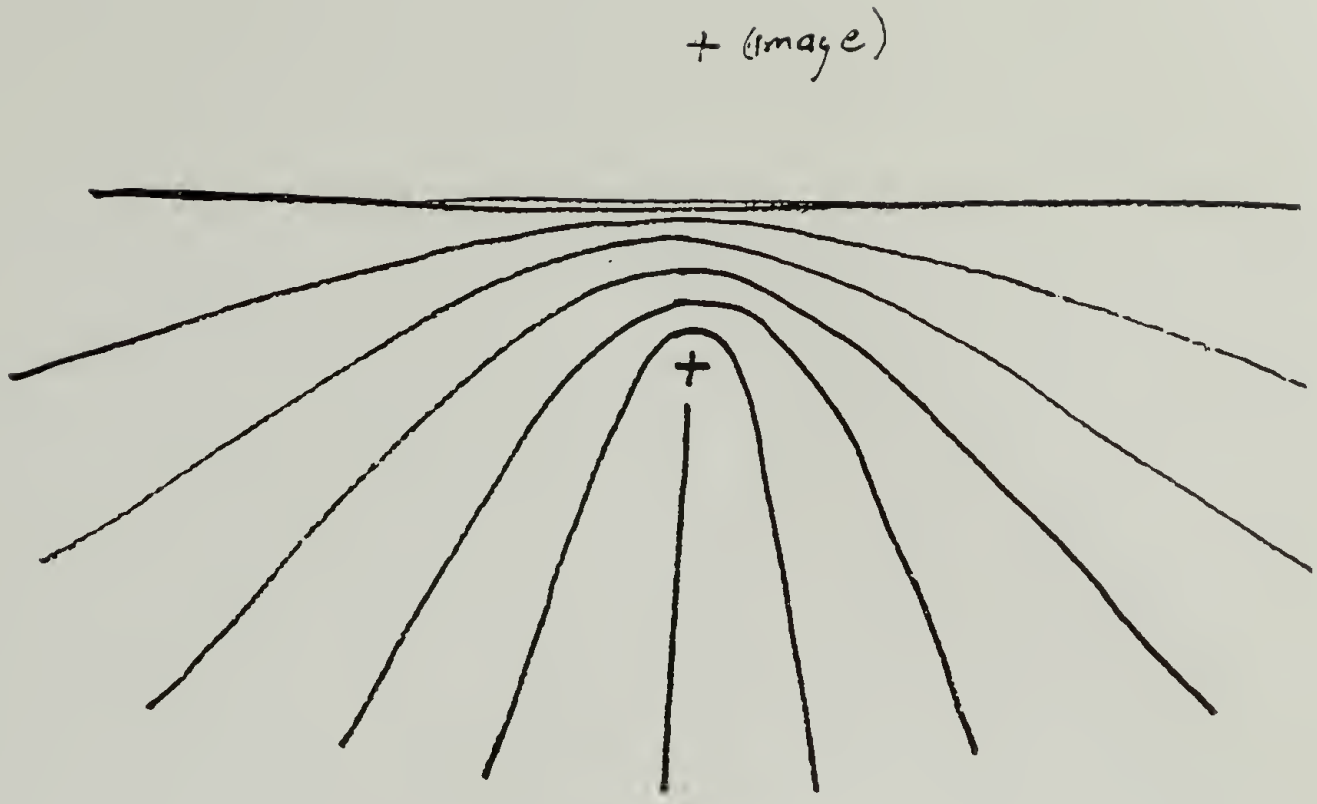

Figure 1.7 The structure of a disclination perturbed by a surface. The director field is the superposition of the disclination and its image. (a) A π disclination near a surface. (b) A π disclination equi-distant from two parallel surfaces has an infinite periodic array of images.

where ϕ_H and ϕ_E are the orientation of the applied magnetic and electric fields respectively. In the subsequent discussion, magnetic field behavior will be discussed. The electric field behavior is analogous.

The two terms in the free energy must balance each other. The linear gradient term tends to disperse the distortions as discussed above. The nonlinear magnetic term, however, globally orients the director and localizes the distortion. Increasing the field strength focuses the distortion into a smaller region. A characteristic length may be defined which is proportional to the size of the distorted region. This measure of the balance of the two terms is found by dividing their coefficients:

$$\xi = (k/(\chi_a H^2))^{1/2}. \qquad (1.15)$$

Let us now discuss the director field as ξ gets small. The Euler-Lagrange differential equation which describes the director field is

$$\nabla^2\alpha + 1/\xi^2 \sin\alpha = 0 , \qquad (1.16)$$

where $\alpha=2\phi$. This is the well known elliptic sine equation, where ξ is the length scale. A solution to the equation is a soliton.

Imagine two surfaces separated by a distance L between which the director rotates by π. For example, consider the above demonstration of a disclination between two surfaces far from the disclination. In this region and at zero field, the director varies linearly with distance:

$$\phi = y\pi/L + \pi/2 , \qquad (1.17)$$

where y varies from -L/2 to L/2. The distortion is dispersed linearly over the entire distance. However, as the field is increased from 0, ξ becomes finite and decreases inversely proportional to H. When $\xi<<L$, the distortion is concentrated into a distance approximately 2ξ. Figure 1.8 shows the resulting solitary (isolated) wave in the director field. This solitary wave in the director field is also called a soliton because its energy and structure is independent of position along x.

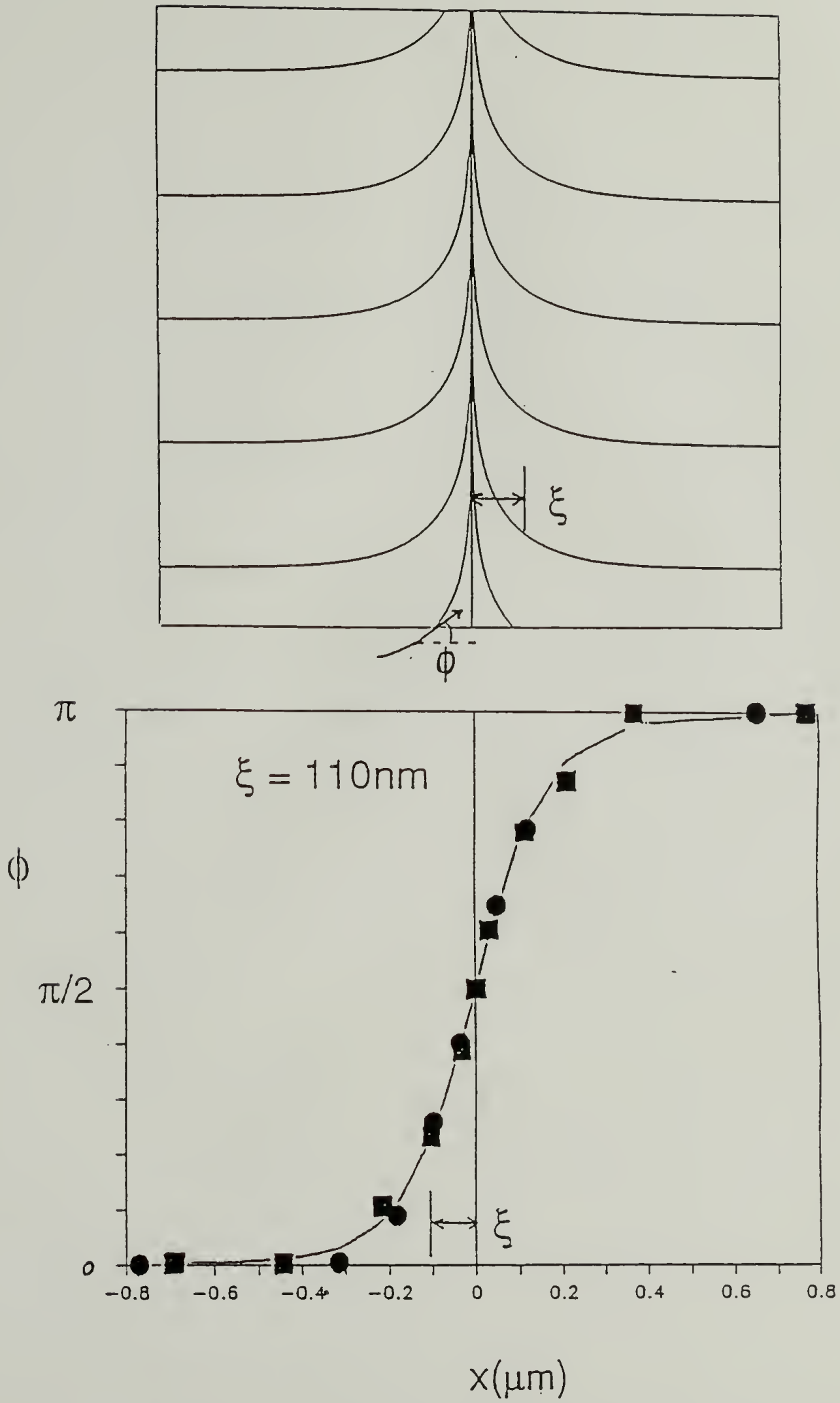

Figure 1.8 Inversion wall. (a) Schematic structure of an inversion wall. (b) Soliton variation of $\phi(x)$. (The symbols represent data taken from TEM images of inversion walls found in extensionally flow aligned thin films.)

The director angle ϕ satisfies the equation 1.16, rewritten below:

$$\nabla^2\phi + 1/\xi^2 \sin\phi\cos\phi = 0. \qquad (1.18)$$

Taking ϕ to be independent of x and z,

$$d^2\phi/dy^2 + 1/\xi^2 \sin\phi\cos\phi = 0. \qquad (1.19)$$

The solution is found by integrating this equation. One integration gives

$$\xi^2 (df/dy)^2 = \sin^2\phi + c_1 . \qquad (1.20)$$

At the boundaries (far from the soliton) both $d\phi/dy$ and $\sin\phi = 0$. The square root may be taken of both sides:

$$\xi (df/dy) = \pm\sin\phi \quad . \qquad (1.21)$$

where the sign of the right hand side determines the handedness of the twist rotation. A second integration gives

$$\phi = 2\tan^{-1}[\exp(\pm(y-y_o)/\xi)] , \qquad (1.22)$$

where y_o is the integration constant which is the position of the center of the soliton. This structure is also called an inversion wall because the director goes through an 180° inversion from one side of the wall to the other. The energy of the soliton/unit area may be calculated:

$$G = 2k/\xi . \qquad (1.23)$$

Since the boundary conditions are specific, the soliton is repelled from the surfaces. The soliton interacts with its image as shown in figure 1.9(a). The pressure that the soliton feels from the surface is [de Gennes, 1974]:

$$p = 4k/\xi \exp[-2d/\xi] , \qquad (1.24)$$

where d is the distance from the center of the soliton to the surface. The soliton is stable between the two repelling surfaces.

If however the boundary conditions were degenerate, the soliton's image would be inverted and the walls would be attracted to the surfaces with the pressure:

$$p = -4k/\xi \exp[-2d/\xi] . \qquad (1.25)$$

In this case the soliton interacts with its opposite image. The soliton simply passes out of the sample; the image and the soliton annihilating one another. When the soliton is exactly

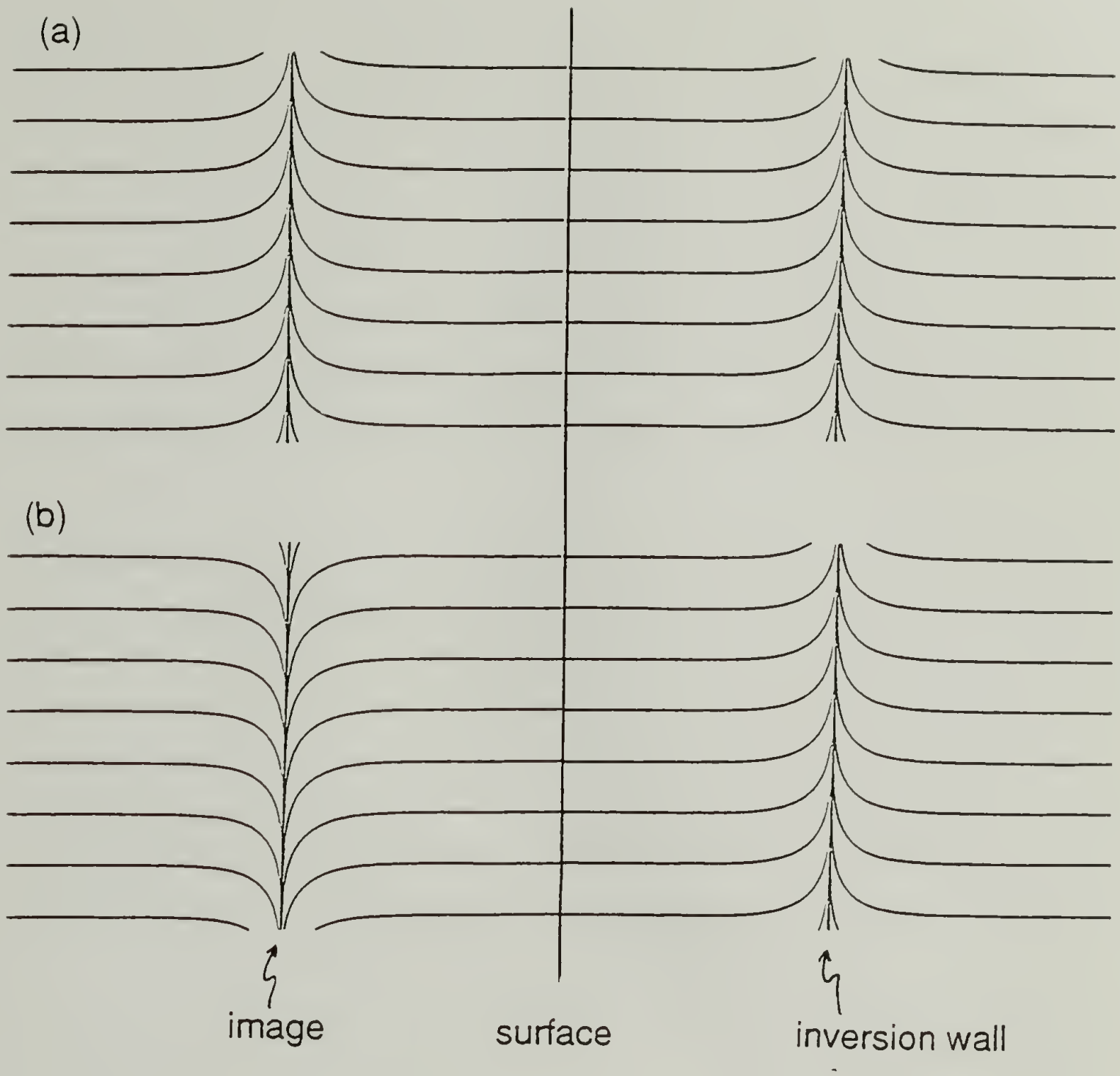

Figure 1.9 Interaction of inversion walls. (a) Like inversion walls repel. (b) Opposite inversion walls attract.

in the center the pressure is zero. However, the soliton is unstable with respect to fluctuations in position.

Consider the neighborhood of the disclination at x = 0. To one side, the inversion wall is observed; on the other uniform alignment. The disclination terminates the wall. Both the disclination and the inversion wall have the same topological charge--π, yet one is a

line and the other is a surface. The contour in real space to characterize the topological charge of an inversion wall is a line from one side of the wall to the other side. This contour yields a rotation of π in order parameter space. Inversion walls are topologically constrained to end only at surfaces or disclinations of like strength, or loop upon themselves [Mineyev and Volovik, 1978]. The director field about such a disclination is not yet theoretically determined. It involves solution of the non-linear differential equation 1.16 in two space dimensions instead of just one. In chapter 6, I calculate the structure very near the disclination using a perturbation expansion.

Like disclinations, inversion walls, too, have different character depending on their orientation with respect to an applied field. If the wall is perpendicular to the applied field, the inversion wall has mostly splay character, as shown in figure 1.10(a). If the wall is parallel to the applied field, the inversion wall may have twist (figure 1.10(b)) or bend character (figure 1.10(c)). If the elastic constants are equal, the energy of a wall is independent of its orientation or character.

The characteristic length, ξ, and the disclination separation, d, together govern the director field. The relative magnitude of these lengths determines the observed director texture (see cartoon figure 1.10). The two limiting cases are obvious. When $\xi >> d$, the field has negligible effect and the disclination interactions are many bodied. The resulting director field is a schlieren texture. When $\xi << d$, neighboring disclinations of opposite sign are separated by an inversion wall. Each disclination only interacts with its mate. One may say that the disclinations cluster, but only dipoles are allowed. Note that inversion walls need not be associated with a disclination; they may meander and form loops.

The third case is when $\xi \sim d$; the disclination interactions are richer and the resulting structure of the director is less obvious. In this case, interactions are limited to only the nearest neighbors. Chapter 6 describes the discovery of clustering of disclinations in order to reduce their long range distortional energy.

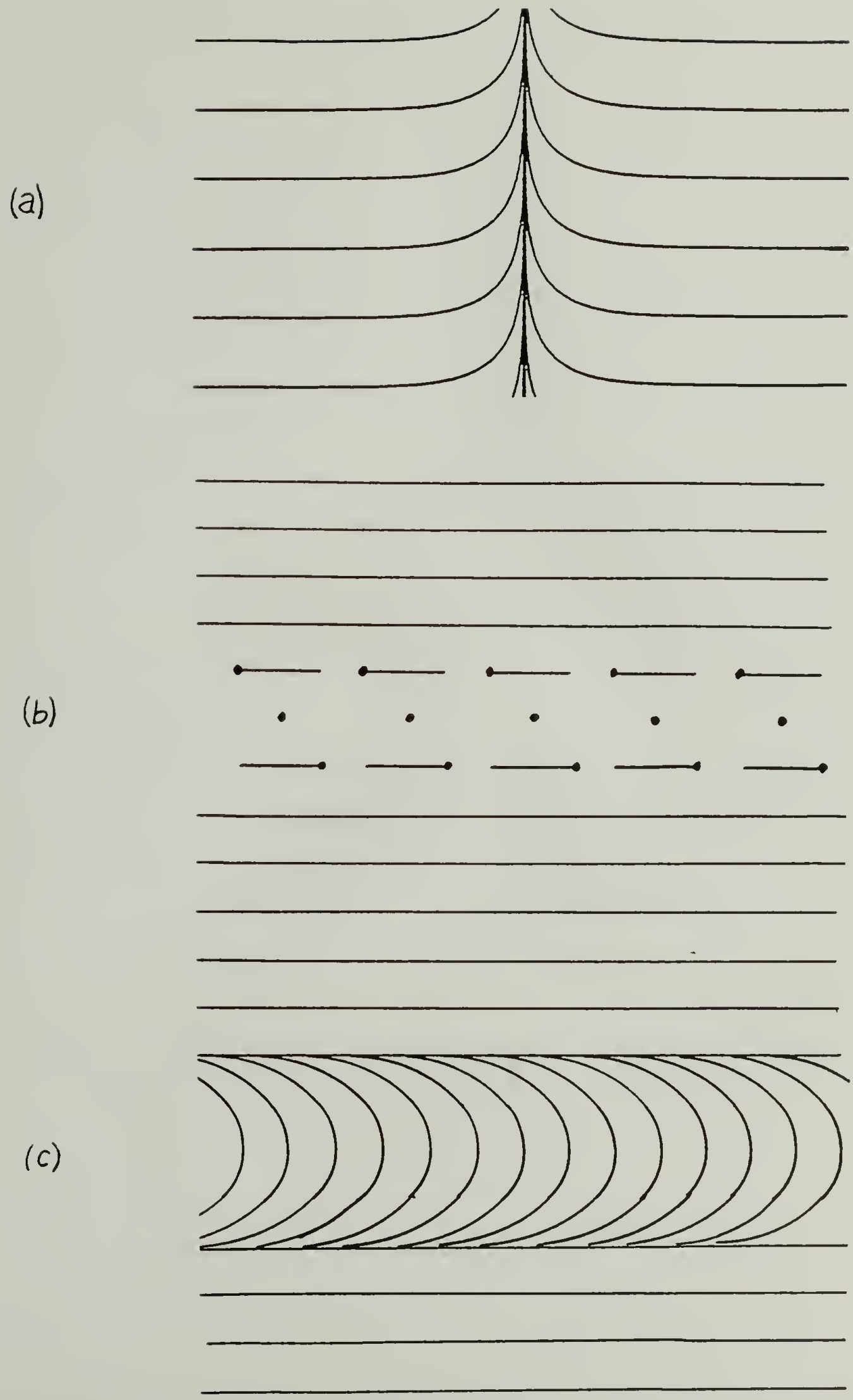

Figure 1.10 $|\pi|$ inversion walls of different character. The applied field is horizontal. (a) Mostly splay. (b) Twist. (c) Mostly bend.

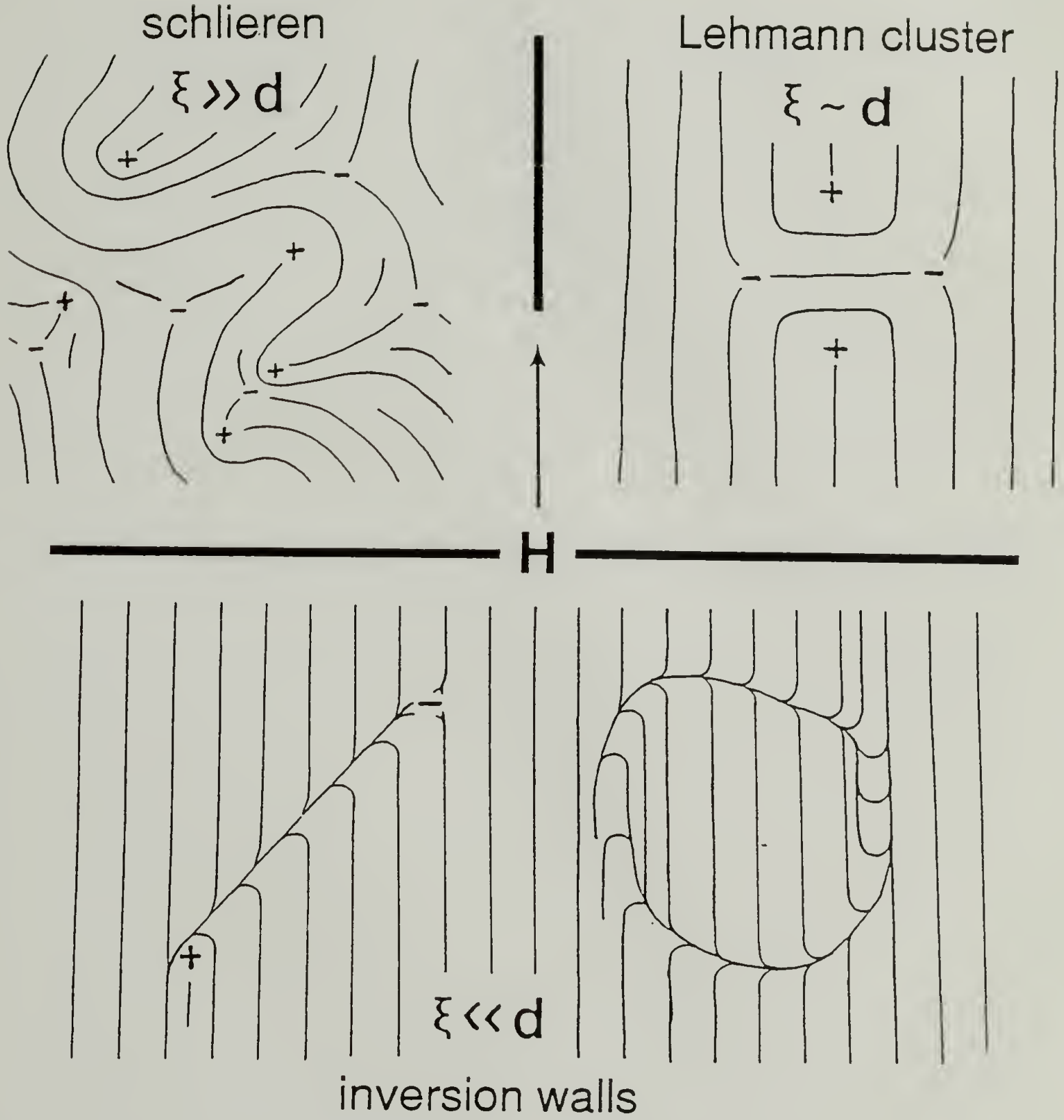

Figure 1.11 Director texture as a function of the characteristic length, ξ, and the disclination separation, d. The applied field is vertical.

1.4.3 Flow

Flow also orients the director field [Stephen and Straley, 1974]. To illustrate this, consider a 2D fluid flowing in the x direction. In order to compare flow alignment with magnetic alignment, the two are superposed. Furthermore the flow may have either or both extensional and shear character. If there is no shear, the flow is irrotational, and so it is easy to imagine that the molecules, and therefore the director, may align along the stretching (flow) direction. In this case there is a precise analogy between extensional flow and electric and magnetic fields. In shear flow, volume elements, thus the molecules, rotate with an average angular velocity equal to the shear rate. However, even with this constant tumbling of the molecules, the director may align. The orientation in shear flow is not completely analogous to that in magnetic fields.

For an arbitrary flow in the x direction the deformation is described by the rate of strain tensor:

$$d_{ij} = \begin{bmatrix} \dot{\epsilon} & \dot{\gamma} \\ \dot{\gamma} & -\dot{\epsilon} \end{bmatrix} \qquad (1.26)$$

The magnetic field and the director have the following form:

$$\mathbf{H} = H\,[\cos\phi_H\,,\ \sin\phi_H] \qquad (1.27)$$

$$\mathbf{n} = [\cos\phi\,,\ \sin\phi]$$

The director orientation is defined by a balance of torques as described by the Euler-Lagrange equation:

$$\partial/\partial x_j\,\Pi_{ij} + f_i + f_i' = \lambda\, n_i \qquad (1.28)$$

where Π_{ij} is the curvature stress tensor, f_i is the elastic and magnetic body curvature force, f_i' is the flow body curvature force, and λ is the Lagrange multiplier. These terms depend on the following quantities:

$$\Pi_{ij} = -\partial g/\partial n_{i,j} \qquad (1.29a)$$

$$f_i = \partial g/\partial n_i \qquad (1.29b)$$

$$f_i' = (\alpha_3-\alpha_2)N_i + (\alpha_3+\alpha_2)d_{ij}n_j \qquad (1.29c)$$

where

$$\mathbf{N} = \dot{\mathbf{n}} - \omega \times \mathbf{n} , \tag{1.29d}$$

the vorticity of the director relative to that of a volume element, and

$$g = 1/2\, k\, (\nabla\phi)^2 - 1/2\, \chi_a H^2 \cos^2(\phi-\phi_H) , \tag{1.29e}$$

the elastic and magnetic free energy density.

Substituting equations 1.29 into the Euler-Lagrange equation and eliminating the Lagrange multiplier, the differential equation for the director field becomes:

$$\begin{aligned} 0 = {} & [(\alpha_3-\alpha_2)\partial/\partial t - k(\partial^2/\partial x^2 + \partial^2/\partial y^2)]\,\phi \\ & + \chi_a H^2 \sin(\phi-\phi_H)\cos(\phi-\phi_H) \\ & - 2(\alpha_3+\alpha_2)\dot{\epsilon}\sin\phi\cos\phi \\ & + 2\alpha_3\dot{\gamma}\cos^2\phi - 2\alpha_2\dot{\gamma}\sin^2\phi . \end{aligned} \tag{1.30}$$

Each of these terms represents a torque on the director. Notice that the magnetic torque is zero when the director is aligned along the field. The irrotational flow torque is zero when the director is aligned along the stretch direction, i.e. the x-axis. For extensional flow alignment, we see that the form of the equation is identical to that of magnetic alignment. As we did before for magnetic alignment, we can define a characteristic length for distortions in irrotational flow:

$$\xi = (k/(2(\alpha_3+\alpha_2)\dot{\epsilon}))^{1/2} . \tag{1.31}$$

The deformation rate is analogous to field strength squared. The same soliton structures described above for magnetic fields will also occur in extensional flows.

Finally, the shear flow torque is zero when:

$$\phi = \phi_\gamma = \tan^{-1}((\alpha_3/\alpha_2)^{1/2}) \tag{1.32}$$

The actual orientation of the director in a general flow in the presence of a magnetic field would be determined by the competition between the three orienting influences: shear flow, irrotational flow, and the magnetic field.

Shear flow, however, does not always align the director. If α_3 and α_2 are of opposite sign, ϕ_γ is undefined and the director will tend to tumble. Cladis and Torza [1976] have

investigated the effect of this instability on the director field. At low shear rates, the orientation defined by the boundary conditions is perturbed by the flow until finally a solitary wave propagates through the sample. At higher shear rates, cellular flow involving the nucleation and rapid growth of disclinations is observed.

If α_3 and α_2 are of the same sign, ϕ_γ is defined. Because these coefficients are also related to a positive rotational viscosity coefficient, $\gamma_1 = \alpha_3 - \alpha_2$, and because we expect $\phi_\gamma < \pi/4$, the viscosity coefficients, α_3 and α_2, have the following relationship:

$$\alpha_2 < \alpha_3 < 0 . \tag{1.33}$$

If ϕ_γ does exist, then it is useful to rewrite the differential equation 1.30 in terms of this angle:

$$\begin{aligned} 0 = {} & [(\alpha_3-\alpha_2)\partial/\partial t - k(\partial^2/\partial x^2 + \partial^2/\partial y^2)]\,\phi \\ & + \chi_a H^2 \sin(\phi-\phi_H)\cos(\phi-\phi_H) \\ & - 2(\alpha_3+\alpha_2)\dot{\epsilon}\sin\phi\cos\phi \\ & + 2(\alpha_3-\alpha_2)\dot{\gamma}\sin^2(\phi-\phi_\gamma) - 4(\alpha_3\alpha_2)^{1/2}\dot{\gamma}\sin(\phi-\phi_\gamma)\cos(\phi-\phi_\gamma) . \end{aligned} \tag{1.34}$$

We see from this equation that even pure shear flow alignment has a term that is completely analogous to magnetic alignment. However, there is another term (the $\sin^2$ term) which has a different symmetry. The $\sin^2$ term tends to rotate the director with the rotation of the fluid. If $\alpha_3 \sim \alpha_2$ (this is approached at temperatures very near to the isotropization), then the $\sin^2$ term is weak and the shear flow too would orient the director analogous to the magnetic field. More commonly, i.e. at lower temperatures, the $\sin^2$ term becomes stronger and the sincos term becomes weaker. In this case, director alignment due to shear and magnetic fields are not analogous. We may still define a characteristic length for distortions in shear flow:

$$\xi = (k/(4(\alpha_3\alpha_2)^{1/2}\dot{\gamma}))^{1/2} . \tag{1.35}$$

Soliton structures will also occur in sheared samples, but the structure will no longer be symmetrical about the center of the wall. The soliton will be skewed; the exact structure has not been solved.

1.5 How to characterize a texture in terms of measurable properties?

If there are no orienting influences the texture is easily described by the average disclination density, ρ_d. This may be measured from microscopy, or approximately measured from light scattering. Unfortunately these methods require either sections of a sample or films only a few microns thick. The sample dimensions, L, which are easily measured also help to define the texture.

In the presence of an orienting field the texture is more difficult to describe. It is necessary to measure the characteristic length, ξ, of distortions in that field. This may be measured via microscopy as is described in chapter 6. Also once the material properties are known, the characteristic length may be calculated from the applied field strength. The surface area of inversion wall/unit volume, ρ_w, is an inverse length which describes the average separation between walls. In some cases, such as a periodic structure of inversion walls, ρ_w may be measured via light scattering, but, in general, ρ_w is most easily measured via microscopy. Also because the orientation correlations are no longer related to the disclination density, the disclination density must be measured by microscopy. To describe clustering, the average disclination separation, d, must also be measured.

It can be rather difficult to simply describe the texture in liquid crystals. However, four length scales are apparent: the disclination separation ($\rho_d^{-0.5}$), sample size (L), the characteristic length (ξ), and the inversion wall separation (ρ_w^{-1}). Characterization of the texture in terms of these parameters is a central theme of my dissertation.

1.6 Introduction to thesis

The principle aim of this thesis is to understand the structure and interaction of the director field features through their direct observation. Properties of isolated disclinations as well as their interaction have been characterized. Interaction both with and without an applied field has been investigated. This work is also a preliminary effort to inventory some

of the appropriate lengths to describe the texture of quiescent and magnetically or flow oriented TLCP's.

The observation of the submicron structure of the director field of thermotropic liquid crystal polymers (TLCP's) was accomplished using Barbara Wood's lamellar decoration technique. I have also extended this technique, using an amine etch, to image sections of bulk samples. Both unoriented and oriented samples have been imaged. I describe the lamellar decoration technique and its extension in chapter 3.

Because crystallization is necessary for the lamellar decoration technique, I describe crystallization in chapter 2. The structure of the liquid crystal phase is also discussed in this chapter.

In unoriented samples, the director field is characterized by an array of disclination defects. Disclination interaction and motion are believed to strongly influence the rheological behavior of liquid crystals at slow deformation rates. Many body disclination interaction in the absence of a field is studied via computer simulation in chapter 4.

The core structure of disclinations in unoriented samples is studied in chapter 5. We are interested in disclination core structure because of its consequences on disclination mobility. Various theories predict inhomogeneous structure at the disclination core, but experimental investigations have been extremely limited--inferring structure from optical microscopy and studies of disclination motion. In our experiments, we measure the relative apparent elastic constants of the material as a function of distance from a disclination. The key to success in investigating the core structure has been the ability to probe where the distortion gets to be nearly 1/L, where L is the molecular length. The molecular length for the polymers studied (~ 100nm) is at an observable scale.

Polymer structure provides a unique variable for the core structure. The distinction between low molecular weight liquid crystals and polymer liquid crystals can often be described by various macroscopic properties, e.g. transition temperatures, elastic constants, and viscosities. The theory reviewed in this chapter is universal to both small molecules and

polymers. The core structure, however, is distinctly different for polymer liquid crystals, as it is determined by molecular parameters. The effect of molecular architecture is described in chapter 5. The aggregation of chain ends observed at the disclination core for some types of molecules is expected to retard disclination motion. These observations are unique, and lamellar decoration is the technique best suited to measure core structure.

Oriented textures are described in chapter 6. In oriented samples, disclinations may still be common. Because disclination positions may be precisely observed, we can gain basic understanding of disclination interaction in magnetically and flow oriented samples. From our observations we are able to illustrate the analogous behavior of extensional flow and magnetic fields. By considering magnetic alignment, we are able to precisely describe the fundamental difference between the disclination interaction in oriented and unoriented samples.

Through the observations and calculations in this thesis, we are gaining insight into the behavior and structure of disclinations and inversion walls.

CHAPTER 2

CRYSTALLINE MICROSTRUCTURES OF THERMOTROPIC LIQUID CRYSTAL POLYMERS

Crystal structure and morphology must be controlled to optimize solid state properties of polymers. Therefore, crystallization was well studied in the early days of polymer science. A variety of microstructures may be obtained depending upon the crystallization temperature, pressure, and time. The deformation rate during crystallization, which may induce orientation, controls the morphological organization of the crystallites. Keller [1968] gives a fine review of these effects.

The recent availability of rigid and semi-flexible polymers which form a nematic phase opens the door to a new set of studies. Atkins et al. [1988] have studied the structure of regular semi-flexible polymers. Biswas and Blackwell [1988] and Windle et al. [1985] have investigated the crystal structure of a nematic random copolymer. In Windle's paper, the crystallites were demonstrated to have lamellar morphology. The morphological organization of lamellar crystallites, however, has been little studied. Hahn [1987] and Jonsson et al. [1989] have studied the morphology of spherulites grown from solutions of semi-flexible polymers.

Wood [1985], Mazelet and Kleman [1988], and Shiwaku et al. [1990] have observed the lamellar morphology of melt crystallized thermotropic liquid crystal polymers (TLCP's). Their results show the unique effect of the precursor nematic phase. They observed lamellae everywhere perpendicular to the local molecular orientation which existed in the nematic precursor. This morphology, termed the lamellar decoration morphology, may be formed by rapidly quenching and annealing the sample. My thesis predominantly uses this technique in order to investigate some physics of the nematic phase. This chapter, however, includes a preliminary investigation of the crystal morphology of TLCP's. Depending on the relative

crystal nucleation and growth rates, the morphological organization of the lamellae can be controlled. The lamellar decoration morphology is favored by rapid nucleation and slow growth. The opposite conditions may be obtained by slow cooling to a relatively high crystallization temperature. In this case, spherulites are observed to grow from a nematic melt for the first time.

Before discussing morphology in the later half of this chapter, I discuss the chemical structure of TLCP's as well as the crystal structure of one of the regular semi-flexible polymers which I have studied.

2.1 Molecular structure of TLCP's

Liquid crystal polymers in general may be either lyotropic or thermotropic. Thermotropic liquid crystal polymers (TLCP's) were later in developing, because rigid polymer molecules often decompose before melting to a liquid crystalline state. Schematic structure of different types of TLCP's is shown in figure 2.1. In order to reduce the melting

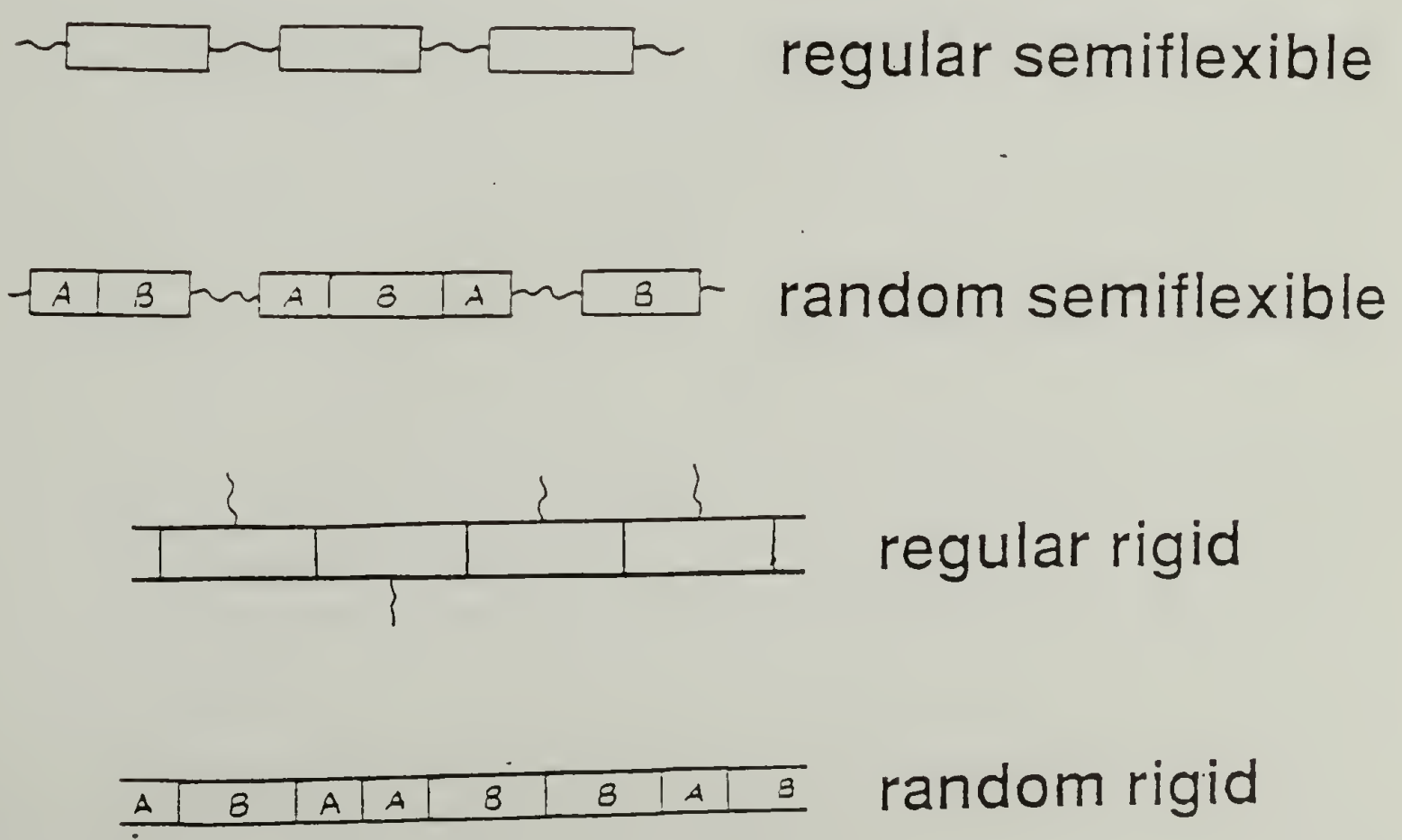

Figure 2.1 Schematic molecular structure of TLCP's.

point of TLCP's some limited flexibility may be included in the main polymer chain in the form of a flexible spacer. If the spacer and mesogen (rigid unit) are strictly alternating, the polymer is called a regular semi-flexible thermotropic polymer. The spacer may also be randomly placed along the polymer chain giving a random semi-flexible thermotropic polymer. In this case, the randomness along the polymer backbone reduces the stability of the crystal and further lowers the melting point. The melting point has also been suppressed in regular rigid molecules using flexible side chains. These flexible side chains mediate intermolecular interactions between chains. Another method of suppressing the melting point of a rigid chain is to randomly copolymerize two different mesogenic monomers in order to form a random rigid TLCP. Although a traditional periodic crystal structure is not possible, x-ray evidence reveals that even aperiodic chains are able to form three dimensional crystals [Biswas and Blackwell, 1988; and Windle et al., 1985]. The crystallites are lamellar and can be imaged via TEM [Windle et al., 1985].

Regular rigid, regular semi-flexible, and random semi-flexible TLCP's have been kindly provided by Professor R. Lenz of the University of Massachusetts and Professor S. Stupp of the University of Illinois. The chemical structures of various polymers are shown in figure 2.2. The transition temperatures and approximate molecular weights and lengths of these polymers are shown in table 2.1. The regular rigid TLCP's [Lenz et al., 1990] have the structure shown in figure 2.2(a). We term these polymers QT-X. The main chain is designated by QT because it is composed of hydroquinone and terephthaloyl units. X signifies the substituent on the hydroquinone unit.

A consistent nomenclature is used for the semi-flexible TLCP's. Figure 2.2(b) shows the chemical structure of TQT10-X [Zhou and Lenz, 1983], where the 10 denotes the ten carbon spacer between mesogens. Figures 2.2(c) and 2.2(d) show other regular semi-flexible TLCP's [Ober et al., 1982]. Figure 2.2(e) shows a random semi-flexible TLCP [Martin and Stupp, 1988]--OQ5a--where the a denotes that the 5 carbon flexible spacer had acid groups at either end.

QT-X

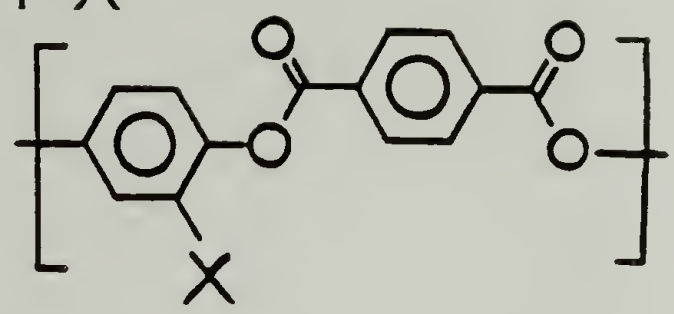

TQT10-X

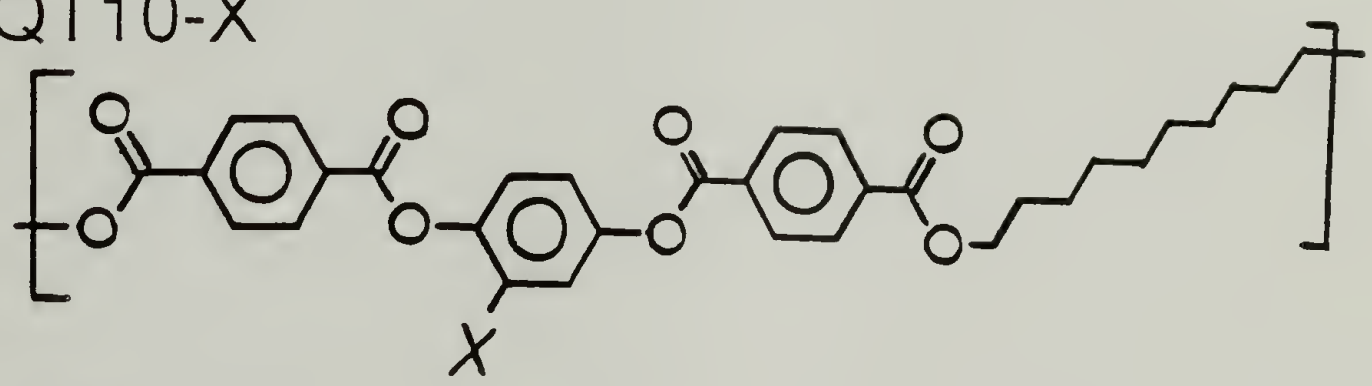

OTO6

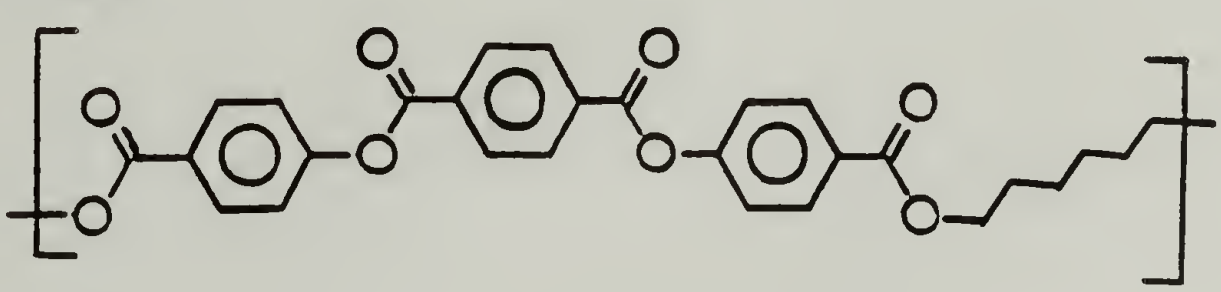

OQO8a

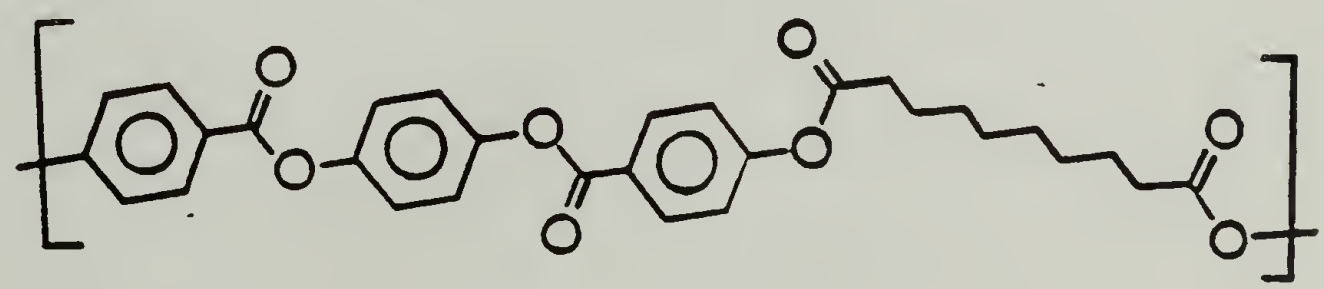

OQ5a

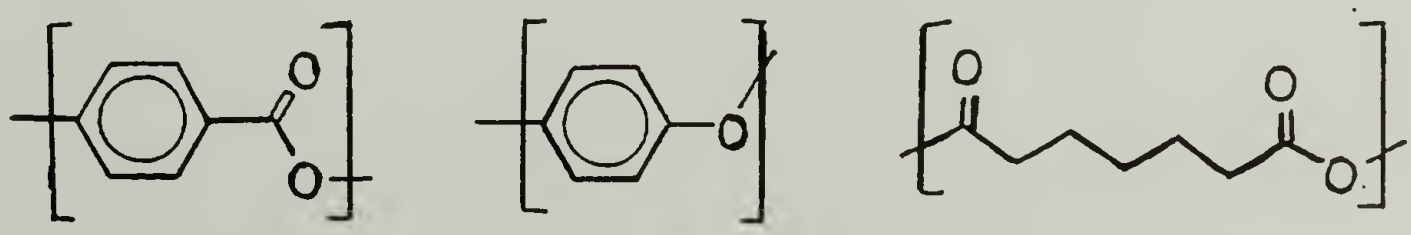

Figure 2.2 Chemical structure of various TLCP's studied. The substituent, X, is randomly attached to one of the four sites on the hydroquinone unit.

Table 2.1. Polymers studied in this thesis.[1]

Backbone	Substituent	T_g (°C)	T_N (°C)	T_I (°C)[2]	M_v (g/mol)[3]	L (nm)[4]
Regular rigid						
QT	OEOM[5a]	120	180	224	~5,000	~25
	OEOE[5b]	110	160	233	~5,000	~25
	OEOEOE[5c]		145	257	~15,000	~70
Semi-flexible						
Regular						
TQT10	H[5d]	67	231	267	~18,000	~100
	M[5e]	44	154	190	~9,000	~50
	O[5f]		105	165	~20,000	~100
OTO6			227	275		
OQO8a			190			
Random						
OQ5a	% spacer[6]			$T_{biphase}$[7]		
#1	33.3		142	226	~3,000	~20
#1	33.3		142	226	~16,000	~100
#6	27.8		180	250	~3,000	~20

Notes:
1. Data included in this table has been measured by those who synthesized the polymers. It is included in the references cited in the text.
2. Transition temperatures are measured by DSC and optical microscopy.
3. Estimates are based on inherent viscosity measurements.
4. Contour length of the polymer chain.
5. Substituents; a: ethoxymethoxy; b: ethoxyethoxy; c: ethoxyethoxyethoxy; d: unsubstituted; e: methyl; f: octyl.
6. Percent spacer in the monomer feed. Solution NMR of resultant polymers shows spacer contents a few percent higher. NMR also shows random dyad structure of the main chain.
7. Above this temperature, isotropic and nematic phases coexist.

The crystallization behavior of these polymers has not been studied before. Since their glass transitions are above room temperature, they can be quenched to form liquid crystalline glasses. If annealed above their T_g, they crystallize readily. TQT10-O is the only polymer included which does not crystallize readily. The lamellar decoration morphology is easily obtained by quenching and annealing. The spherulitic morphology has only been obtained from the nematic melt of OTO6.

2.2 Crystal structure

The crystal structure of one polymer, TQT10-M, has been investigated using density measurements, x-ray diffraction, and TEM. The unit cell and the general features of the crystal structure have been solved.

The density of the polymer was measured using a density gradient column. 10 and 30 weight percent NaBr solutions were proportionally mixed to fill the column with a solution with a linear density gradient from approximately 1.12 to 1.23 g/cm^3. Glass beads of known density were allowed to settle to their equilibrium depths. The calibration curve is shown in figure 2.3.

Beads of the polymer were formed by melting some polymer powder onto a piece of Teflon heated by a hotplate. Two beads were made. The samples were quenched by dunking

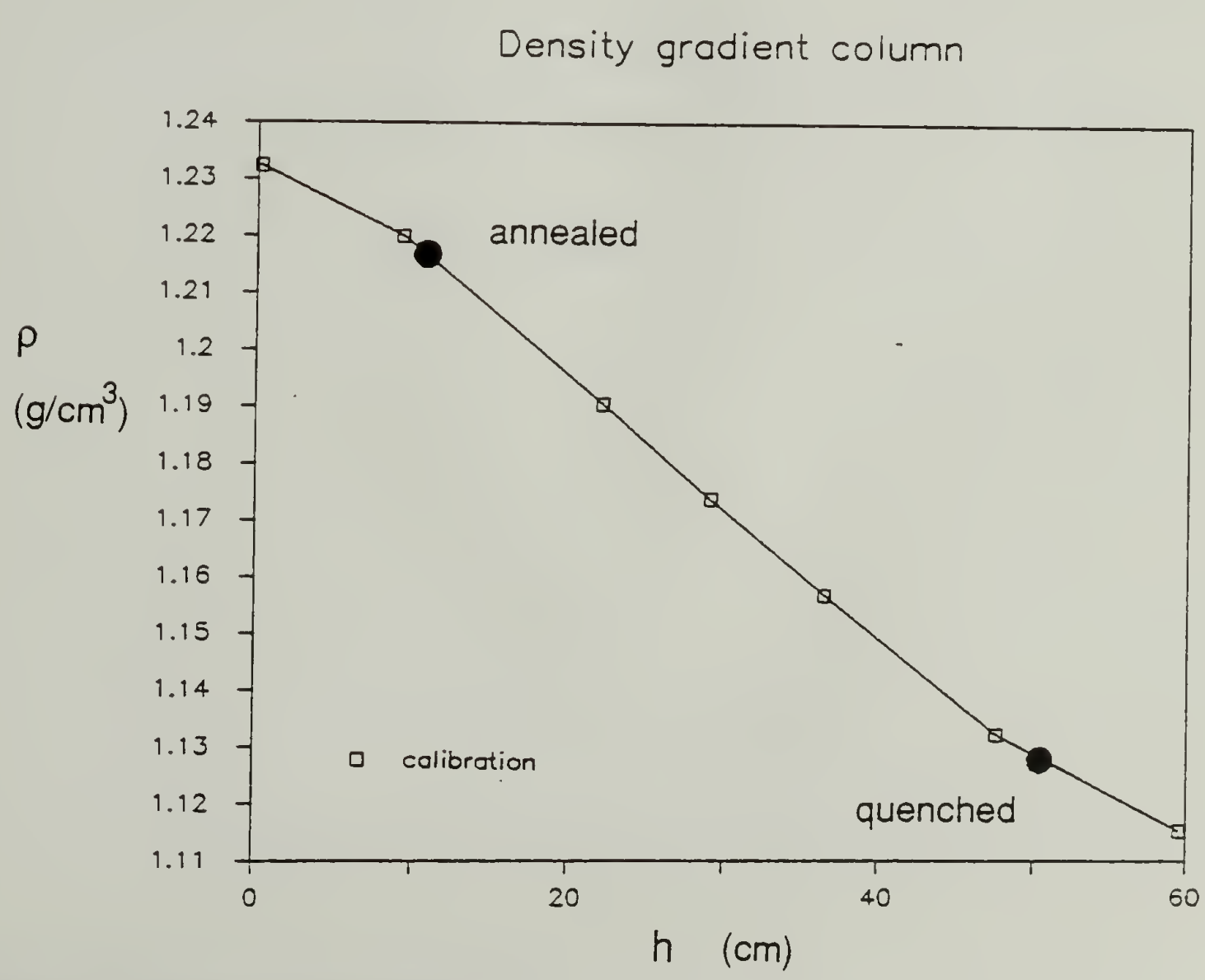

Figure 2.3 Density gradient column data.

the Teflon into an acetone/dry ice bath. One bead was analyzed as quenched while the other was annealed at 135°C for 21 minutes. Figure 2.4(a) shows the x-ray scattering from the quenched bead. The strong diffuse ring at wide angles is due to side to side correlations in the frozen nematic (glassy phase). Weak inner rings are due to correlations along the chain. The density of the quenched sample was found to be 1.13 g/cm^3 (see figure 2.3). Figure 2.4(b) shows the x-ray diffraction from the annealed sample. The crystallinity of the sample appears to be quite high. The density of the semi-crystalline sample was found to be 1.22 g/cm^3. Crystallization has caused a 8% density increase.

The diffraction pattern of a sample may be predicted by using a construction developed by Ewald--the intersection of the reciprocal lattice of the crystal with a sphere of radius $1/\lambda$. The origin of the reciprocal lattice is on the sphere (always a forward scattered

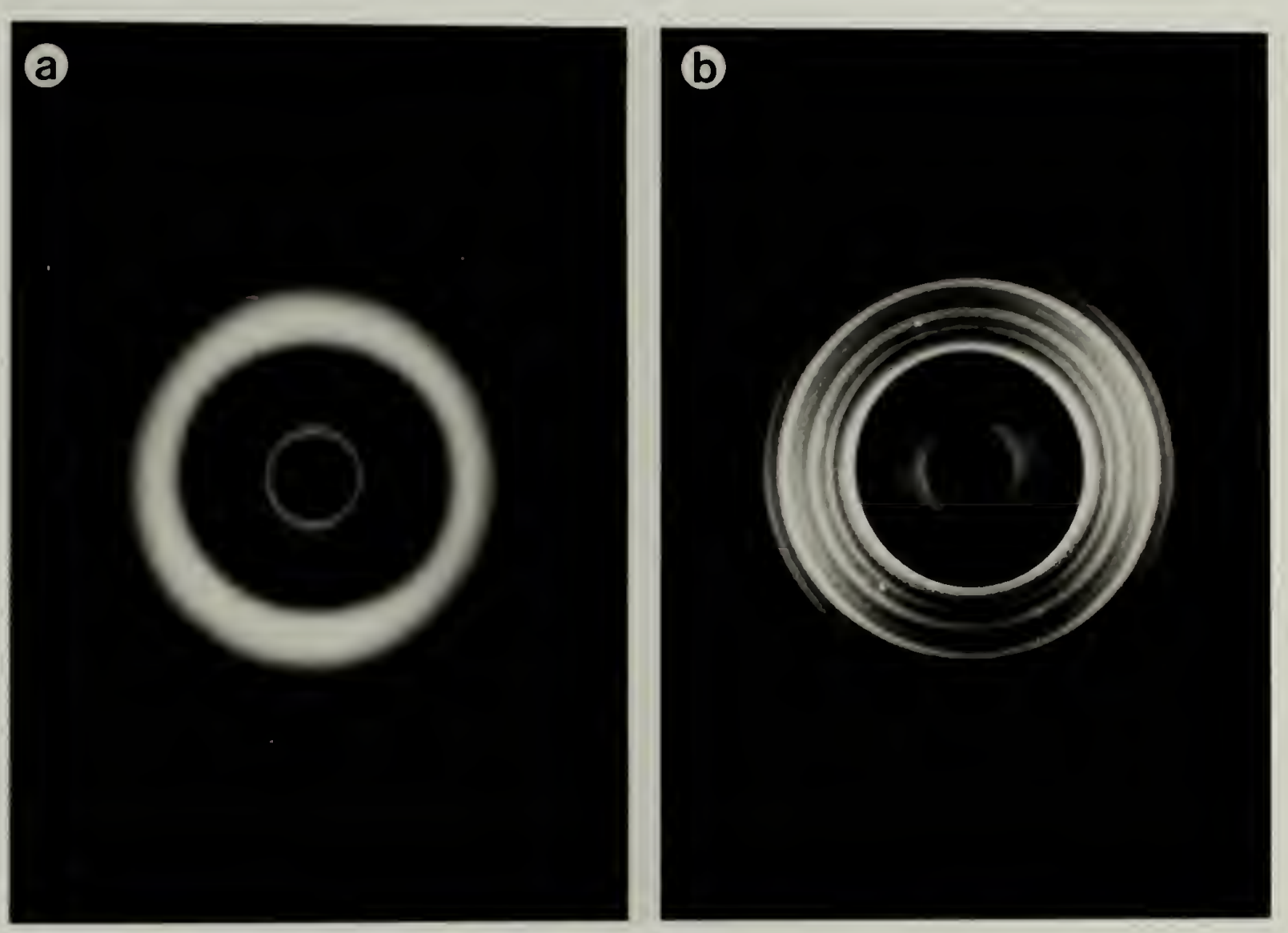

Figure 2.4 X-ray diffraction of unoriented TQT10-M polymer. (a) Quenched and (b) Annealed. The densities of these samples is recorded in figure 2.3

beam). For a single crystal (having one specific orientation), very few of the reciprocal lattice sites will intersect the Ewald sphere. Only those crystal planes which are oriented properly will reflect x-rays. The sample has a distribution of crystal orientations. For an unoriented sample each of the reciprocal lattice sites is distributed over a sphere. In this case, any reciprocal lattice sphere smaller than the Ewald sphere will intersect the Ewald sphere to form a ring. Each type of crystalline plane forms a ring in the diffraction pattern, as shown in figure 2.4(b).

Density measurements and x-ray diffraction combine very effectively to determine the crystal structure. Although much of the data regarding the unit cell of crystal structure is included in the x-ray diffraction of the bead, unit cell determination is significantly easier if the sample may be oriented. In this way, it is possible to differentiate equatorial reflections (crystal planes parallel to the polymer chain axis) from meridional reflections (planes perpendicular to the chain axis) and straight away make some conclusions regarding the structure.

Oriented samples for x-ray scattering may be formed by pulling a fiber from the melt. The liquid crystalline structure is presumed to be frozen in as the material quenches in air.

An oriented polymer thin film, suitable for TEM, may be formed by surface tension spreading of the polymer on hot H_3PO_4. The process is shown schematically in figure 2.5. Solid polymer is placed on the surface of hot phosphoric acid. It melts and spreads due to its lower surface tension (figure 2.5(a)). Initially the deformation is biaxial, with the largest component of extension in the radial direction. Subsequently, fingers develop radially (figure 2.5(b)). Some orientation develops in this first stage of deformation if the spreading is rapid enough. The sample is quenched by transferring it to a room temperature bath of H_3PO_4. A large degree of orientation may be achieved in this second stage of deformation if the hot acid and polymer are rapidly poured into the quench bath. The thin TLCP film skates across the surface in parallel fingers which experience planar elongational flow (figure 2.5(c)). Some shear deformation is expected through the thickness of the film. However, the shear

deformation may be minimal, because the viscosity of the polymer is expected to be greater than that of the fluid substrate. The resulting TLCP film is glassy and highly oriented. The film is then transferred to a water bath to wash the film before placing it on a copper TEM sample grid. The sample may be viewed directly and/or annealed before observation in the TEM.

X-ray scattering patterns of air-quenched fibers are shown in figure 2.6(a). The regular chemical structure of the polymer gives rise to periodic layer lines perpendicular to

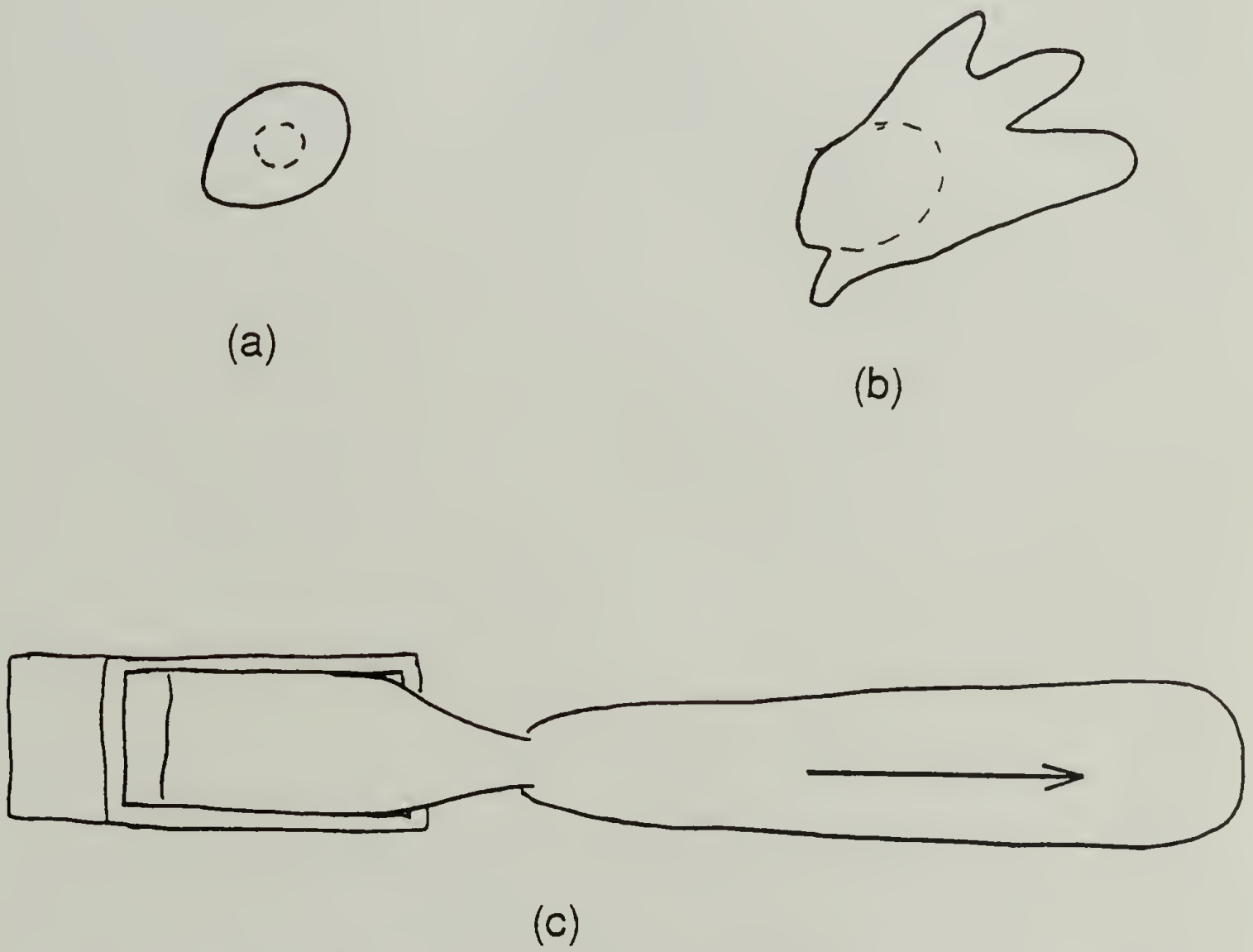

Figure 2.5 Surface tension spreading of TLCP on a hot fluid substrate. Drawings are looking down normal to the TLCP film. (a) Initially the deformation is biaxial with the largest component of deformation in the radial direction. A dotted line depicts the droplet at a previous time. (b) Fingers form in the radial direction. (c) Highly elongational planar flow occurs as the polymer film is poured from the trough (shown in perspective) onto the quench bath. The elongation is in the direction shown by the arrow. The stretched film is drawn only as one finger for clarity.

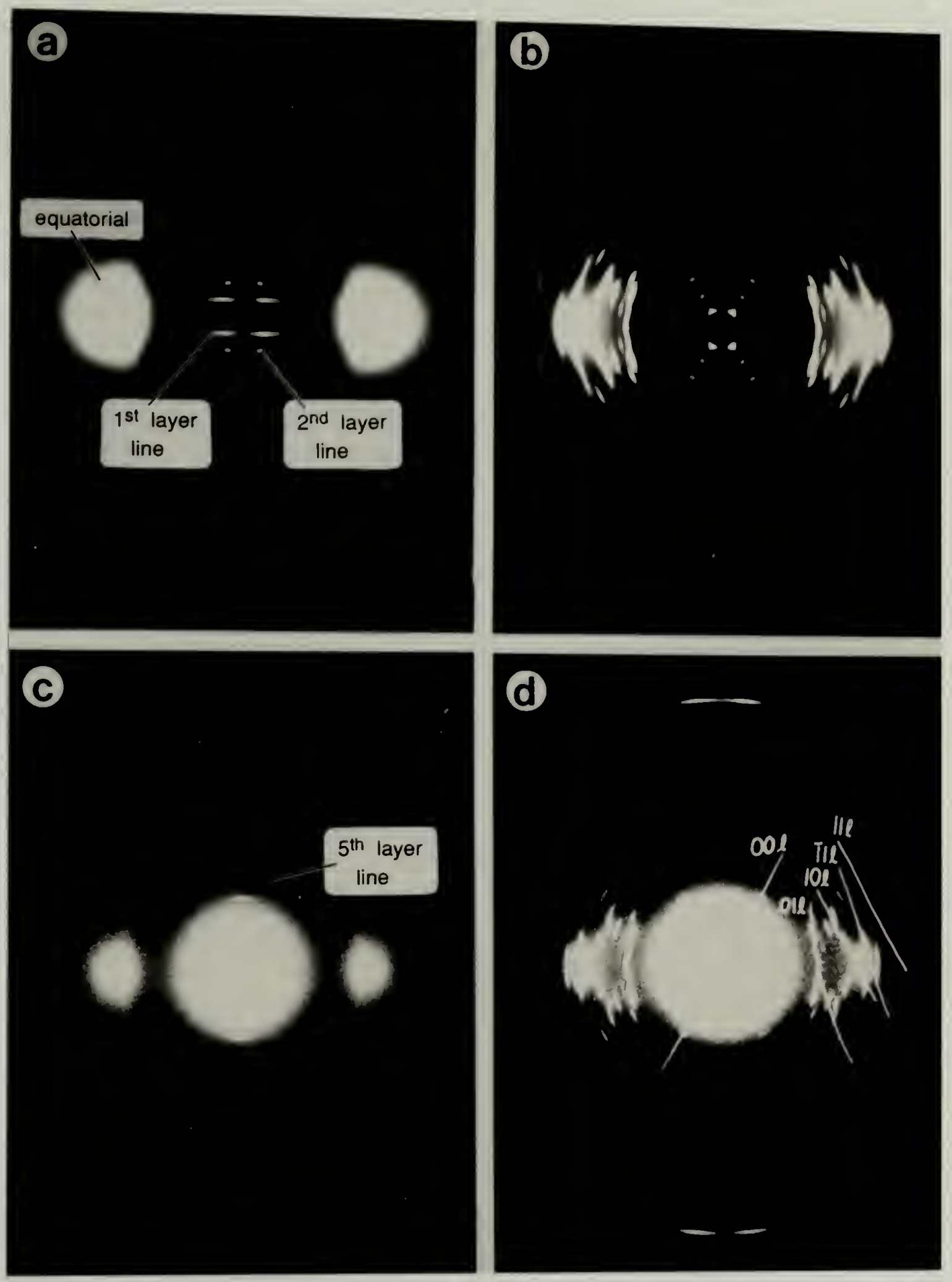

Figure 2.6 Scattering patterns of oriented TQT10-M. (a) X-ray diffraction of quenched fiber. (b) X-ray diffraction of annealed fiber. (c) Electron diffraction of quenched oriented thin film. (d) Electron diffraction of annealed oriented thin film.

the chain axis. If the quenched sample were truly glassy nematic, the axial shift between neighboring chains would be random. In this case, the scattering pattern is determined by the scattering from a single chain. Each layer line would be diffuse, having an intensity modulation due to the modulation of the Fourier transform of an individual molecule. If the sample were crystalline, diffraction spots would appear on these layers. This is observed in figure 2.6(b) which shows the diffraction pattern from the sample after annealing at 135°C for 18 minutes. Uniaxial texture is expected in the case of the macroscopic fiber examined by x-ray. For a uniaxial texture each reciprocal lattice point forms a ring about the orientation direction. This ring then intersects the Ewald sphere at a point.

The quenched sample is not crystalline, and the diffuse first layer line in figure 2.6(a) indicates considerable axial shift disorder, characteristic of the nematic state. The sharper spots on the 2^{nd} and 4^{th} layer lines are puzzling, however. Note too that in the semi-crystalline state the 4^{th} layer line spot has disappeared. In the electron scattering pattern of a quenched and oriented thin film, figure 2.6(c), the 5^{th} layer line is diffuse indicating again axial disorder. The large blobs of intensity on the equatorial, shown in both figures 2.6(a) and 2.6(c), indicate non-crystalline side to side packing between chains.

The electron diffraction pattern shown in figure 2.6(d) of a uniformly oriented semi-crystalline domain is very similar to the x-ray pattern shown in figure 2.6(b). Both exhibit the cross pattern at the origin and the same pattern of spots along and just above and below the equator (horizontal axis). The main differences are seen along the vertical axis or meridian. This effect is not due to a difference in structure but only due to the difference in wavelength between the x-rays and the electrons. In terms of the Ewald construction, the Ewald sphere ($r \sim 1/\lambda$) is much flatter in the case of electron diffraction, so that wider angle meridional reflections may be observed. In the case of x-rays, only small angle meridional reflections may be observed without tilting the fiber. The spots observed in x-ray along the vertical axis are off-meridional spots which intersect the Ewald sphere.

The similarity of the two patterns suggests that the thin film also has a uniaxial texture. This is easily verified in the TEM by tilting the sample about the orientation direction. Uniaxial symmetry was observed for tilts of ±54°.

Before deriving a unit cell, it is instructive to learn the crystal symmetry from the general features of the diffraction pattern. The unit cell is chosen to be the repeat unit of the crystal with the highest symmetry. The edges of this cell define three vectors, $\mathbf{v}_j$ (**a**, **b**, and **c**). The diffraction pattern has a symmetry defined by the reciprocal lattice.

$$\mathbf{a}^* = \mathbf{b} \times \mathbf{c} / (\mathbf{a} \cdot \mathbf{b} \times \mathbf{c}), \qquad (2.1)$$

$$\mathbf{b}^* = \mathbf{c} \times \mathbf{a} / (\mathbf{a} \cdot \mathbf{b} \times \mathbf{c}),$$

$$\mathbf{c}^* = \mathbf{a} \times \mathbf{b} / (\mathbf{a} \cdot \mathbf{b} \times \mathbf{c}),$$

where $\mathbf{a}^*$, $\mathbf{b}^*$, and $\mathbf{c}^*$ are the basis vectors of the reciprocal lattice. These three vectors have the reciprocal property:

$$\mathbf{v}^*_i \cdot \mathbf{v}_j = \delta_{ij}\,; \qquad (2.2)$$

where $\delta_{ij} = 1$ when $i = j$ and zero otherwise. In general, however, $\mathbf{v}^*_i$ is not parallel to $\mathbf{v}_i$. They are parallel for an orthorhombic crystal where the unit cell vectors are mutually perpendicular.

In a drawn, highly oriented fiber we expect that the polymer chain axis is along the fiber axis. We define the repeat in this direction as the unit cell vector **c**. If **c** is perpendicular to both **a** and **b**, then **c** and $\mathbf{c}^*$ are parallel. In this case, we expect then diffraction spots along vertical columns as is shown in figure 2.7(b). Figures 2.7(a) and 2.7(b) are x-ray scattering patterns of quenched and annealed fibers of TQT10-O. From the semi-crystalline sample we see that the crystal symmetry is at least monoclinic (**c** perpendicular to **a** and **b**).

The cross pattern at the origin of the diffraction pattern in figure 2.6(b) (p.40), however, indicates that **c** is not perpendicular to both **a** and **b**. The unit cell may be monoclinic or triclinic. In the TQT10-M crystal structure, there exists therefore an axial displacement between neighboring chains in the crystal.

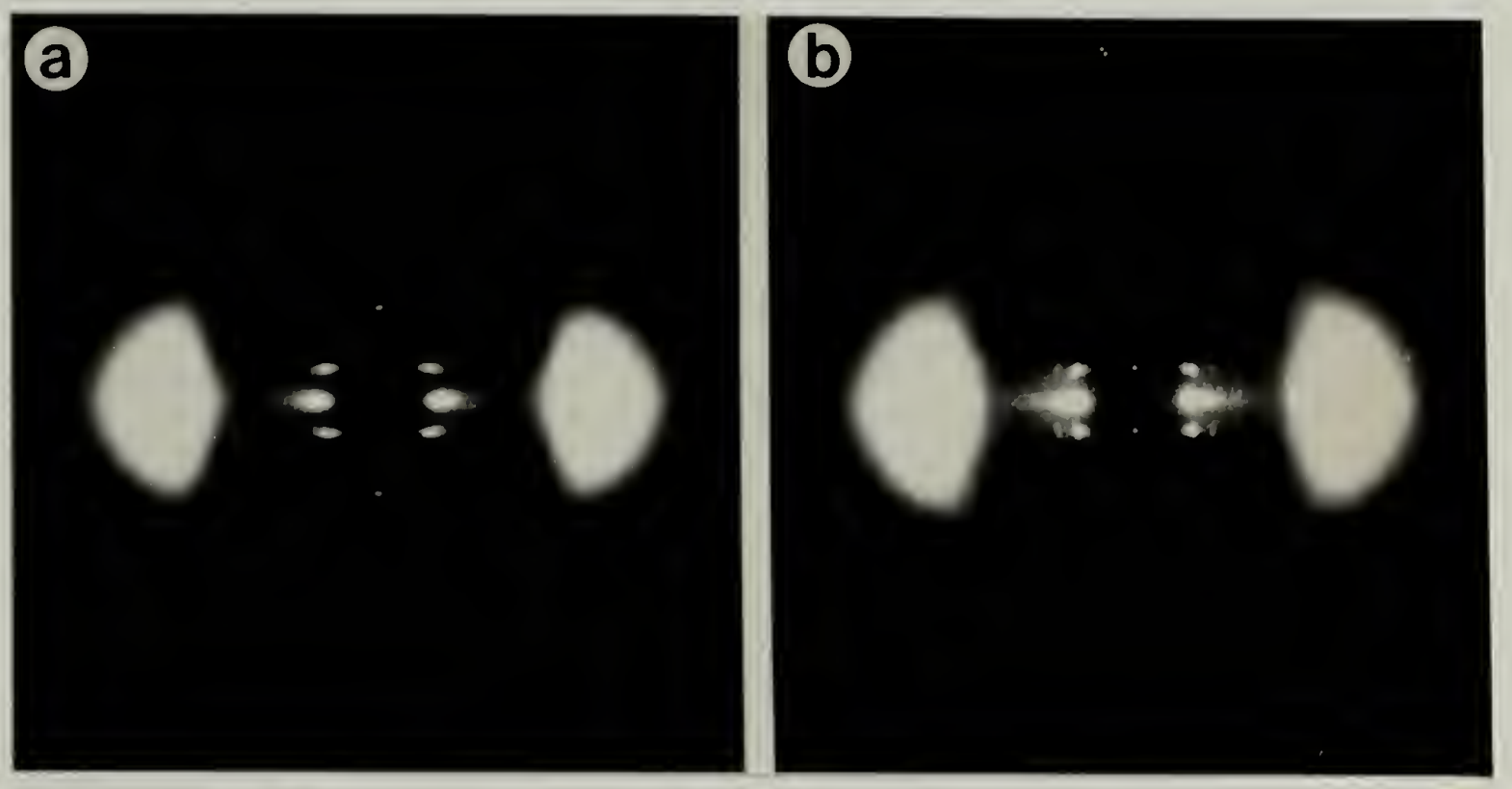

Figure 2.7 X-ray scattering patterns of oriented TQT10-O. **c** and $\mathbf{c}^*$ are parallel. (a) Quenched. (b) Annealed at 102°C for 2 hours.

Consider diffraction from a triclinic crystal structure with a uniaxial texture about the chain axis. What is the pattern formed by a series of hkl reflections where h and k are fixed? (h, k, and l are coordinates of the reciprocal lattice in units of the basis set: $\mathbf{a}^*$, $\mathbf{b}^*$, and $\mathbf{c}^*$.) This question can be answered by calculating the distance between the chain axis and an axis in the reciprocal lattice, where h and k are fixed. The resulting equation is a hyperbola, and the resulting diffraction pattern gives spots which lie along hyperbolae. Figure 2.6(d) (p.40) shows the electron diffraction pattern with hyperbolae traced over the spots of constant h and k.

From the diffraction pattern then we are able to determine that the crystal structure has low symmetry. We have also been able to determine which reflections are grouped in families. The unit cell then becomes quite trivial to calculate. The positions of the reflections are measured, and their intensities are also grossly estimated, ranging from very weak to very strong. Unit cell parameters are entered in order to minimize the error

between the measured and the calculated atomic plane spacings. In order to account more strongly for the more intense reflections, the error for each reflection may be arbitrarily weighted by its intensity. Using a hand iterative procedure the various parameters can be solved as shown in table 2.2. The comparison between the calculated and measured spacings is good. The general accuracy of the unit cell may also be seen by comparing the diffraction pattern in figure 2.6(d) with the schematic electron diffraction pattern shown in figure 2.8.

We conclude that the chain is nearly fully extended, because the value of 3.214nm for the c-axis corresponds to the value of 3.322nm for an extended chain. The fully extended chain conformation was calculated using tabulated values for bond lengths in similar compounds. Using the (002) and the (003) reflections from the x-ray diffraction of the annealed sample which was used for density measurements (figure 2.4(b)) yields a value of 3.195nm for the c-axis repeat. The chain is also nearly fully extended in unoriented semi-crystalline samples.

The very strong (100) equatorial reflection corresponds to planes having a spacing of 0.37nm. This spacing is typical for aromatic ring stacking. Therefore we assume that the molecule in the all trans state having a planar conformation lies in the b, c plane of the unit cell.

Assuming one monomer repeat per unit cell, the crystal density calculated from these parameters is 1.38g/cm^3. The percent crystallinity in the annealed sample for which a density of 1.22 was measured is therefore 36%. This value is lower than that expected based upon the well ordered appearing x-ray diffraction pattern shown in figure 2.4(b). Perhaps the unannealed sample was not quenched fast enough to prevent some crystallization.

Information on the chain in the nematic liquid state may be calculated from the quenched x-ray diffraction patterns. Both oriented and unoriented samples (with scattering patterns shown in figures 2.6(a) and 2.4(a)) are found to have 3.115nm repeat distances along the polymer chain. The flexible spacer is therefore assumed to be nearly fully extended even in the nematic phase.

Table 2.2 Unit cell calculated from x-ray diffraction data for TQT10-M.

Sample: TQT10-M TLCP 558.6 g/(mol repeat)
Camera L: 49.27 mm
Wavelength: 0.1542 nm

Unit cell parameters:

a :	0.451 nm	α :	96.8°
b :	0.562 nm	β :	121.9°
c :	3.214 nm	γ :	95.7°
V_{uc} :	0.674 nm^3	ρ :	1.376 g/cm^3

error*: 0.0543 (nm)

reflection			intensity	position (mm)		spacing (nm)	
h	k	l		y	z	d_{meas}	d_{calc}
0	0	1	vs	1.50	2.43	2.66	2.67
0	0	2	m	2.98	4.79	1.35	1.34
0	0	3	m	4.44	7.27	0.90	0.89
0	0	6	vw	8.88	14.96	0.46	0.45
0	0	7	vw	10.44	17.85	0.39	0.38
0	0	9	w	13.45	24.23	0.30	0.30
0	1	0	s	14.39	0.00	0.54	0.55
0	1	1	w	15.08	2.53	0.51	0.52
0	1	2	s	15.92	5.10	0.47	0.47
0	1	3	s	16.89	7.79	0.43	0.43
0	1	4	s	17.96	10.46	0.39	0.39
0	-1	1	m	13.93	2.27	0.55	0.56
0	-1	2	vs	13.54	4.76	0.55	0.55
0	-1	3	s	13.38	7.36	0.51	0.52
0	-1	7	w	14.54	17.98	0.35	0.35
1	0	0	vs	21.98	0.00	0.37	0.38
1	0	1	w	23.30	1.81	0.35	0.35
1	0	3	w	26.81	6.59	0.31	0.29
-1	0	1	s	20.21	1.25	0.40	0.40
-1	0	2	s	18.46	4.03	0.42	0.43
-1	0	3	w	16.86	6.22	0.44	0.44
-1	0	9	w	6.38	22.23	0.35	0.34
-1	1	0	vs	24.15	0.00	0.34	0.34
-1	1	1	w	23.30	1.81	0.35	0.36
-1	1	2	vs	21.68	4.04	0.37	0.37
-1	1	3	s	20.83	6.99	0.37	0.37
-1	1	4	s	19.80	9.47	0.37	0.36
-1	-1	0	w	28.74	0.00	0.30	0.29
-1	-1	1	w	26.68	3.98	0.31	0.30
-1	-1	2	w	25.10	6.22	0.32	0.31
-1	-1	3	w	23.33	9.22	0.33	0.33

*Note: The error is defined as the root sum square difference between the calculated and the measured d spacings. The difference squared was arbitrarily weighted according to the intensity of the reflection as follows:
vw: 1.0; w: 1.4; m: 2.0; s: 2.8; vs: 4.0

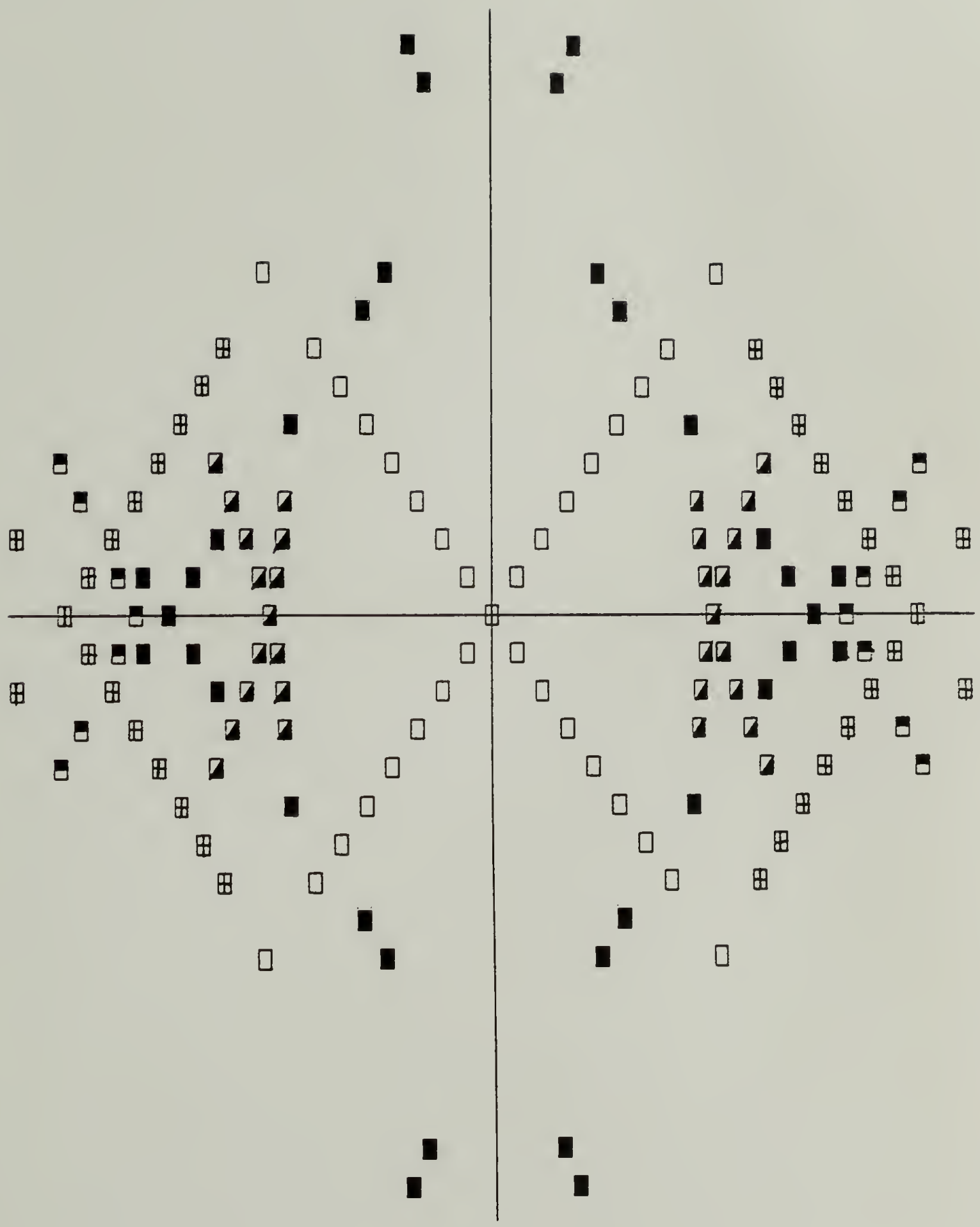

Figure 2.8 Schematic electron diffraction pattern generated from the unit cell parameters given in table 2.2.

key: □ 00ℓ ◪ 01ℓ ■ 10ℓ ▬ $\bar{1}$1ℓ ⊞ $\bar{1}\bar{1}$ℓ

2.3 Crystal morphology

TLCP crystals are similar to those of typical flexible chain polymers. They are observed to be lamellae whose thickness is inversely related to the undercooling. The morphological organization of lamellae can be controlled by the precursor state, and the relative primary nucleation and growth rates. When nucleation is rapid and growth slow, a unique morphology develops where the lamellae are everywhere perpendicular to the director in the precursor nematic phase. When nucleation is slow compared to the growth rate, spherulites are observed to grow from the nematic.

2.3.1 Lamellae size

The lamellae shape could be obtained from the diffraction pattern by measuring the width of various peaks: L_a, L_b, and L_c from (h00), (0k0), and (00l) reflections respectively. The lamellar repeat (the long period) could be obtained from small angle x-ray diffraction. These techniques are quantitative, provided the model used for interpretation is correct. Imaging is superior for qualitative understanding and direct visualization of local correlations. Using TEM, the crystallites are easily observed to be periodically spaced lamellae, which are locally parallel.

Figure 2.9 shows a bright field diffraction contrast TEM image of a melt spread thin film. The defocus was approximately zero, so density differences in the material do not contribute significantly to the image. An objective aperture was used to block electrons scattered at large angles. The diffracting electrons are blocked by the aperture, and the lamellae oriented such that they satisfy the Bragg condition for diffraction appear dark. The lamellae thickness along the chain direction is typically observed to be 15nm, while the lamellar periodicity is 30nm. The lateral dimension of the lamellae varies with polymer sample and with cooling rate from the nematic state. In figure 2.9 is shown a rapidly quenched melt spread sample of OQO8a polymer and the lateral size of the lamellae is

observed to be approximately 200nm. In rapidly quenched TQT10-M samples the size is approximately 80nm.

Dark field images have been obtained by tilting the incident beam in order to image diffracting crystals. Lamellae are also observed in rigid chain TLCP samples. Figure 2.10 shows dark field micrographs of a QT-OEOM melt spread thin film. Figure 2.10(a) was formed using an equatorial reflection. The randomly dispersed lamellae, as in figure 2.9, are characteristic of a uniaxial texture. Figure 2.10(b) is formed using a meridional reflection. The diffraction from this polymer shows that $\mathbf{c}^*$ is parallel to $\mathbf{c}$, so crystals of all orientations about $\mathbf{c}$ may be observed in (00l) dark field. Lamellae are not, however, observed throughout the field of view because of slight orientation fluctuations of the director about the flow

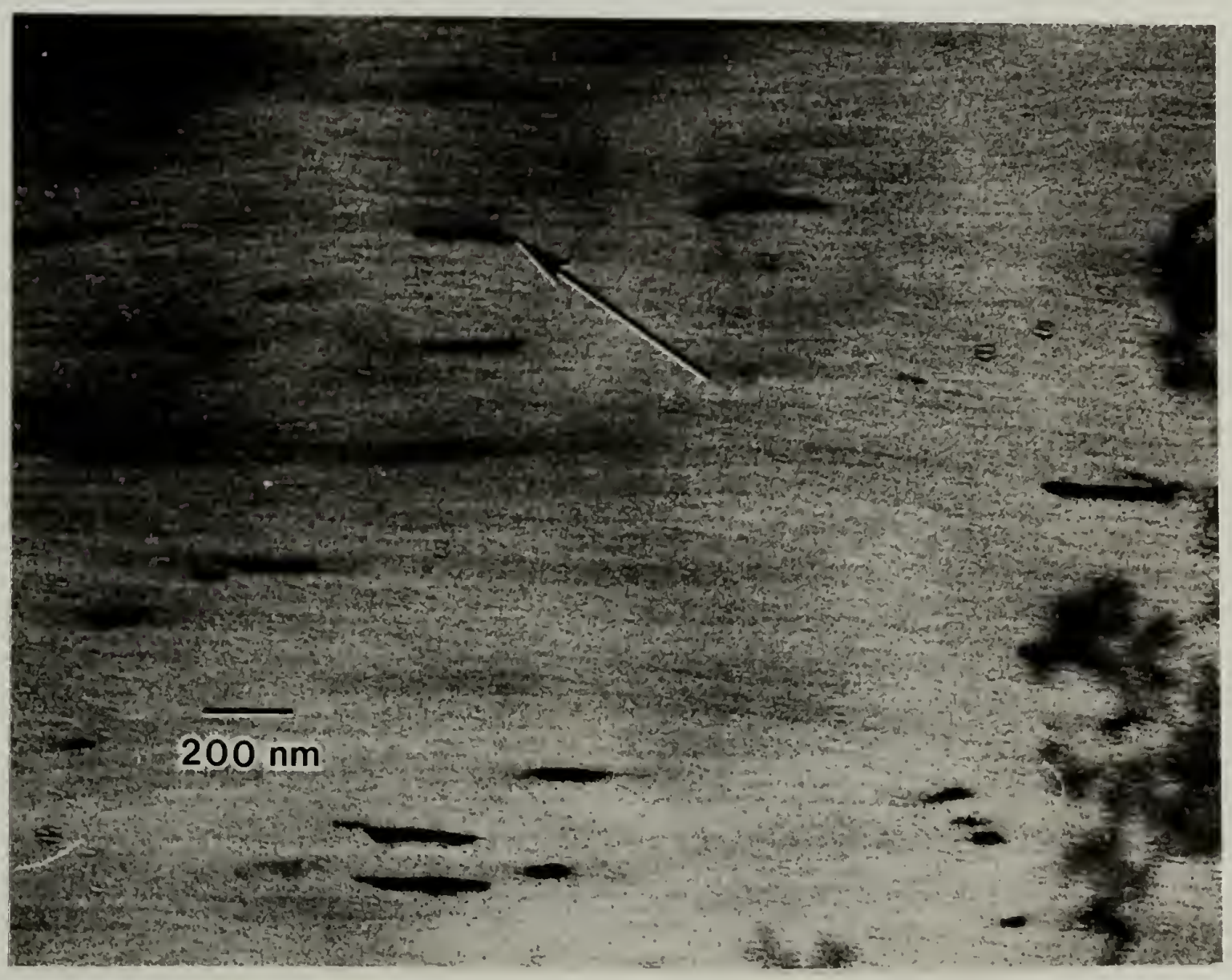

Figure 2.9 Crystalline lamellae of OQO8a observed in bright field TEM. Diffracting lamellae (~ 20x200nm) appear dark using diffraction contrast. One of the diffracting lamellae is arrowed.

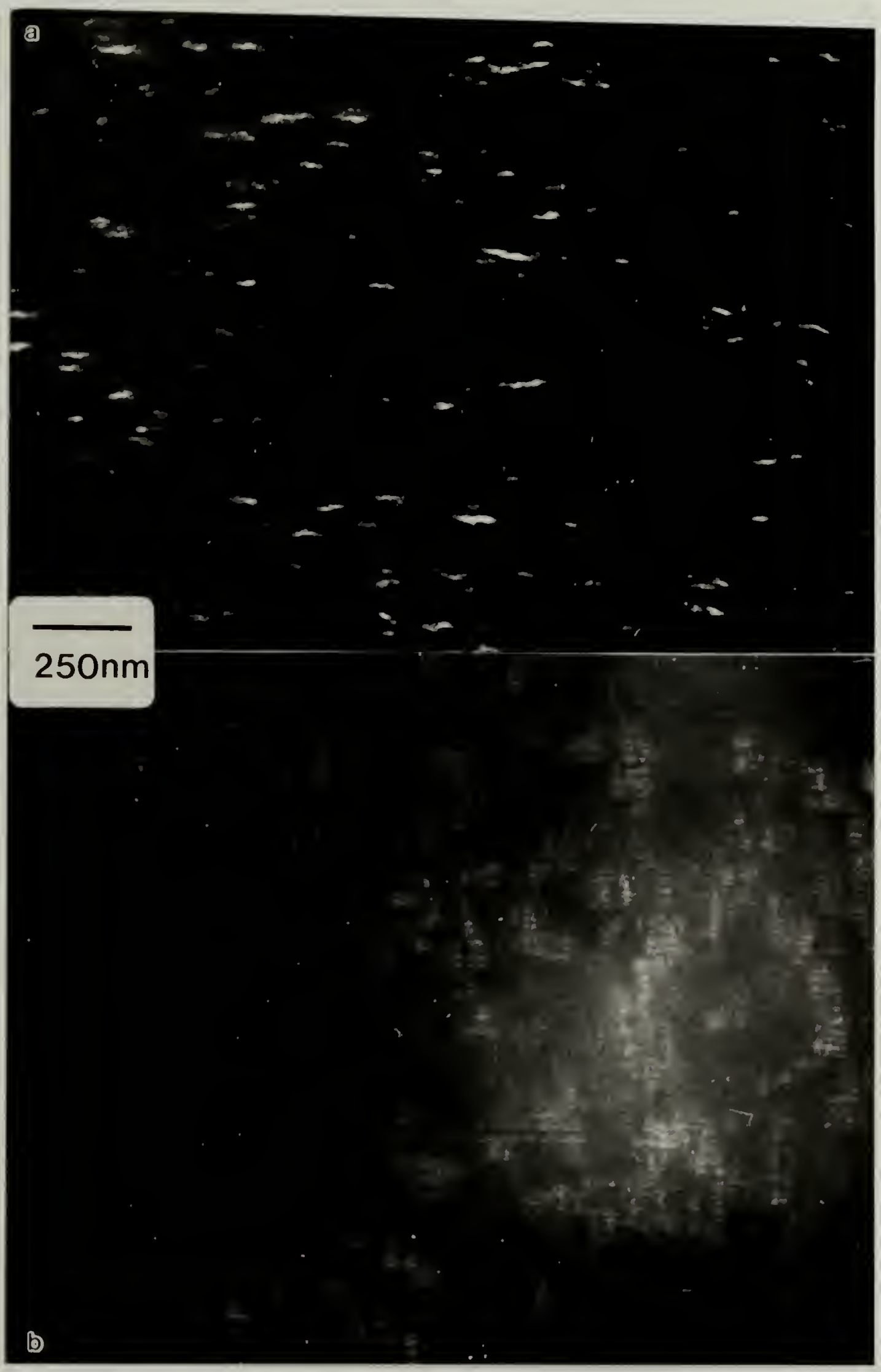

Figure 2.10 Crystalline lamellae of QT-OEOM observed in dark field TEM. (a) Equatorial dark field. (b) Meridional dark field.

direction. Where the lamellae are observed, the background is also brighter because the glassy nematic between lamellae is scattering electrons through the aperture. The chain axis in both the lamellae and the glassy nematic are therefore parallel. Further demonstration of this will come in the next chapter.

2.3.2 Nucleation density control of morphology

Although it is noteworthy that TLCP's, and even more interesting that rigid TLCP's (QT-OEOM), form lamellar crystals, the foundation for this thesis is the unique morphology formed when TLCP's are quenched and subsequently annealed. When cooling at 100°C/sec, almost no crystals grow during the quench. Electron diffraction of quenched samples (figure 2.6(c)) shows no evidence of crystallinity. In order to crystallize the sample, it is relatively slowly reheated at ~ 1°C/sec to approximately 20°C below the melting point. By the time it reaches this temperature, the sample is assumed to be already densely populated with crystal nuclei, and the resultant crystals are small. The nuclei, and therefore the lamellae, derive their orientation from the local orientation which existed in the supercooled nematic. The molecular orientation is unperturbed by the crystallization process. Lack of reorientation is also encouraged by lower diffusion coefficients at lower crystallization temperatures. This morphology (shown in figure 2.9) is termed the lamellar decoration morphology, because the lamellae, which can be observed via TEM, decorate the nematic director field without observable alteration of the chain axis from the precursor nematic to the semi-crystalline state. The region shown in figure 2.9 was a uniformly oriented nematic monodomain. Figure 2.11(a) shows disclinations which introduce distortion into the director field. Note that the disclinations are not characteristic of the semi-crystalline state, but they pre-existed in the nematic. Note from figure 2.11(a), that even in regions where the distortion of the director has been concentrated to small regions, the crystal size is small enough to reveal that the director varies smoothly. Observation of the lamellar decoration morphology is further discussed in the following chapter.

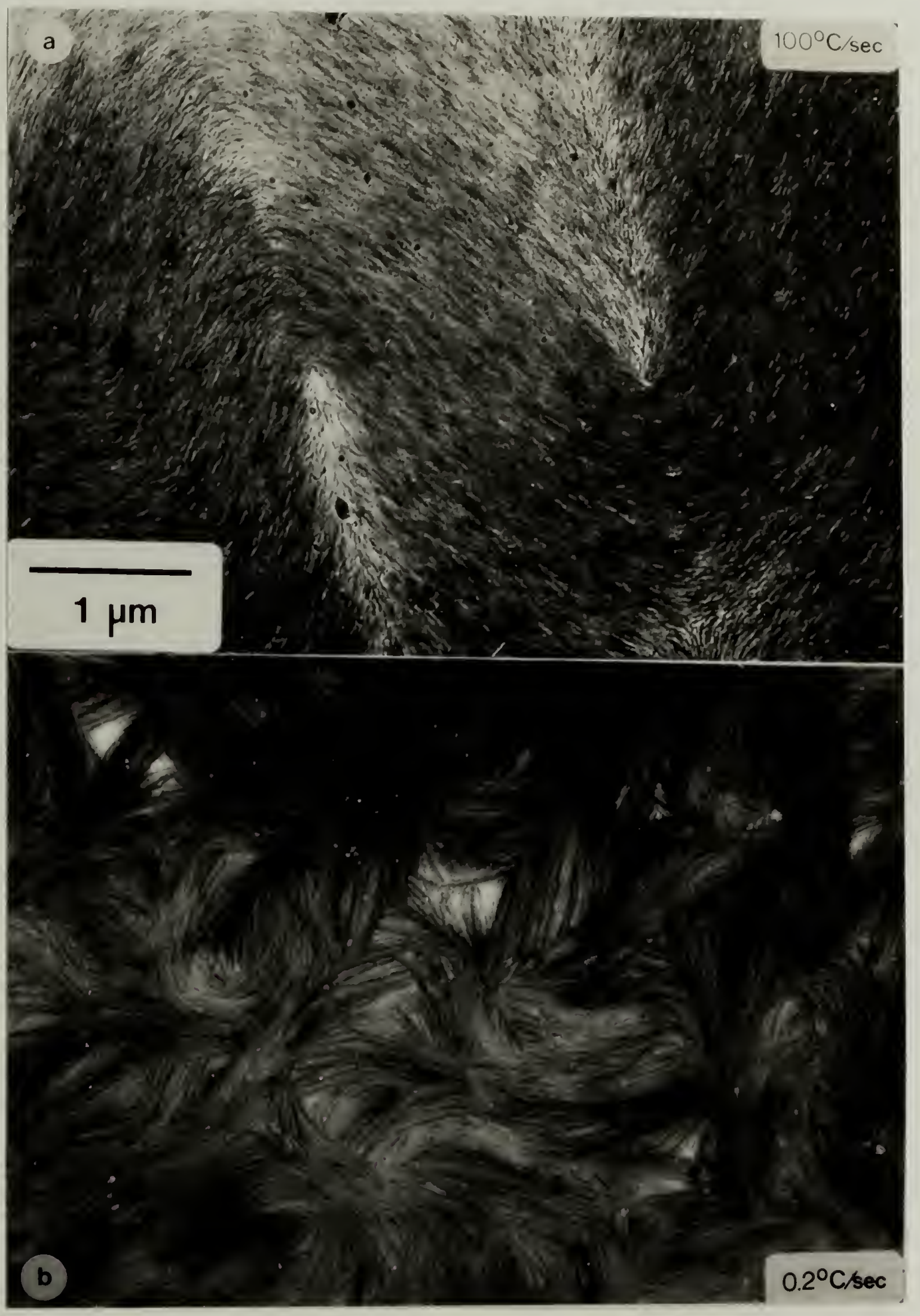

Figure 2.11 Morphology of TQT10-M for (a) rapid (100°C/sec) and (b) slow (0.2°C/sec) cooled samples. The lamellae in (b) are thicker and larger than those in (a). The lack of spherulites in (b) may be due to a high defect density in the precursor nematic, or perhaps TQT10-M is less likely to form spherulites than OTO6 shown in figure 2.12. See text for sample preparation.

Although the lamellar decoration morphology is unique to nematic TLCP's, somewhat analogous results have been obtained with flexible polymers such as polyethylene. In the case of a flexible polymer, the orientation existing before crystallization must be induced by processing, since there is no inherent orientation in isotropic melts as there is in nematic melts. If the material is drawn prior to and during crystallization, lamellae are observed to grow perpendicular to the orientation direction [Keller, 1968]. The lamellae therefore decorate the draw direction. At some deformation rates, long needle-shaped crystals may grow parallel to the stretching direction [Keller, 1968].

The preorientation may also be induced by a precrystallization. Lotz [1989] first grew large spherulites in an isotropic polyethylene melt by crystallizing at a high temperature. These crystals were then mostly melted then recrystallized at a lower temperature. The original spherulite structure was destroyed, but the nuclei for the second crystallization (unmelted crystals) had their orientation defined by the spherulitic structure of the first crystallization. The second crystallization produced smaller spherulites not much larger than a sheaf. Their sheafs decorated the large precursor spherulite, and the light scattering pattern of the final sample showed two sizes of spherulites--or spherulites within spherulites. This is not lamellar decoration as is observed in TLCP's, but this morphology is intermediate between lamellar decoration and spherulitic.

TLCP's may also exhibit both intermediate and spherulitic morphologies. The spherulitic morphology is favored by low nucleation density and rapid growth. Because crystallization may occur as soon as the material is cooled below the melting temperature, the quench rate can dramatically affect the morphology. During cooling, the polymer may nucleate and grow crystals characteristic of the temperature at which they are formed. A cooling rate of about 10°C/sec is necessary to obtain lamellar decoration in these polymers.

Figure 2.11 (p.50) compares the morphology of the TQT10-M semi-flexible polymer for two different quench rates. The sample shown in (a) was prepared on phosphoric acid, and quenched at approximately 100°C/sec by rapidly pouring it onto a quench bath. In order

to control more accurately the quench (cooling) rate, a thin film sample was cooled from the nematic in a Metler hotstage at 0.2°C/sec. This sample is shown in (b). (A sample prepared in a similar fashion but quenched rapidly is shown in figure 4.5.) Significant crystallization occurred during slow cooling, so that subsequent annealing was not necessary. In (a) the lamellae appear to be ~ 13nm thick with a periodicity of ~ 26nm. In (b) the lamellae appear to be ~ 25nm thick with a periodicity of ~ 35nm. The crystallinity in (b) is apparently greater. The lamellae in (b) also appear larger and straighter than those in (a), and their orientation does not vary smoothly. The small regions (250 nm in size) which appear lighter are regions where the film is thinner. These regions where the film is thinner are predominantly where the director was highly distorted (perhaps the cores of the disclinations). During crystallization the material diffused away from such highly strained regions in order to contribute to the growth of neighboring crystals. This cooling rate clearly does not produce the lamellar decoration morphology. Neither does it produce a spherulitic texture.

OTO6 is a polymer which is observed to form a lamellar decorated morphology when it is rapidly quenched and annealed. Spherulites were grown, however, in slowly cooled samples as shown in figure 2.12. The sample, whose nematic temperature is 227°C, was cooled slowly (0.1-0.2°C/min) to 184°C, where spherulites were observed to nucleate and grow. To obtain isolated spherulites as shown in figures 2.12(b) and 2.12(c), the sample was quenched during the crystallization process into a room temperature water bath. Subsequent annealing at 184°C caused no further growth of the spherulite. Small crystals of the lamellar decoration morphology are presumed to have grown during the subsequent annealing.

The type of the spherulite obtained from the nematic OTO6 melt was characterized to be negative. Using a quarter wave plate and an optical microscope, the orientation of the birefringence was observed to be tangential. This is interpreted as chain folded lamellae radiating from the spherulite center.

Figure 2.12 Optical micrographs of the spherulitic morphology formed while crystallizing OTO6 at 184°C after cooling 0.1-0.2°C/sec from the nematic melt. (a) A completely crystallized sample viewed with crossed polars.

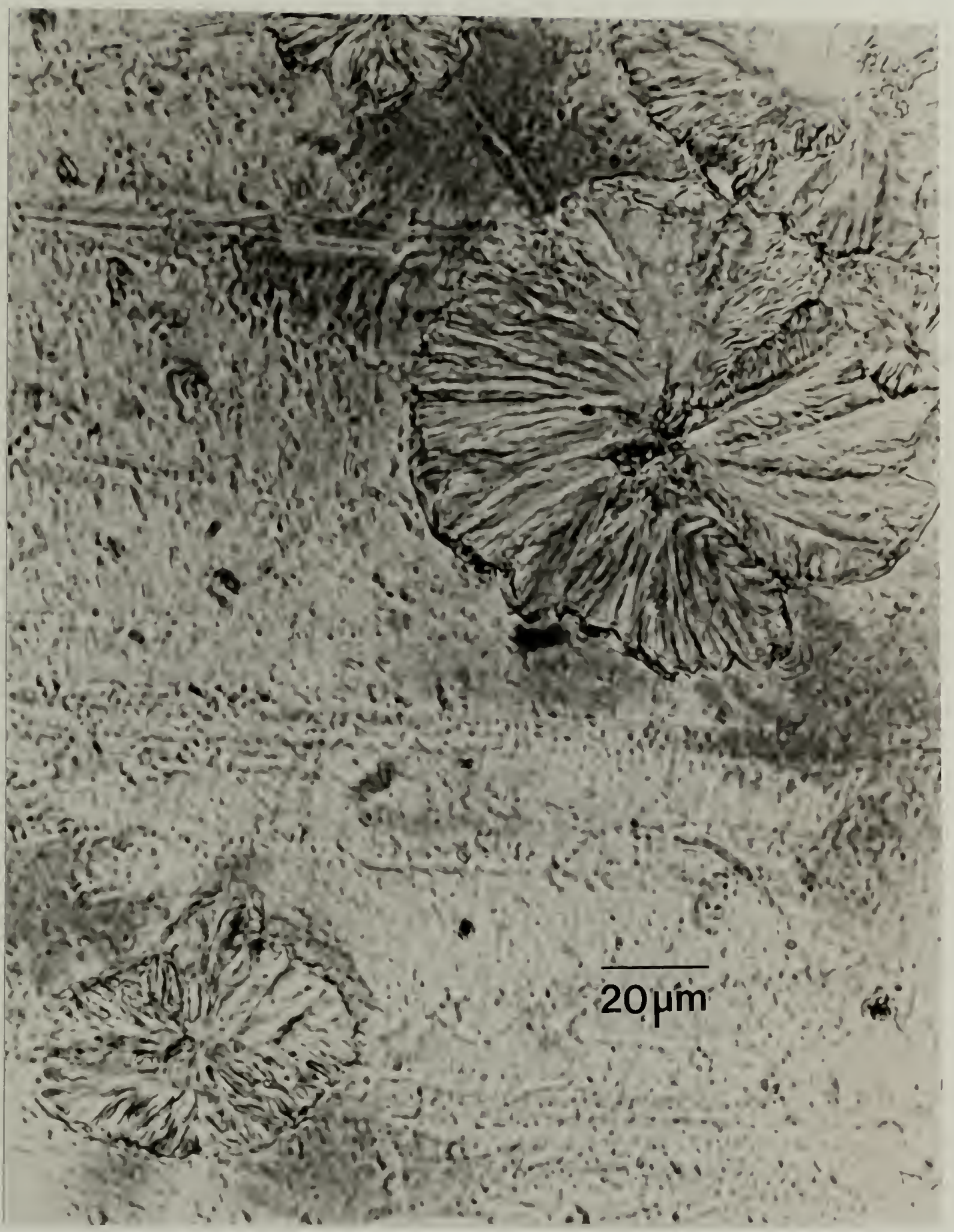

Figure 2.12 Optical micrographs of the spherulitic morphology formed while crystallizing OTO6 at 184°C after cooling 0.1-0.2°C/sec from the nematic melt. (b) Isolated spherulites obtained by quenching the sample during growth. The sample is viewed with no polarizers.

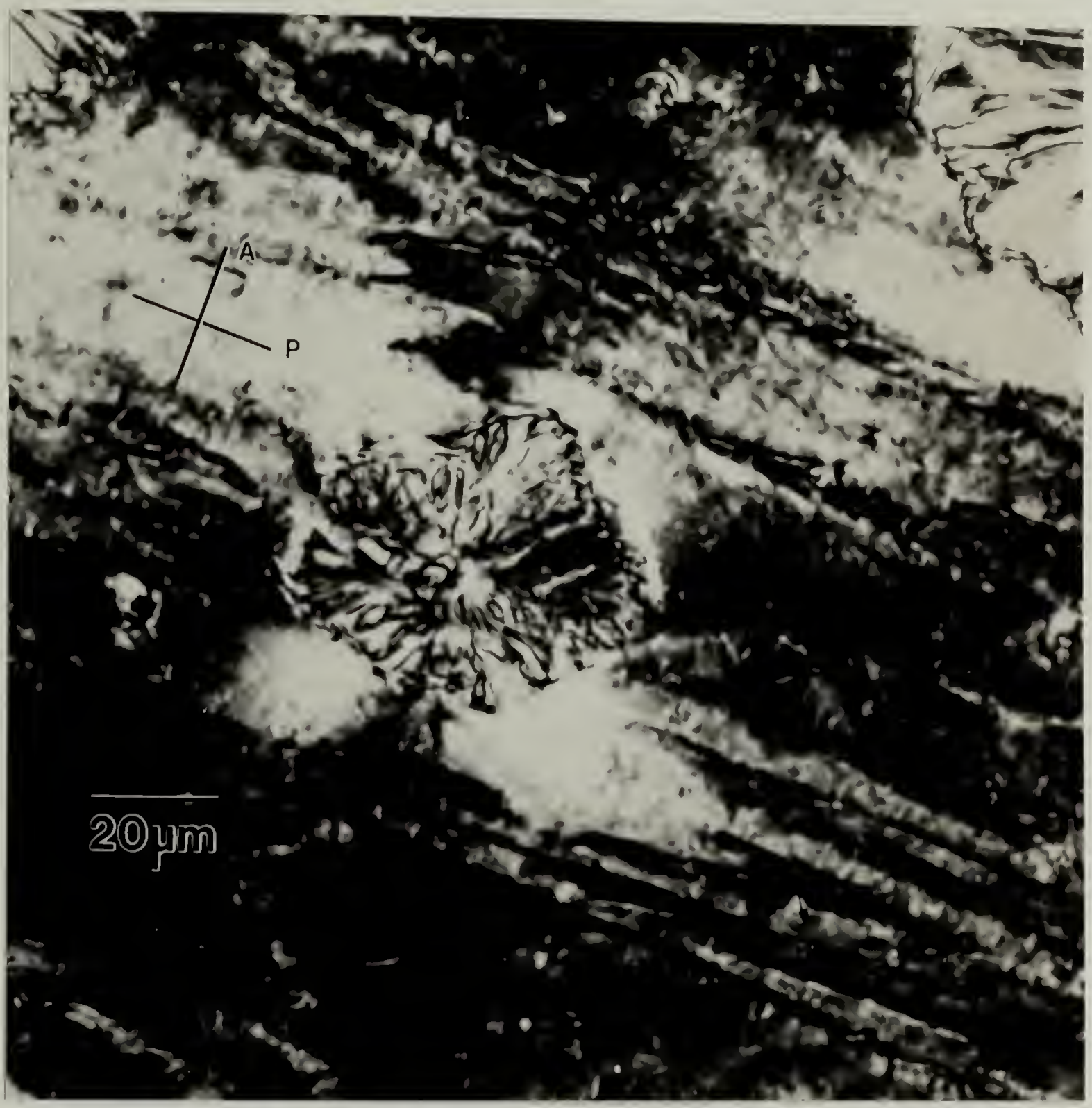

Figure 2.12 Optical micrographs of the spherulitic morphology formed while crystallizing OTO6 at 184°C after cooling 0.1-0.2°C/sec from the nematic melt. (c) Isolated spherulites viewed between crossed polarizers. Note the white lobes outside the spherulite in the supercooled nematic. The growing spherulite appears to have reoriented the melt in front of the growing crystal.

Figure 2.12(c) shows an isolated spherulite in a quenched sample viewed between crossed polars. This figure demonstrates the unique relationship found in TLCP's between a growing crystal and the supercooled nematic. In isotropic flexible chain melts, the field of view is completely dark outside of the spherulite. In figure 2.12(c), the surrounding supercooled nematic is highly oriented. Because the orientation of the surrounding nematic is along the polarizer the field of view is dark. However, outside each quadrant of the spherulite, the nematic appears bright. The growing spherulite therefore tends to reorient the director in the nematic, which may mean that the molecular orientation is continuous across the nematic-spherulite boundary.

Approximately the same cooling rate was used for the OTO6 and the TQT10-M samples. The TQT10-M sample did not, however, produce a spherulitic texture. This is most probably due to the faster crystallization rate of TQT10-M. The effect of the texture of the precursor, however, is not known, and the higher disclination density of the TQT10-M sample may have inhibited spherulite growth.

2.3.3 Future work

This work may be the first time that spherulites have been grown from a nematic. Jonsson and co-workers [1989] and Hahn [1987] have both grown spherulites from solution. Further work must be done to examine the mechanism for spherulite growth from a nematic melt. Obviously, the relative nucleation and growth rates largely determine whether or not spherulites appear. But questions still remain about what molecular properties are required. Classically, the spherulite morphology develops due to segregation of non-crystallizable impurities [Keith and Padden, 1964]. Since a random semi-flexible TLCP could segregate more flexible segments, would spherulites form more easily?

Aims for future work include observation of spherulitic samples via TEM. To do this spherulites grown in thin films for direct observation are desired. However, using the etch technique described in the next chapter, one will be able to investigate the morphology of

spherulites in thick films. It would be interesting to investigate whether there is any effect of the texture of the precursor nematic state. Is spherulite morphology independent of disclination density? Further investigation of the interface between the supercooled nematic and the growing spherulite should also be done. Is the orientation continuous across the boundary? Are any defects created or destroyed by the crystallization?

2.4 Summary

The relative nucleation and growth rates are observed to determine the morphology of the semi-crystalline state of TLCP's; this is reviewed in the schematic figure 2.13. A unique morphology occurs when the primary crystal nucleation rate is high. In this case, the local molecular orientation is relatively unperturbed by crystallization. The crystallite morphology is lamellar, where the thickness varies from 12-25nm and the lateral dimension from 80 to several hundred nm, with smaller crystals being obtained at lower crystallization temperatures. Lamellae grow perpendicular to the local orientation and therefore decorate the director field of the precursor nematic phase. If the primary nucleation density is low, spherulites are observed. Spherulitic growth in a previously uniformly oriented nematic is observed to reorient the director of the nematic phase at the spherulite boundary. The crystal structure of TLCP's was also investigated via diffraction and density measurements. Low symmetry triclinic or monoclinic crystals typically occur. The crystallinity varies with crystallization conditions and is approximately 35-70%.

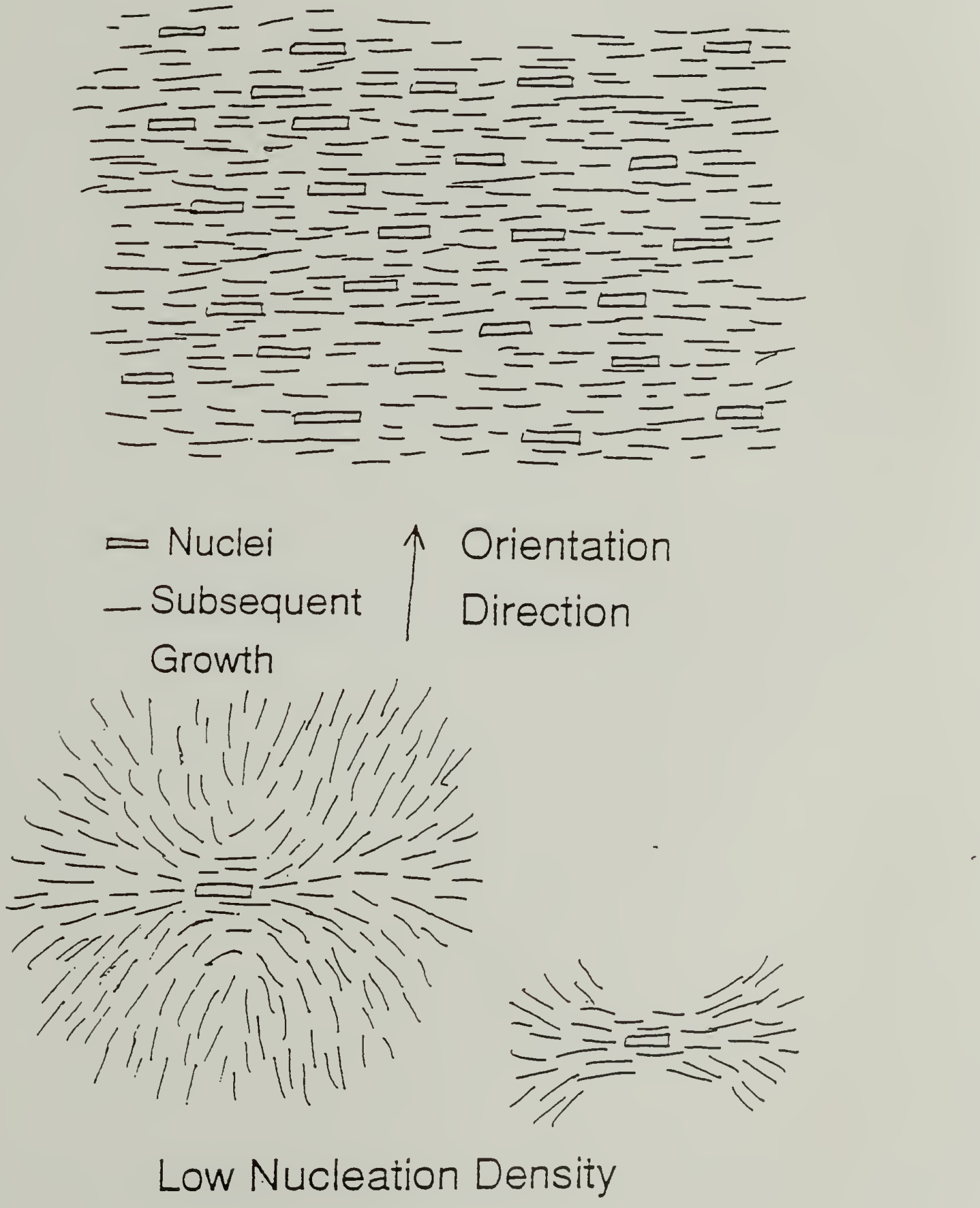

Figure 2.13 A schematic depicting the effect of primary nucleation density on the crystal morphology of a TLCP sample which prior to crystallization was a uniformly oriented nematic.

CHAPTER 3

OBSERVATION OF TEXTURES AND OF FEATURES

There is strong interest in observing the textural features found in liquid crystalline polymers (LCP) because of their influences on the properties of these materials. An excellent time-honored method is optical microscopy [Friedel, 1922]. Since LCP's are birefringent, the orientation of the optic axis (coincident with the nematic director) can be observed if the sample is placed between cross polars. For planar samples, the contrast is easily interpreted. Orientations of the director parallel to either polarizer produce an extinction of the light intensity. For non-planar samples, the director and also the polarization of the light rotate while passing through the sample, so extinction is not generally observed. Disclinations can be observed as dark threads, because they strongly scatter light. Optical microscopy is very versatile; it can be used for thick, flowing, or heated samples. However, the relatively poor resolution of the optical microscope, just under a micron, is a major limitation.

Small angle light scattering (SALS) has also been used to measure structure of the director field. This technique is useful for special cases when the director is simply defined. For schlieren textures (where disclination positions define the director field), the relative disclination density can be monitored using SALS [Rojstaczer et al., 1988]. SALS has the advantage of easily averaging the disclination density over the whole sample. The type of average, however, is not known. Also, in order to interpret the SALS data it was necessary to first use microscopy to show that the schlieren structure coarsened through disclination annihilation [Nehring and Saupe, 1972]. SALS has also been used to monitor the relaxation behavior of lyotropic LCPs after shear flow [Nivard, 1989]. During relaxation, the director (which during flow is approximately oriented along the flow direction) is imagined to buckle to form a banded texture where the director is alternately tilted up and down away from the

flow direction. The periodicity of this banding is easily measured by SALS. SALS is only useful when the director field can be interpreted simply.

The superior resolution of the transmission electron microscope (TEM) has been used recently to image director textures of very thin films of liquid crystal polymers [Wood and Thomas, 1986]. This lamellar decoration technique was first developed by Thomas and Wood [1985]. In the previous chapter, I discussed the lamellar decoration morphology, which occurs when the primary crystal nucleation density is high. In this chapter I wish to describe this morphology. From these TEM images, we can quantify some of the major parameters determining the director field: the disclination density (ρ_d), the characteristic length for distortions (ξ), and the wall density (ρ_w). This capability is useful in investigating effects of history on the sample texture. We can also obtain information about disclination structure. We can observe disclination interaction because we can measure precisely relative disclination positions. We can also investigate the director field of an inversion wall or that of a disclination in an orienting field.

In addition to TEM of thin films, we use image processing to quantitatively measure the director. An amine etch technique was developed to image director textures in bulk samples via TEM replication and HRSEM.

3.1 Lamellar decoration of the director and TEM

3.1.1 General scheme

Controlled growth of small lamellar crystals is used to decorate the director field to permit direct observation via the TEM. To obtain the lamellar decoration morphology as described in the previous chapter, the primary nucleation density of crystals must be large while crystal growth is relatively slow. Thin film samples are prepared in the liquid crystalline phase, quenched to room temperature, and finally annealed above T_g and below the melting temperature. During annealing the quenched nematic polymer partially crystallizes in a lamellar morphology, where the director of the remaining glassy liquid

crystal is normal to the lamellae. The technique is schematically depicted in figure 3.1. Because the director lies in the plane of the film, the lamellae will be viewed edge-on in bright field TEM. The higher density lamellae appear dark, and serve to decorate the underlying molecular arrangement of the frozen nematic, revealing a 30nm resolution map of the director field. To get effective decoration the crystals should be smaller than the size of the distortions. When this condition is met, the director is observed to vary smoothly with position.

3.1.2 Phase contrast

In the previous chapter we have already taken advantage of diffraction contrast to observe the lamellar size and shape of TLCP crystallites. In order to image the map of the director field, phase contrast must be used. The objective lens must be defocused to properly image the lamellar periodicity. In figure 3.2, a lamellar decorated sample is observed at focus and underfocus to display the effect of phase contrast.

In the defocused image, the lamellar repeat is clearly evident. The defocus used in figure 2b is useful for measuring the average orientation of the lamellae as a function of position.

The non-diffracting lamellae are not clearly visible in figure 3.2(a). The reason for this is that the in-focus condition actually filters out low frequency information. There are a number of factors in electron microscope imaging which damp high frequency information, but the principle factor in damping low frequency information is the focusing of the objective lens as described by the contrast transfer function (CTF) for a weak phase object:

$$CTF = \sin(\pi C_s \lambda^3 k^4/2 + \pi\lambda\Delta f k^2) \qquad (3.1)$$

C_s is the spherical aberration coefficient, λ is the wavelength of the electrons, k is the object frequency (distance^{-1}), and Δf is the defocus. Small k is always damped, especially when $\Delta f = 0$. The CTF acts as a filter in Fourier space, so the resulting image is a convolution of the object with the CTF. The amplitude of the Fourier transform is proportional to the

Lamellar Decoration Technique

Crystalline lamellae decorate the director field

Resolution ~ 30nm

Thomas & Wood, Faraday Disc.Chem.Soc. 79, 229 (1985).

Figure 3.1 Schematic of lamellar decoration technique.

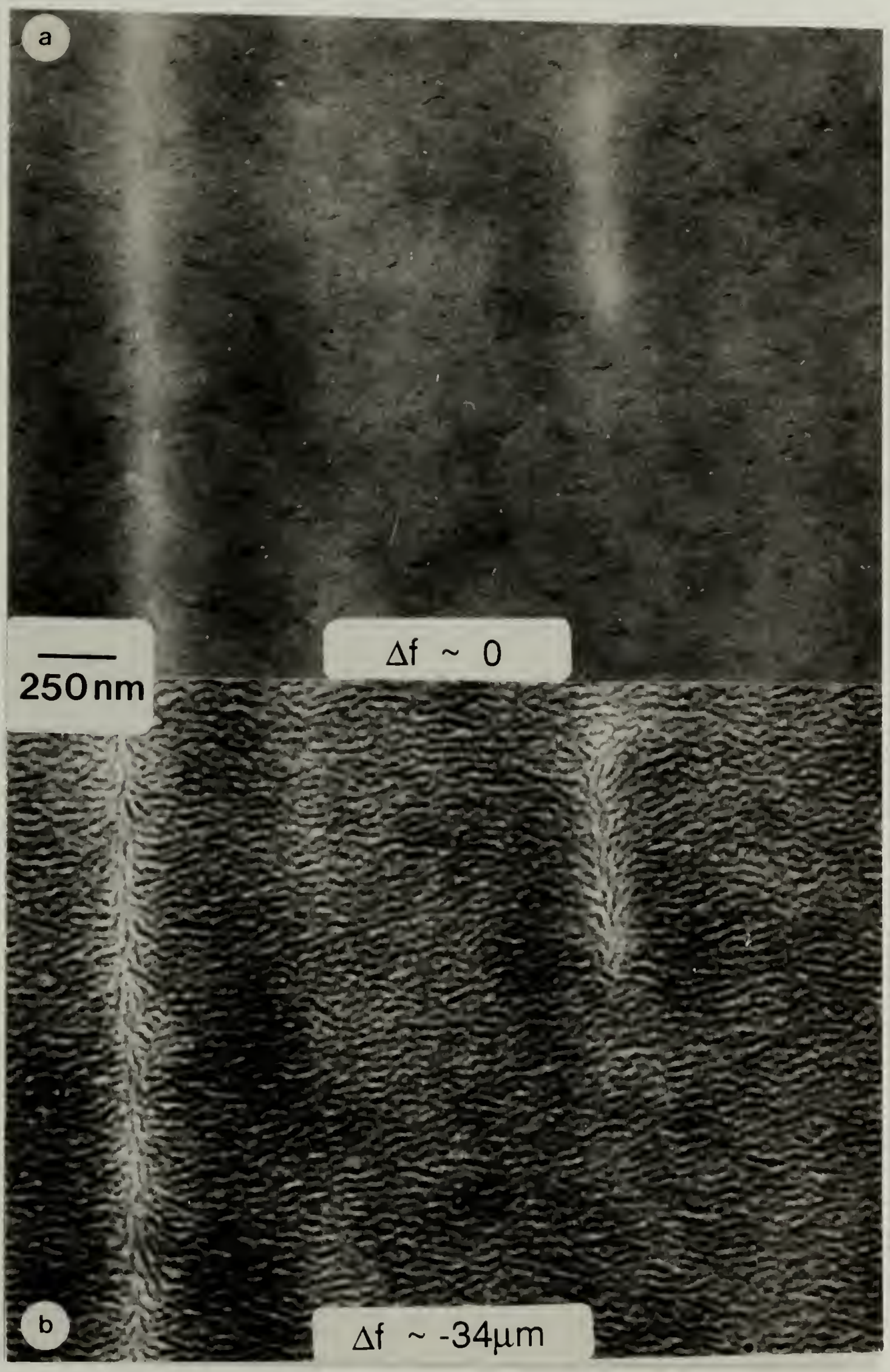

Figure 3.2 Phase contrast. (a) TEM image at zero defocus. (b) TEM image at underdefocus of - 34μm.

(Continued next page.)

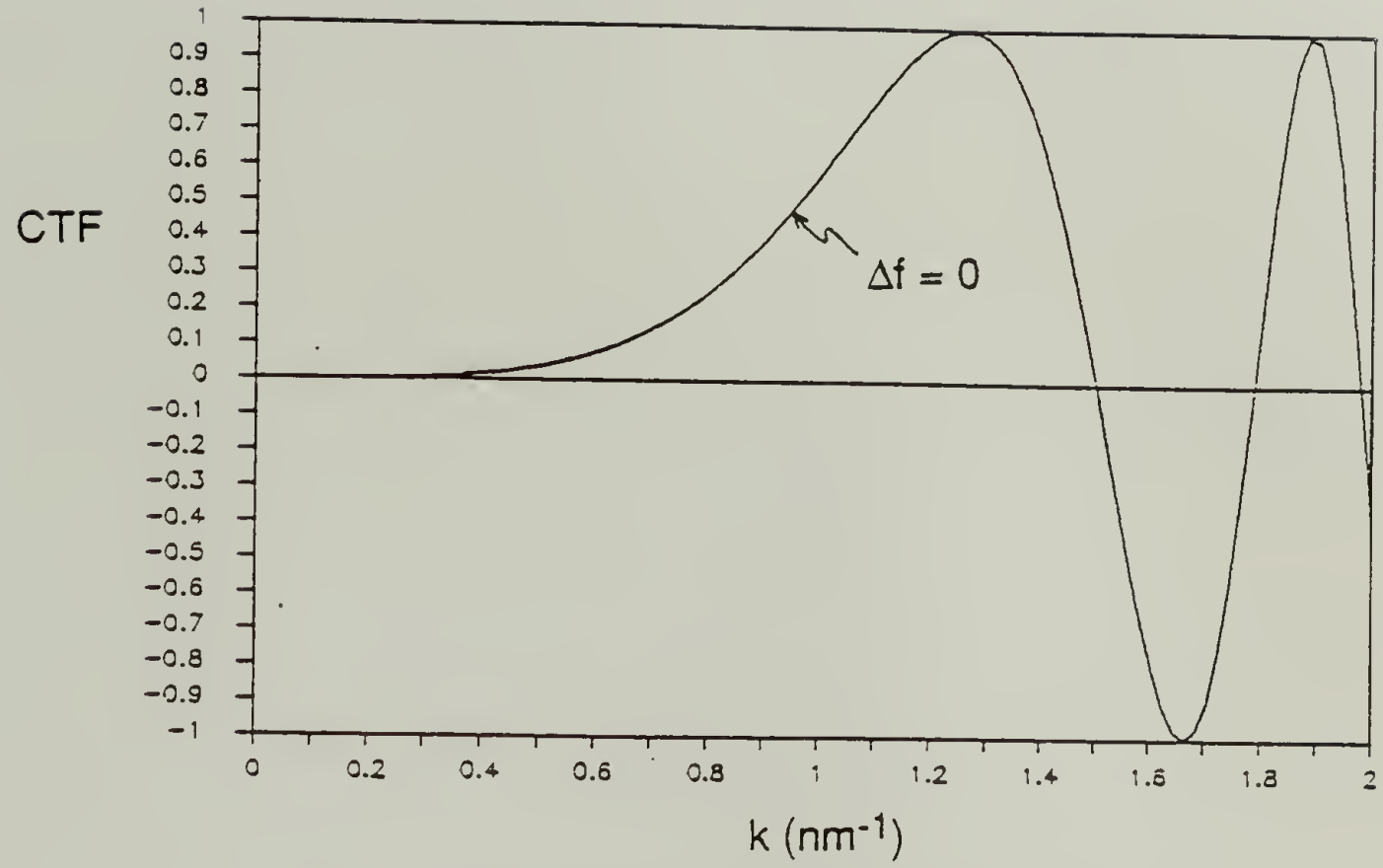

(c) Contrast transfer function at zero defocus.

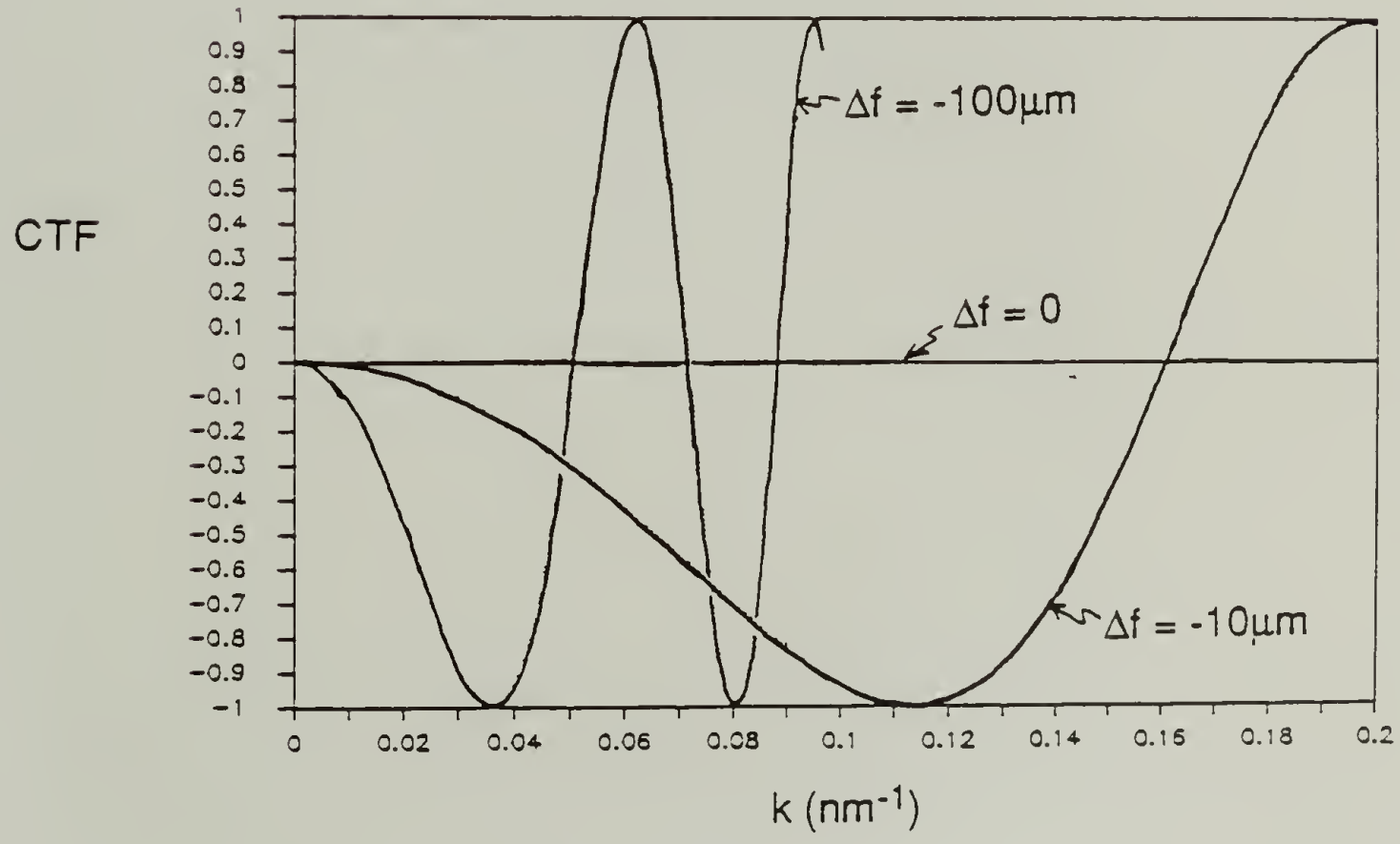

(d) Contrast transfer function as a function of object frequency and defocus.

Figure 3.2 Phase contrast.

density differences in the object. Since the difference in density between the crystal and the glassy nematic is approximately 20%, the CTF does not need to be very large to image the lamellae.

For the 100CX JEOL TEM in our laboratory, C_s = 6.7mm and the wavelength at 100 keV = 3.7pm. From figure 3.2(c), we see that the microscope at zero defocus has a pass band from approximately 1.6 to 0.7nm. The signal from larger features is damped while at high frequencies the signal is very confused since the CTF oscillates wildly from positive to negative. From our data, we know that the periodic spacing of lamellae is approximately 30nm (k=.033 nm^{-1}). This distance is almost completely damped at zero defocus; the CTF(k=.033 nm^{-1},Δf=0) = $7x10^{-7}$. As the defocus becomes more negative, the pass band is shifted to lower and lower frequencies as shown in figure 3.2(d). Although the 'optimal defocus', for best contrast is

$$\Delta f_{opt} = d^2/2\lambda = (30nm)^2/(2(0.0037)) = 120\mu m, \qquad (3.2)$$

a defocus of -10μm gives better images because both contrast and resolution are necessary. Figure 3.2(b) shows the sample at defocus of approximately -34μm. The lamellae periodicity is apparent, but the individual crystals are somewhat blurred in the image.

3.1.3 Director and lamellae are orthogonal

Electron diffraction shows that the director (of the remaining glassy liquid crystal) is normal to the lamellae [Wood, 1985]. By superposing the diffraction pattern and the bright field image formed from the 000 spot (figure 3.3(a)), it is shown that the chain direction, or molecular director, is perpendicular to the lamellae. Also from the diffraction pattern alone, we see that both the crystal and glassy nematic equatorial reflections are superposed, i.e. **c** (of the crystal) is parallel to **n** (of the glassy nematic). The orthogonal relationship between the chain direction and the lamellae is further elucidated in figure 3.3(b). This figure shows a crack which has grown following the chain direction in a sample with a banded texture.

The director field here has a sinusoidal-type variation due to incomplete flow alignment as described in chapter 6.

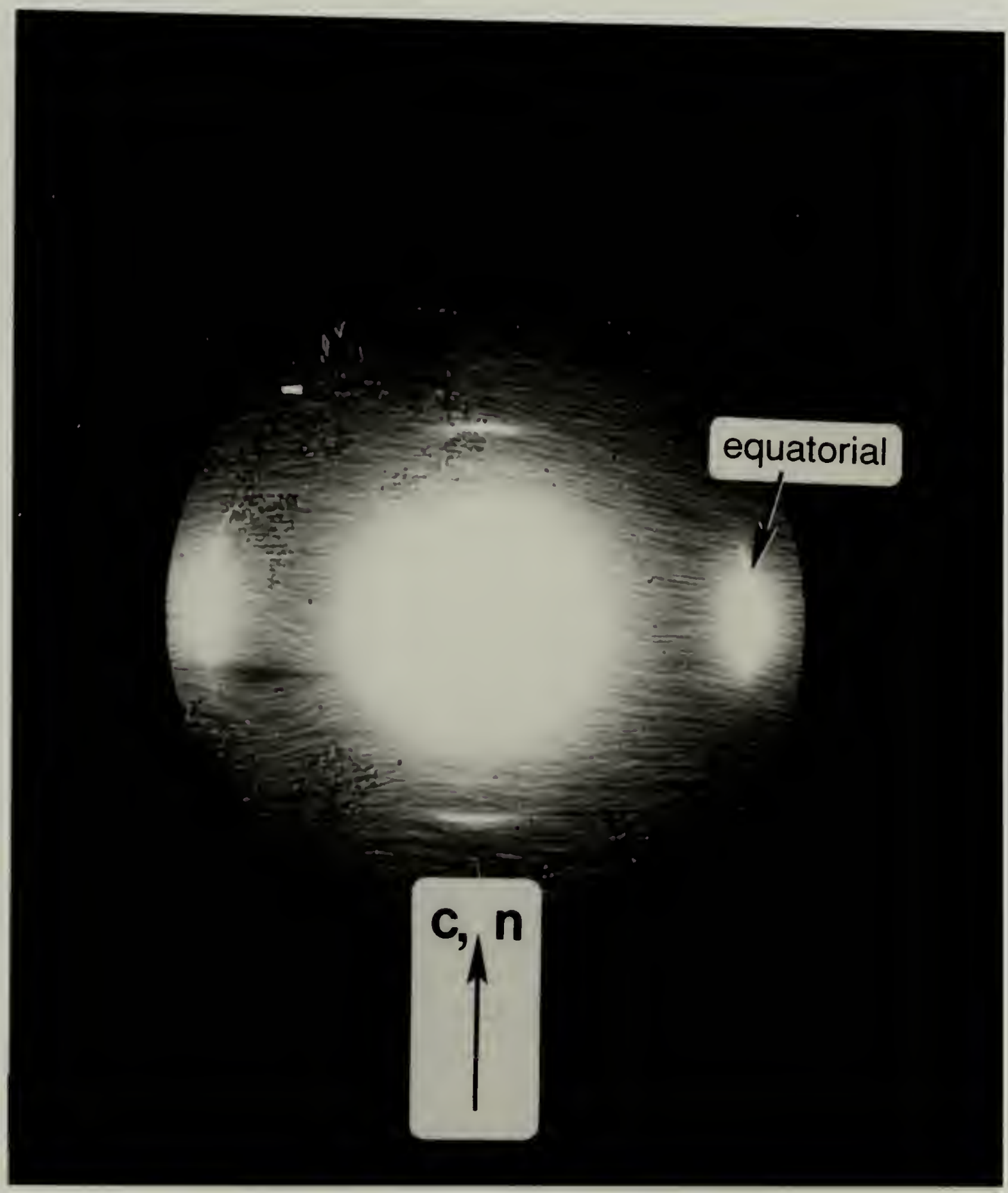

Figure 3.3 The director is orthogonal to the lamellae. (a) Superposition of the diffraction pattern and the bright field image formed from the 000 spot establishing the orthogonal relation between the long dimension of the lamellae and the chain axis. Because the equatorial reflection of both the glassy nematic (the diffuse spot) and the crystalline lamellae (the sharp arc) are superimposed, the chain axis in the crystal is parallel to the director in the remaining glassy nematic. (Continued next page.)

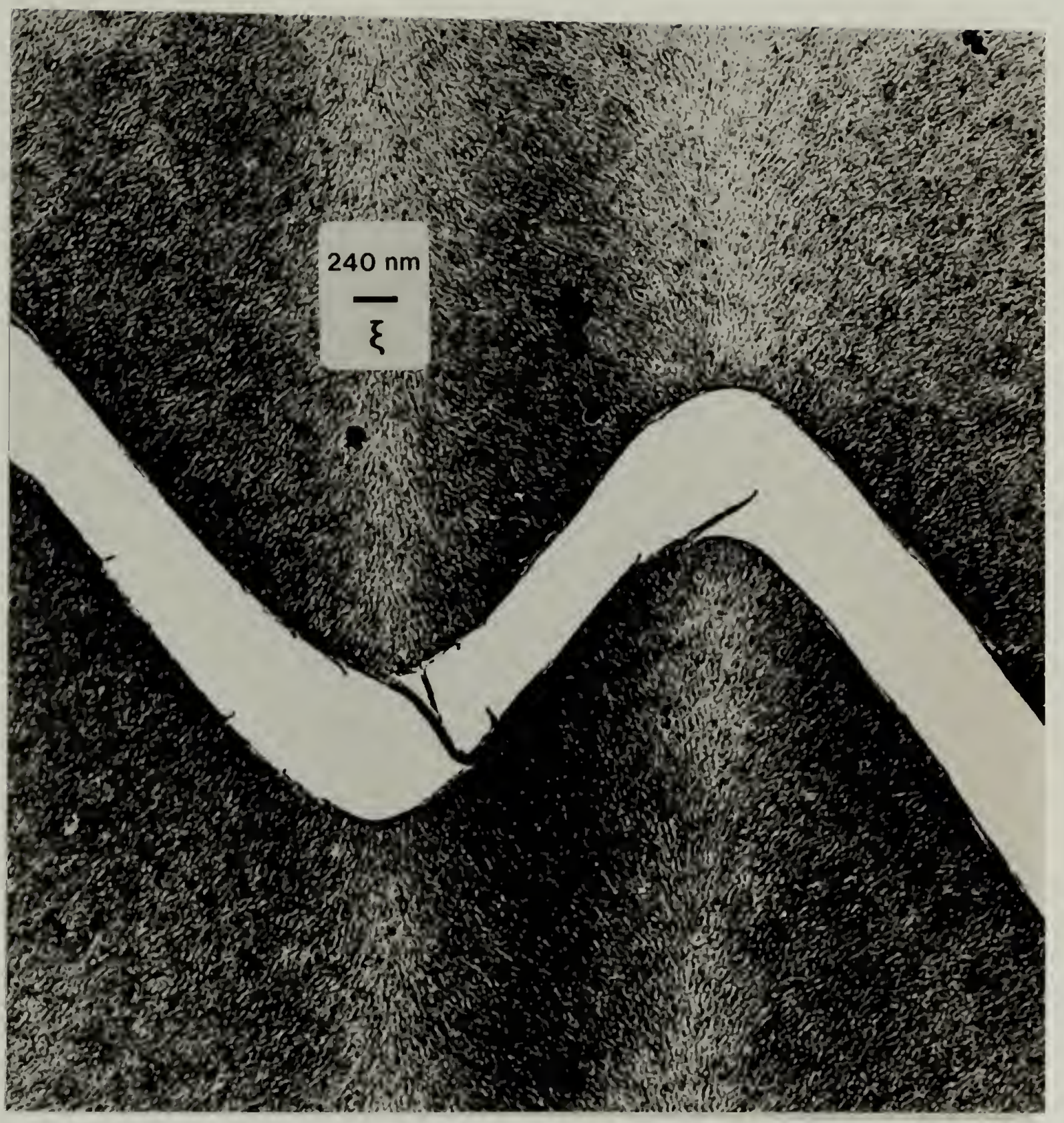

Figure 3.3 The director is orthogonal to the lamellae. (b) A banded texture in a thin film which has been subsequently subjected to stress. A crack has followed the sinusoidal trajectory of the molecules.

3.1.4 Resolution

The images reveal features in the field of oriented lamellae. Both inversion walls and disclinations are seen in figure 3.2(b). The disclination lines and inversion walls are both perpendicular to the film surface. Figure 3.4 shows a schematic TEM image of a disclination. The disclination in the lamellar field is rotated with respect to that in the director field. The most common types of disclinations seen in these polyesters are those of strength, s, equal to +1/2 and -1/2.

Figure 3.5 shows a melt spread sample of TQT10-M, where the disclination density is approximately 7/μm^2. In this image, there are 115 π disclinations and 114 -π disclinations. (The sum of the strengths of disclinations in a sample tends to zero in order to make the

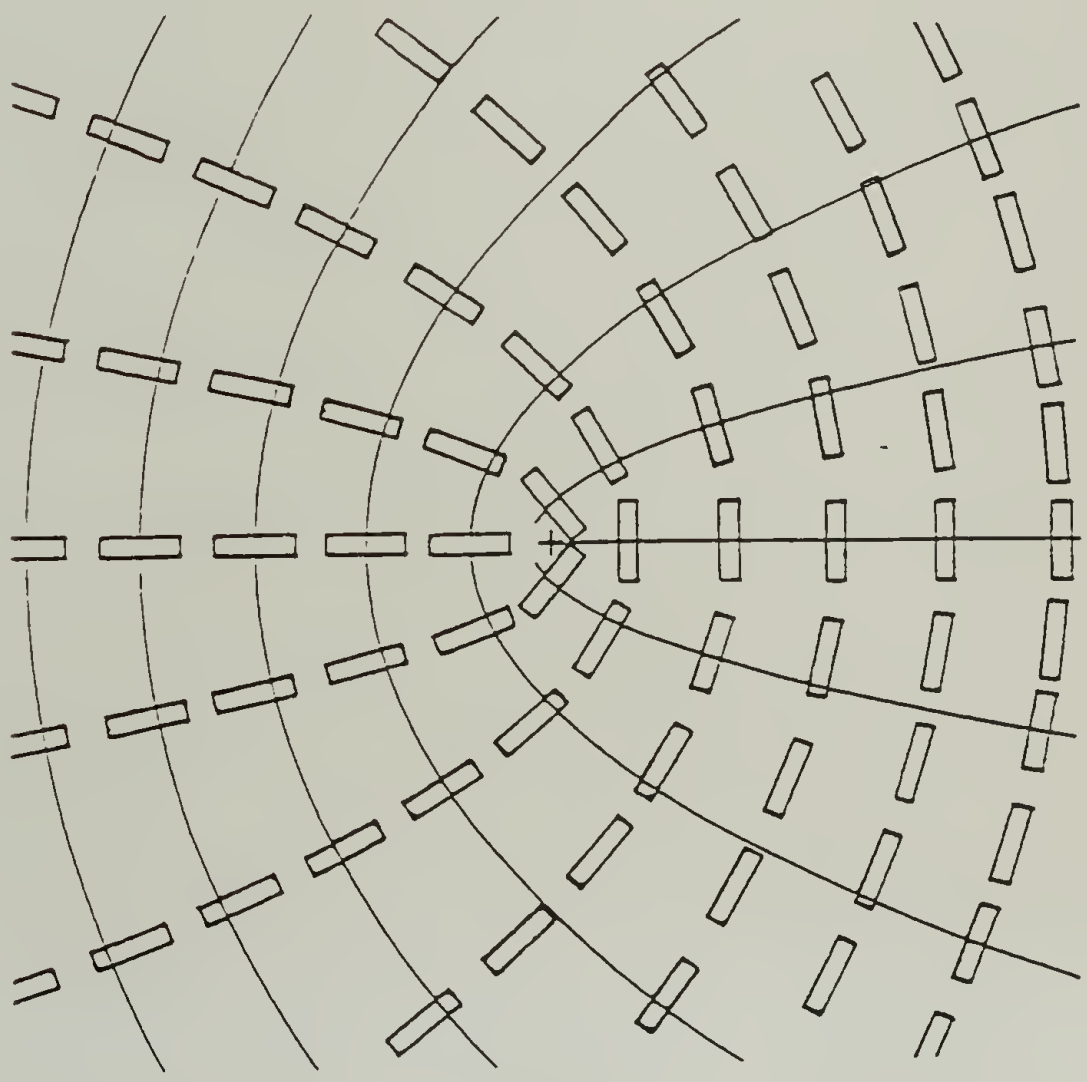

Figure 3.4 Schematic TEM image of a disclination. Lines represent director field; boxes represent lamellae.

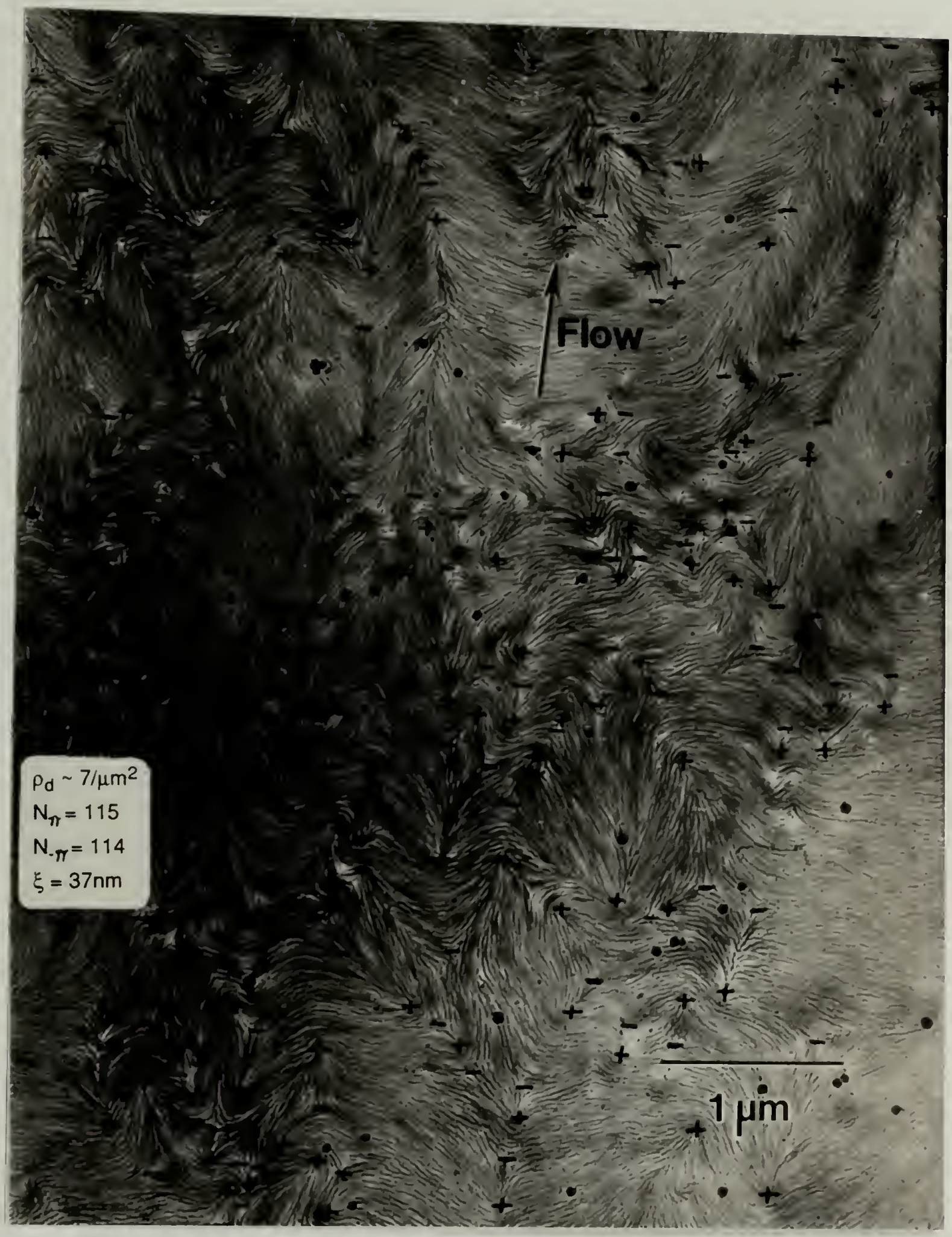

Figure 3.5 TEM image showing ~200 disclinations. This sample was melt spread (flow direction is approximately vertical) and the director may be characterized by the following measurements: $\rho_d \sim 7/\mu m^2$, $N_{\pi} = 115$, $N_{-\pi} = 114$, $\xi = 37nm$.

distortional free energy finite.) This image shows the disclinations well resolved--even at separations of 100nm. The disclinations in this image would not be observed in an optical microscope image since 500nm is the maximum resolution possible. The lamellar decoration technique permits visualization of the texture at high resolution.

3.2 Image processing to measure the director

We are interested in measuring ϕ as a function of x and y in order to learn about the physics of the material and of the defects contained in the material. The angle ϕ can of course be measured at any point using a protractor. However, the process quickly becomes tedious.

To facilitate unbiased data collection of $\mathbf{n}(\mathbf{r})$, an image processing algorithm has been developed. The process is demonstrated in figure 5.6. An image of a disclination is digitized, as shown in figure 5.6(a), using a video camera. Only the center 256x256 of the 512x512 image is used in order to avoid peripheral image distortions introduced by the camera. The image is scanned, and at each step, an image is extracted, as shown in (b). The extracted image is filtered with a Hamming window, as shown in (c). The Hamming window has the following transmission as a function of radius:

$$T = 0.54 + 0.46 \cos(2\pi r/d), \qquad \text{for } r < d/2 \tag{3.3}$$

$$T = 0 \qquad \text{for } r > d/2$$

where d is the size of the extracted image. The windowed image is Fourier transformed (figure 5.6(d)), and the director orientation is determined from the angular position of the peak in the power spectrum. Because the Hamming window is circularly symmetric, artificial orientations are not introduced in the Fourier transform. Additionally, the cosine dependence as a function of radius eliminates circular ringing in the transform.

Application and results of this technique are described in chapter 5 [Hudson et al., 1990].

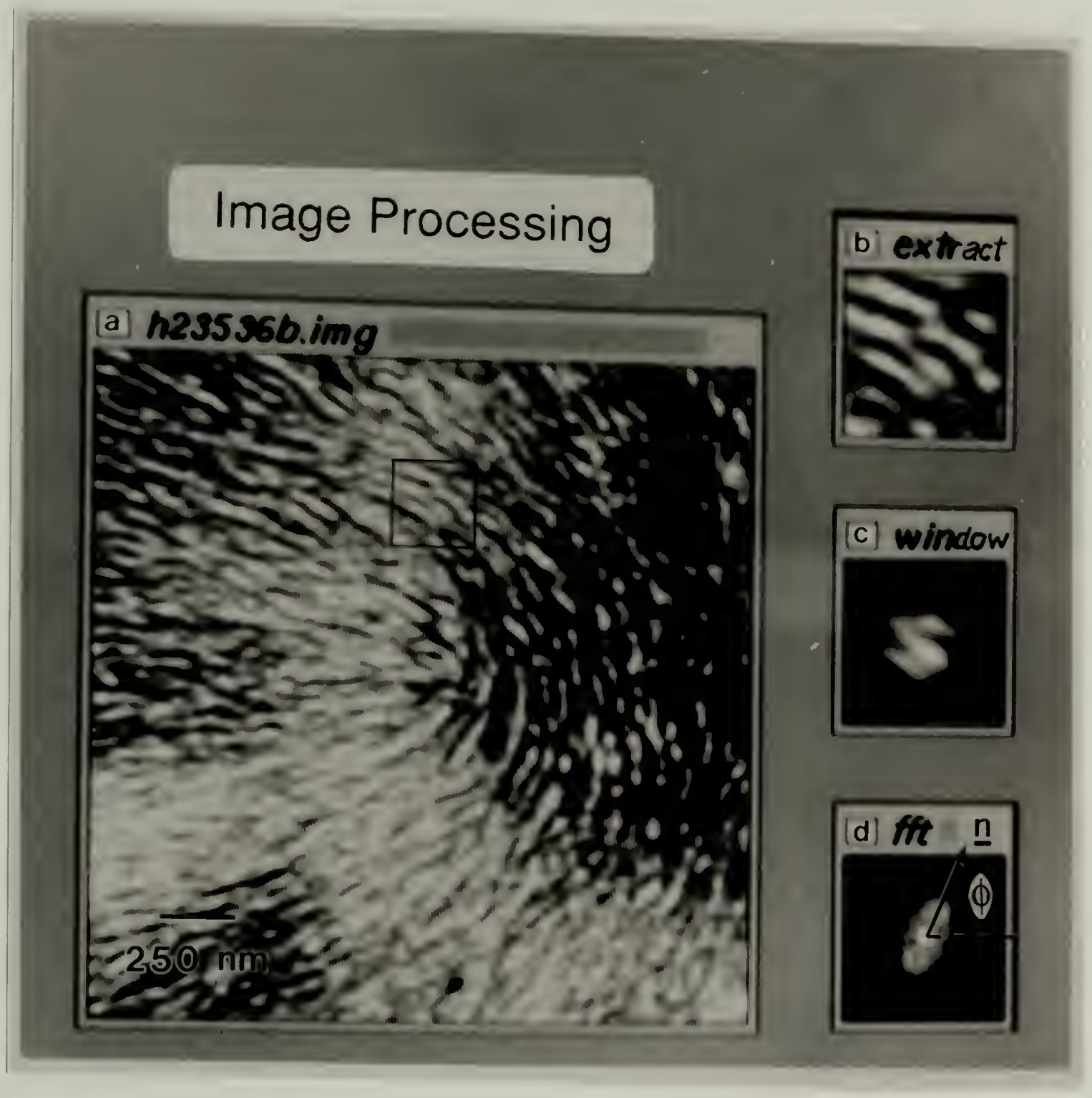

Figure 3.6 Image processing algorithm. (a) Digitized image. (b) Extracted image from boxed region in (a). (c) The extracted image filtered through the Hamming window. (d) The Fourier transform of the windowed image.

3.3 Amine etch technique

The lamellar decoration technique to image the director field of thin film liquid crystal polymers is extended to bulk samples. Interlamellar material is selectively etched in a methylamine solution, and the polymer surface is observed via transmission and high resolution scanning electron microscopy (TEM and HRSEM). Optical and electron microscope images are compared. Resolution of distortions in the director field are limited, not by microscope resolution, but by the periodicity of the lamellae (~ 30nm) used to decorate the director field. Regular and random semi-flexible and regular rigid crystallizable polyesters have been successfully imaged.

Thin films are very useful for studying material and disclination defect properties. In the case of thin films, the orientation of the molecules is confined to lie in the plane of the film. The distortions in the director field are well defined and only bend and splay exist. Bulk samples do not provide well defined constraints for distortions; however, other studies using bulk samples are possible. These studies include texture-rheology relationships at high resolution and the effects of flow on disclination core structure. In this section, I present observations of films too thick to be observed directly in TEM, yet thin enough that the distortions are well controlled. Use of thick films can facilitate observations of director field features.

The method for imaging bulk samples is a straightforward extension of the thin film lamellar decoration technique of Thomas and Wood. To image bulk samples, the sample is again prepared in the liquid crystalline phase, quenched, and annealed. The same lamellar morphology nicely decorates the director. The sample is too thick to directly view in the TEM, so a surface is prepared for etching and replicating. The surface may be an external surface or material may be cut away to prepare an internal surface.

The surface is then replicated following Organ and Barham's method [1988]. The polymer is etched for 10-60 minutes in 5-30% methylamine solution in water at 20-40°C. Conditions vary since different polymers have drastically different etch rates. The amine

cleaves ester linkages, forming an amide and an alcohol. After etching, the sample is washed in water and methanol. TEM of etched thin films indicates that the noncrystalline material etches faster than the crystalline. Therefore, after the etch, the edge-on lamellae protrude from the polymer surface.

Subsequently, the surface may be shadowed with Pt at 30°, and coated with carbon to prepare a replica suitable for TEM. There is inevitable loss of detail where the lamellae are parallel to the shadowing direction. To obtain the replica, the polymer is dissolved in fuming H_2SO_4. This method is a general scheme which can be applied to any crystallizable polyester.

The etched polymer surface may also be directly observed by low-voltage HRSEM. The sample is first sputtered with Au/Pd for approximately 15 seconds. This preparation reduces charging due to the electron beam even though the coating is thin and probably non-continuous. Actual sputtering time is sample dependent. The sample is then observed via secondary electron emission using a Hitachi S-900 field emission, immersion lens SEM at 1.0 keV. The low accelerating voltage used reduces charging because it is close to the crossover voltage for these polymers. The reduction of charging due to operation at low voltage in turn reduces the amount of conductive coating (which will obscure surface detail) that must be applied to successfully image these samples. The HRSEM images, in this chapter and in chapter 6, were taken by D. L. Vezie.

This etch technique enables observation of magnetically oriented TLCP films. Films thin enough to be directly observed via TEM (circa 50-100nm) do not orient readily due to a relatively strong interaction with the substrate surface. However, 1-2μm thick films of OQ5a#6, the random semi-flexible polymer, have been aligned in a magnetic field at the Bitter National Magnet Laboratory. To create a texture of inversion walls, the sample is first oriented by shearing prior to magnetic alignment. Optical microscopy reveals that a high degree of orientation is achieved as polymer in the nematic phase is sheared on a glass slide using a spatula. The shearing direction is placed orthogonal to the applied magnetic

field direction. As the field is applied, the director rotates clockwise in some regions while in others it rotates counter-clockwise. Initially a periodic structure of inversion walls forms, as first described by Guyon et al. [1979]. Subsequently walls pinch off and annihilate each other. The resulting structure consists of loops of inversion walls of various size and shape.

A sample of the random semi-flexible material, that was oriented in this way (13.5T field at 230°C for 90 minutes), was etched in 5% methylamine/H_2O at 20°C for 40 minutes. Optical and low and high magnification HRSEM images of inversion walls are compared in figure 3.7. In the HRSEM images in figures 3.7(b) and 3.7(c) the lamellae appear bright and the selectively etched interlamellar spaces that contained noncrystalline material appear dark.

The variations in the director field are easily revealed by the lamellae, and the structure of the inversion wall is observed in the high magnification HRSEM image. Other applications of this technique will be described in the following chapters.

3.4 Future Work

Bulk samples having nonplanar textures can be observed using this etch technique as well. In that case the lamellae would not appear edge-on. Any out of plane component of the director, ψ, should result in a increase in the apparent period of the lamellae:

$$p \sim p_o / \cos\psi \quad , \tag{3.4}$$

where p_o is the lamellar period. I do not expect, however, that it would be easy to measure ψ due to uncertainties in viewing angle, local fluctuations in the lamellar period, tilting of the chain axis with respect to the lamellae normal, and local distortions in the director field. To evaluate such effects, macroscopically oriented samples could observed. Bulk samples could be oriented via a magnetic field, and internal surfaces having different orientation with respect to the applied field could be prepared.

The appearance of an image of a disclination would depend on both the character of a disclination (twist or wedge) and on the angle that the disclination line makes to the surface.

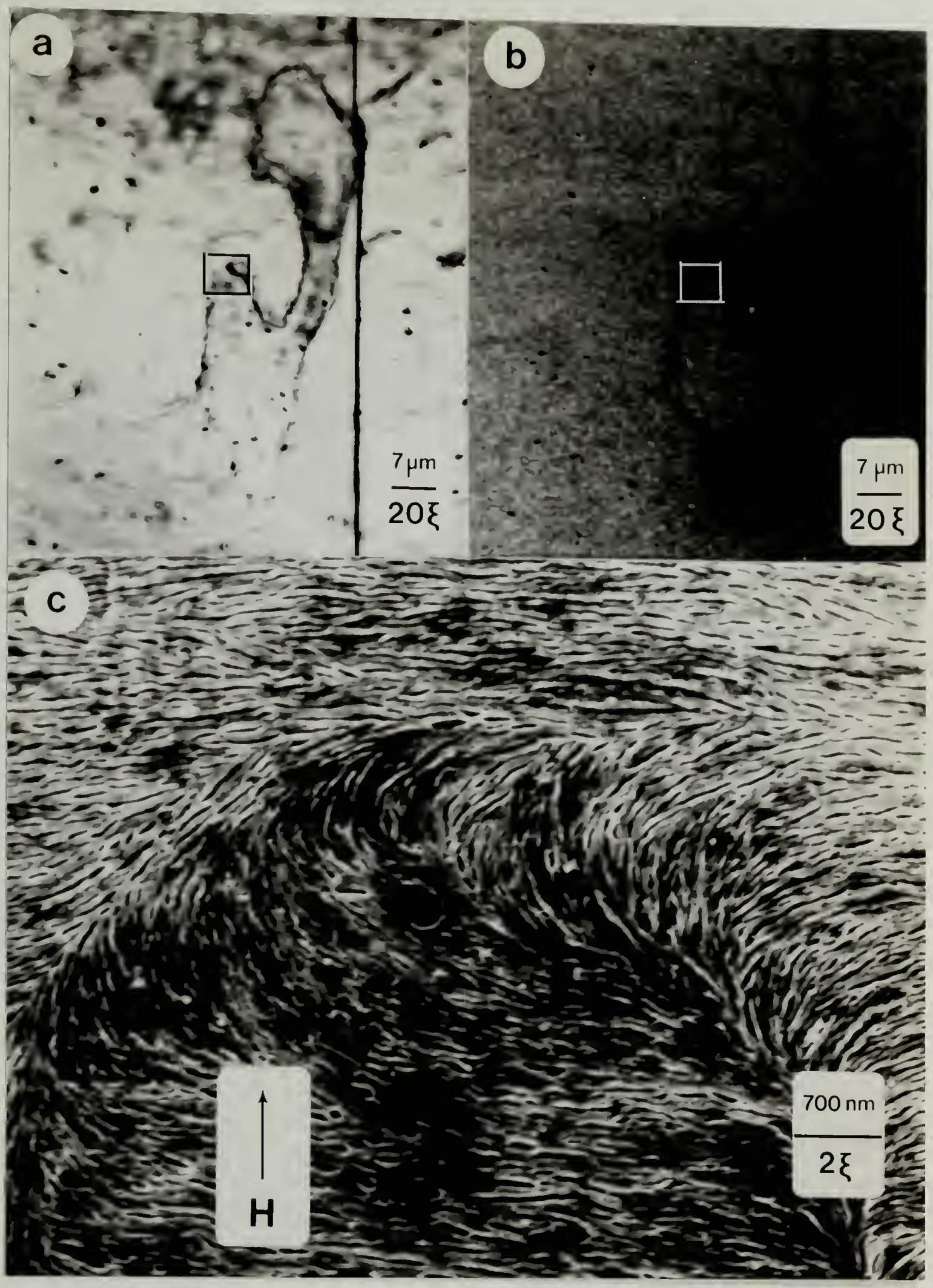

Figure 3.7 Optical and HRSEM micrographs of magnetically oriented film of a random semi-flexible TLCP (13.5T, 230°C, 90 minutes). a.) Optical micrograph. The magnetic field direction is vertical. Crossed polars are oriented 45° with respect to the field direction. Two inversion wall loops are shown.
b.) HRSEM micrograph of the identical region in figure 2a.
c.) Higher magnification view of boxed region in figure 2b.

Well defined disclinations may be prepared by making a sandwich of three uniformly oriented films. The director in the two outer films should be parallel while the director of the middle layer is orthogonal to that in the outer films. Some disclinations will be formed in the sandwiching process. If the director lies in the plane of each film, then disclinations having only twist character are formed. Cutting surfaces which intersect the disclination at different angles would be useful for establishing image interpretation. Thick sandwiches (a few mm) are desired in order to observe the sample cross section. If the director of the middle film is aligned perpendicular to the film, then disclinations having both twist and wedge character are formed.

3.5 Summary

In both this chapter and the previous one, the lamellar decoration technique has been shown to accurately reveal the director field texture of the nematic precursor. Phase contrast is responsible for properly imaging the higher density lamellae, which grow perpendicular to the director. This technique has been used to obtain quantitative information of both disclination position and the director field. The image processing program used to measure the local orientation of the director from a TEM image further increases the techniques applicability. A versatile etch technique to directly image the director texture of bulk samples of crystallizable liquid crystalline polyesters is also presented. Polymers of different molecular architecture have been imaged by OM, HRSEM, and TEM. The superior resolution of the lamellar decoration technique combined with the opportunity to investigate thicker samples enables novel observations of inversion wall and disclination structure.

CHAPTER 4

ANNEALING:
DISCLINATION INTERACTION IN QUIESCENT, UNORIENTED SAMPLES

The pairwise interaction of disclinations in the absence of any orienting field is fundamentally understood (assuming equal elastic constants); it is analogous to electrostatic interactions of line charges. However, complication arises when calculating the annihilation rate of a collection of disclinations because each disclination interacts with all others in the system. Topics of interest are the asymptotic time dependence of annihilation and the structure of the annealed sample. Other workers have experimentally investigated the time dependence using microscopy [Shiwaku et al., 1987] and light scattering [Rojstaczer et al., 1988]. The investigations give similar results for the annihilation behavior: $\rho_d \sim t^{-0.7}$, where ρ_d is the disclination density. The annealing of an initially random array of disclinations is simulated in this chapter. The viscous force of disclination motion is assumed to cancel the elastic force on each disclination. Assuming equal elastic constants and viscosity independent of orientation causes both the force and the velocity of a disclination due to another to be along the line of separation between disclinations. The simulation reproduces the known result of annihilation time of a pair of disclinations proportional to the square of their separation. The disclination density of a large collection was observed to obey the power law: $\rho_d \sim t^{-0.84}$, over two decades of time. This value is consistent with experiment, but larger simulations and better experiments are necessary to more confidently measure the asymptotic time dependence. The dipole moment of the collection of disclinations was calculated throughout the simulation. It was found that the dipole of an initially random collection of disclinations decays slower than if the disclinations annihilated randomly. Disclination annihilation is observed to slow dipole decay. The structure of an annealed sample is concluded to be disordered yet not random. Pair distribution functions calculated

reveal that an initially random distribution is depleted at small r/d, where d is the average disclination separation. This effect is more prominent for the pair distribution of like-signed disclinations.

4.1 Theory

As we have seen from the introductory chapter, the disclination is the characteristic defect in nematic materials. Their behavior in the presence of various applied fields is of great interest. However, in this chapter, we wish to discuss the simplest case where the defects interact only among themselves. Understanding this behavior is prerequisite to understanding more complex behavior. The basics of disclination interaction have been known for some twenty years. We wish to review these as well as investigate some new questions involving large numbers of interacting disclinations.

We first consider the case of equal elastic constants, where the basics of disclination interaction are well understood, and later the effect of elastic anisotropy which is understood for nearest neighbor interactions is reviewed.

The director field, as described by ϕ, must satisfy the Laplacian. This differential equation is linear, so solutions may be superimposed:

$$\phi = \Sigma\, s_i \tan^{-1}((y-y_i)/(x-x_i)) + \phi_0 \ , \qquad (4.1)$$

where the i^{th} disclination has strength s_i and is positioned at $\mathbf{r}_i = (x_i, y_i)$. We consider 2 dimensions; the situation is equivalent in 3 dimensions when the structure is invariant in the third dimension. In this case the disclinations run parallel to the third dimension (or thickness of the film). The distortional free energy density is given as:

$$g = k/2\,(\phi_x^2 + \phi_y^2) \ , \qquad (4.2)$$

where subscripts denote differentiation. Substituting equation 4.1 into 4.2,

$$g(\mathbf{r}) = k/2[s_{tot}\,\Sigma\{s_i/(\mathbf{r}-\mathbf{r}_i)^2\} - \Sigma\{s_i s_j(\mathbf{r}_j-\mathbf{r}_i)^2/(\mathbf{r}-\mathbf{r}_i)^2(\mathbf{r}-\mathbf{r}_j)^2\}] \ . \qquad (4.3)$$

The total energy is only finite if

$$s_{tot} = \Sigma s_i = 0 \ . \qquad (4.4)$$

We also need to consider the disclinations to have some finite core size, r_c, and energy, g_c, because the energy diverges when $\mathbf{r}\text{-}\mathbf{r}_i = 0$. With these assumptions, the total distortional free energy, G, is:

$$G = \Sigma -2\pi k s_i s_j \ln(r_{ij}/r_c) + G_c, \qquad (4.5)$$

where r_{ij} is the distance between the i^{th} and j^{th} disclinations and G_c is the total core energy. Although the effect of each disclination extends to infinity, the distortion due to a given disclination dies out with distance because of its interaction with others. The force on a disclination i due to disclination j is found by differentiating equation 4.5.

$$\mathbf{f}_{ij} = -2\pi k s_i s_j \mathbf{r}_{ij}/r_{ij}^2 \ , \qquad (4.6)$$

where $\mathbf{r}_{ij}$ is the vector: $\mathbf{r}_j - \mathbf{r}_i$. This interaction is exactly analogous to two dimensional electrostatics. The force/unit length between disclinations (no matter how long) is analogous to the electrostatic force/unit length of an infinite line charge. It is easy to see, in light of this analogy, why the strength of a disclination is sometimes called a topological charge. A useful construct which I use both in this chapter and in chapter 6 is that of a dipole moment of a collection of disclinations.

Note from equation 4.6 that like signs repel and opposite signs attract. If disclinations combine, they produce a new disclination having a strength equal to the sum of those combining. Disclinations of opposite sign, which attract each other, tend to approach each other and annihilate. Because this process is spontaneous, the number of disclinations in a quiescent liquid crystal sample tends to decrease with time. The director field structure therefore coarsens with time. It would be useful to know at what rate the texture coarsens and to know the interdisclination structure of an annealed sample.

In addition to the elastic forces, there are viscous drag forces on a moving disclination. By dimensional arguments, the force /unit length of a disclination is:

$$\mathbf{f}_v \sim \gamma_{eff}\mathbf{v} \ , \qquad (4.7)$$

where $\mathbf{v}$ is the velocity of the disclination and γ_{eff} is an effective rotational viscosity coefficient (assumed independent of the orientation of the director). Both this assumption

and the equi-constant assumption mean that both f_v and f_e act along the line of disclination separation. In addition, pseudo-equilibrium is assumed, so these forces acting on a disclination are equal and opposite. Or stated another way, all of the change in elastic energy is dissipated during flow. If r is the disclination separation, this assumption leads to the following relationship (from equations 4.6 and 4.7):

$$dr/dt \sim 1/r \,, \tag{4.8a}$$

and integrating,

$$t \sim r^2 \,. \tag{4.8b}$$

For an isolated pair, therefore the time to annihilate is predicted to be proportional to the square of the separation. Dreizin and Dykhne [1972] are credited with first deriving this result. Sonin et al. [1976] were the first to experimentally verify it. They studied 10 - 20μm thick films of MBBA between two metallized glass plates. Upon application of an AC electric field, disclination pairs were formed. The disclination lines were perpendicular to the film, so two dimensional behavior was observed. The initial disclination separation and the time required for their annihilation were measured using optical microscopy. The actual rate of disclination motion depended strongly on film thickness, because the distortional energy providing the driving force is proportional to the thickness, L, but the anchoring energy, which is one source of drag, is independent of L. For each thickness, however, the annihilation time was proportional to the initial separation squared.

4.2 Experimental work

Many bodied interaction of disclinations has been investigated using optical microscopy by Shiwaku et al. [1987] and using light scattering by Rojstaczer et al. [1988]. Shiwaku et al. solvent cast polymer films with one free surface onto a coverslip. These isotropic films were then heated rapidly to a set temperature at which the polymer became nematic. Disclination lines were observed perpendicular to the film, so two dimensional

behavior was observed. The disclinations were counted as a function of time. They found that the disclination density varied as:

$$\rho_d \sim t^{-0.70 \pm 0.15} . \qquad (4.9a)$$

Unfortunately, less than an order of magnitude in time, from 25 to 140 seconds, was investigated. The disclination density was approximately $0.1/\mu m^2$.

Rojstaczer et al. performed similar experiments. A solution cast film was first heated briefly to the isotropic phase before quenching it to the nematic. They measured the peak intensity position of the scattered light as a function of annealing time. The peak position (distance^{-1}) is assumed proportional to the square root of the disclination density. Their results are very similar to Shiwaku et al.'s:

$$\rho_d \sim t^{-0.74 \pm 0.2} . \qquad (4.9b)$$

They too only investigated approximately a decade in time, from 10min to 240min. Their time scale is significantly longer than Shiwaku et al.'s because their polymer has a smaller elastic constant. The disclination density is estimated to be approximately $0.1/\mu m^2$.

4.3 Computer simulation

In computer simulation, we have the capability to easily measure both the asymptotic time dependence of the disclination density and the structure of disclination positions. Equal numbers of positive and negative disclinations are initially randomly placed in a square region embedded in a disclination free region of infinite extent. The force on each disclination due to all others is calculated. The velocity of each disclination is assumed proportional to the force. During a small time step, the disclinations are allowed to move with their prescribed velocity. The length of time is chosen so as to let the disclination which has the largest velocity (i.e. the one which has the closest neighbor) to move the smaller of either a fixed distance (1/128 of the original square region) or half the distance to its closest neighbor. All other disclinations will move less. After each time step the velocities are again calculated, and the process is repeated. When disclinations of opposite sign meet (separation

~ 10^{-6} unit square), they are said to be annihilated and are removed from calculation. Calculation continues until no disclinations remain.

The same assumptions used to derive $t \sim r^2$, are used in the computer simulation. In light of this, the computer simulation was checked against this relation as shown in the plot of disclination separation vs. time, figure 4.1. The time scale in these simulations is arbitrary. In reality the time scale will be proportional to γ_{eff}/k. This has been qualitatively demonstrated by Rojstaczer and Stein [1988]. The time scale will also be influenced by other effects. The effect of film thickness and surface anchoring has been demonstrated by Sonin et al. [1976]. The specific structure of the core is expected to affect the mobility of a disclination and the time scale of annihilation, because some disclinations may need to drag chain ends with them to accommodate the large amount of splay contained within the core. Mazelet and Kleman [1986] have observed much higher mobility for a $-\pi$ disclination than for a π disclination in a semi-flexible TLCP melt. If the disclination motion is very fast the flow of material around the disclination core will also be a factor [Cladis et al., 1987].

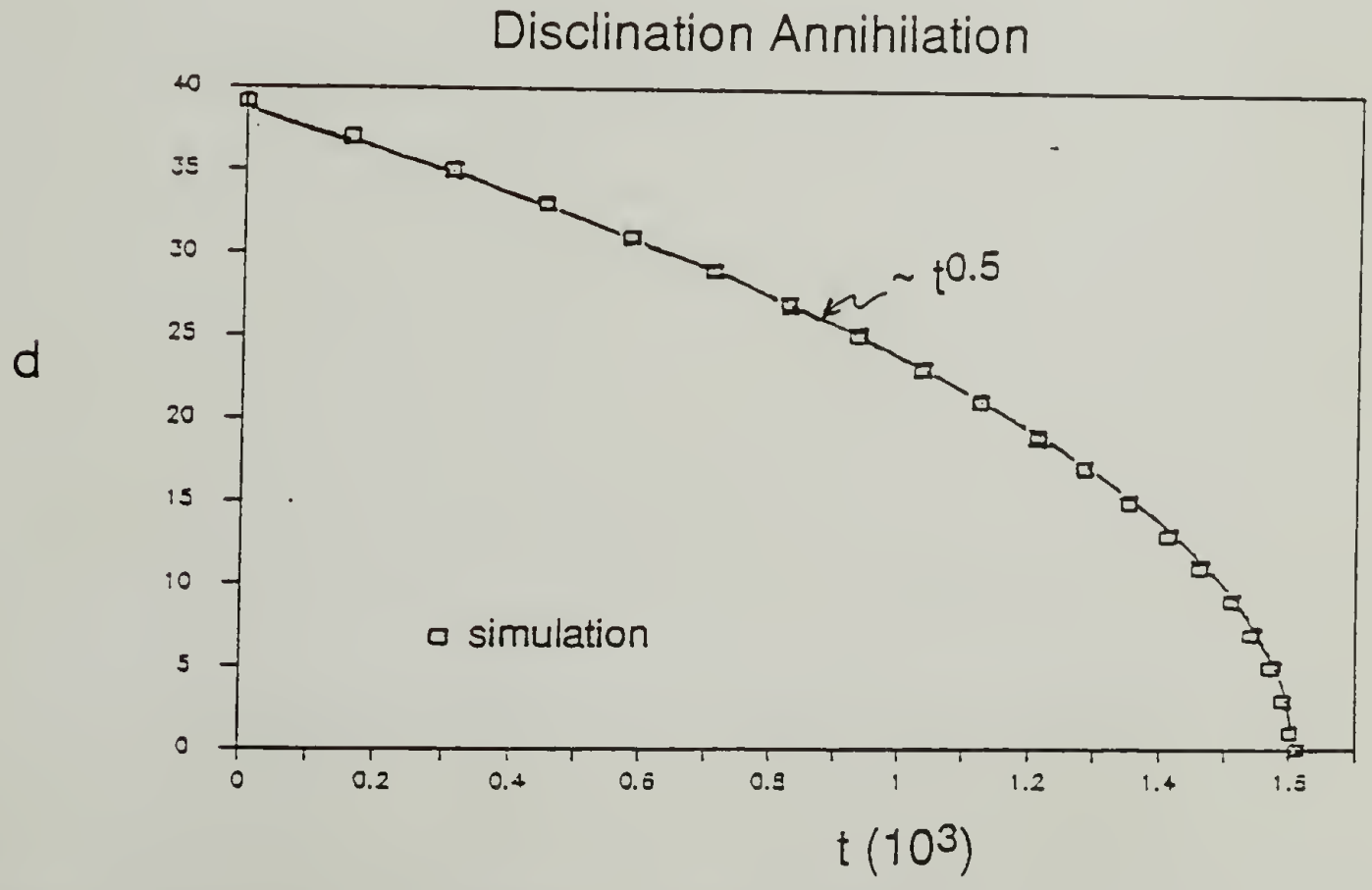

Figure 4.1 Annihilation of a $\pm\pi$ disclination pair. Disclination separation, d, vs. time.

Simulations were run with an initial number of randomly placed disclinations ranging from 200 to 1500. The number of disclinations was recorded as a function of time. The plots of disclination density versus time may all be superposed by scaling the disclination density by the initial disclination density, ρ_d°. The time must also be scaled by $1/\rho_d^\circ$. Figure 4.2 shows data from six different simulations superimposed by this scaling. The asymptotic slope is also drawn and measured to be:

$$\rho_d \sim t^{-0.84 \pm 0.1} . \tag{4.10}$$

The experimental and simulation results are in good agreement with each other, considering the large error estimates for both. The simulation results span approximately two decades of asymptotic behavior. Larger simulations are needed to more accurately determine the

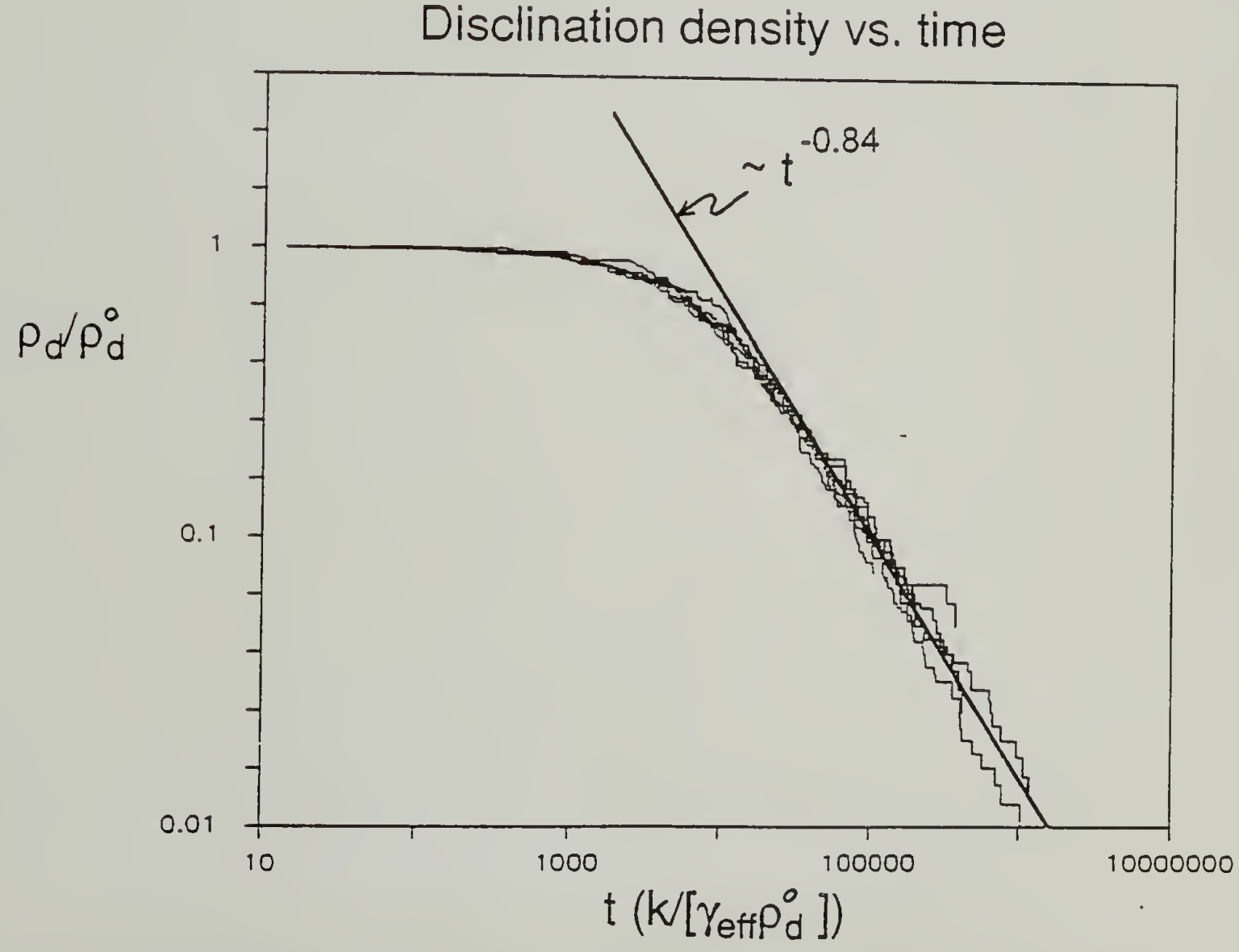

Figure 4.2 Disclination density vs. time. Simulations of initially random 200, 400, 600, 800, 1000, and 1500 disclinations are superposed by the scaling indicated by the axes. After an induction period, asymptotic power law behavior is observed.

asymptotic time dependence. Note that there is an induction period before asymptotic behavior is reached. This induction period would go to zero as the initial density goes to infinity.

To characterize the structure of the annealed disclination array, the dipole moment, **m**, of the array was calculated at each step:

$$\mathbf{m} = \Sigma s_i \mathbf{r}_i \quad . \tag{4.11}$$

If the array were random,

$$m \sim \rho^{0.5} \quad . \tag{4.12a}$$

However, the observed behavior in figure 4.3 is:

$$m \sim \rho^{0.4} \quad . \tag{4.12b}$$

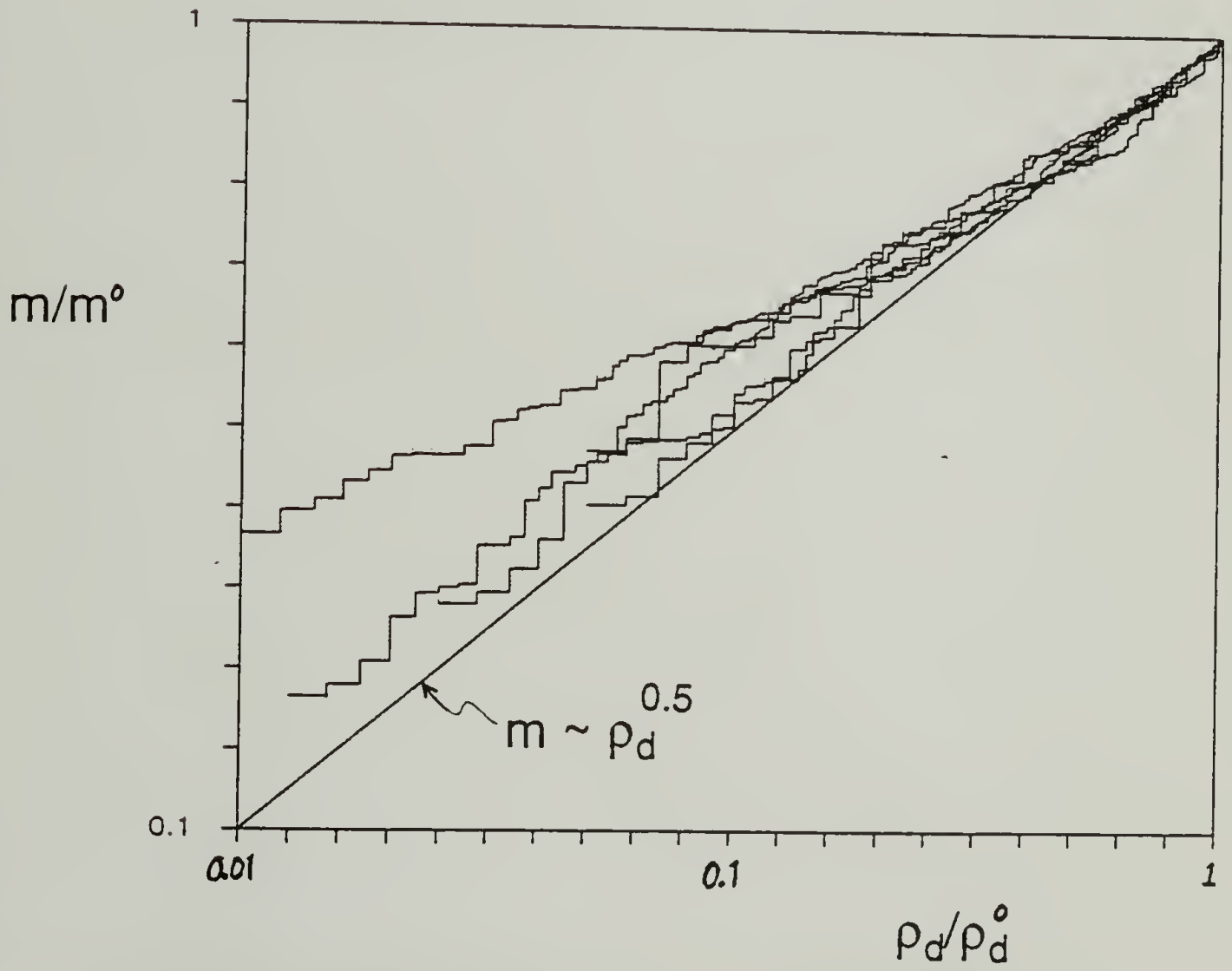

Figure 4.3 Reduced disclination dipole moment vs. reduced disclination density. The straight line has a slope equal to 0.5. If the disclinations disappeared randomly, the simulation results would be expected to fall on this line. The results, however, are systematically above this line.

The total dipole moment therefore decays slower than if the disclinations annihilated randomly. Of course the disclinations do not annihilate randomly; the close disclinations annihilate first. Also we can see from the very end of the simulation that annihilation slows the rate of dipole decay. Just prior to annihilation, the total dipole moment decays rapidly as the contribution to the total dipole from the one pair (disclination dipole) is removed.

The structure of an annealed sample is disordered yet not random. This structure is commonly known as a schlieren texture. A snapshot of a typical asymptotic structure is shown in figure 4.4. The initially random array of 1000 disclinations has annealed to this collection of ~ 90 disclinations. Note that some regions are concentrated in one type of defect. Some nearly Lehmann type clusters are also observed.

Initial results of pair distribution calculations reveal that an initially random distribution is depleted at small r/d, where d is the average disclination separation. The pair distribution function of opposite sign disclinations is nearly zero for radii less than a few tenths of the average disclination separation. For like-signed disclinations, this depletion distance is approximately doubled. More accurate pair distribution functions need to be calculated by averaging over many time steps.

TEM observations of quiescent samples have also been done. A thin film of TQT10-M was solution cast onto a carbon coated glass slide and annealed for 2 hours at 180°C in order to develop a schlieren texture. After quenching and annealing, the sample was placed on a microscope grid and viewed directly in TEM. The film thickness was approximately 100nm. Figure 4.5 shows the lamellar decoration morphology formed from the schlieren precursor. The disclination arrangement appears to be very similar to that observed in the simulation snapshot figure 4.4. If many (~ 1000) disclinations were imaged, the pair distribution function could be measured from TEM micrographs. Microscopy and computer simulation have a clear advantage over light scattering in the ability to measure the interdisclination structure.

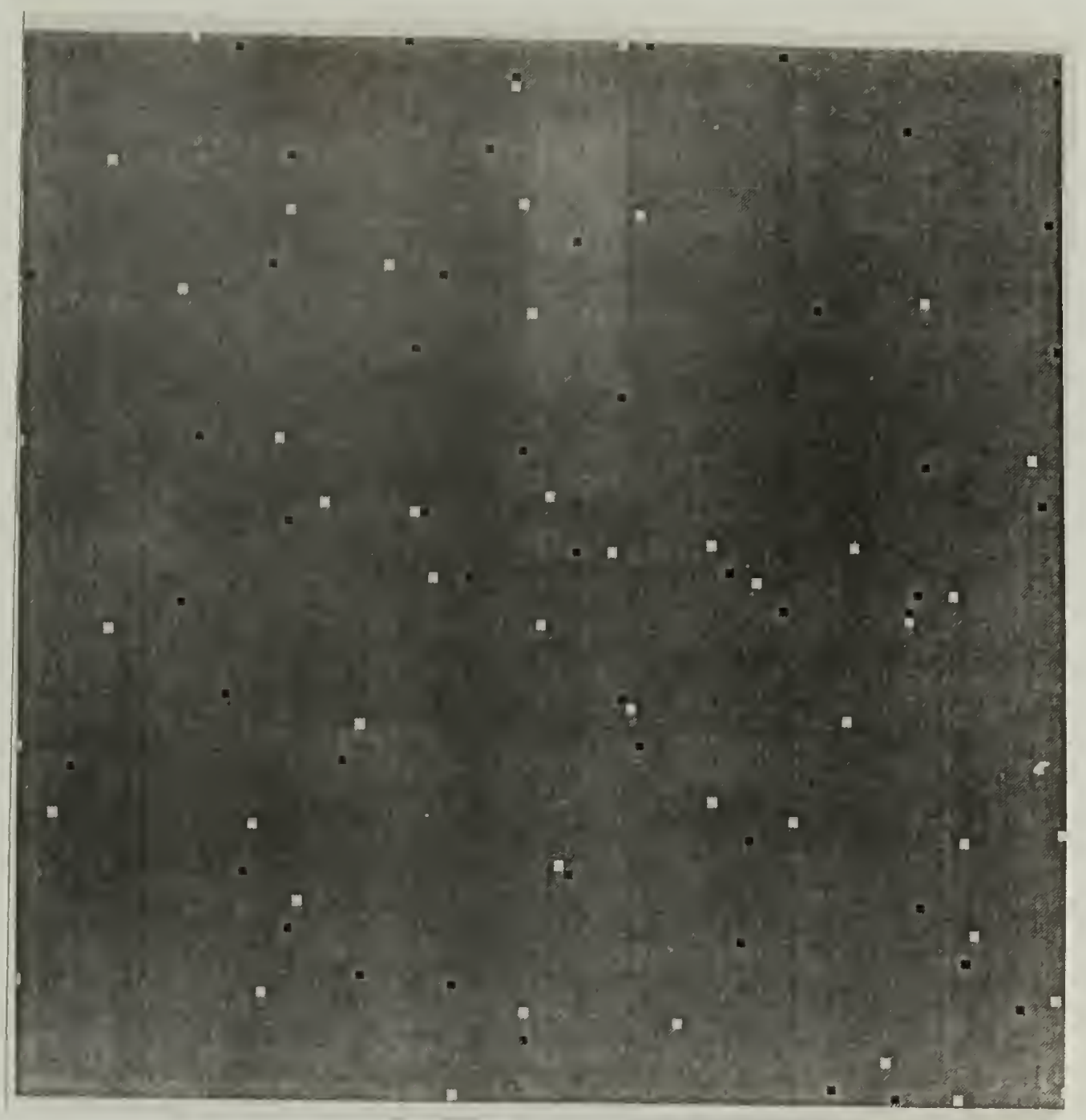

Figure 4.4 Snapshot of structure formed upon annealing an initially random array of 1000 disclinations. Approximately 90 are shown remaining. π disclinations are shown white and $-\pi$ disclinations are shown dark. The figure is 0.9L on a side, where L is the size of the initial area within which the disclinations were randomly placed.

4.4 Future work

As I have mentioned, in order to better measure the asymptotic time dependence, larger simulations are necessary. Using the present scheme of calculating the force on one disclination due to all others, however, the total calculation time goes as $(\rho_d{}^o)^3$, so it is sensible to make the algorithm more efficient. Although it is rigorously true that each disclination interacts with all others in the sample, it is unnecessary. The effect of a given

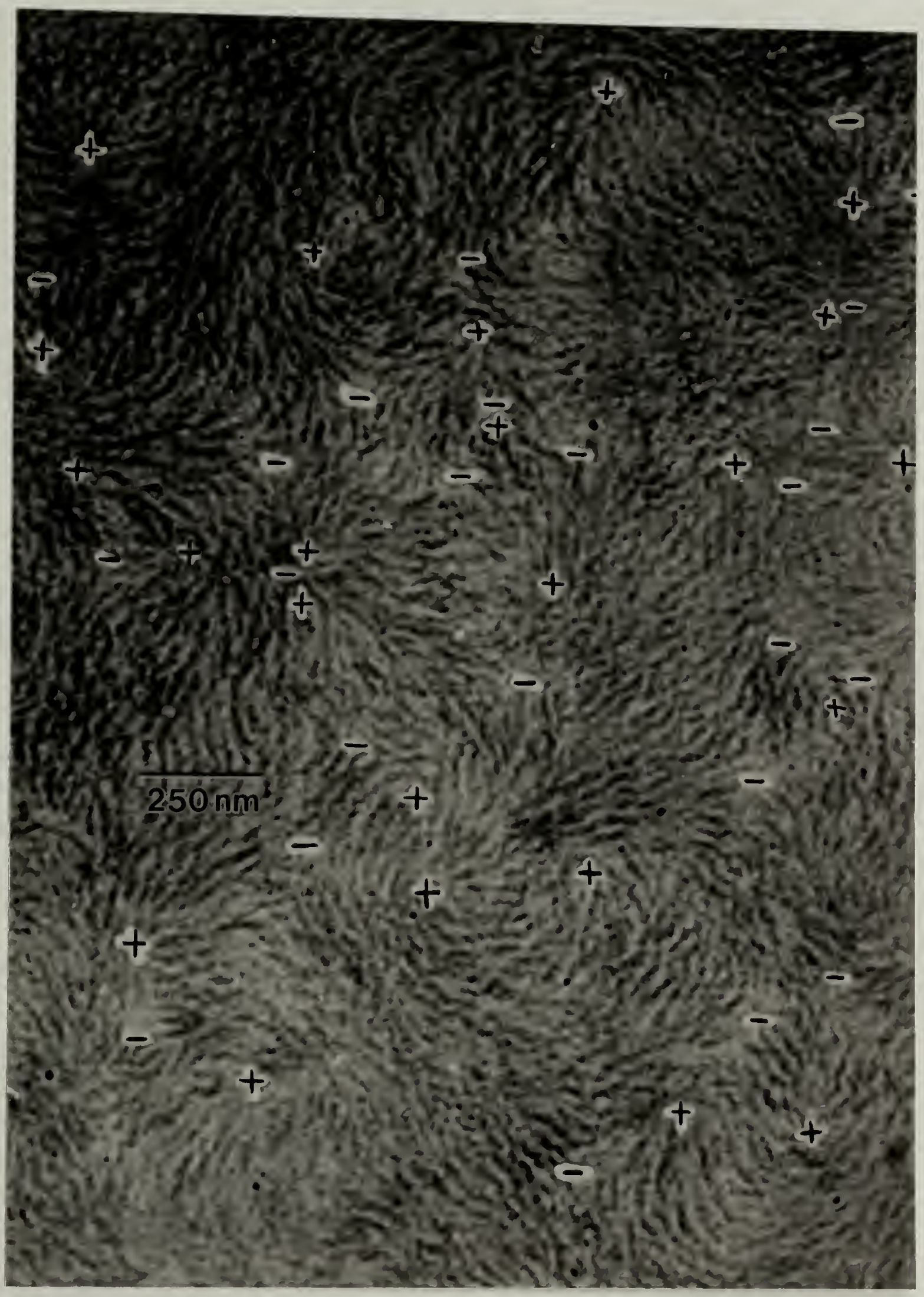

Figure 4.5 TEM micrograph of a quiescently prepared thin film of TQT10-M. The positions of the + and - π disclinations are marked with a plus and minus signs.

disclination dies out fairly rapidly due to cancelation of effects by its nearest neighbors. If only a set of disclinations surrounding a given disclination were used to calculate the force on the disclination, the total calculation time would go as $(\rho_d{}^o)^2 \ln(\rho_d{}^o)$. Keeping track of the nearest neighbors can be done using a Voronoi mesh defined by the disclination positions. However, more than one shell of neighbors is probably necessary to accurately calculate the force. The main problem is deciding which neighbors to include. The effect of two disclinations close together will cancel each other. However, if only one of the pair is included the effect of that one will be far out of balance. To minimize this problem, the criterion for selection should be distance and not shells of neighbors, so that the probability of including only one member of a disclination pair is reduced. The criterion distance should be a few times the average disclination separation. To update the neighbor list which fits the criterion, only the nearest neighbors of the outermost disclinations will be checked.

To measure the interdisclination structure, the pair distribution function will be calculated. Also other pair distribution functions can be calculated between like-signed disclinations and also between opposite signed disclinations. The distance will be scaled by the average disclination separation in order to determine if the structure is self-similar in the asymptotic regime.

Other investigations could easily be done. It might be interesting to calculate the annealing behavior when the mobilities of positive and negative disclinations are dramatically different. The next chapter describes recent observations of aggregation of chain ends at $+\pi$ disclination cores. This aggregation of chain ends is expected to retard disclination motion if the velocity of the disclination is comparable to the diffusion rate of chains. This implies that the time scale of disclination annealing is expected to depend on whether the average disclination velocity is less than or greater than the characteristic velocity defined by the diffusion rate.

CHAPTER 5

DISCLINATION STRUCTURE

The TEM lamellar decoration technique, discussed in chapter 3, enables direct visualization of the molecular orientation of a liquid crystalline polymer. Determination of the bend to splay elastic constant ratio from the measurement of the relative amounts of distortion produced by a disclination was first proposed by Frank [1958]. Previous experiments on small molecule liquid crystals [Nehring and Saupe, 1972] were unsuccessful due to a lack of resolution. The 30nm resolution of the lamellar decoration technique is sufficient to allow quantitative measurement of the bend to splay elastic anisotropy.

Until recently elastic constants of only a few materials have been measured. Most commonly investigators have used a critical field to produce some distortion (a Freedericksz transition) [Zheng-Min and Kleman, 1984], or have measured the amplitude of thermal fluctuations by light scattering [Se and Berry, 1987]. Both of these techniques require the formation of a uniformly aligned sample, which is relatively easy for a small molecule liquid crystal. These techniques yield independent measurements of the elastic constants. It is, however, sometimes difficult to remove all the defects in thermotropic liquid crystal polymer samples.

Since disclinations produce distortions in the director field, relative elastic constants can be obtained from measuring the relative amounts of distortions produced by a disclination. The true value of these observations, however, lies in their potential to yield information of disclination core structure.

In order to ascertain the core structure of π disclinations, the apparent splay and bend elastic anisotropy, ε_a, is measured as a function of radial distance. Both a rigid and a semi-flexible main chain liquid crystal polyester are studied. Results demonstrate a special structure of the core at radii less than about several molecular lengths. The rigid material

splays significantly more at the core. At a distance of 100nm, ε_a is approximately -0.4, yet the asymptotic value, ε, (at a distance of 1μm) is approximately 0. In contrast, the flexible material bends more at the core; $\varepsilon_a(100nm) \sim 0.1$ and $\varepsilon \sim -0.15$. These results can be understood in terms of the molecular lengths and relative rigidities of these liquid crystalline materials. The presence of hairpins in the flexible chain polymer is thought to be slight. The core structure observed results from large distortions present at the core.

5.1 Disclination structure as a function of elastic anisotropy

In a thin film, the director may be confined to lie in the plane of the film. In this case, the director has only one degree of freedom, ϕ, the angle with respect to some fixed axis contained in the plane. Disclination lines are normal to the surfaces. Also, only two distortions -- splay and bend -- are present. The distortional free energy density due to a single isolated disclination at the origin is given in polar coordinates as:

$$g = k/2r^2 \ (\partial\phi/\partial\theta)^2 (1 + \varepsilon\cos2(\phi-\theta)) \qquad (5.1)$$

where ϕ is independent of r. ε is the elastic anisotropy:

$$\varepsilon = (k_{11}-k_{33})/(k_{11}+k_{33}) \qquad (5.2)$$

where k_{11} is the splay and k_{33} is the bend elastic constant. $k = (k_{11} + k_{33})/2$ is the mean elastic constant. Minimizing the total free energy, G, leads to the following second order non-linear differential equation.

$$0 = \partial^2\phi/\partial\theta^2 (1 + \varepsilon\cos2(\phi-\theta)) + (2\partial\phi/\partial\theta - (\partial\phi/\partial\theta)^2)\varepsilon\sin2(\phi-\theta) \qquad (5.3)$$

In the case where $\varepsilon = 0$, the equation is linear and was solved by Frank [1958]. The general case where $-1 \le \varepsilon \le 1$ was solved by Dzyaloshinskii [1970].

$$\theta = p\int_0^{\phi-\theta} ((1+\varepsilon\cos2x)/(1+p^2\varepsilon\cos2x))^{1/2}dx \qquad (5.4)$$

where p is a constant (such that $p^2 < 1/|\varepsilon|$) and is defined by the condition that ϕ be single valued:

$$\pi = (s\text{-}1)p\int_0^{\pi}((1+\varepsilon\cos 2x)/(1+p^2\varepsilon\cos 2x))^{1/2}dx \qquad (5.5)$$

where s is the strength of the disclination as defined before.

Solutions of $\phi(\theta)$ for π disclinations (s = +1/2) and the corresponding director patterns are shown in figure 5.1(a). It is evident that the structure of these defects depends dramatically on the elastic anisotropy, ε. At the limits where ε reaches ± 1, the director field is completely void of the more costly distortion.

Figure 5.1(b) shows that the minimum free energy configurations for $-\pi$ disclinations depend only weakly on the elastic anisotropy. Due to the symmetry of this defect, $\phi(\theta)$ has more nodes, and the amplitude of deviations from the equiconstant case ($\phi = -\theta/2$) is limited. For this reason, we concentrate our measurements on π disclinations. Note that for the $-\pi$

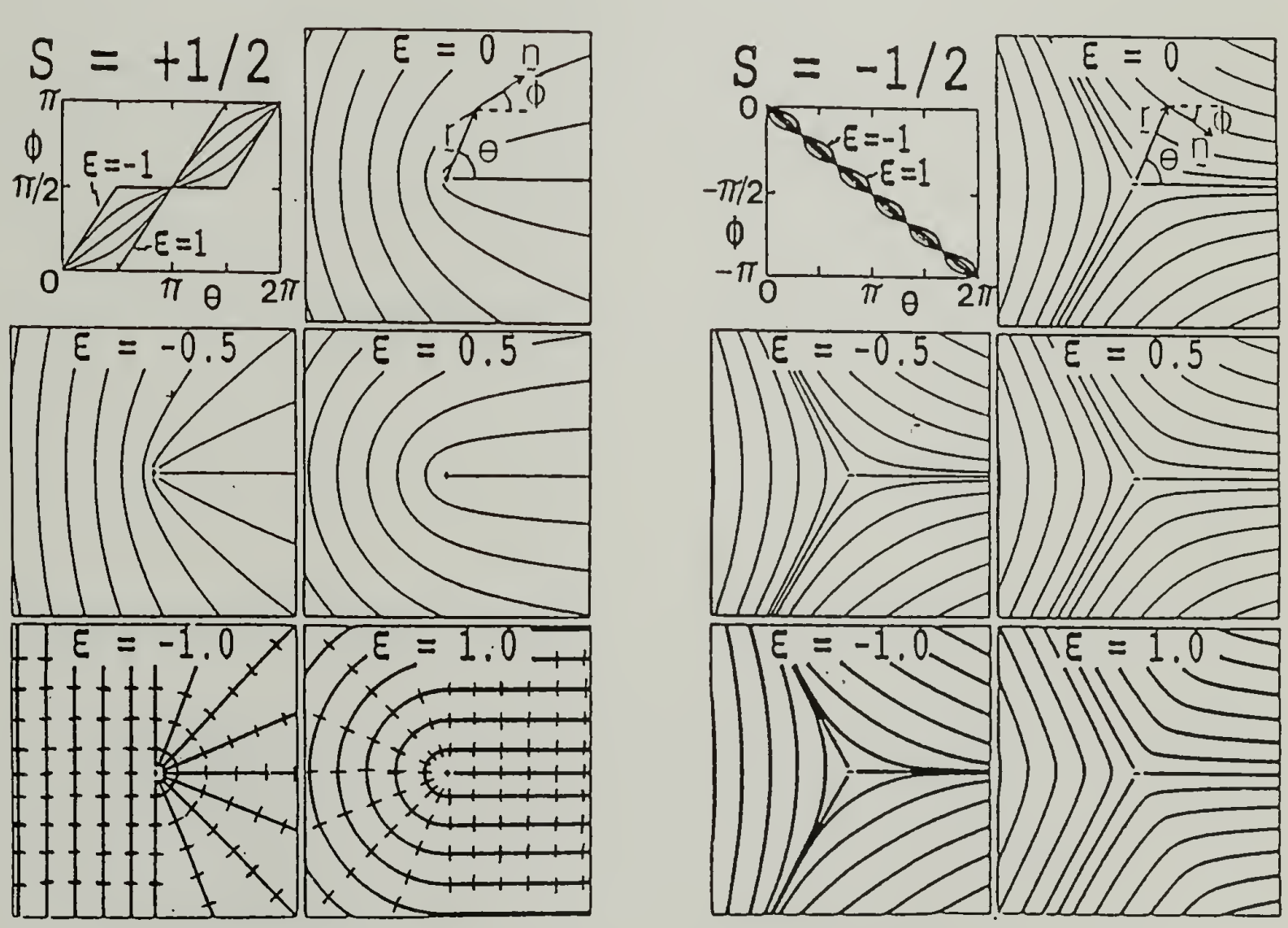

(a) (b)

Figure 5.1 Minimum free energy configurations calculated for (a) π (b) $-\pi$ disclinations as a function of ε. A change in the sign of ε produces an orthogonal configuration and vice versa.

disclination, at the limits where the elastic anisotropy is ±1, the director field cannot adjust to completely remove the more costly distortion. For both types of disclinations, a change in sign of ε produces an orthogonal director field. Therefore bend of the lamellae indicates splay of the director and vice versa. To illustrate this, hash marks, corresponding to the lamellae, are drawn perpendicular to the director in figure 1a ($\varepsilon = \pm 1$).

Because the structure of disclinations can be observed via TEM and the lamellar decoration technique, the value of ε can be measured form TEM images of disclinations. Furthermore, the core structure may be investigated by measuring the apparent elastic anisotropy, ε_a, as a function of radius. Near the disclination center, the distortions become large. Two different consequences of the increased distortion may be envisioned. First, non-linear corrections to the Frank elastic theory described above become important when the distortion becomes large compared to the molecular size. These corrections lead to an apparent rise in the splay constant when the splay distortion approaches 1/L, where L is the molecular length. Similarly, they lead to an apparent rise in the bend constant when the bend approaches 1/p, where p is the persistence length. Second, because these materials are polydisperse, the distortion may promote segregation of different species at the core leading to <u>real</u> changes in the elastic constants. Regardless of these ambiguities, we are able to measure real structural variation at the disclination core by measuring the apparent elastic constant as a function of radial distance from the disclination center.

5.2 Core structure review

The structure of disclination defects in liquid crystals is interesting for various reasons. The defects show a wide variety of topological structures [Mermin, 1979]. They also appear to dominate rheological behavior at some deformation rates [Marrucci, 1984]. At the heart of both of these issues is the structure of the disclination core. Unfortunately, however, the structure of the core is little known. Even theoretical work is not well

advanced. Disclinations of strength $\pm 2\pi$ in uniaxial materials are free to escape into the third dimension and therefore have a non-singular core as described by Meyer [1972].

The $\pm\pi$ disclinations, however, can not escape--unless the material undergoes a phase transition. The unescaped structure has a singularity at the core. Such a structure has infinite energy density at the center. Obviously, the material will distort in some way to avoid this singularity. The mode of distortion is not obvious, however. Biaxial nematics may avoid a singularity in the weak directors by escaping to a uniaxial core [Chandrasekar and Ranganath, 1986]. This phase change may be second order resulting in a diffuse boundary between the phases. For uniaxial nematics, the situation is less clear. Ericksen [1970] proposed that approaching the singularity, the material would experience a first order transition to an isotropic core. The interface between nematic and isotropic would be sharp, and the core is predicted to be of molecular size. Outside the core the structure may be affected by a number of factors unconsidered by Ericksen: surface tension, director anchoring energies, and elastic anisotropy [Chandrasekar and Ranganath, 1986]. The elastic constants in the highly strained core may have values different from that in the bulk.

Schopohl and Sluckin [1987] have recently calculated the structure of $\pm\pi$ disclinations within the Landau-deGennes framework. They find that the material near the core continuously changes from uniaxial to biaxial, with maximum biaxial character at some distance from the center of the core. The radius of maximum biaxiality may change with temperature.

In light of these studies which predict inhomogeneous structure at the core of a disclination, we wish to investigate the apparent splay and bend Frank elastic constant anisotropy as a function of radial distance from the disclination. To date, the most informative experimental study of disclination core structure is that of Mazelet and Kleman [1986]. They studied a polymeric system where the splay-bend elastic anisotropy is nearly 1. From optical microscopy evidence, they conclude that the π disclination core is larger and scatters light much more strongly than the $-\pi$ disclination. They suggest a large

concentration of chain ends at the π disclination with vertical director alignment for the -π disclination core. An aggregation of chain ends at the π disclination core would introduce splay distortion. This increase in splay distortion would reduce the apparent elastic anisotropy near the core.

A core of different apparent elastic anisotropy in small molecule liquid crystals (SMLC) (if it were possible) might not greatly influence the mobility of a disclination. In polymers, however, such a concentration of chain ends would make disclination motion non-conservative and significantly decrease their mobility. Cladis [1987] has observed the dynamics of -π disclinations in small molecules. The disclination core drags surrounding material with it as it moves, in order to reduce director rotations. In polymers, a concentration of chain ends at a disclination core may enhance this behavior. Mazelet and Kleman [1986] observed higher mobility for the -π than for the π disclination.

The present work concerns the static structure of the core. Such an investigation is made possible by the TEM director imaging technique developed by Thomas and Wood [1985]. The director is revealed in the TEM images by crystalline lamellae 15nm thick. Therefore we are able to probe the radial structure from approximately the scale of the lamellae to a fraction of the separation between disclinations (~ 1μm). This technique then is significantly better than any other presently available to measure the structure of disclination cores.

We use image processing to automate measuring the director. The apparent elastic anisotropy is then measured as a function of distance from the disclination in order to gain understanding of the core of a disclination.

5.3 Sample preparation

In this chapter, I compare the core structure of two different polymers. One is semi-flexible, TQT10-H. This polymer has its glass transition at 67°C, becomes nematic at 231°C and isotropic at 267°C. The molecular weight is estimated to be ~ 18,000 g/mol from

intrinsic viscosity measurements. The length, L, for the fully extended polymer is approximately 100nm. Because the repeat unit contains a 10 carbon flexible spacer, the polymer may fold or form hairpins [de Gennes, 1977]. If many hairpins are present the effective length, L_{eff}, is significantly reduced. The other polymer, QT-OEOM, is rigid. This polymer has its glass transition at 120°C, becomes nematic at 180°C and isotropic at 224°C. Estimating the molecular weight to be 5,000, L is approximately 25nm. In this case, due to inherent molecular rigidity, hairpins are impossible.

To measure the apparent elastic anisotropy as a function of distance from a disclination, we would ideally like isolated disclinations. Disclination interaction is a very important effect and can dominate the results. For a π disclination, the measured value of ε_a (assuming weak anisotropy) differs from the true value by:

$$\Delta\varepsilon_a \sim 2r/3d \qquad (5.6)$$

where r is the radius at which the apparent elastic anisotropy is measured and d is the distance to the neighboring disclination. (This equation will be derived in later discussion.) If we want to limit the effect of disclination interaction to $\Delta\varepsilon_a \sim \pm 0.1$, then we desire disclination separations greater than 7μm. The effects of many neighboring disclinations may or may not cancel.

This requirement for disclination separation is difficult to achieve in typical thermotropic liquid crystal polymers (TLCP's). The technique of surface tension spreading on hot phosphoric acid may work well sometimes. The acid is at a temperature above the crystal-nematic transition yet below the isotropization temperature of the polymer. The solid polymer melts to the mesophase and spreads on the acid. After allowing the film to relax for at least several seconds, the film is quenched by transferring the film on hot acid onto room temperature acid. During transfer, the film floats as a semi-solid body, so the resulting texture is not significantly oriented. The director field is then near equilibrium. The TQT10-H sample was spread at a temperature of 240°C. This technique lacks reproducibility, however, as distortions are sometimes introduced during the flow.

A more reproducible method of obtaining a schlieren texture of disclinations separated by several microns has been developed which works especially well for the rigid material. Polymer, placed between a glass slide and a coverslip, is melted on a hotplate to form a film approximately 1μm thick. The film is thin enough to ensure a planar texture. The coverslip is oscillatory sheared by hand with slow rate and small amplitude. A coarse schlieren texture results. The sample is cooled to liquid nitrogen temperatures, and the two slides are cleaved apart. The sample is heated again to the mesophase to allow the fracture surface to smooth itself. The QT-OEOM sample presented here was held at approximately 200°C for a few minutes. Finally, the sample is quenched in room temperature water. The resulting polymer is glassy with few crystals. Figure 5.2 shows a glassy schlieren texture of QT-OEOM. This especially brittle polymer cracked along the local molecular director during quenching, resulting in the meandering pattern of hairline cracks seen in figure 5.2. These cracks present an interesting decoration method of their own. Also however, their presence raises the issue of polymer shrinkage upon quench. Shrinkage is not expected to cloud the results of this work. Isotropic shrinkage has no effect on the measured values of ε_a. Anisotropic shrinkage (different shrinkage parallel and perpendicular to the chain) changes slightly the value of ε_a, but the change in ε_a is independent of r.

Wood and Thomas' lamellar decoration technique requires thin films, so the oscillatory shear sample preparation technique described above, requiring films at least 1μm thick, is not directly useful. We therefore use the etch technique described in chapter 3. Figure 5.3 shows a replica image of a disclination present in the QT-OEOM sample. The hairline cracks, seen in figure 5.2, appear as the large dark features in figure 5.3. There is inevitable loss of detail in the upper right of this figure where the lamellae are parallel to the shadowing direction. This loss of detail presents a complication.

The core structure which has been measured in this work may also be qualitatively seen by eye. To demonstrate, figure 5.4 shows sketches and images of disclinations having either more bend or more splay at the core.

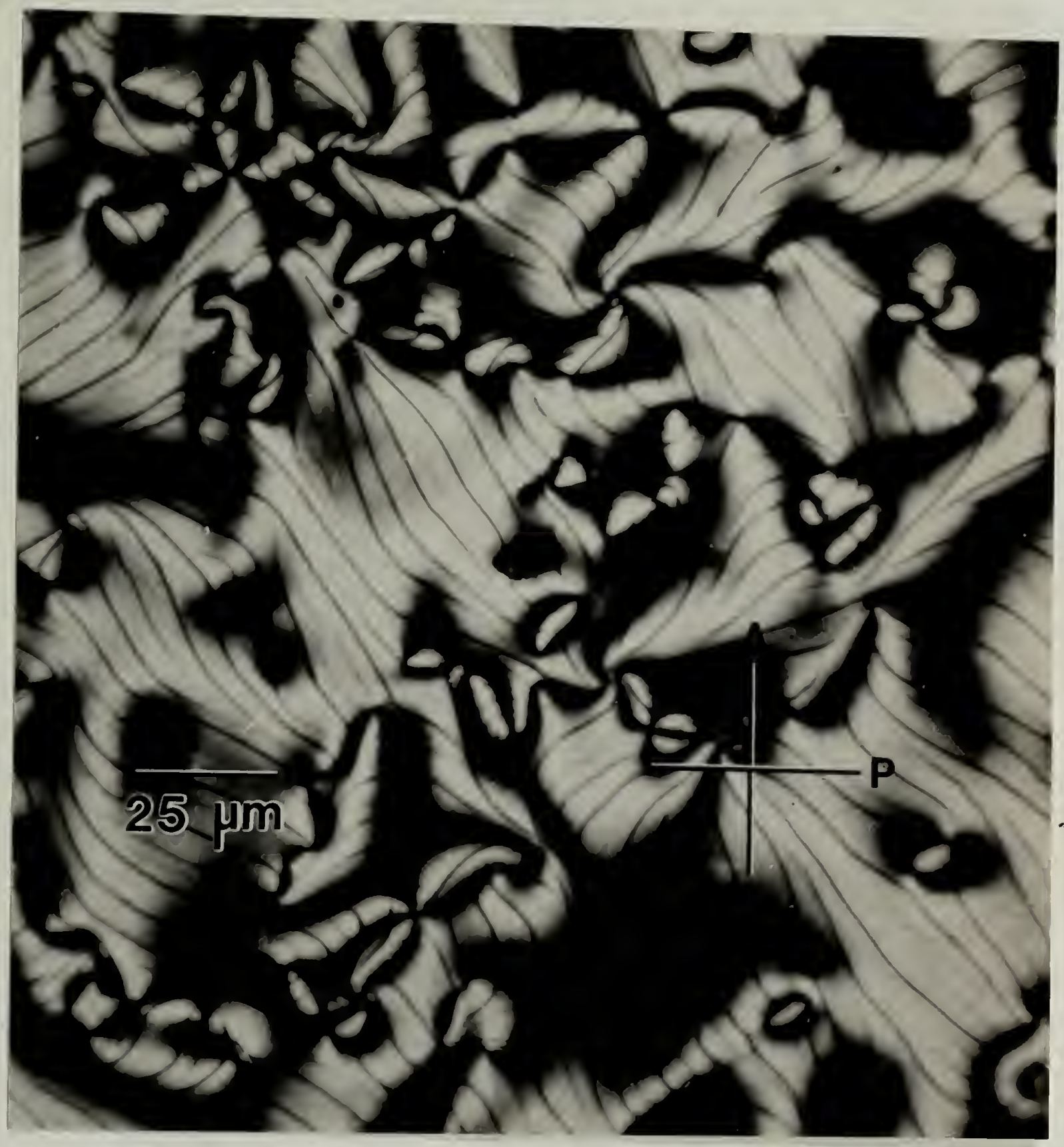

Figure 5.2 Optical Micrograph of QT-OEOM thin film in the glassy state. A schlieren texture is frozen in. The thin dark filaments shown are hairline cracks which formed when the polymer was quenched to room temperature. These cracks are parallel to the director.

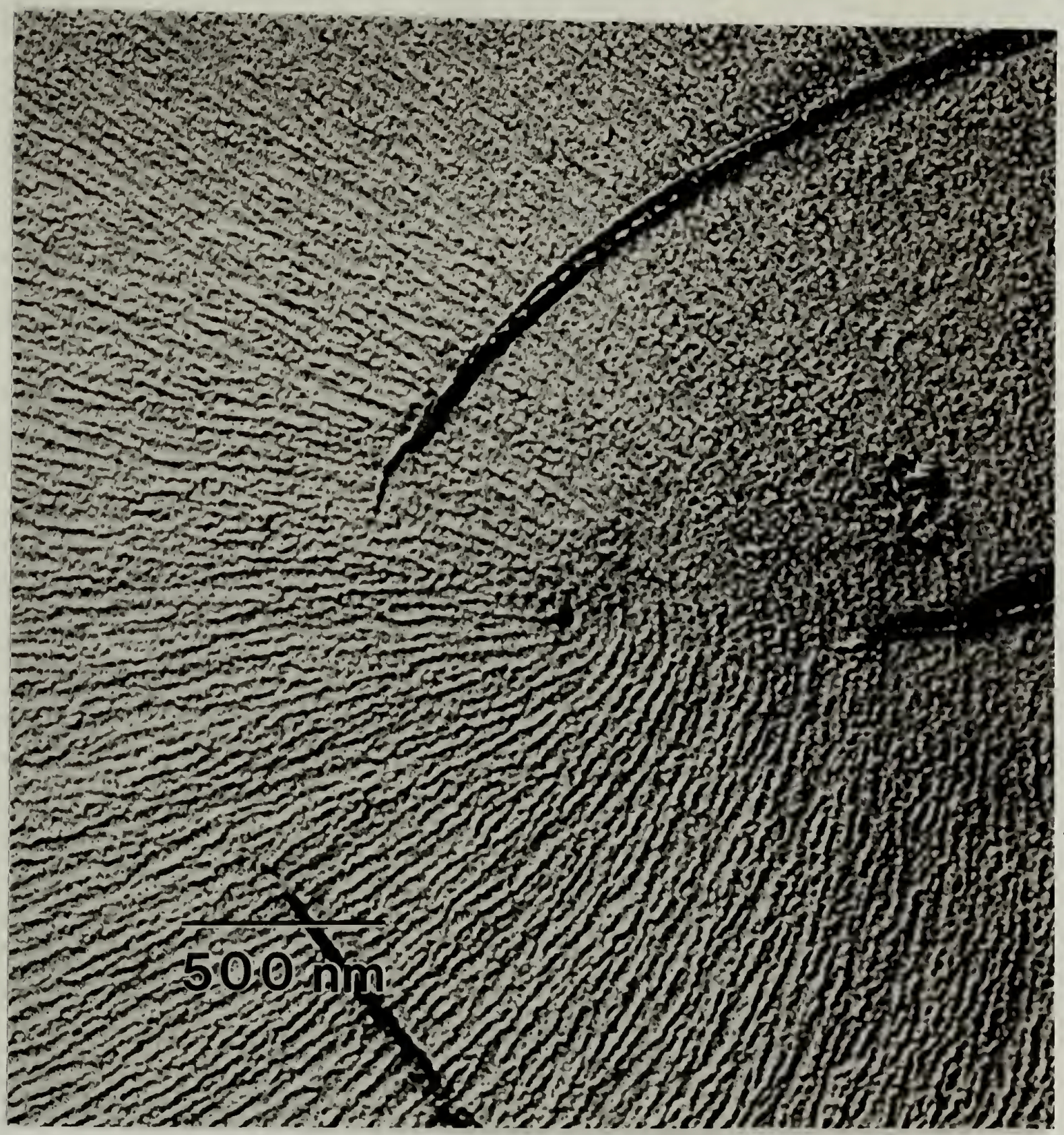

Figure 5.3 TEM replica micrograph showing the core region of a π disclination in QT-OEOM. The large dark features are the cracks which were observed in figure 5.2. The striations are due to the lamellar crystals which are normal to the director.

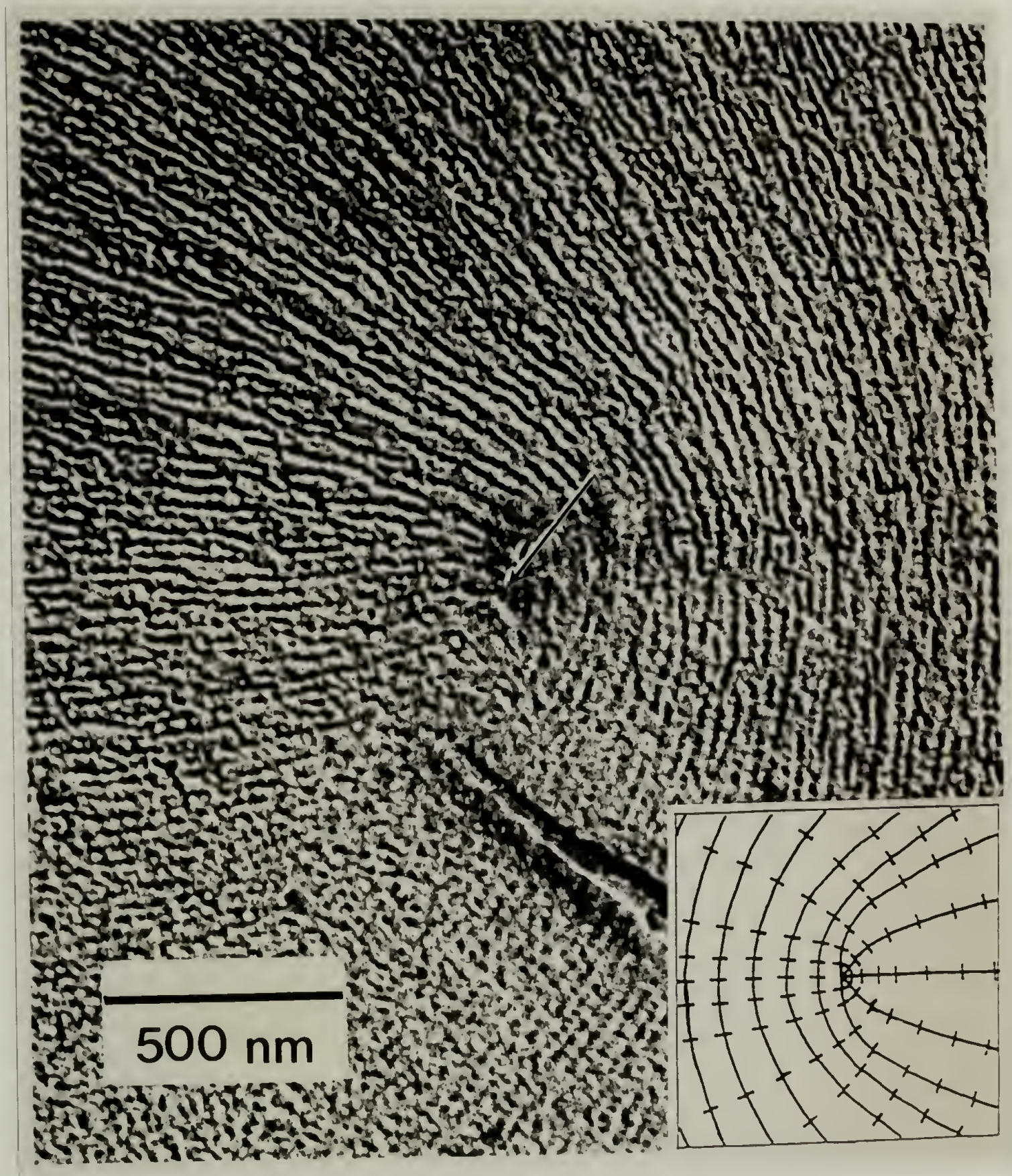

Figure 5.4 TEM micrographs comparing the disclination core structure of QT-OEOM and TQT10-H. (a) A π disclination of the rigid polymer QT-OEOM which has more splay at the core. Because the lamellae are perpendicular to the director, the lamellae appear to bend more at the core (see also figure 5.3). The disclination center is marked with an arrow. Inset is a sketch of a disclination having more splay at the core. The director is shown as the solid line while the lamellae which are perpendicular to the director are drawn as hash marks. (Continued next page.)

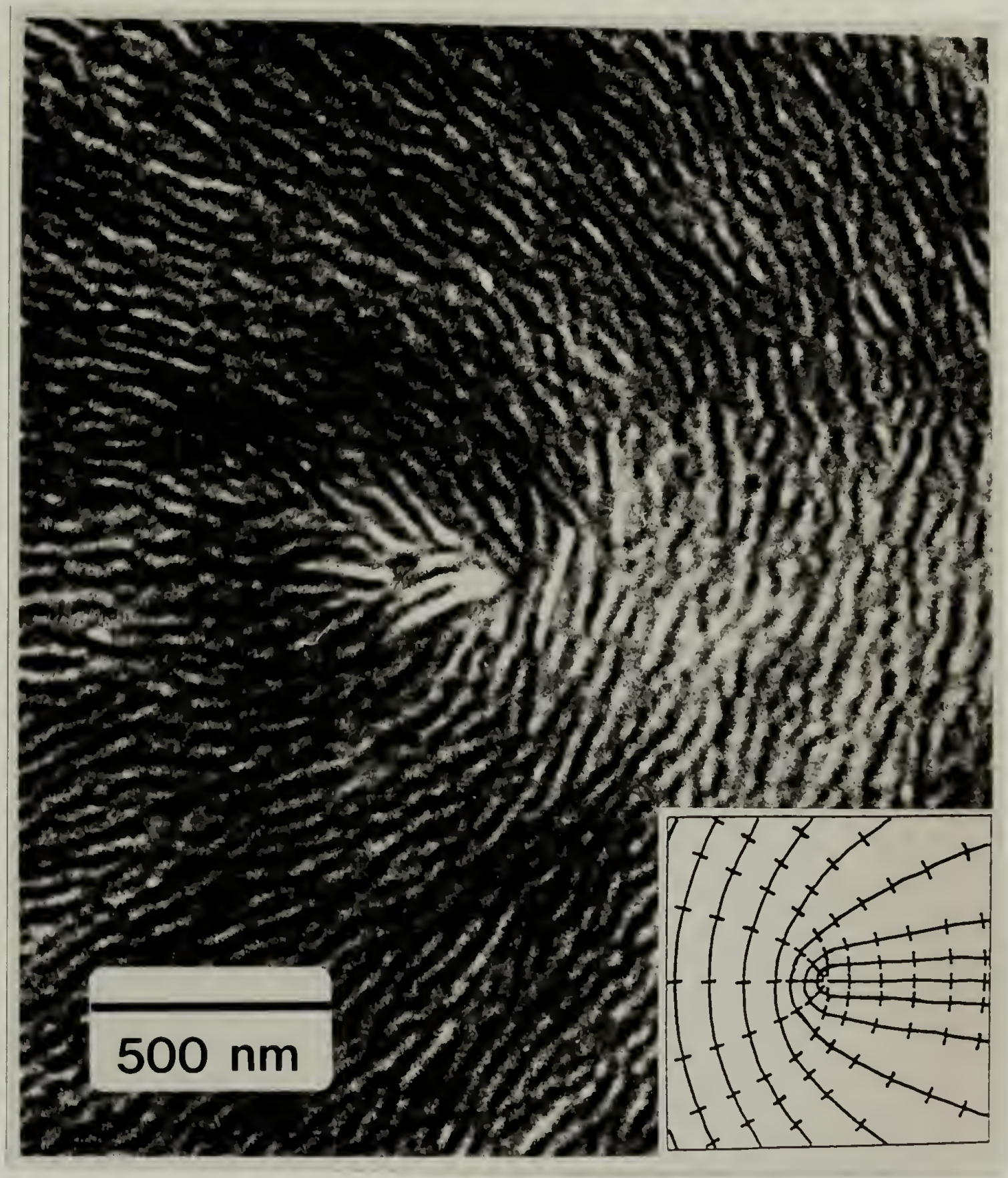

Figure 5.4 TEM micrographs comparing the disclination core structure of QT-OEOM and TQT10-H. (b) A π disclination of the flexible material which has more bend at the core. The lamellae appear to splay more. Inset is a sketch of a disclination having more bend at the core.

5.4 Data collection

Initial measurements were done using a protractor. Figure 5.5(a) is a TEM micrograph of a π disclination in the TQT10H sample. In order to determine the elastic constants from the director field of a defect, we measure the orientation of the lamellae at various positions about the disclination with respect to a fixed axis. To obtain ϕ, the orientation of the director, 90 degrees is added. Figure 5.5(b) shows the data $\phi(\theta)$ collected from (a) at a radius of 1.6μ. The elastic anisotropy is determined from a least squares fit of the theory to the data.

To facilitate unbiased data collection of $\mathbf{n}(\mathbf{r})$, the image processing program descibed in chapter 3 has been used. A soft Hamming window is stepped over the image. At each step, the windowed image is Fourier transformed, and the director orientation is determined from the angular position of the peak in the power spectrum.

Although the lamellae in an image such as figure 5.3 are clearly seen by eye, there is sufficient noise where the lamellae are parallel to the shadowing direction, that the local power spectrum does not contain a strong peak corresponding to the lamellae. Because the lamellae are clearly seen by eye, the image can be accurately and reproducibly traced with a pen. The tracing is then digitized and processed. Figure 5.6 shows the superposition of a trace, and the map of local normals to the director field calculated from the trace. The radius of the Hamming window, as characterized by the radius at half maximum transmission, used in processing this image is 77nm. The calculated director field accurately reproduces the trace.

The images of the flexible polymer, TQT10-H, are of thin films which were not replicated. They do not suffer the problem due to shadowing, so both traces and the images themselves were processed to calculate the director field. The window radius at half max used in processing was 67nm.

(a)

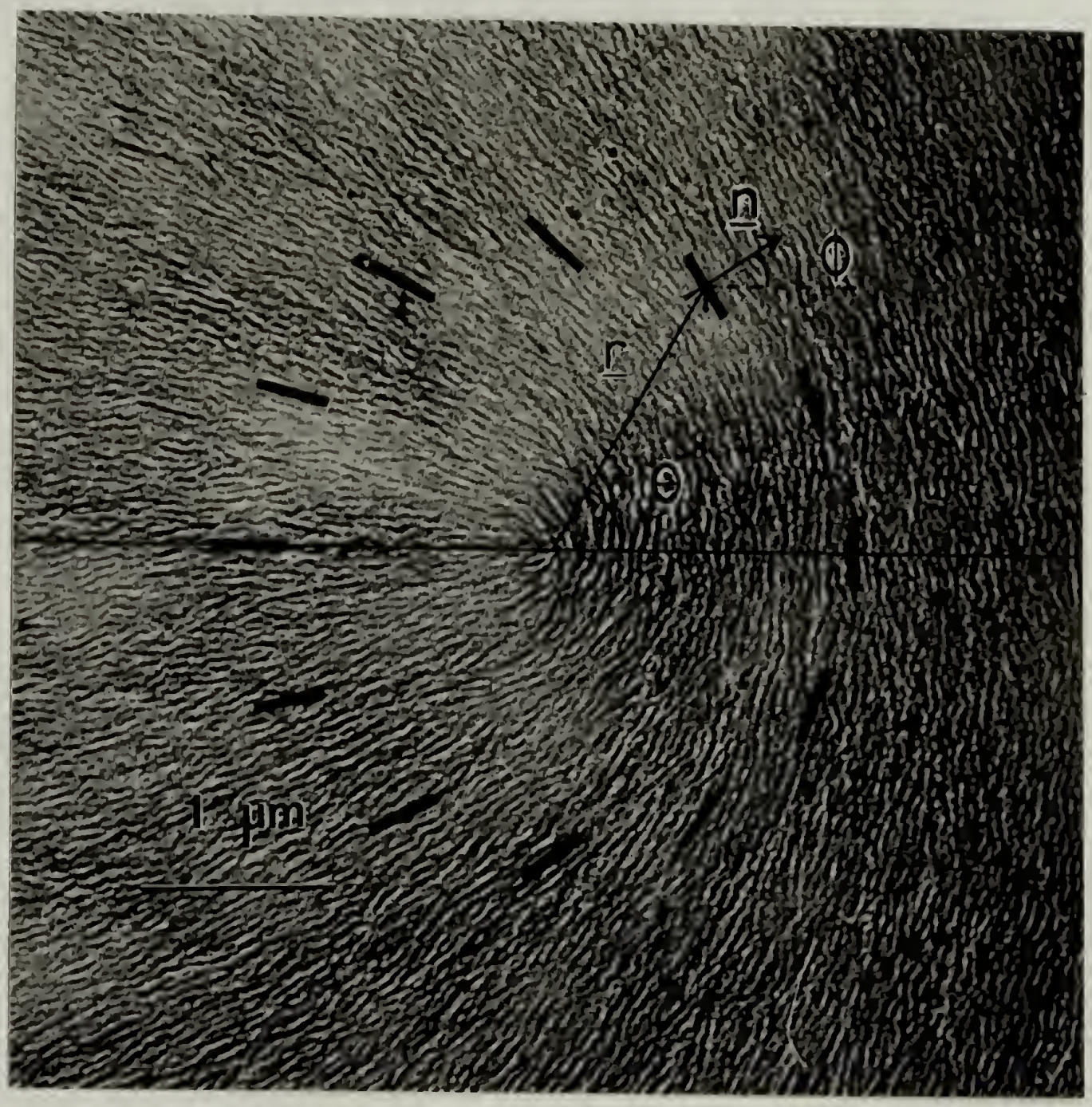

(b)

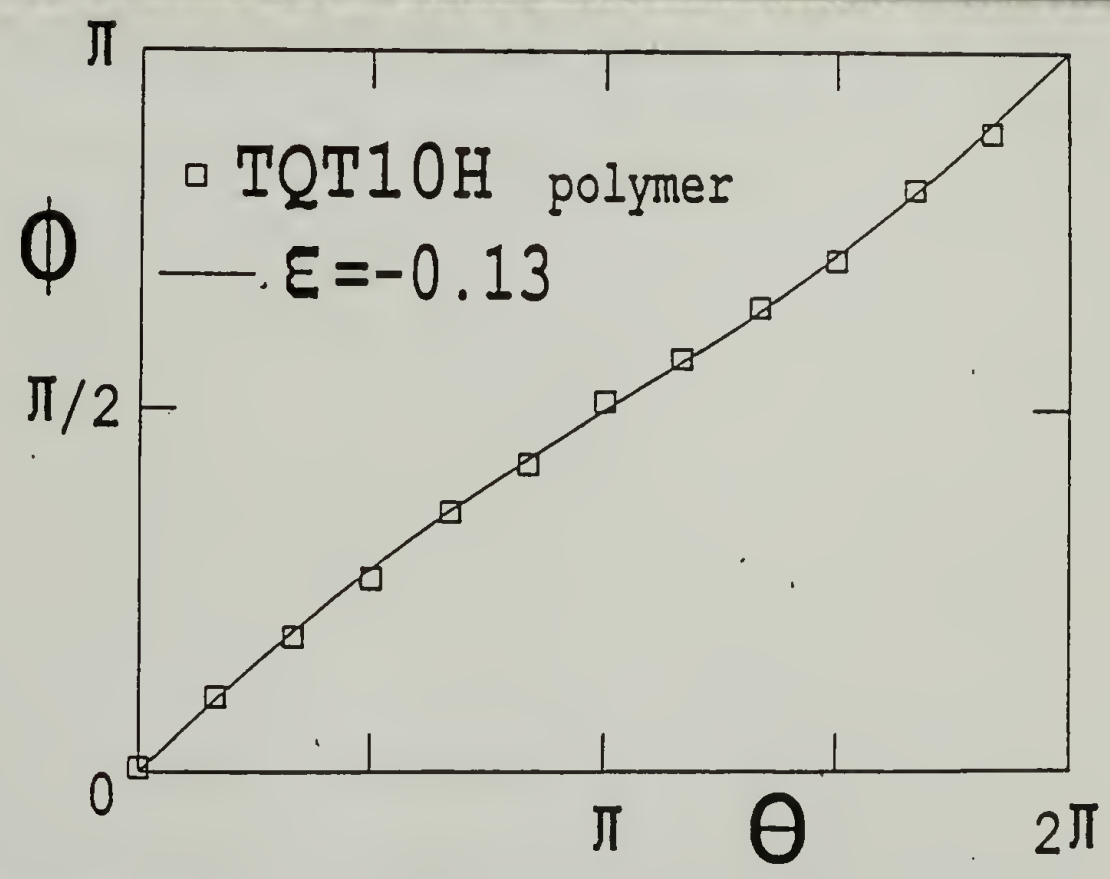

Figure 5.5 (a) Electron micrograph of the TQT10-H polymer showing a π disclination used for measuring ε. (b) Data taken from (a). The line through the data was fit by varying ε.

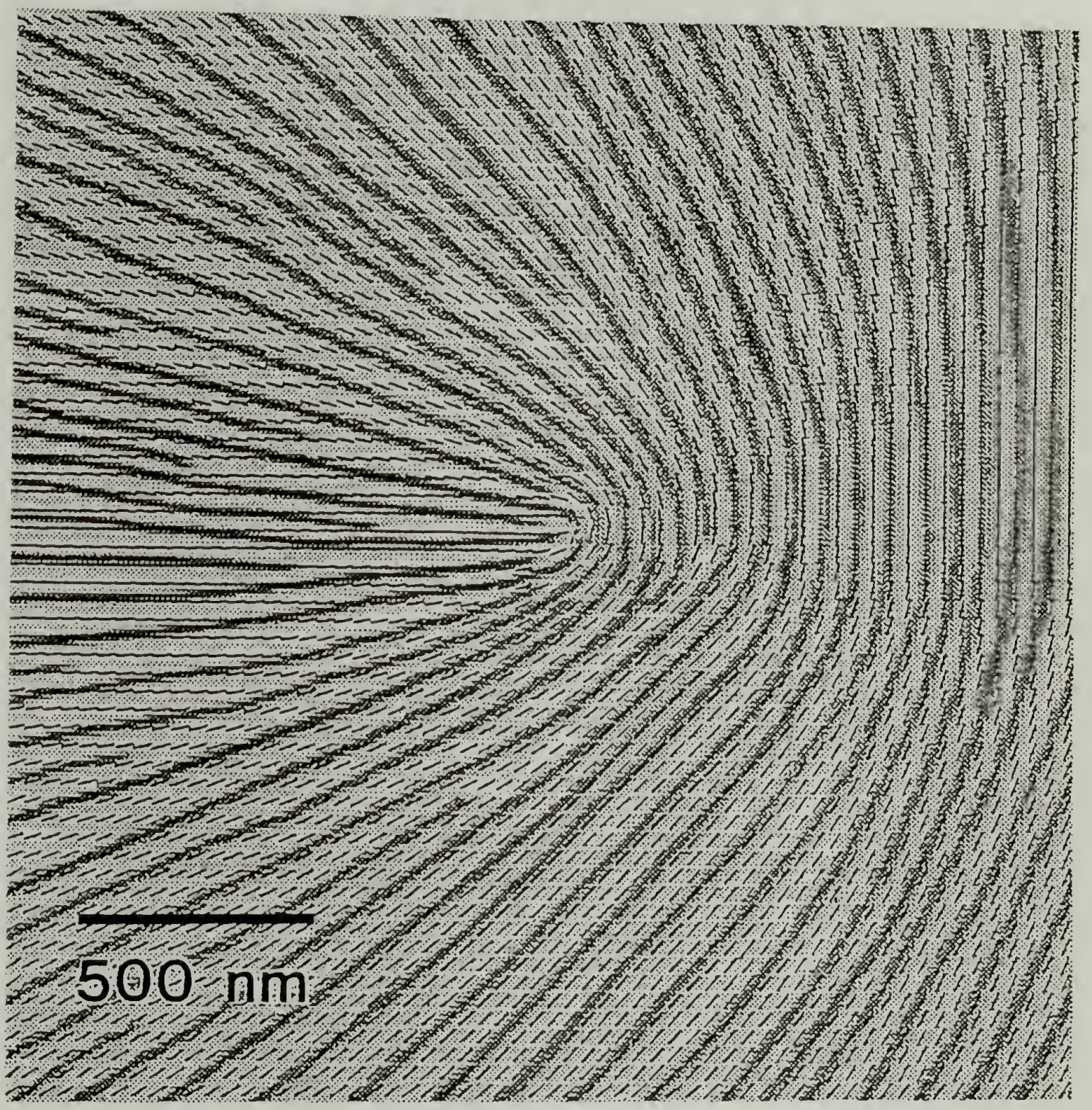

Figure 5.6 Results of the image processing (shown as hash marks) overlaid on a trace of figure 5.3. Both the trace and the hash marks are perpendicular to the calculated director.

5.5 Data analysis

Output from the processing program is the director angle, ϕ, at data points corresponding to the location of the center of each window. The position of the disclination can easily be measured from the superposition of the image (or trace) and the director field. To measure the apparent elastic anisotropy as a function of distance from the disclination,

$\phi(r,\theta)$ data is desired. All data points inside the shell between r and r+Δr are included in $\phi(r,\theta)$. The number of data points increases with radius. Figure 5.7 shows $\phi(r,\theta)$ data obtained from figure 5.3; $\Delta r = 39nm$.

The apparent elastic anisotropy, ε_a, is determined by the least squares fit of the data, $\phi(r,\theta)$, to the first order perturbation expansion in terms of ε_a [Caroli and Dubois-Violette, 1969].

$$\phi_{calc}(\theta) = n\theta_o/2 + n\theta/2 - \varepsilon_a\, n(4-n)/(4(2-n)^2)\, \sin((2-n)(\theta-\theta_o)) \qquad (5.7)$$

where n is the Frank index, and θ_o is the orientation of the disclination. Because the perturbation is a sine function, ε may be calculated from the Fourier coefficients of the

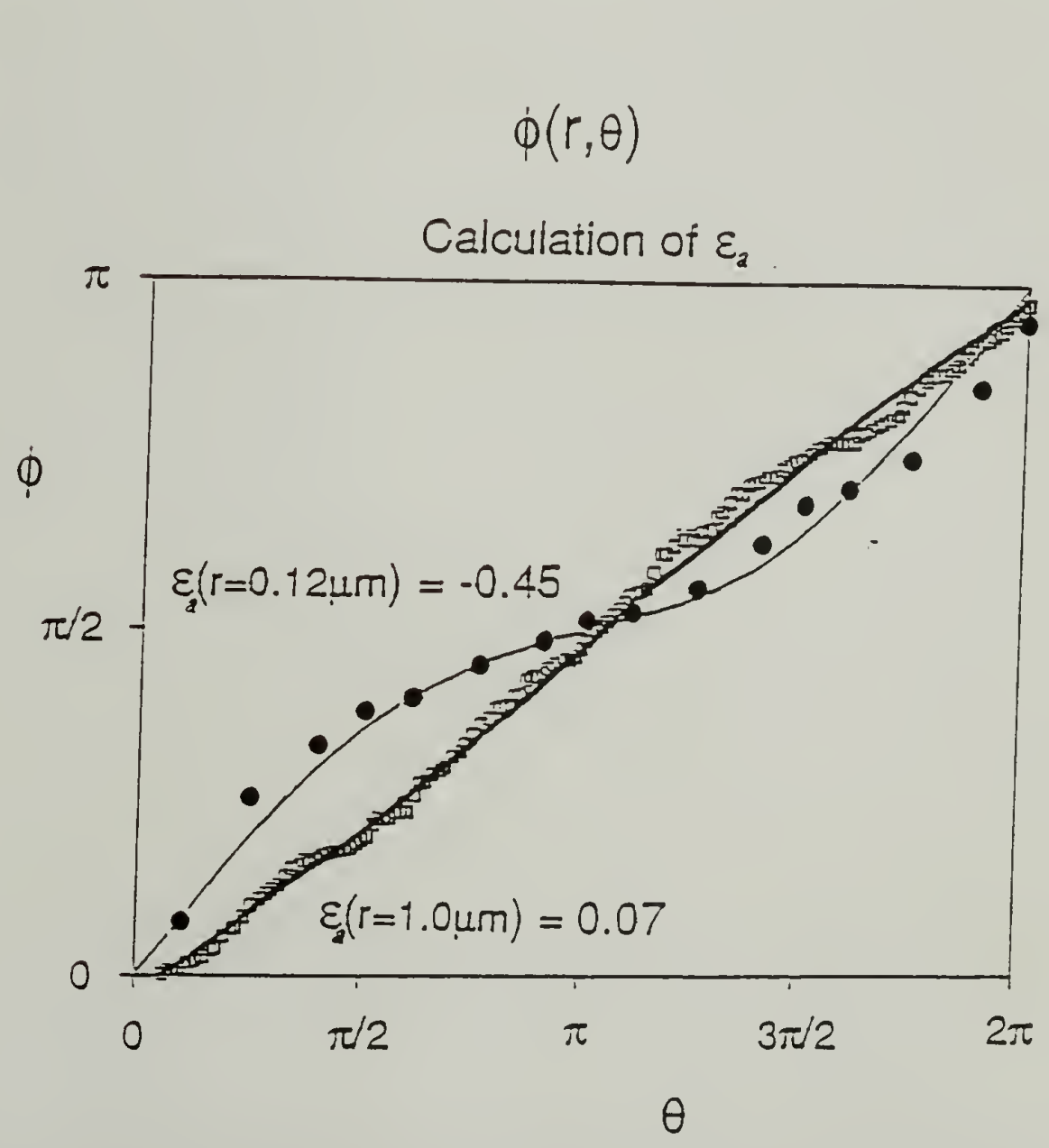

Figure 5.7 Data taken from figure 5.6 at two different radii. The curves which fit the data are generated from the Fourier coefficients calculated from the data as described in the text. ε_a at 0.12μm is -0.45; ε_a at 1.0μm is 0.07.

perturbation part of the data ($\phi(r,\theta)$ - $n\theta/2$). These Fourier coefficients are known to give a least squares fit to the data. Because ϕ_{calc} is independent of r, each radius is treated independently. Only the pertinent Fourier coefficients are calculated: a_o, a_i, and b_i, where i = 2-n. (a_i is the i^{th} cosine coefficient.)

θ_o and ε_a are calculated from the coefficients as follows:

$$\theta_o = a_o/n \quad , \tag{5.8a}$$

$$\varepsilon_a = 4(2-n)^2/(n(n-4))\,(a_i^2 + b_i^2)^{1/2}\cos(\alpha) \quad \text{,and} \tag{5.8b}$$

$$\alpha = a_o - \tan^{-1}(a_i/b_i) \quad . \tag{5.8c}$$

α is a measure of the phase shift between the i^{th} Fourier coefficients and the orientation of the disclination. α, therefore, determines the sign of ε_a. For an isolated symmetric disclination, α is an integer multiple of π.

If the disclination is distorted, a_i and b_i may both include a contribution from the distortion. If the type of distortion is known, then the effects of the distortion may be subtracted from the coefficients. Distortions due to disclination interactions are discussed in the next section.

If there is noise in the data, $\phi(r,\theta)$, only the contribution due to the noise which is in phase with the orientation of the disclination will be included. The effect of noise is to increase the error bars in the calculation of ε_a.

Figure 5.7 shows data from figure 3 at r = 0.12μm and 1.01μm and the calculated fitting function in each case. The root sum square error is 0.445 and 0.633 radians respectively.

5.6 Results and discussion

Figure 8a shows $\varepsilon_a(r)$ for a few π disclinations of QT-OEOM. Figure 8b shows the same for TQT10-H. Figure 8c shows the respective types of curves in a and b averaged. Various isolated measurements on other samples are listed in table 5.1.

(a)

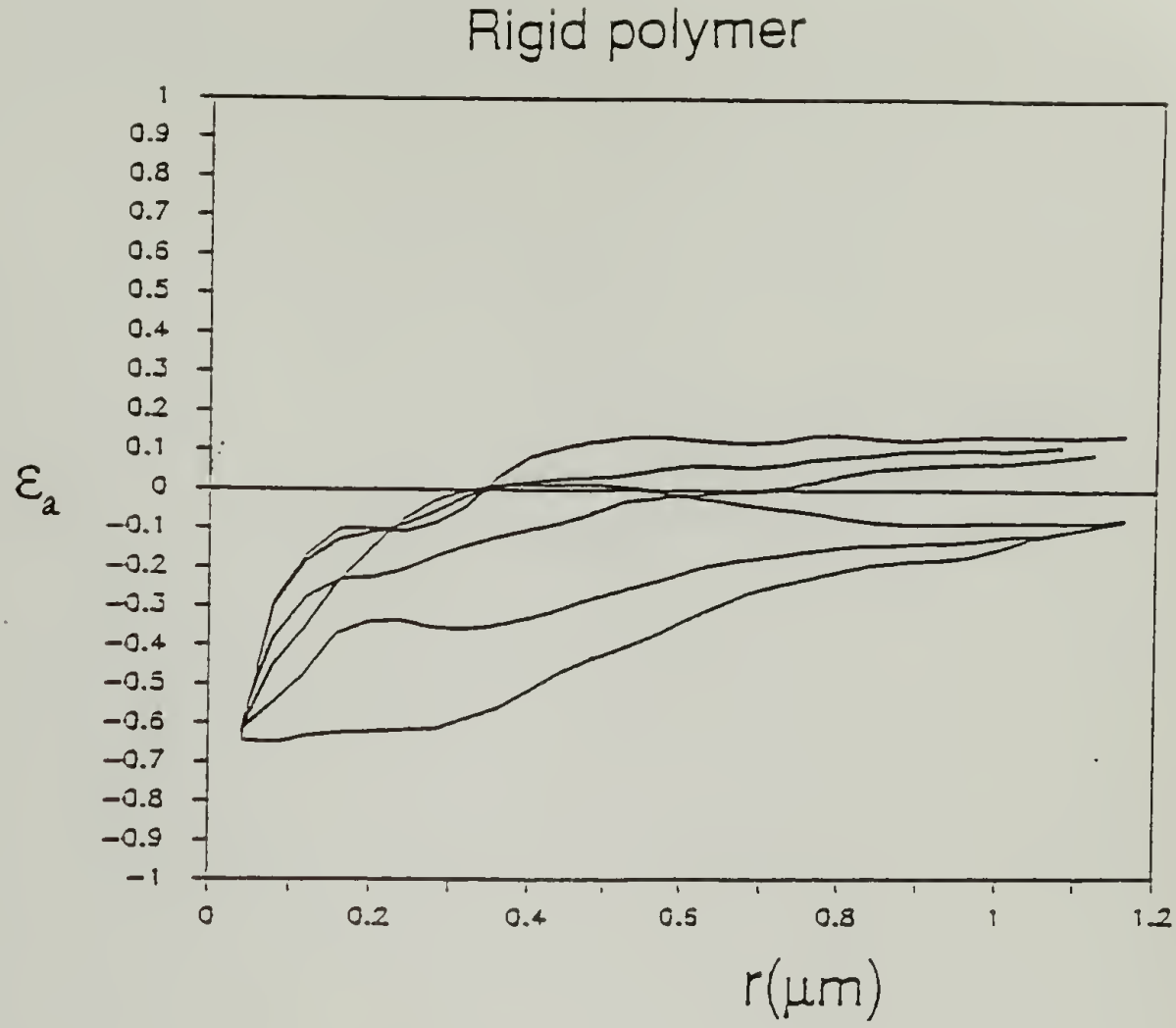

(b)

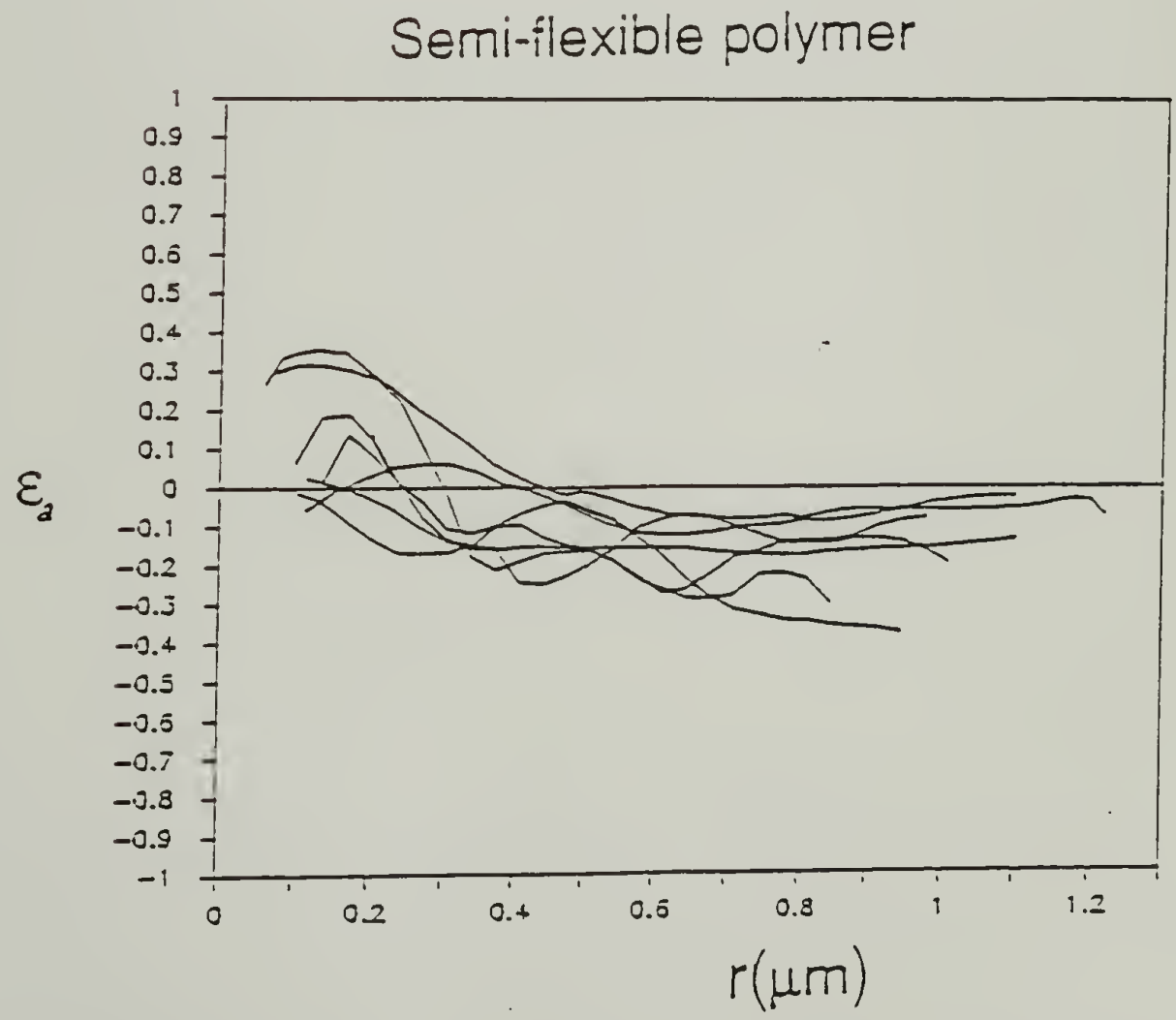

Figure 5.8 $\varepsilon_a(r)$ results for (a) QT-OEOM , (b) TQT10-H and (c) average curves for both polymers.

(Continued next page.)

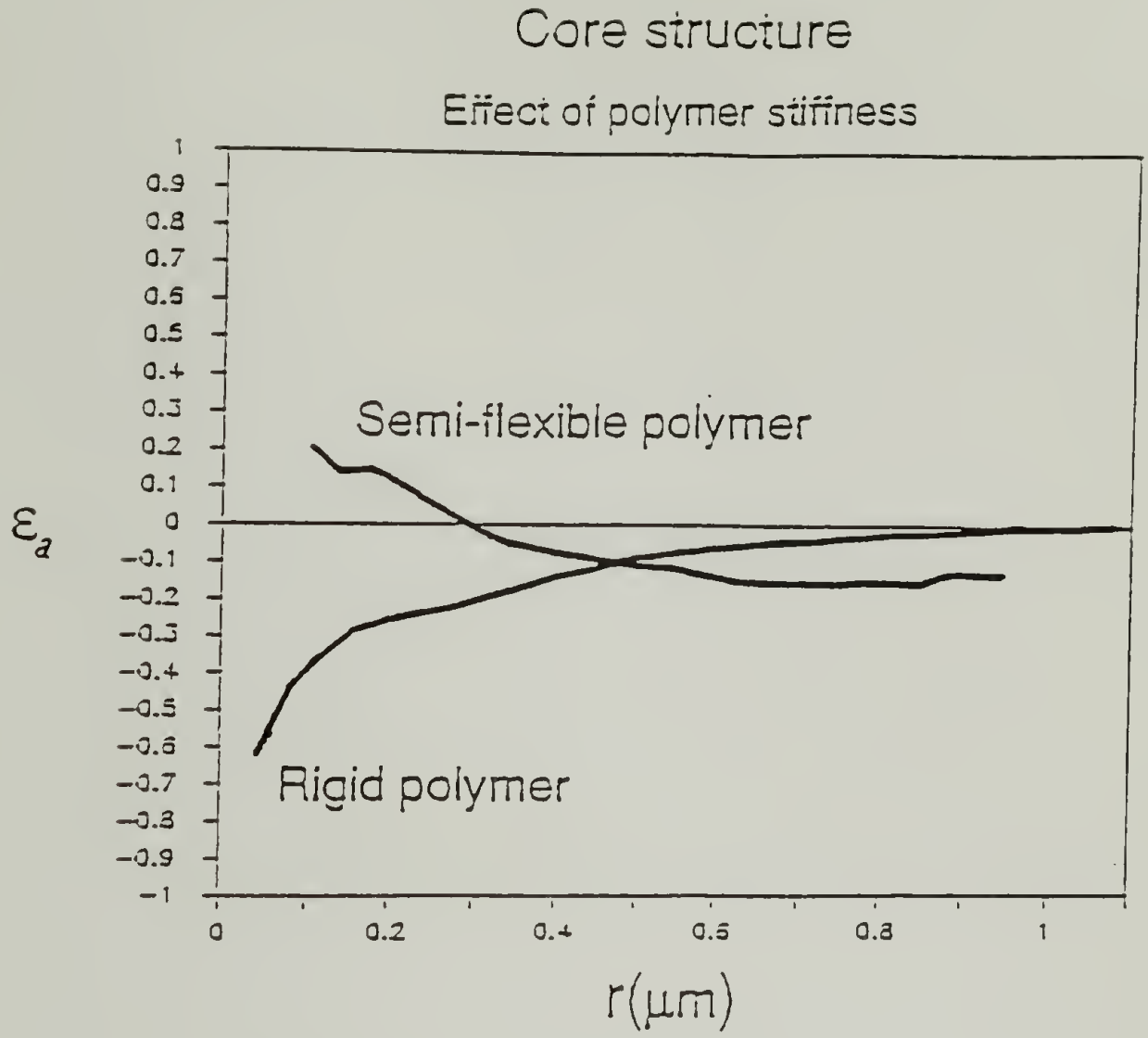

Figure 5.8 (c)Average curves for both polymers.

Table 5.1 Other elastic anisotropy measurements.

polymer	radius	ε_a
TQT10-M	200nm	0.15
	200nm	0.16
	200nm	0.29
OQ5a#1	100nm	0.03

Results demonstrate that there is a special structure of the core at radii less than about 400nm. Note that the core region is diffuse rather than having a sharp boundary. The rigid material splays significantly more at the core. At a distance of 100nm, ε_a is approximately -0.4, yet the asymptotic value, ε, (at a distance of 1μm) is approximately 0. In contrast, the flexible material bends more at the core; ε_a(100nm) ~ 0.1 and ε ~ -0.15.

These results follow the trend expected for rises in the apparent elastic constants due to non-linear corrections to Frank theory. Splay requires the aggregation of chain ends (or hairpins, if they are possible). Aggregation of chain ends, however, costs the system entropy and results in the splay elastic constant proportional to the molecular length, L [Meyer, 1982]. Nonlinear corrections become significant and increase the splay constant when the amount of splay approaches 1/L. Similarly, the bend constant increases when the amount of bend approaches 1/p, where p is the persistence length. For flexible liquid crystals, where p<<L, the splay constant will be increased significantly before any change is observed in the bend constant. For rigid materials, however, where p is at least L, the bend constant is observed to be larger than the splay constant [Odijk, 1986].

Approaching a disclination, both bend and splay distortions tend to grow as 1/r. Therefore at radii less than a few L, flexible polymers will tend to bend more in order to reduce the aggregation of chain ends or hairpins. The bend elastic constant will be independent of radius while the splay constant will apparently increase. ε_a will increase near the disclination. If, however, the polymer is stiff, the entropy penalty of aggregating chain ends will be paid to avoid bending. The apparent bend constant will increase more rapidly towards the disclination center than the splay constant. Consequently, ε_a will decrease at the core. These trends precisely are observed in figure 8. The change in ε_a at radii less than 400nm is consistent with the molecular length of each polymer--approximately 25-100nm. Since the effect of hairpins is principally to reduce the effective molecular length thus reducing the core size, we expect that no more than a few hairpins/chain are present. And hairpins are not more abundant within the core because ε_a increases there.

Not only the trend of ε_a, but the asymptotic value, ε, is also indicative of the molecular structure. For both polymers, ε is nearly 0 even though the stiffness of the molecules are very different. These polymers neither behave as flexible molecules of infinite length ($\varepsilon \sim 1$) or as completely rigid rods (ε approaching -1). Increased stiffness of a molecule

tends to decrease ε, while increased molecular length tends to increase ε. For both of these polymers, the molecular length may not be its effective length. Chain ends cause a stress field which may be canceled by the coupling of an opposite chain end [Meyer, 1982]. Coupled chains are effectively longer. This coupling may be enhanced by hydrogen bonding of acid end groups [Mazelet and Kleman, 1986]. The flexible polymer may also reduce its effective length by forming hairpins in the chain. The ten carbon spacer is certainly capable of forming a tight fold. Although the similar values of ε for the two polymers suggest either chain end coupling in the rigid polymer or some hairpins in the flexible polymer, the existence of chain end coupling or hairpins cannot be proven without observations of $\varepsilon_a(r)$ as a function of molecular weight. Changes in both the radii of the core and the values of ε as a function of molecular weight would reveal the presence and importance of either chain coupling or hairpins.

Impurities and polydispersity of molecular weight may also be important. To increase the concentration of chain ends near the core, lower molecular weight material may be segregated. The increased concentration of chain ends near π disclinations in rigid polymers may retard their mobility.

We now turn to a discussion of possible sources of error and limitations to our approach. First, we discuss the fitting function used to find ε. The fitting function is a perturbation function valid only when ε is small. How good is this approximation? It works to our advantage that ε never gets very big: $-1<\varepsilon<1$. The quality of the fit also depends on the strength of the disclination and the number of data points. The effect of the number of data points, however, is not significant, since low frequency coefficients are being calculated. For a π disclination and infinitely many data points, the calculated value of ε is 0.85 when ε=1, and 0.48 when ε=0.5. Near the core, there are fewer data points to calculate the coefficients. At the disclination core the number of data points may be as few as 8 points. When only 8 data points are used, ε is calculated to be 0.89 when ε=1. So for the extreme values of ε, the fitting function is off by at most 15%. For typical values of ε, and for both ±π disclinations,

the fitting function is accurate to better than 5%. Clearly the trends observed in figures 8a and b are not significantly affected by our choice of a simple fitting function.

The effect of disclination interaction can be, on the other hand, quite significant. Taking the limit when the elastic anisotropy is very small, the effect of a neighboring disclination is dominated by the isotropic part:

$$\phi(\theta) = n\theta_o/2 + n\theta/2 - \varepsilon\, n(4-n)/(4(2-n)^2)\sin((2-n)(\theta-\theta_o)) + n_d/2\tan^{-1}((y-d\sin\theta_d)/(x-d\cos\theta_d)) \quad (5.9)$$

where d, θ_d is the position of the neighboring disclination with Frank index n_d. To find the effect of the neighbor on the calculated value of ε, simply calculate the appropriate Fourier term of the last term in equation 5.9. For a π disclination interacting with one neighbor, the director field is approximately:

$$\phi(\theta) = \theta_o/2 + \theta/2 - \varepsilon\, 3/4\sin(\theta-\theta_o) + n_d(\theta_d-\pi)/2 - n_d/2\, r/d\sin(\theta-\theta_d) \quad (5.10)$$

The effective change in the observed ε is:

$$\Delta\varepsilon = n_d\, 2/3\, r/d\cos(\theta_d-\theta_o). \quad (5.11)$$

This can then be subtracted from the calculated value of ε to get a corrected value. Figure 5.8(a) showed data corrected for disclination interaction in this way. Figure 5.9 shows the uncorrected data from QT-OEOM. A variety of orientations and distances for the neighboring disclinations are represented. The correction well accounts for the divergent behavior of the uncorrected data.

The -π disclination is much more immune to the effects of neighboring disclinations. The three fold symmetry of the -π disclination which limits the effect of ε, also limits the effect of neighbors.

A similar analysis can be made of the effect of miscentering the origin on the disclination:

$$\phi(\theta) = n/2\ \tan^{-1}((y-\Delta r\sin\theta_d)/(x-\Delta r\cos\theta_d)) \qquad (5.12)$$

$$- \varepsilon\ n(4-n)/(4(2-n)^2)\ \sin((2-n)(\theta-\theta_o))$$

$$+ n\theta_o/2$$

where Δr, θ_d is position of the disclination with respect to the coordinate origin. For a π disclination, the director field is approximately:

$$\phi(\theta) = \theta/2 + \Delta r/2r\ \sin(\theta-\theta_d) \qquad (5.13)$$

$$- \varepsilon\ 3/4\ \sin(\theta-\theta_o) + \theta_o/2$$

And the effective change in the calculated value of ε is:

$$\Delta\varepsilon = 2/3\ \Delta r/r\ \cos(\theta_d-\theta_o). \qquad (5.14)$$

Note that this effect goes as 1/r. The observed structure in figure 5.8 also is approximately

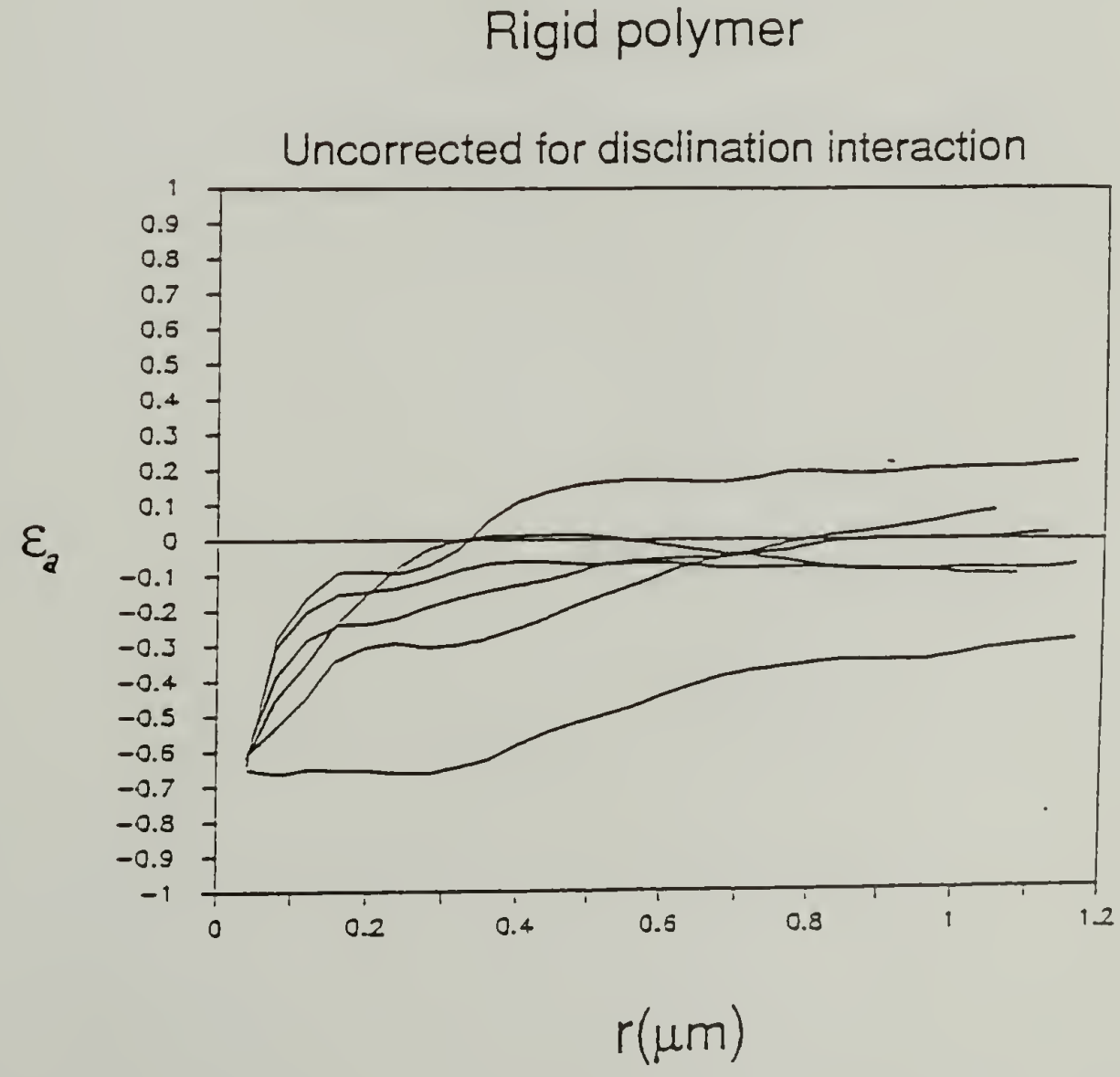

Figure 5.9 $\varepsilon_a(r)$ raw data for QT-OEOM. Figure 5.8(a) shows data corrected for neighboring disclination interaction.

1/r. Obviously, it is very important to evaluate how much of the observed effect could be due to miscentering. In good quality images as in figure 5.3, the error in miscentering is less than or equal to the lamellar period. This amount of error could contribute at most 1/3 the observed effect.

Thermal fluctuations, which will vary with film thickness, mean elastic constant, and sample temperature before quench, may contribute to spread in the data. Assuming that the sample is thin and that the fluctuation inside a radius R is independent of radius, the root mean square error in the elastic anisotropy is given as:

$$\langle \Delta\varepsilon^2 \rangle^{1/2} \sim (k_B T / kt\pi \ln(R/r_c))^{1/2}$$

where k is the mean elastic constant, t is the film thickness, and r_c is the radius of the core of the disclination. We can estimate from our conditions ($k \sim 10^{-6}$dyne, $t \sim 5\times10^{-6}$cm, $R/r_c \sim 500$, and $T \sim 400°K$) that $\langle \Delta\varepsilon^2 \rangle^{1/2} \sim 0.02$. This is a slightly smaller deviation than those mentioned above.

Finally, other contributions to error may be avoided by careful experimental procedure. Rapid quenching assures minimal errors due to the crystallization, or decoration, process. Low electron dose when directly imaging thin films minimizes error due to radiation damage. Chemical crosslinking, which occurs as the sample is irradiated with electrons, causes shrinkage normal to the lamellae, or along the chain direction. Highly damaged samples therefore give a measurement for ε that is more negative. We find for these samples that doses less than $10^{-3}C/cm^2$ result in negligible shrinkage. This dose is more than an order of magnitude smaller than the crystal lifetime (4×10^{-2} C/cm^2) as measured by the fading of the equatorial diffraction spots. All micrographs used for our measurements were obtained with a dose of less than $10^{-3}C/cm^2$. Note that the replicated samples do no suffer from this restriction.

In conclusion, there are a number of factors which may introduce error to these elastic constant measurements. The largest source of error is neighboring disclination interaction. Fortunately, for these polymers with weak elastic anisotropy, the major

contribution due to neighboring disclinations may be calculated and subtracted from the results. Non-linear effects of disclination interaction can not be evaluated at the present time. The second largest contribution to the error is misjudging the center of the disclination. The effect of this type of error is strongest at the disclination.core. The error, however, is estimated to contribute, at most, 1/3 of the observed structure at the core.

5.7 Future work

This work is a very interesting start in exploring the core structure of disclinations. Perhaps more, however, it is a demonstration of what happens when the distortion gets large compared to the molecular size. It just so happens that the distortion only gets this large near a disclination.

The next step should most certainly be to compare π and $-\pi$ disclinations. And the two defects should be strikingly different! The sign of splay for these two defects relative to the gradient in distortional energy density is opposite. Positive and negative splay are shown in figures 5.10 (a) and (b). The splay is positive for π disclinations and negative for $-\pi$ disclinations.

The difference between splaying from a region of high distortion to a region of low distortion (as in the case of π disclinations) and splaying from a region of low distortion to a region of high distortion (as in the case of $-\pi$ disclinations) should be a very significant effect when the distortion becomes nearly the molecular size. In the case of the π disclination, an arbitrary amount of splay can be accomodated, as shown in figure 5.10(c). In the case of a $-\pi$ disclination, the splay may only reach approximately 1/L before the structure must be altered to avoid the large density fluctuation shown in figure 5.10(d). In thin films, the film thickness can easily vary to accomodate the desired density fluctuations. For thin films spread on phosphoric acid, both Wood [1985] and I observe that the film thickness is increased at π disclination cores and it is decreased at $-\pi$ disclination cores. In bulk samples, in order to fill in the gap where a molecule will no longer be able to accomodate splay, several

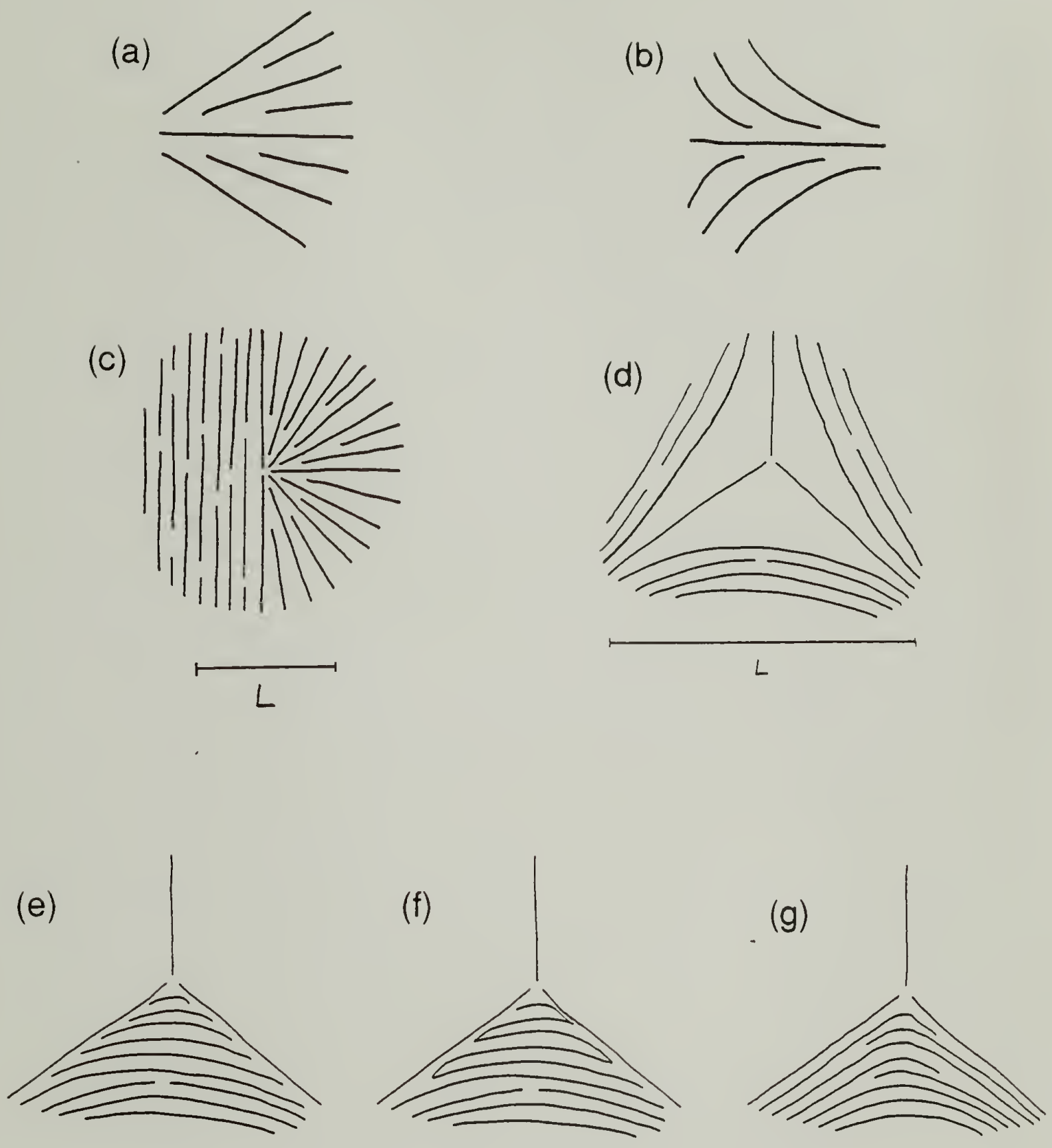

Figure 5.10 Sketches of splay distortion near a -π disclination. (a) Positive splay. (b) Negative splay. (c) An arbitrary amount of splay may be accommodated at a π disclination. (d) Rigid monodisperse rods cannot accommodate an arbitrary amount of splay at a –π disclination. A large density fluctuation is shown. If the sample is polydisperse, lower molecular weight material can segregate to the core to accommodate the splay distortion as shown in (e). If the chains are flexible, hairpins may aggregate at the core as shown in (f). If neither (e) nor (f) are possible, twist and/or bend distortions may compensate as shown in (g).

things may happen. 1.) Successively lower molecular weight fractions may be segregated (figure 5.10(e)). 2.) The polymer may form hairpins if it can (figure 5.10(f)). 3.) Twist or bend distortions may increase (figure 5.10(g)), i.e. increasing the observed elastic anisotropy.

Figure 5.11 shows a TEM image of a -π disclination in the QT-OEOM sample described before. Comparing this figure to figure 5.1(b), it appears that the lamellae splay more at the core, i.e. the director may twist or bend at the core to avoid splay distortions, which at the core require density fluctuations. Because the relative amounts of splay and bend can only be moderately altered, their measurment is subject to greater uncertainty. Perhaps a larger molecular weight polymer producing a larger core size will aid in this investigation.

As mentioned above, varying the molecular weight of the polymer should give interesting results on the relative importance of chain end coupling or hairpins in that particular polymer.

Investigation of these molecular structures can also be aided by precise temperature control and extremely rapid quenching. Measurements very near to the isotropization temperature should give very different results. Hairpins should be much more prevalent. It would also be interesting to observe the sample during a phase transition to the isotropic. Is the core structure altered? Is the core perhaps a nucleation site for the isotropic phase [Ericksen, 1970]? (If not, investigations of the phase transition, both from nematic to isotropic and isotropic to nematic, will be interesting in their own right. How the phase is nucleated and the nature of the interface between phases have not been investigated.)

Blending of various materials together provides another useful perturbation of the system. If a small amount of flexible component were blended with a stiff TLCP, it might conceivably segregate at the disclination cores, relaxing the distortion. Both miscible and immiscible blends should be studied. The random semi-flexible polymers are blends themselves of molecules of varying flexibililty. Above the biphasic temperature, the most

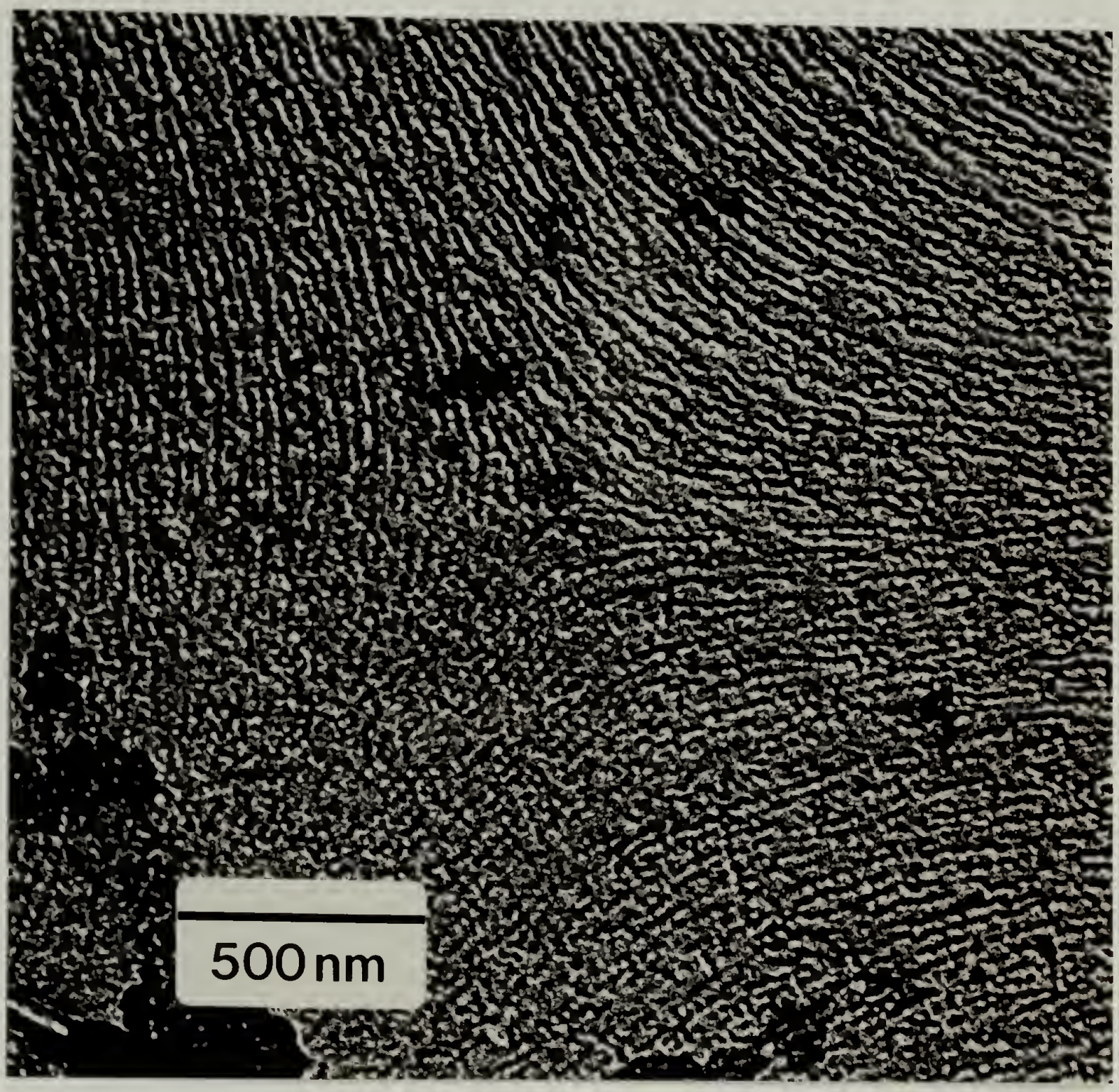

Figure 5.11 TEM micrograph of a replica showing the core region of a -π disclination in the QT-OEOM polymer.

flexible molecules segregate to the isotropic phase. The nematic phase is now richer in stiffer molecules. How does this segregation alter the core structure?

5.8 Conclusions

The high resolution of electron microscopy together with the lamellar decoration technique of Wood and Thomas enables observation of disclination core structure in polymer liquid crystals. The core structure is analyzed in terms of the apparent bend and splay elastic anisotropy, ε_a, which is measured as a function of radial distance from π disclinations. Results demonstrate a special structure of the core at radii less than about 400nm. The size of the core is much bigger than we would expect for a small molecule liquid crystal, and it is expected to be proportional to effective molecular length. The core for a rigid liquid crystal polyester is observed to be different from the core structure in a semi-flexible main chain liquid crystalline polymer. The rigid material studied splays significantly more at the core. At a distance of 100nm, ε_a is approximately -0.4, yet the asymptotic value, ε, (at a distance of 1μm) is approximately 0. In contrast, the flexible material bends more at the core; $\varepsilon_a(100nm) \sim 0.1$ and $\varepsilon \sim -0.15$. These results can be understood in terms of the molecular lengths and relative chain rigidities of these liquid crystalline materials. Because the size of the core in the flexible material is a few molecular lengths we conclude hairpins are few. Chain ends are strongly aggregated at the core of the rigid material. ε for both polymers is found to be nearly 0. The effect of neighboring disclinations is found to be fairly well accounted for by an expression which assumes weak anisotropy.

CHAPTER 6

ORIENTED TEXTURES

In practice, liquid crystal polymers are very often oriented by an electric field or by flow. In chapter 1, we saw that an orienting influence causes the energy density to be dependent on orientation as well as on the gradients of the director. As a consequence, distortions are no longer arbitrarily long range but die out over a length, ξ, which is equal to the square root of the ratio of the coefficients in the energy density expression. The resultant structure of the director field may be an inversion wall having a soliton structure. The width of this wall is approximately 2ξ.

In chapter 1, it was suggested that the relative values of ξ and d (the average disclination separation) together govern the director field texture, as illustrated in figure 1.11. In the presence of weak fields, where $\xi >> d$, disclinations form a schlieren texture, and the presence of the field is inconsequential. A schlieren texture has been observed, for example, in figure 4.5 (p.89). The director field may be described most rudimentally by the average disclination density, ρ_d.

At intermediate field strengths, where $\xi \sim d$, disclination interaction has never been studied before. Because disclination positions may be precisely observed via TEM, we can gain basic understanding of disclination interaction in magnetically and flow oriented samples. We are able to precisely describe the fundamental difference between the disclination interaction in oriented and unoriented samples, and a new principle of disclination interaction is discovered. When $\xi \sim d$, disclinations interact in such a way as to reduce the dipole moment of their cluster; pair interactions no longer dominate. The number of interactions are limited to only nearest neighbors, and clusters of disclinations form which have zero topological dipole moment. The simplest example which is commonly observed is the quadrupole or Lehmann cluster.

At high fields, where $\xi << d$, inversion walls form between disclination dipoles. The director field is further characterized by the wall density, ρ_w.

Each of the types of textures in figure 1.11 is observed via microscopy. Through these observations we are able to characterize the texture in terms of the few general lengths introduced in chapter 1. The disclination and wall densities can be measured directly from the micrographs, and ξ (and the elastic constant) may be measured from the observed structure of complete inversion walls. Director textures induced by flow and magnetic alignment are discussed. Interpretation of extensional flow oriented textures is simplified by recognizing the analogy to magnetic alignment.

The evolution of the director field during alignment is discussed. If the director field is initially aligned perpendicular to the applied field, a periodic structure of incomplete inversion walls forms. Subsequently, the walls interact and annihilate; the wall density is reduced. The surface is shown to strongly retard director alignment in thin films. This retardation also contributes to the formation of the periodic structure which is observed.

Disclinations in the presence of an applied field have been very little studied. In this chapter, I discuss both their structure and their interaction. The structure of a disclination in a magnetic field is derived using a perturbation expansion. Their interaction is determined by measuring the relative positions of disclinations in oriented samples. Discussion of the energetics of the Lehmann cluster is aided by finite element calculations.

6.1 Sample preparation

6.1.1 Magnetic field alignment

Magnetic field alignment was performed at Bitter National Magnet Laboratory, Cambridge, MA, using a 15 Tesla superconducting magnet equipped with a heater as shown in figure 6.1. A thin film sample (~ 1μm thick) is prepared on a glass substrate, which is wide enough to just fit inside a 6mm inside diameter glass carrier tube. The tube is then placed parallel to the magnetic field, so that the field direction lies in the plane of the film.

Magnetic Field Experiments

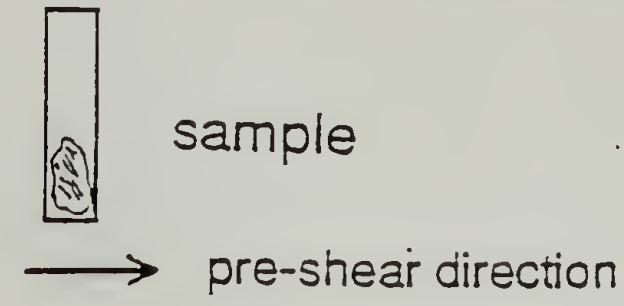

Bitter National Magnet Laboratory

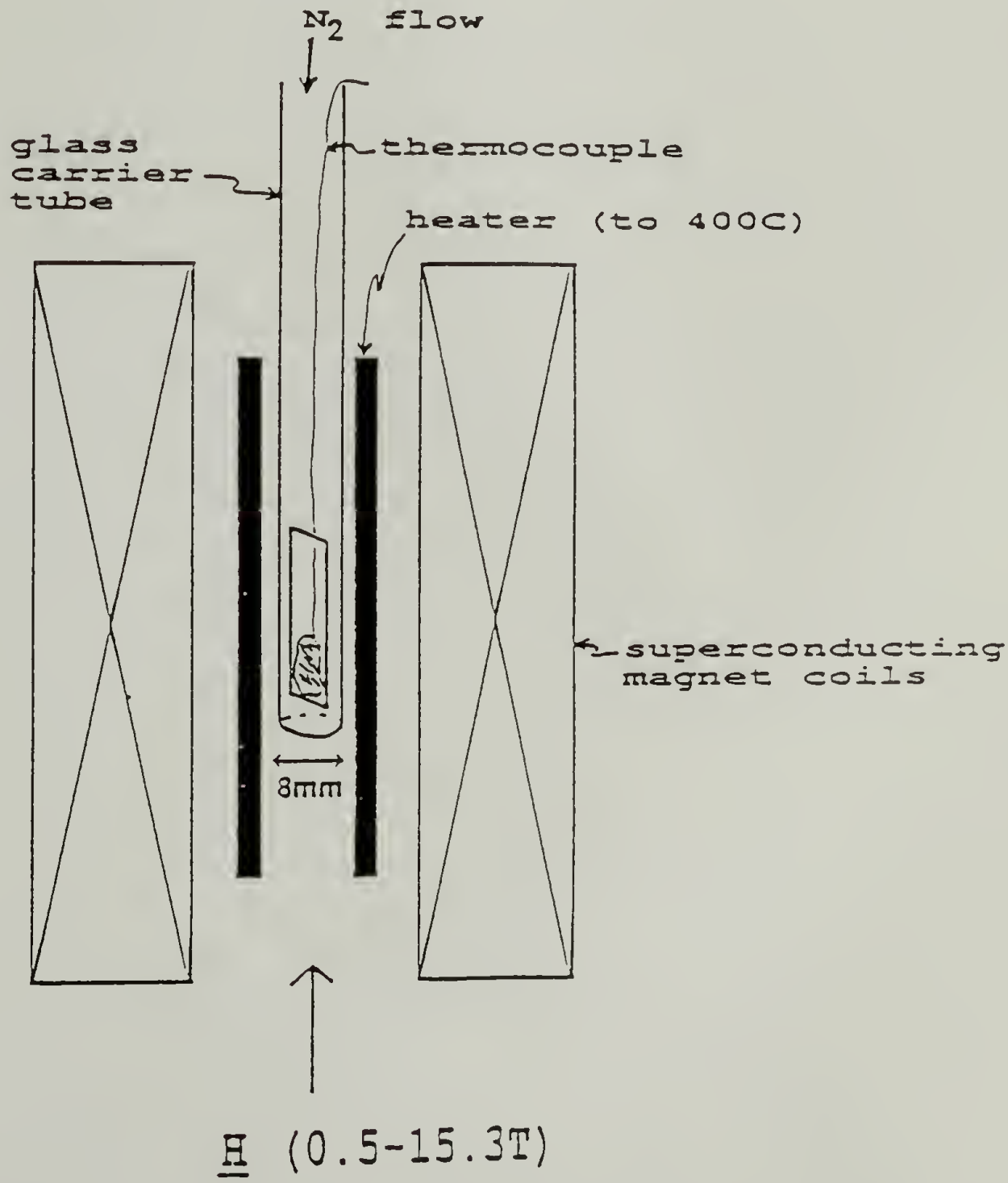

Figure 6.1 Schematic of magnetic field alignment apparatus at the Bitter National Magnet Laboratory.

The magnetic field may range continuously from 0.5 to 15.3T. The magnetic field is quite uniform; over the length of the sample (~ 1cm), the variation of the magnetic field is less than 1%. The temperature may also be controlled in the range from 20 to 400°C. The sample is first flushed with N_2 (4 psi for one minute) to provide an inert atmosphere. During heating, the N_2 flow is reduced to that which can barely be heard when the quarter inch rubber tube is placed in one's ear. After a specified alignment time, the sample is quenched to room temperature at a rate of 10-20°C/sec to room temperature with a flow of N_2 gas (again using 4 psi). Because the temperature of the atmosphere in contact with the sample is measured, the true quench rate of the sample is expected to be slightly slower.

Subsequently, the sample can be observed outside the magnet using either optical or electron microscopes. Four different TLCP's have been aligned at fields ranging from 3 to 15T.

6.1.2 Pre-shearing alignment

To create a texture of inversion walls (i.e. where $\xi << d$), polymer in the nematic phase was first sheared on a glass slide using a spatula. A high degree of alignment was achieved as verified by polarizing optical microscopy. Subsequently, the magnetic field was applied perpendicular to the shearing direction. A periodic structure of inversion walls initially formed during alignment.

6.1.3 Extensional flow alignment

An oriented polymer thin film, suitable for TEM, may be formed by surface tension spreading of the polymer on hot H_3PO_4 as described in chapter 2 (pp.38-39). Solid polymer is placed on the surface of hot phosphoric acid. It melts and spreads due to its lower surface tension. The type and rate of flow, however, are not well controlled. The flow rate may vary with temperature and with the type of TLCP material. If the rate is slow little orientation develops, whereas if it is more rapid, moderate orientation develops. In all samples the flow

is extensional, but the relative planar or biaxial character may vary. The deformation is initially biaxial with the largest elongation in the radial direction. Observation of these samples in the optical microscope reveals walls radiating out from the droplet parallel to the radial (extension) direction. Typically, the spreading droplet soon breaks up forming fingers which flow away radially as shown in figure 2.5 (p.39). The deformation within the fingers may be planar. The sample may be quenched by transferring it to a room temperature bath of H_3PO_4. The hot acid is dipped into room temperature acid while the TLCP film remains floating on the surface. The deformation rate in this step may be minimal.

It is in the quench step, however, that the amount of orientation can be most easily controlled. Instead of carefully dipping the hot acid into the room temperature acid, the hot acid may be rapidly poured into the acid quench bath. The TLCP skates on the surface and is stretched rapidly into several generally parallel fingers. During this rapid planar elongational flow, a large degree of orientation is achieved.

After quenching, the resulting film is glassy. After washing the film on a water bath, the sample may be annealed to develop the lamellar decoration morphology described in chapter 2. The sample may be observed via TEM or by optical microscopy.

6.2 Inversion walls ($d>>\xi$)

6.2.1 Short alignment times

6.2.1.1 Periodic structure in magnetically aligned samples

Using the techniques described above, we can use either magnetic or extensional flow fields to align the TLCP's. The presence of either field applies a torque to each molecule which tends to align them along the applied field. The torque per molecule in a magnetic field is much smaller than in an extensional flow field [de Gennes, 1974]. In both cases, the director field is aligned over macroscopic lengths.

When the magnetic field is applied perpendicular to the director orientation of a pre-sheared sample, the perpendicular orientation is unstable, and a banded texture may form.

As the field is applied, the director rotates towards the field. In some regions it rotates clockwise, while in others it rotates counter-clockwise. Because **n** = -**n**, both rotation senses lower the free energy. Between these regions the material shears as shown in figure 6.2(a). Because the viscosity for shear flow is typically less than that for pure rotation, the dissipational energy is reduced. In polymers, the difference in viscosities may be large [de Gennes, 1982]. The shear flow in turn also increases the reorientation. Periodic walls, parallel to **H**, form as shown in figure 6.2(a). The periodic structure does however increase the bend distortional energy. The wavelength of the periodic structure which forms is that which can be formed fastest. This optimum wavelength decreases with magnetic field strength and viscosity anisotropy, and it increases with increasing elastic constant [Lonberg et al., 1984]. The speed of response is also related to the film thickness and the density (inertia) of the sample [Guyon et al., 1979]. For thick films, where inertial effects dominate, Guyon et al. have derived the expression for the wavelength of the periodic structure:

$$\lambda = [2\gamma_1 k_{33}^{1/2}/(\chi_a H^2 \rho^{1/2}(\alpha_2/\eta_c)^{3/2})]^{1/2} \qquad (6.1)$$

where γ_1 is the rotational viscosity coefficient, α_2 and η_c are shear viscosity coefficients, ρ is the density, χ_a is the diamagnetic susceptibility anisotropy, k_{33} is the bend elastic constant, and H is the field strength. As the film thickness decreases and the surface begins to retard the alignment, the wavelength of the periodic structure decreases [Lonberg et al., 1984].

A near monodomain sample of the OQ5a#6 polymer was prepared by pre-shear alignment. Assuming $\Delta n/n_e \sim 0.1$, the film was estimated from the silver birefringence color to be about 1μm thick. The orientation direction was placed perpendicular to the applied field. The sample was aligned in a 13.7T field for 10 minutes at 230°C. The resulting texture after partial alignment, shown in figure 6.2(a), may be described by a low disclination density, $\rho_d < 10^{-6}\mu m^{-2}$, a small characteristic length, ξ = 350nm (this will be measured later), and a high wall density, $\rho_w \sim 5000 cm^{-1}$. The wavelength of the periodic structure is 4μm. The orientation of the director in the alternating domains is not fully aligned along **H**. Therefore I call the walls incomplete inversion walls. The structure of

(a)

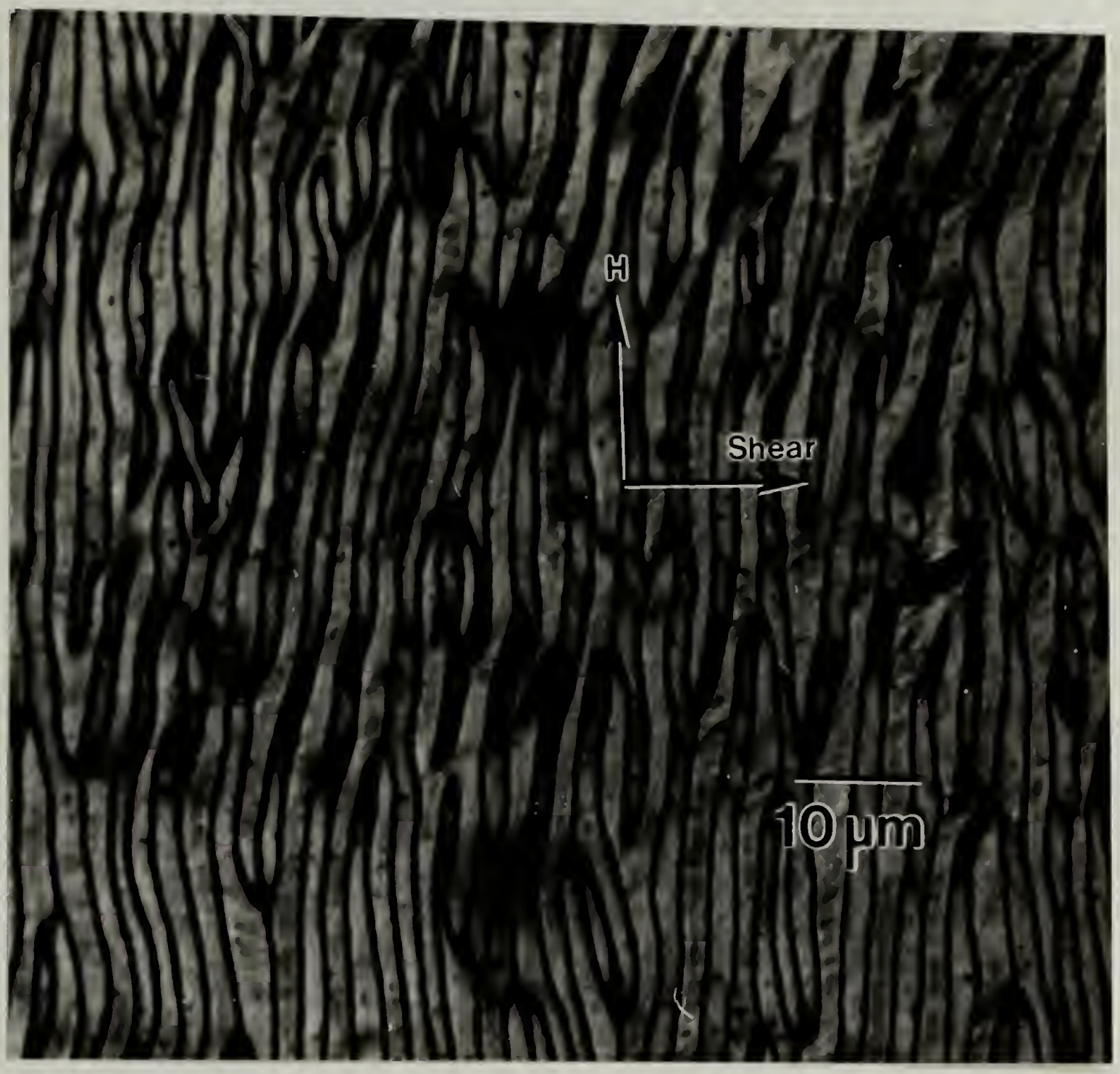

(b)

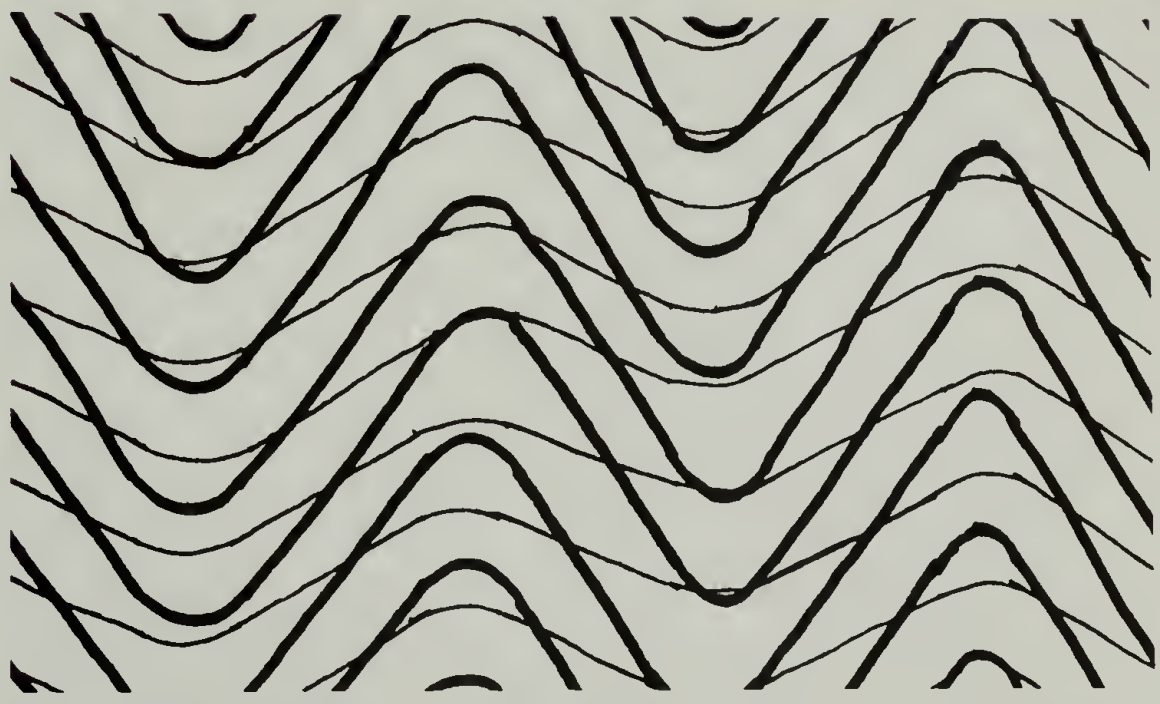

Figure 6.2 Periodic structure formed at short alignment times. (a) Optical micrograph. (b) Schematic director pattern in sample. Bend inversion walls are forming. The orientation at the substrate surface, shown with fine line, lags the bulk orientation, shown with bold line.

these walls will be discussed later. The orientation of the director in each set of incompletely aligned domains can be measured by optical microscopy. When the sample is viewed with crossed polars, the stage may be rotated alternately to make one set of the domains dark. In each set of domains the director is measured to be oriented 22±2° with respect to the field direction. Therefore, during the 10 minute alignment, the director in each set has rotated 68±2°.

The importance of the substrate for the formation of the periodic structure may be evaluated by substituting appropriate values into equation 6.1. The wavelength is calculated in this way to be approximately 500μm. Obviously, the substrate surface strongly retards the alignment and significantly reduces the wavelength of the resultant structure.

6.2.1.2 Periodic structure in extensionally aligned samples

Quasi-periodic incomplete inversion walls have also been observed in extensional flows. Figure 6.3 shows a droplet of TQT10-H that was melt spread at 235°C, a temperature a few degrees above the melting transition.

In melt spreading, the orientation of the initial sample is not uniformly perpendicular to the applied field, so the periodic structure is not formed via the same instability discussed above. Large orientation fluctuations are preexisting in the sample. In the highly stretched regions (a and b) in figure 6.3, the director may be observed perpendicular to the striations in figure 6.3. In regions a, the director is shown parallel to the flow direction (radial), and walls are not observed there. Where the walls are observed, the director was predominantly oriented tangentially with respect to the droplet. Bands are formed as some regions rotate clockwise towards the flow where as it rotates counterclockwise in the other regions.

Incomplete inversion walls in such a melt spread sample were shown in figure 3.3(b). What is the structure of the incomplete inversion walls? Incomplete inversion walls are, of course, controlled by the same characteristic length as when the alignment is complete. We

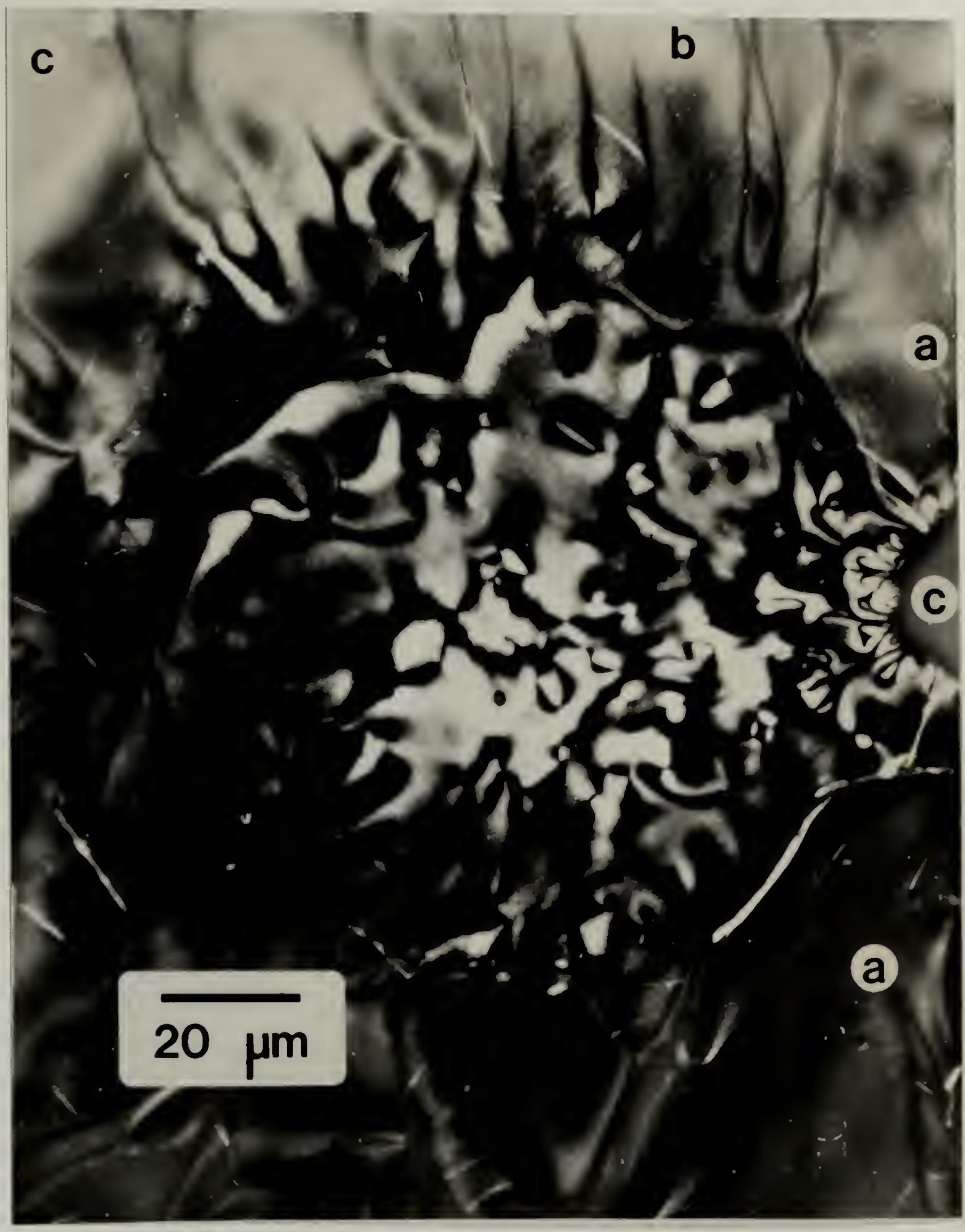

Figure 6.3 Texture development of a nematic droplet of TQT10-M during surface tension spreading. The droplet spreads radially from the center as described in the text (pages 38-39 and 126). The center region shows the precursor schlieren texture. The droplet has begun to finger, and holes are labeled c. Incomplete inversion walls appear in the region marked b. The orientation of the director is perpendicular to the striations shown. Uniformly oriented regions are labeled a. (In order to image both the thick (~ 1µm) center region (originally bright) and the thin (~ 100nm) peripheral regions (originally very dark), a diffuse mask was used during printing of the negative.)

also expect that the functional form of the director is similar to that in complete inversion wall.

The soliton structure of an inversion wall was first calculated by Helfrich [1969].

$$\phi(x) = 2\tan^{-1}[\exp(\pm(x-x_o)/\xi)] \quad , \tag{6.2}$$

where the center of the alignment inversion wall is positioned at x_o, and the width of the wall is proportional to the characteristic length of alignment distortions, ξ. There is a characteristic length for each splay, twist, or bend distortion:

$$\xi_{ii} = (k_{ii}/(\chi_a H^2))^{1/2} \quad , \tag{6.3}$$

where H is the magnetic field strength, k_{ii} is the splay, twist, or bend elastic constant, and χ_a is the anisotropy of diamagnetic susceptibility of the material. The relative contribution of the splay and bend elastic constants (and therefore the width of the wall if there is any elastic anisotropy) varies with the orientation of the wall with respect to the magnetic field.

In the transient structure, however, the director is not yet aligned along H. The minimum free energy possible is that of a uniform domain at some angle to H. We choose to model incomplete inversion walls, therefore, by assuming that locally the field is oriented in this free energy minimum, as shown in figure 6.4(a). This is equivalent to assuming pseudo-equilibrium where the static structure of the model is assumed to accurately depict the instantaneous transient structure. Using this model the incomplete inversion wall has a structure similar to that of a boundary layer calculated by de Gennes [1974]:

$$\phi = 2\tan^{-1}[\exp(x/\xi)\tan(\phi_i/4)] \qquad x < 0 \tag{6.4}$$

$$\phi = \phi_i - 2\tan^{-1}[\exp(-x/\xi)\tan(\phi_i/4)] \qquad x > 0$$

where ϕ_i is the amount of director rotation. $\phi_i = \pi$ for a complete inversion wall. Data taken from figure 3.3(b) is shown in figure 6.4(b). The model appears to be quite sensible.

6.2.1.3 Future work for studying short alignment times

1. For incomplete inversion walls formed in a magnetic field, does the proposed model fit for various times of alignment?

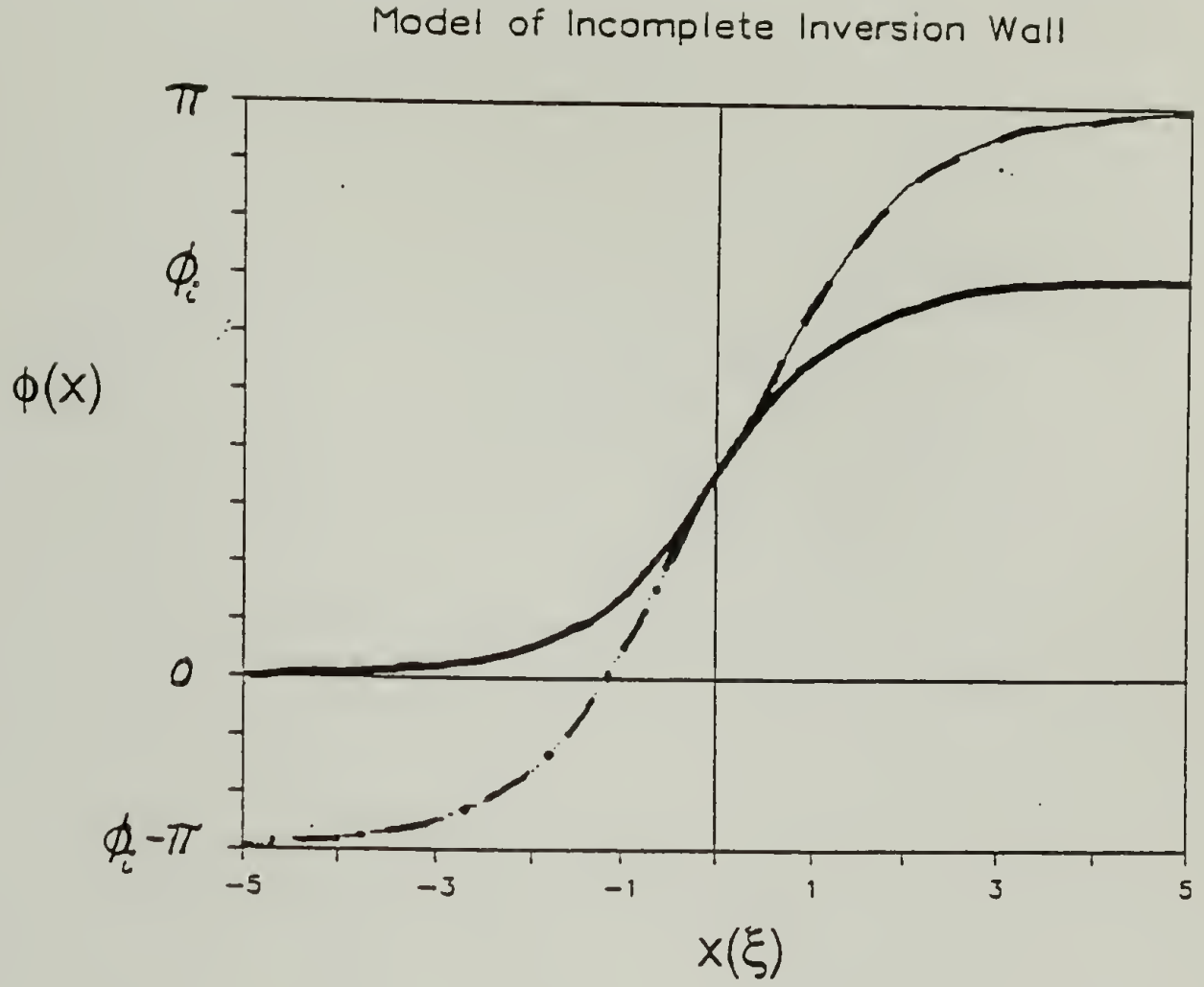

$$\phi = 2\tan^{-1}[\exp(x/\xi)\tan(\phi_i/4)] \qquad x < 0$$

$$\phi = \phi_i - 2\tan^{-1}[\exp(-x/\xi)\tan(\phi_i/4)] \qquad x > 0$$

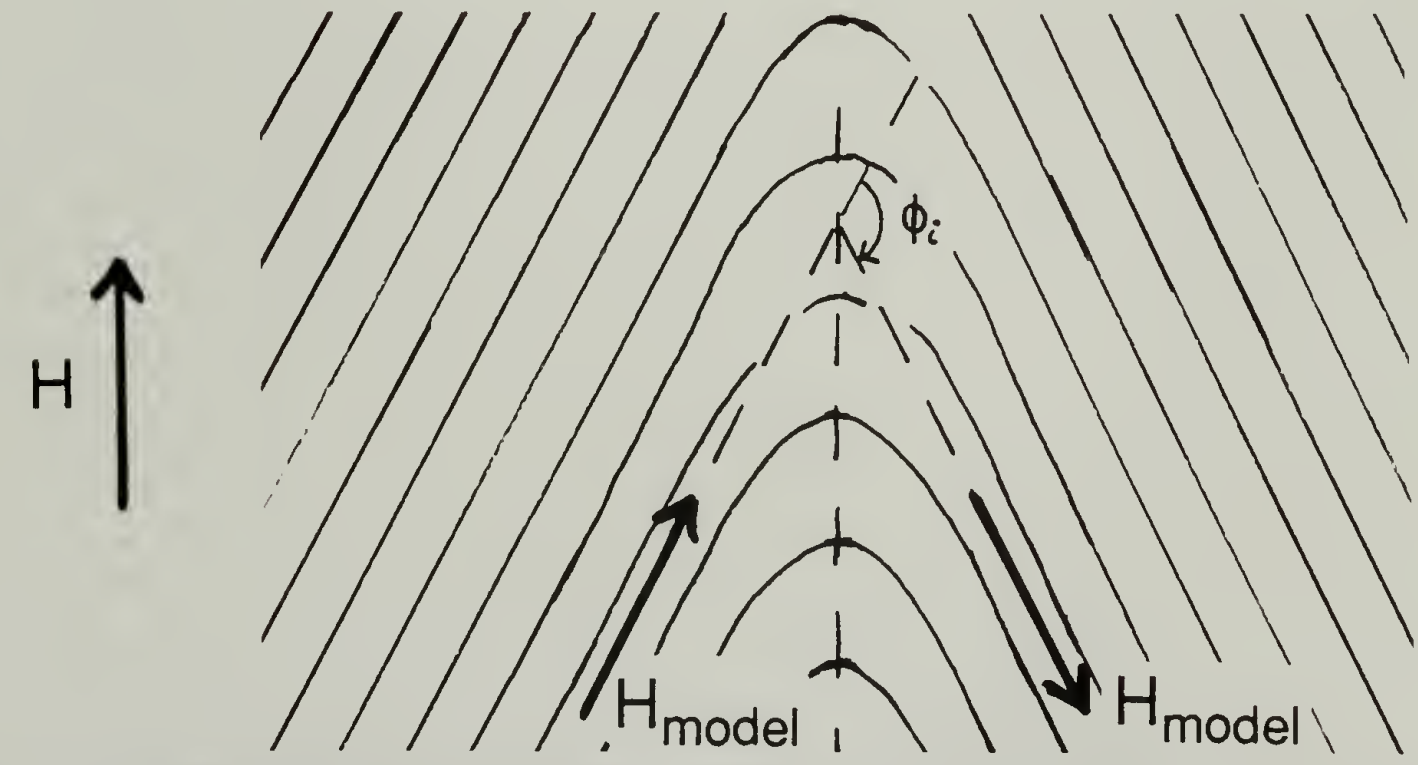

Figure 6.4 The structure of an incomplete inversion wall found in extensional flow aligned samples. (a) Model. The solid curve is the actual structure which is formed from pieces of solitons. The dashed curve shows the continuation of the piece on the left, and the dot and dash curve shows the continuation of the piece on the right. In the lower figure, the original director orientation is horizontal, and the magnetic field direction is vertical. H_{model} is originally horizontal and rotates towards the vertical.

(Continued next page.)

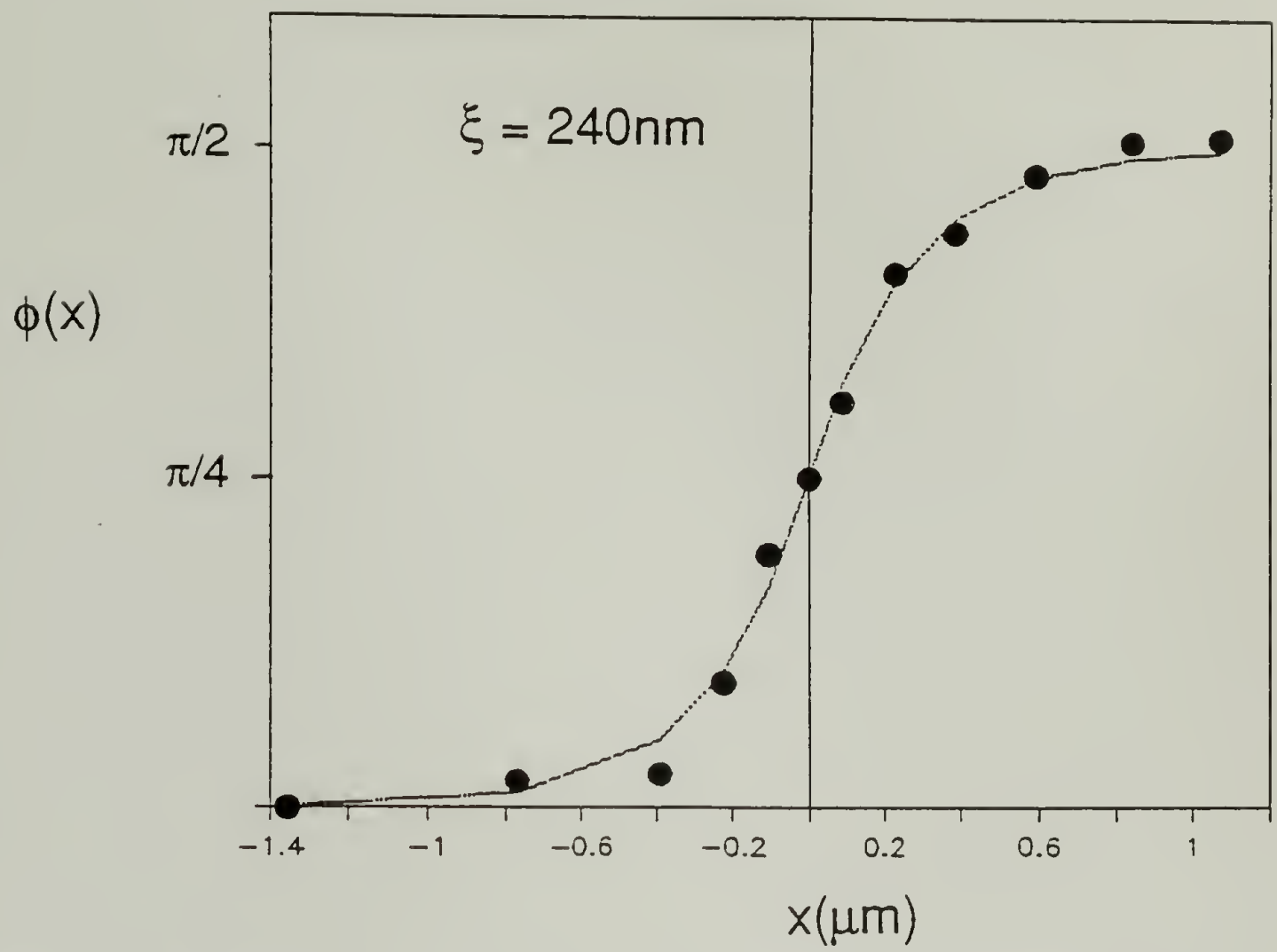

Figure 6.4 The structure of an incomplete inversion wall found in extensional flow aligned samples. (b) Data taken from figure 3.3(b).

2. Observe the affect of the substrate in magnetic alignment by varying the film thickness.

   Measure alignment of a single film by optical microscopy sequentially (e.g. after 5, 10, and 20 minutes) in order to measure a reorientation time constant. The time constant is expected to get very large as the film thickness decreases. Bulk and surface time constants may be determined.

   Measure alignment by EM images. does it agree with OM?

3. Observe the effect of the substrate in magnetically aligned samples directly. Image via HRSEM both the free surface structure and the substrate surface structure.

6.2.2 Long alignment times

6.2.2.1 Observed inversion wall structure of magnetically aligned samples

Pre-sheared samples were also aligned for longer times. Figure 6.5(a) shows inversion walls in a slightly thicker (~ 2μm, having a gold birefringence color) OQ5a#6 sample aligned in the same conditions as above for 90 instead of 10 minutes. Two main characteristics of the texture have changed. The director is now aligned, within a degree or two, along the field direction. Also, the wall density has dramatically decreased from $5000cm^{-1}$ to $100cm^{-1}$. Walls formed in the initial periodic structure are of opposite sense. During alignment, these inversion walls attract one another as described in chapter 1. When the walls meet, they annihilate, and the texture coarsens.

The aligned sample was annealed and etched as described in chapter 3, and the sample was observed using HRSEM (figure 3.7). The variations in the director field are easily revealed by the lamellae, which are perpendicular to the lamellae. Therefore the quench rate induced by the 4psi N_2 flow is rapid enough to inhibit crystallization during quench. The structure of the inversion wall is observed in the high magnification HRSEM image.

ϕ was measured as a function of distance from a straight section of wall oriented approximately 40° with respect to the magnetic field direction. A wall oriented at 40° with respect to the field consists of nearly equal amounts of both splay and bend distortion. Therefore the width of such a wall is determined by an average of the splay and bend elastic constants. The data, as shown in figure 6.5(b), was fitted to equation 6.4 using least squares in order to measure ξ. ξ was found to be 350nm. Hardouin et al. [1985] have measured χ_a of a chemically similar polymer to be $1.0x10^{-7}$ emucgs/g. Using this value of χ_a, and assuming a density of $1.0g/cm^3$, gives a value of $k = 2.3x10^{-6}$ dynes. This value is typical of small molecule and semi-flexible polymer nematics.

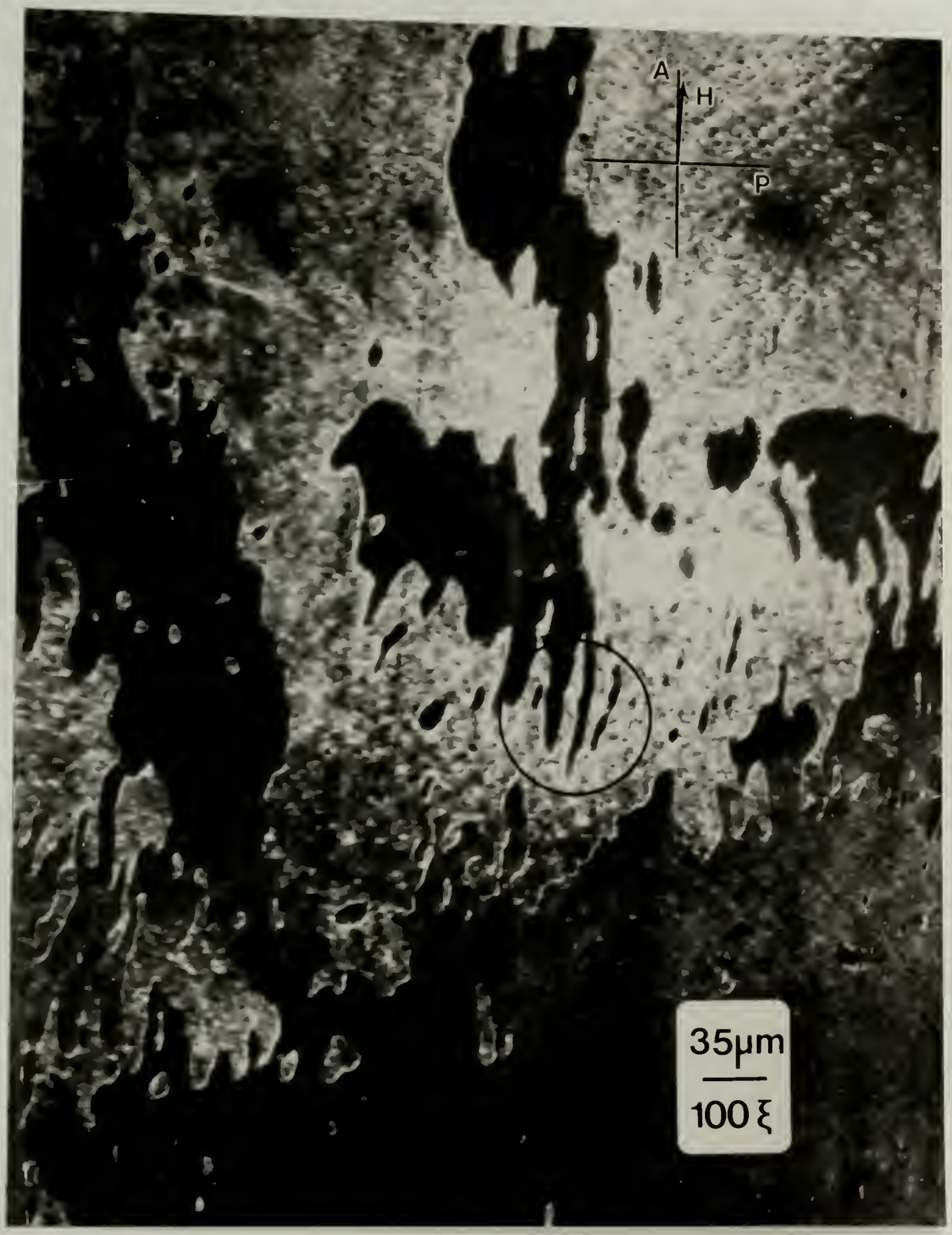

Figure 6.5 Inversion wall texture after long alignment times. (a) Coarsened texture of inversion wall loops. Contrast between domains is due to a slight misorientation between them. The sample, viewed between cross polars, is rotated so that regions which have rotated clockwise are aligned along the analyzer and appear dark. Regions which rotated counter-clockwise, being oriented a few degrees from the analyzer, are brighter. Interacting pinching off walls, reminiscent of the periodic precursor texture, are circled. (Continued next page.)

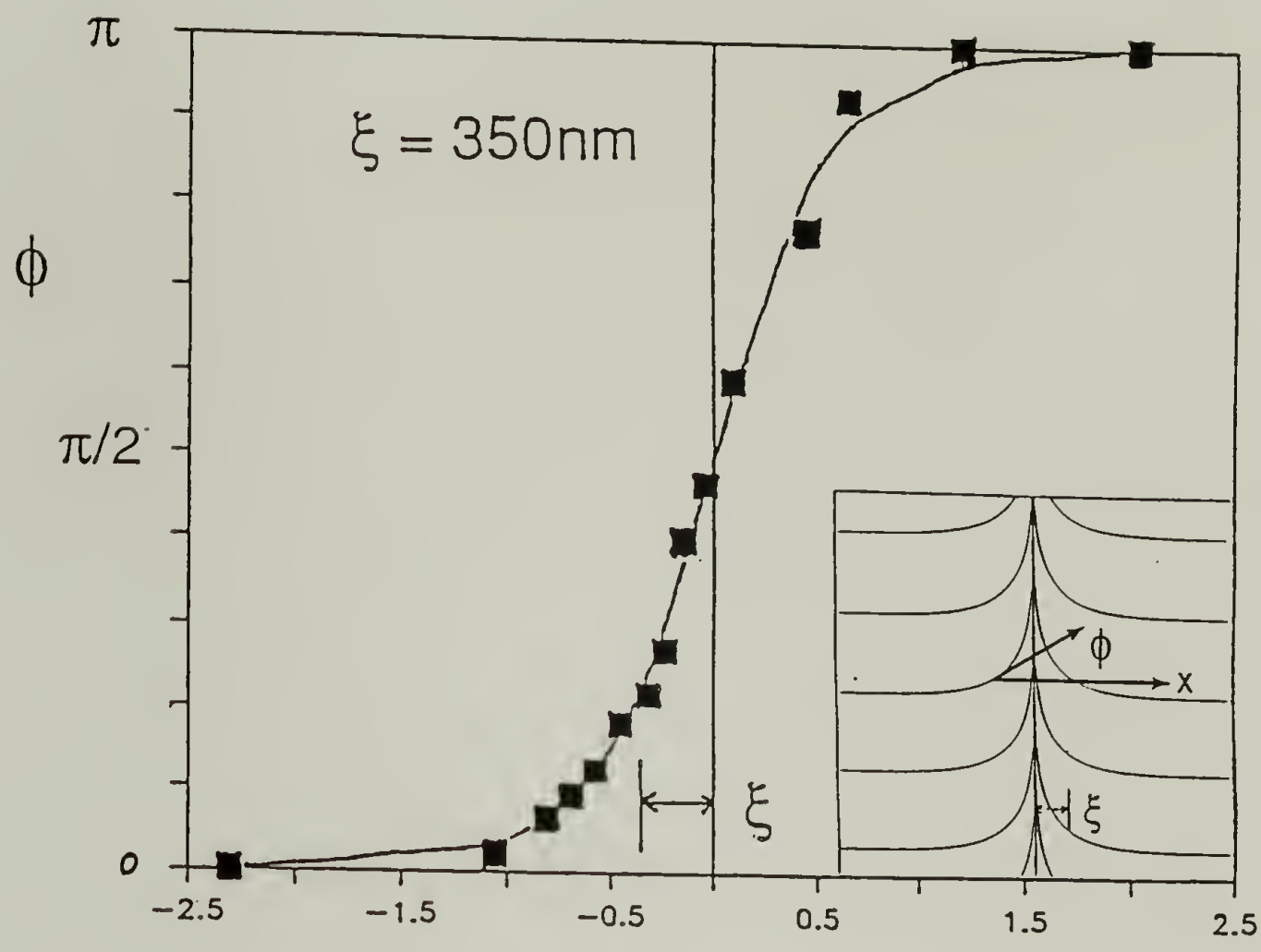

Figure 6.5 Inversion wall texture after long alignment times. (b) Inversion wall structure measured from a HRSEM image of the sample observed in (a).

6.2.2.2 Effect of substrate surface on the kinetics of magnetic alignment

A pre-sheared sample of TQT10-M having a varying thickness from 100nm to 1μm was aligned in 13.5T field for 2 hours at 184°C (see figure 6.6). The pre-shear alignment direction was placed normal to the applied field direction. The characteristic length, ξ, has been measured from three different inversion walls in this sample to be 350nm. Within experimental uncertainty, the width of the walls in TQT10-M is independent of orientation with respect to the applied field. Also, the elastic constants of TQT10-M and OQ5a#6 are very nearly equal in spite of slight differences in chemical structure. Both the average mesogen and the flexible spacer are shorter in the OQ5a#6 polymer.

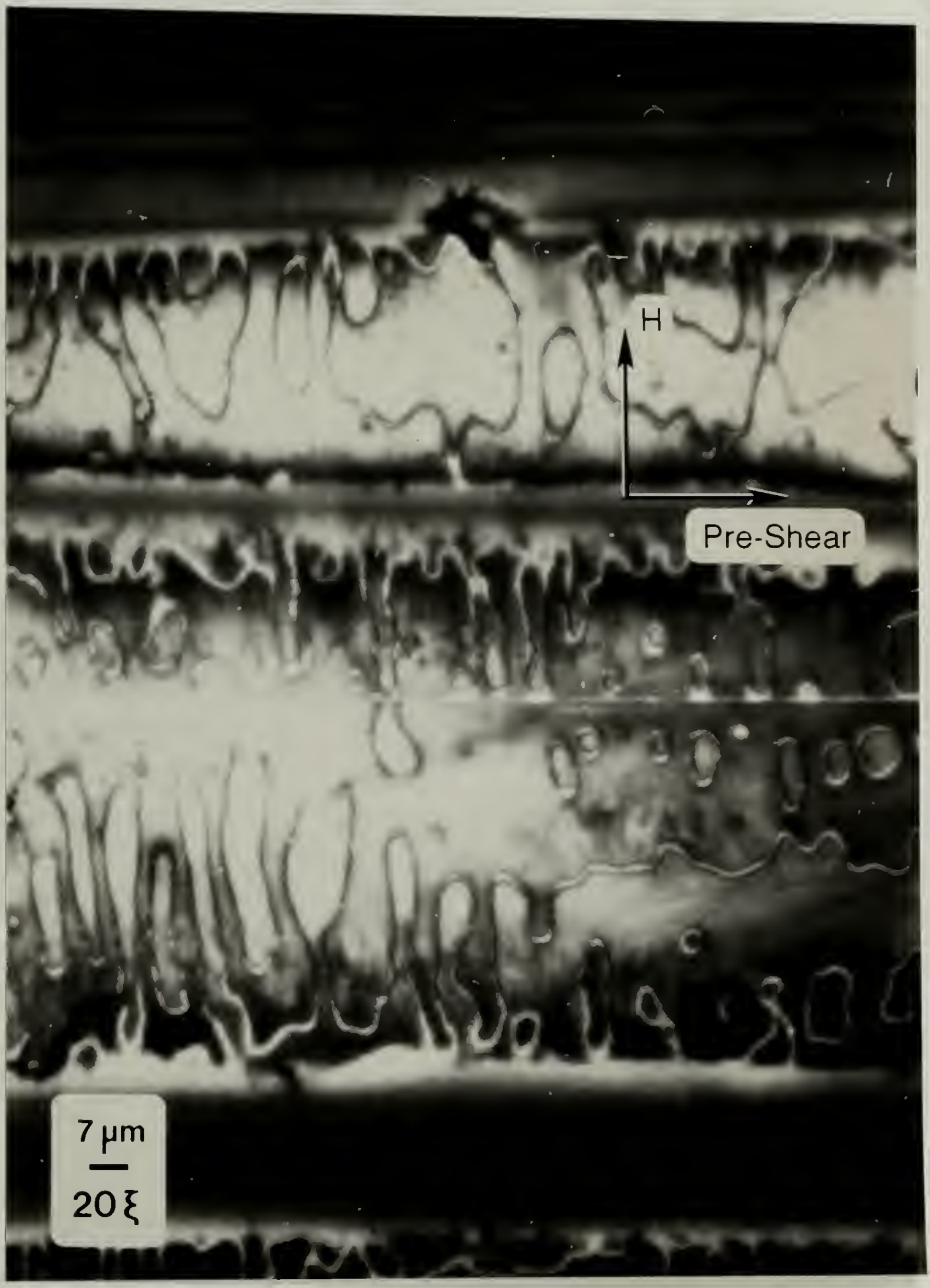

Figure 6.6 Retardation of alignment in thin films due to substrate interaction. Inversion wall loops are shown in a sample of TQT10-M after long alignment times. The horizontal featureless regions, at the top and the bottom of the figure, are thinner regions which are still completely aligned along the pre-shear direction. The regions containing inversion walls are thicker and have aligned along the magnetic field.

Because of the inhomogeneous thickness of the TQT10-M polymer sample, the effect of the surface on reorientation kinetics may be observed. In the thicker regions, the director is aligned along the field direction, whereas in the thinnest regions (~ 100nm), the director is still aligned along the pre-shear direction. The films were thin enough so that the orientation direction could easily be discerned by observing the orientation of the birefringence using a quarter wave plate.

To model the effect of the surface, we recognize that if the surface orientation, ϕ_o, lags behind the bulk orientation, a twist distortion through the film results. This twist distortion applies a torque which opposes the torque due to the applied field. The distortion will be locallized at the surface within approximately the twist characteristic length. As in equation 6.4, de Gennes [1974] has calculated the structure of a boundary wall in a thick film. He also calculated the energy per unit area of such a boundary wall:

$$G(\phi_o) = 2k/\xi\,[1 - 1/(1+\tan^2(\phi_o/2))]\ . \tag{6.5}$$

For a thin film the energy is easily calculated to be:

$$G(l,\phi_o) = 2k/\xi\,[1/(1+\exp(-2L/\xi)\tan^2(\phi_o/2)) - 1/(1+\tan^2(\phi_o/2))]\ . \tag{6.6}$$

where L is the film thickness. If $L >> \xi$, this equation reduces to equation 6.5.

During steady state reorientation of a thin film the viscous torque/unit area balances the magnetic and elastic torque/unit area.

$$T_v + T_m = 0\ . \tag{6.7}$$

The subsequent development follows that of bulk samples [Wise et al., 1975] with appropriate modification for surface effects. The viscous torque/unit area is

$$T_v = (\delta(y)A + \gamma_1)\, d\phi/dt\, dy\ , \tag{6.8}$$

$$= [A + \gamma_1\ \ d\phi/d\phi_o\, dy]\, d\phi_o/dt\ ,$$

where A is a surface viscosity and γ_1 is the bulk rotational viscosity. The magnetic and elastic torque/unit area can be found by differentiating the magnetic and elastic energy with respect to the surface orientation. To simplify the calculation of a characteristic

reorientation time, I consider the case where ϕ_o is small. This assumption should not affect the time constant in any way. The torques become:

$$T_v = [A + \xi\gamma_1 - \xi\gamma_1 \exp(-L/\xi)]\, d\phi_o/dt \; ; \qquad (6.9)$$

$$T_m = k/\xi \;\; \phi_o[1 - \exp(-2L/\xi)] \, .$$

The resulting solution for ϕ_o is:

$$\phi_o = \phi_o' \exp[-t/\tau] \, , \qquad (6.10)$$

$$\tau = (\xi A + \xi^2\gamma_1 - \xi^2\gamma_1 \exp(-L/\xi)) \,/\, (k(1-\exp(-2L/\xi))) \, .$$

where τ is the time constant.If $L >> \xi$, then

$$\tau = (\xi A + \xi^2\gamma_1)/k \quad = A/(k\chi_a H^2)^{1/2} + \gamma_1/\chi_a H^2 \quad = \tau_s + \tau_b \, , \qquad (6.11)$$

where τ_s and τ_b are the surface and bulk time constants. τ_b is the time constant with no surface present. Note that the surface term weakly depends on the elastic constant. Although both terms are affected by magnetic field strength, the bulk term is much more strongly affected, being proportional to $1/H^2$.

The relative values of the two time constants may be estimated from typical values. We might expect A to be on the order of the surface energy, i.e. 10dynes-sec/cm. The viscosity coefficient, γ_1, has been measured for a polydomain sample of a similar polymer by Moore and Stupp [1987] to be ~10^4P, while Zheng-Min and Kleman [1984] have measured it for a monodomain to be 10^2P. When $H=10^5$G, k ~ 10^{-6}dynes, and χ_a ~ 10^{-7} emucgs/g; τ_s ~ 300sec and τ_b ~ 1sec. Therefore we expect our films to be strongly influenced by surface effects.

For thin films, where $L << \xi$, τ can be calculated by expanding the exponentials:

$$\tau = \xi^2 A/2kL + \tau_s/2 + \tau_b/2 + \ldots \quad = A/(2\chi_a H^2 L) + \tau_s/2 + \tau_b/2 + \ldots . \qquad (6.12)$$

When $L < \xi$, the first term dominates, and the time constant for reorientation is inversely proportional to the film thickness. This development then explains why we do not observe reorientation in the thinnest regions of our films, where the time constant gets exceedingly long.

6.2.2.3 Twist inversion walls near the substrate surface

In the previous discussion, we have considered the reorientation of the surface, ϕ_o. We have seen that it may depend on both the surface and the bulk time constants. In thicker films (when $l>>\xi$; l ~ 1-2μm), however, most of the film reorients before the boundary layer. This reorientation is governed by the bulk time constant.

We have observed twist walls in films which may be ~ 2μm thick and have been reoriented for 1.5hrs in 13.7T magnetic field. Figure 6.7(a) shows optical micrographs focused on the free surface and on the substrate surface of the same area. Some inversion walls are clearly seen in both settings. Other inversion walls, which are clearly seen only when focused on the substrate surface, are blurry when focused on the free surface. These walls are interpreted as a twist walls shown in figure 6.7(b).

6.2.2.4 Inversion walls in extensional flow oriented samples

Complete inversion walls have also been observed in extensional flow oriented samples as shown in figure 6.8(a). Data of the director orientation as a function of distance from the wall fits well with the soliton equation as shown in figure 6.8(b). The analogous relationship between extensional flow and magnetic field as derived in chapter 1 is illustrated here. The characteristic length in figure 8a is observed to be 290nm. Assuming a value of 100P for the rotational viscosity coefficient, gives a reasonable value for the extensional deformation rate of $10sec^{-1}$. Inversion walls due to various rates of extension have been observed. The characteristic length has varied from 9.5μm for a very slow flow to 37nm for a very rapid flow.

6.2.2.5 Future work

1. Observe the top and bottom of magnetically oriented thin films. Is the bottom aligned along the field? Compare the wall density between the top and the bottom surface.
2. Are inversion walls observed in shear flow? What is their structure?

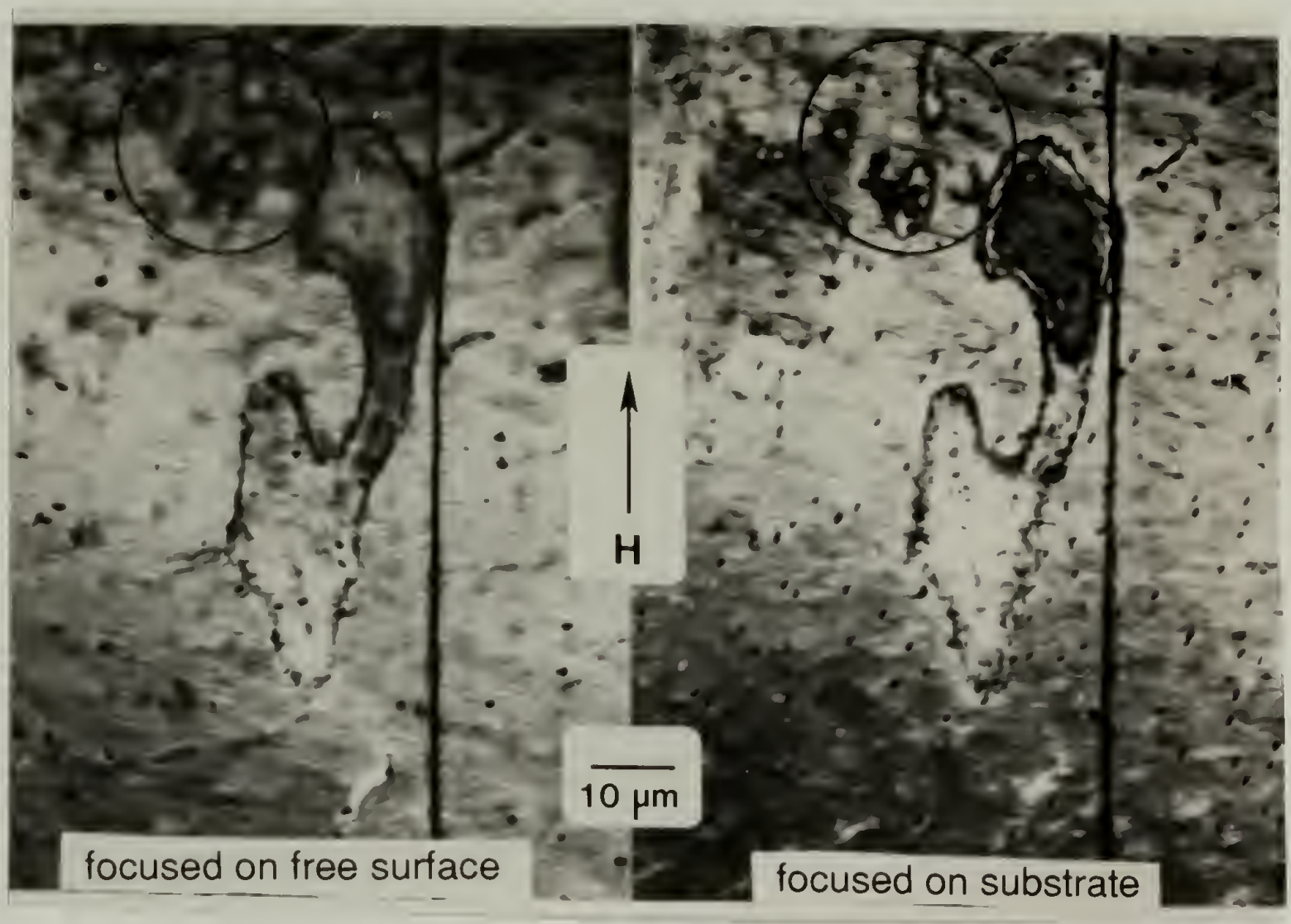

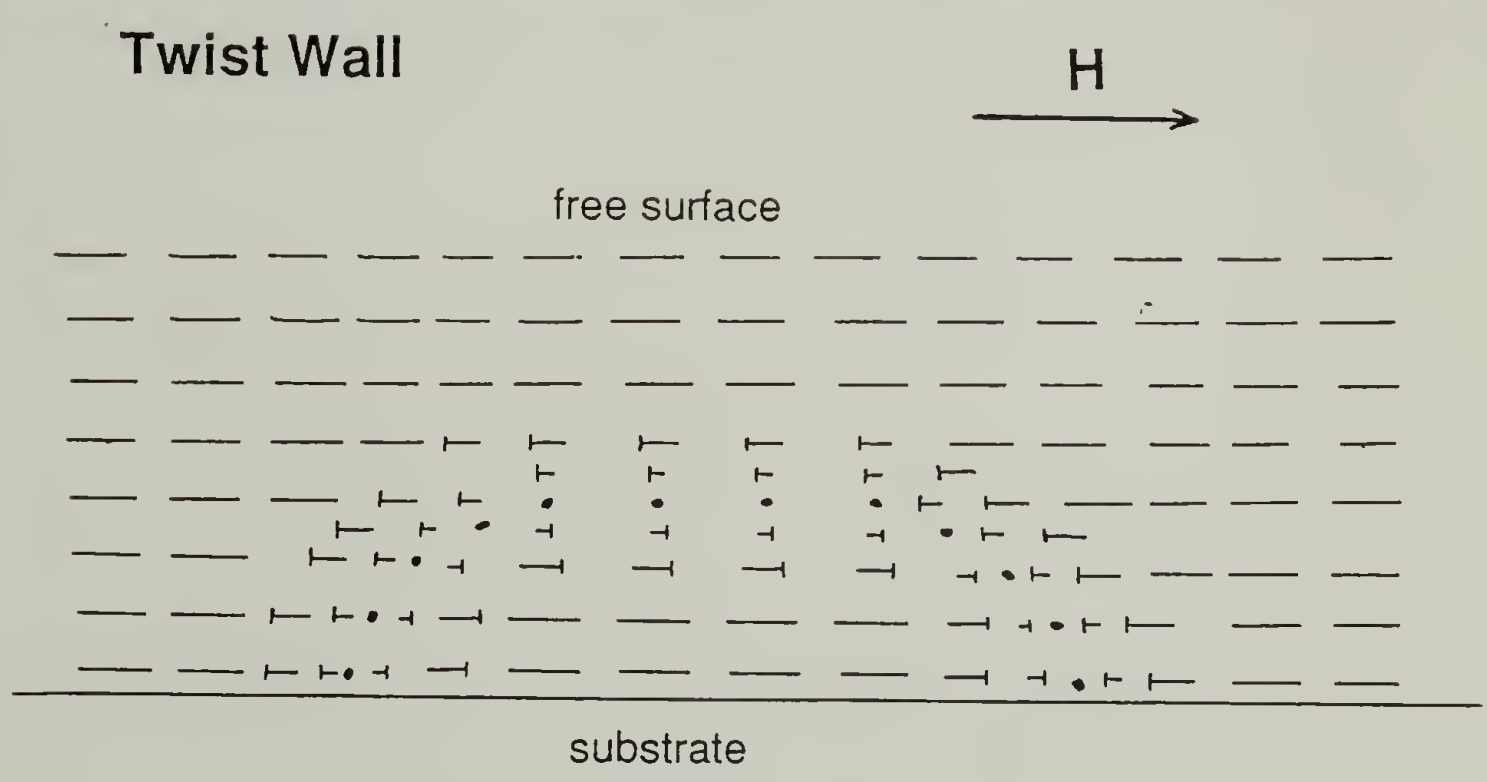

Figure 6.7 Twist inversion wall loops in thicker samples. Circled are three inversion wall loops which are in focus on the right but are blurry on the left.

Figure 6.8 Inversion walls observed in extensional flow aligned samples. (a) TEM image of an inversion wall. (Continued next page.)

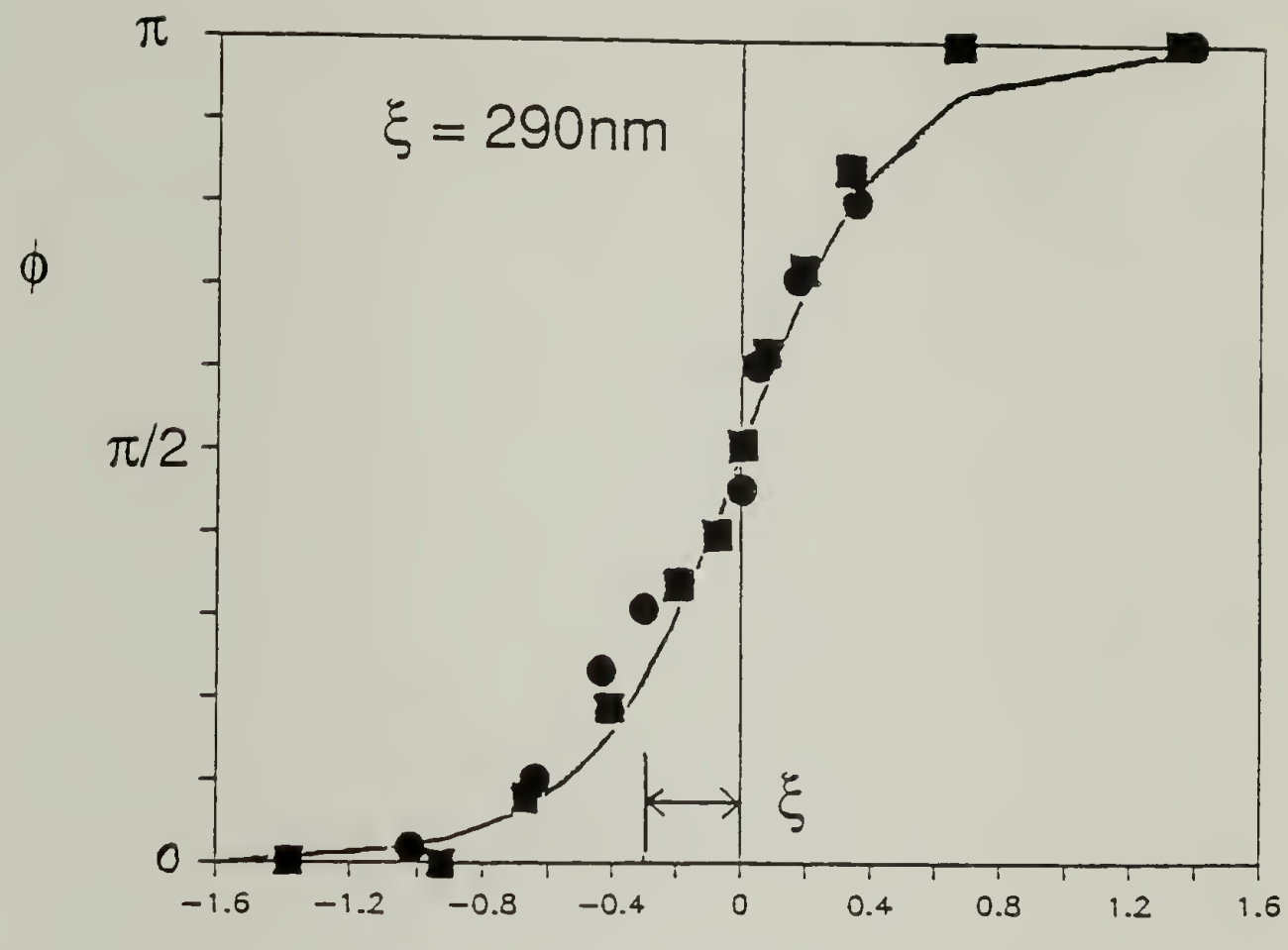

Figure 6.8 Inversion walls observed in extensional flow aligned samples. (b) Structure measured from inversion wall in (a).

6.3 Disclinations in an orienting field

6.3.1 HRSEM image of disclinations ($d >> \xi$)

The structure of inversion walls was discussed in the previous section. Inversion walls exist when $d >> \xi$. When disclinations exist in such a strong magnetic field, they appear at the edges of inversion walls, because of the topological relationship between disclinations and inversion walls. As discussed in the introductory chapter, the walls must either loop or end on surfaces or disclinations of like topological strength.

Figure 6.9(a) shows another optical micrograph of the OQ5a#6 polymer sample which was aligned for 90 minutes. The disclination density in this region is higher: $\rho_d \sim 10^{-4}\mu m^{-2}$; ($d \sim 100\mu m$). Inversion walls are visible as the dark lines. Where the wall terminates, there exists a disclination. Note that the horizontal sections of the walls are wider. This may be due to a large splay constant compared to the bend constant. Alternatively this effect may be due to a slight shear flow caused by gravity during alignment. (The magnetic field is vertical).

Figure 6.9(b) shows both ends of a π inversion wall which is terminated by $|\pi|$ disclinations. The ability to image the director at such high resolution enables unique observation of a disclination at the end of an inversion wall. Similar images have been obtained in flow oriented samples [Thomas and Wood, 1985]. The director field about such a disclination is not yet theoretically determined.

6.3.2 Structure of the director field about a disclination

The director field of a disclination in a magnetic field must satisfy the differential equation given in equation 1.19:

$$\nabla^2\phi + 1/2\xi^2 \sin 2\phi = 0. \qquad (6.13)$$

The difficulty is that the equation must now be solved in two dimensions. (The inversion wall is only a one dimensional solution.) I have, however, calculated the structure very near the disclination using a perturbation expansion. The director field becomes: $\phi = \phi^o + \psi$, where ϕ^o is the zero field solution, and ψ is a small perturbation. Because $\nabla^2\phi^o = 0$, and ψ is small, the differential equation becomes:

$$\nabla^2\psi = -1/2\xi^2 \sin 2\phi^o \ . \qquad (6.14)$$

For an isolated $\pm\pi$ disclination, $\phi^o = \pm\theta/2$. Therefore the right hand side is only a function of θ. If $\psi = R(r)\Theta(\theta)$, then $R = r^2$, and Θ satisfies the following differential equation:

$$4\Theta + \partial^2\Theta/\partial\theta^2 = -\pm 1/2\xi^2 \sin\theta \ . \qquad (6.15)$$

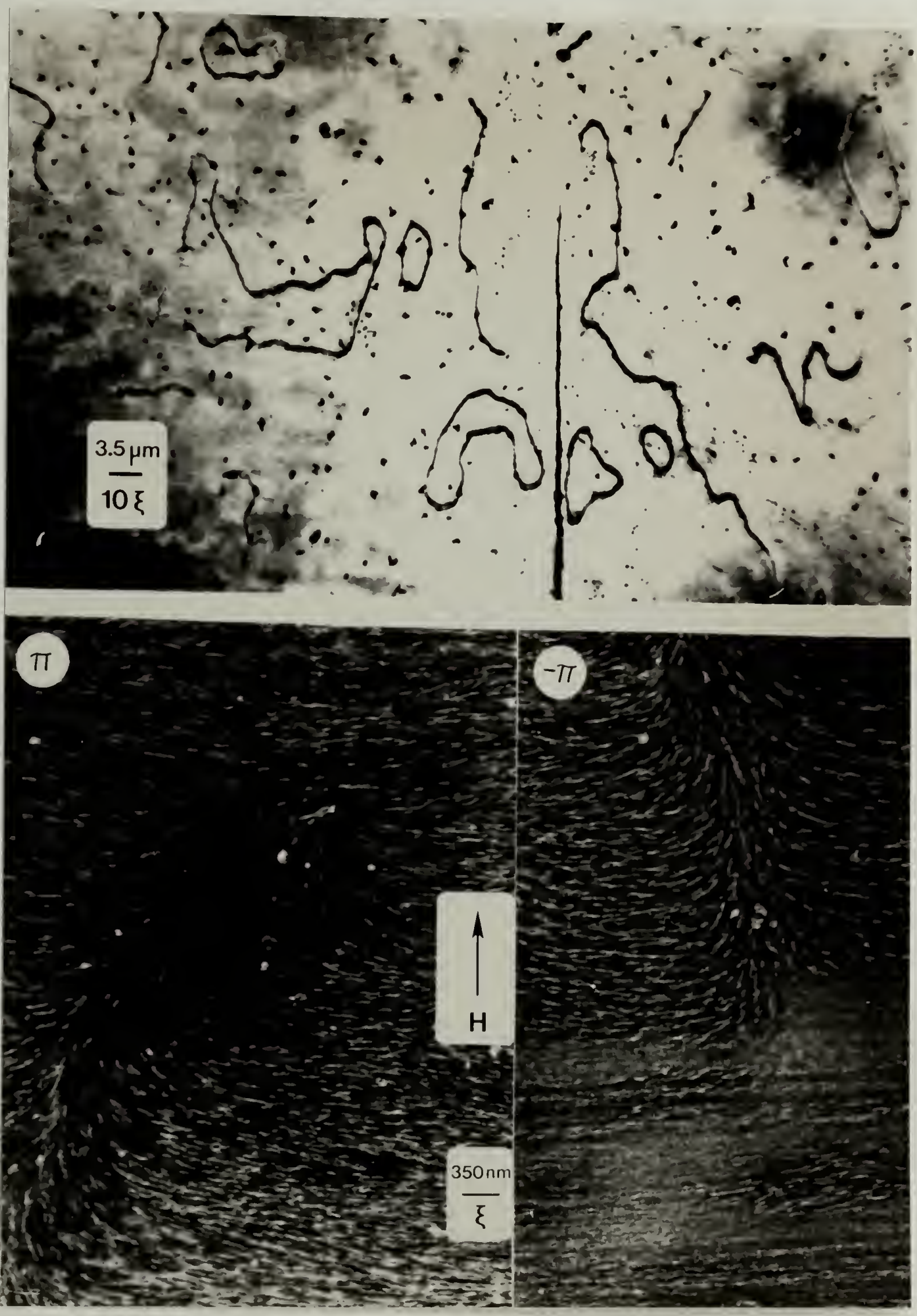

Figure 6.9 Disclinations at the end of an inversion wall. (a) Optical microscope image. (b) HRSEM image.

The perturbed director field about a π disclination is therefore:

$$\phi = \theta/2 - 1/6\,(r/\xi)^2 \sin\theta \quad . \tag{6.16}$$

This expression is valid when $r << \xi$. Although this expression is derived this considering an isolated disclination, i.e. $\xi << d$, it is also valid when $\xi >> d$. The effect of the neighboring disclination on the director field (equation 5.7) is added to that due to the applied field. In future core structure measurements, it would be interesting to observe the core in a sample quenched during magnetic or flow alignment, and it would be useful to examine any deviations from the structure predicted in this section.

6.3.3 Interaction of disclinations

The applied field not only changes the structure of a disclination, but it also changes their interactions. When $\xi << d$, disclinations of opposite sign are connected by an inversion wall having the same topological strength, e.g. $|\pi|$. The interaction energy between disclinations is no longer logarithmic, but it is proportional to the area of inversion wall between the two disclinations. Because this area is proportional to disclination separation, the force on a disclination is independent of disclination separation. The disclinations will be attracted to one another at a constant velocity [Cladis et al., 1987]:

$$v \sim H/\gamma_1 \; (\chi_a k/\pi)^{1/2} \quad . \tag{6.17}$$

Eventually the separation decreases until $d << \xi$, andthe force on each disclination will increase as 1/d. The annihilation of a disclination pair as a function of field strength is shown in figure 6.10.

In the case of zero field, we saw in chapter 4 that though the pairwise interaction of disclinations is understood, many-body interactions make it difficult to predict the asymptotic annihilation rate. In the presence of a sufficiently strong field, however, where $\xi << d$, the annihilation is easy to predict because only two-body interactions exist. Each pair will attract at the same rate. The disclination density will be:

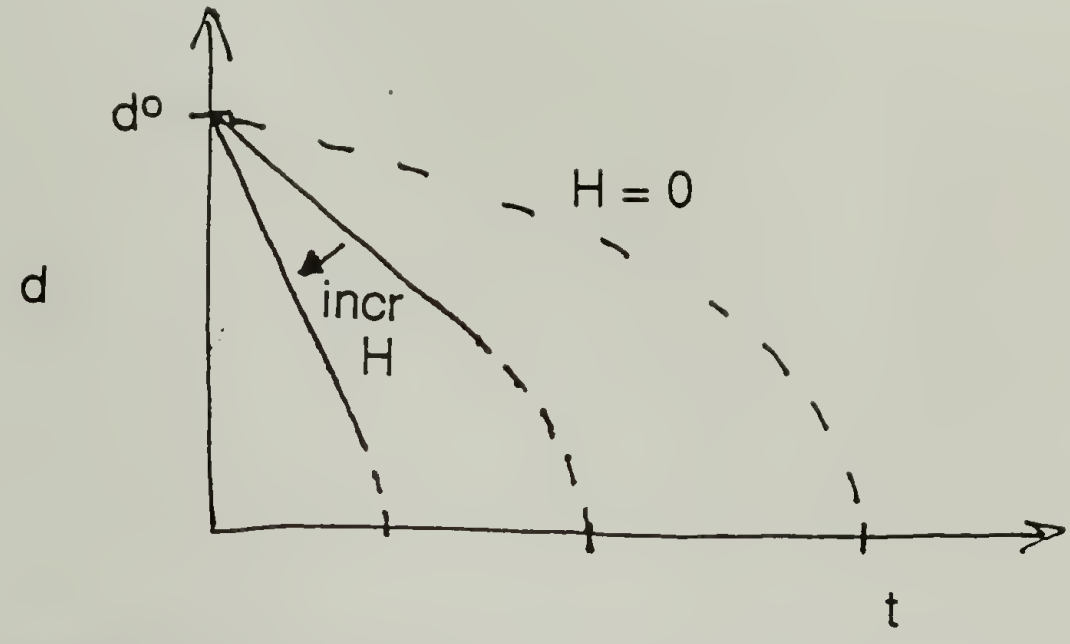

Figure 6.10 Disclination pair interaction affected by a magnetic field. Disclination separation, d, v. time.

$$\rho_d = \rho_d^{\circ} \int_0^{\sim t} (1 - f(s))ds \ , \qquad (6.18)$$

where ρ_d° is the initial disclination density and f(s) is the distribution function of disclination separation.

6.4 Polygonalization of disclinations

The interaction of disclinations in liquid crystals is varied and complex. Each of the three types of textures shown in figure 1.11 result from three distinct types of disclination interaction. As described in chapter 4, in the absence of any field, the structure of a nematic melt is described by a schlieren texture, where the disclinations are disordered. The interactions are many-bodied and the interaction force goes as 1/r. In the presence of a field, the number of interactions decreases as the characteristic length (ξ) decreases. The limit of very high field where only two-body interactions remain was discussed in the previous section. When $\xi \sim d$, disclination interaction has not been examined until now. This is a preliminary study investigating the interactions of disclinations in extensional flow and magnetic field. More questions remain especially regarding shear flow.

6.4.1 Experimental observations

We have commonly observed specific clustering of disclinations in flow oriented thin film TLCP samples prepared by spreading on phosphoric acid. Figure 6.11(a) shows a TEM image of melt spread TQT10-M. The direction and the characteristic length of the flow is indicated. The alignment is nearly complete. We define the quadrupolar arrangement of disclinations shown as a Lehmann cluster; Lehmann, in his 1918 book, drew such an arrangement. The dipole moment of the cluster is zero. The disclination separation is 3.2ξ. The director field of this cluster is antisymmetric about both the axis containing the positive disclinations and the axis containing the negative ones. The disclinations appear to define a domain boundary within which the director is oriented perpendicular to the flow. Wood and Thomas [1986] were the first to observe this clustering. In fact, because the clustering was so common place in their samples (figure 6.11(b)), they wondered if clusters of disclinations often define effective domain boundaries. However, the appearance of clusters, such as the Lehmann cluster, is clearly process dependent.

The Lehmann cluster is also common in magnetically oriented thin films, where $d \sim \xi$. To obtain director textures where $d \sim \xi$, a film of TQT10-M was first cast from dilute solution in methylene chloride. After the solvent was rapidly evaporated at room temperature, the film was heated into the nematic state for a few minutes to develop a schlieren texture and then quenched. The sample was then oriented in 15.2T magnetic field at 180C for nearly four hours. A TEM image of a replica of this sample is shown in figure 6.11(c). Note the Lehmann clusters. The quadrupole structure of disclinations is strikingly different from that observed with no field. Although Lehmann clusters are not commonly observed in quiescently prepared samples, they are abundant in oriented samples when $d \sim \xi$. To understand the occurrence of the Lehmann cluster, its energetics are examined as a function of field strength.

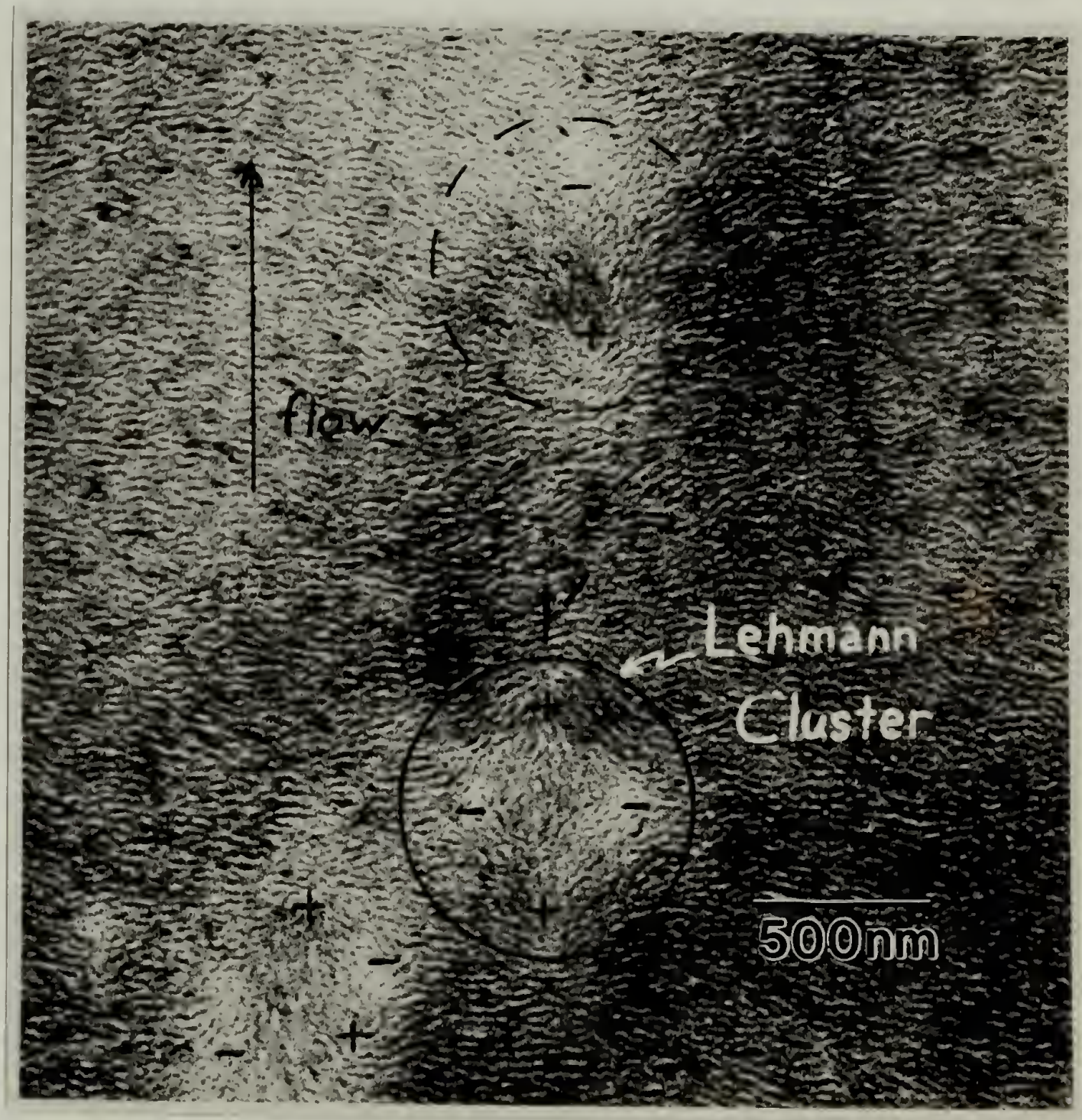

Figure 6.11 The Lehmann cluster observed when $\xi \sim d$. (a) Extensional flow oriented sample. (Continued next page.)

Figure 6.11 The Lehmann cluster observed when $\xi \sim d$. (b) Extensional flow oriented sample from Wood [1985]. (Continued next page.)

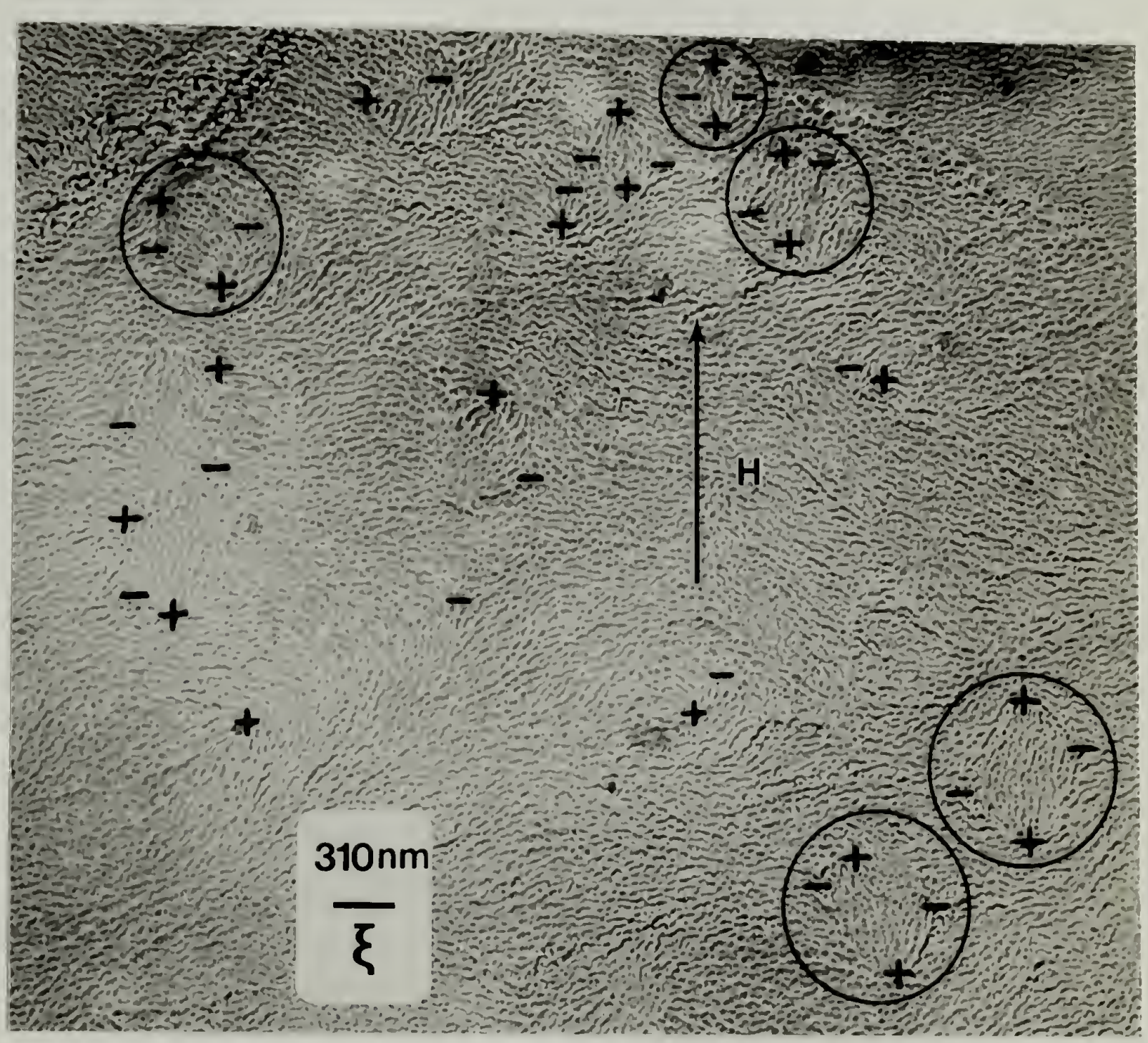

Figure 6.11 The Lehmann cluster observed when $\xi \sim d$. (c) Magnetically oriented sample.

6.4.2 Energetic analysis of the Lehmann cluster

At zero field, the disclination interaction is analogous to electrostatics of line charges, as described in chapter 2. Each disclination is attracted radially to the center of the cluster, but any tangential fluctuation of the disclination positions causes the cluster to become unstable. Pair interactions dominate, and the disclination annihilation process accelerates.

Figure 6.12 shows the total energy, G, for the zero field case, of the Lehmann cluster as the position of one disclination is varied. Each disclination in the Lehmann cluster is

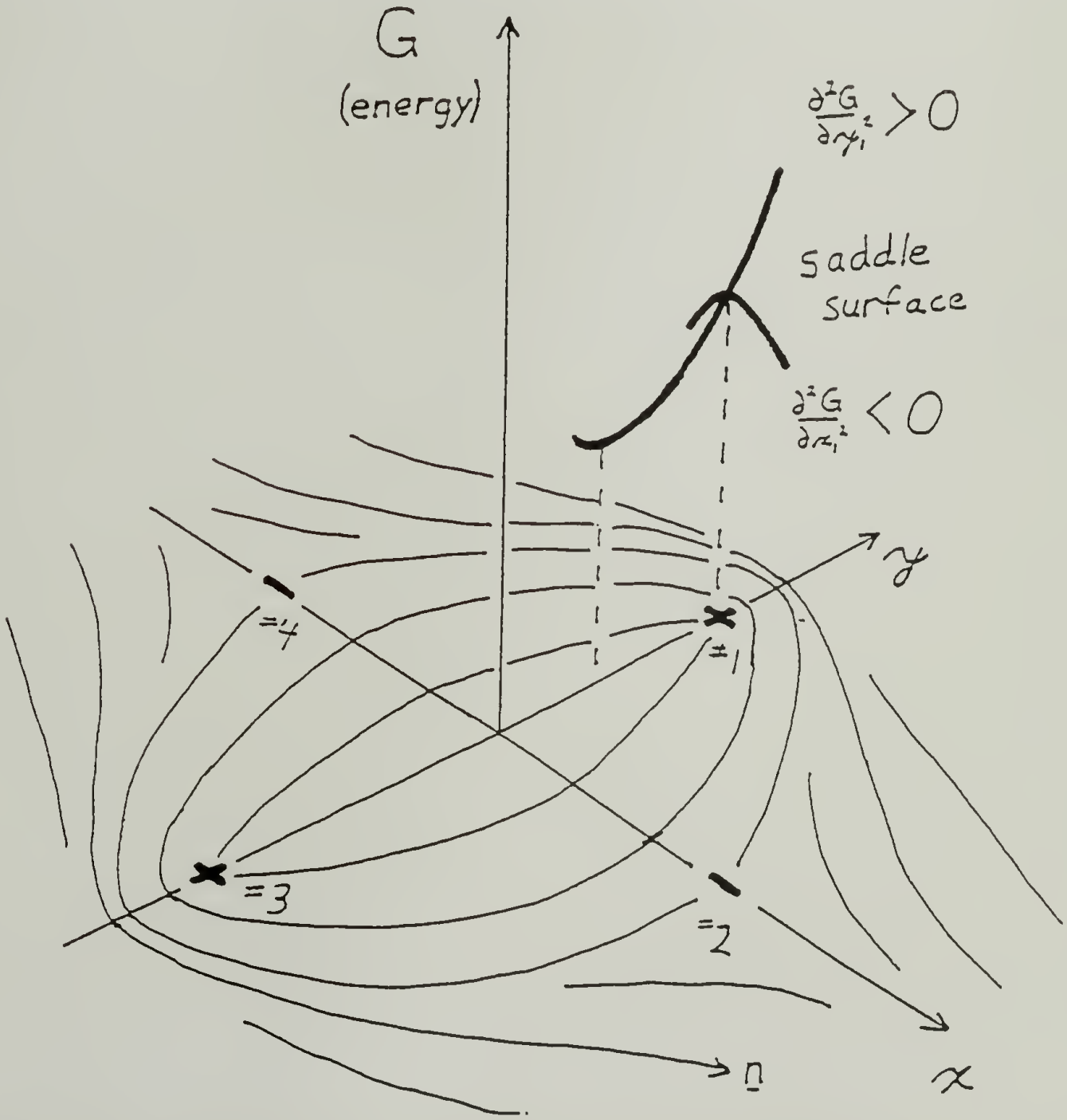

Figure 6.12 Energy of the Lehmann cluster at H=0 as a function of disclination position. Disclinations #2, 3, and 4 are fixed and the total cluster energy varies with the position of disclination #1.

attracted radially to the center of the cluster. Since each disclination feels the same force, the cluster remains self-similar as it shrinks uniformly. However, because the curvature of the energy is negative as the position of a disclination is varied in the tangential direction, the cluster is unstable to any tangential fluctuation. This result explains why Lehmann clusters are not frequently observed in unoriented films (schlieren texture). At zero field, this curvature is

$$\partial^2 G/\partial x_d^2 = -\pi k/(4\sqrt{2}\, d) \quad . \tag{6.19}$$

This parameter defines the stability of the cluster with respect to tangential fluctuations in disclination position. Since the long range distortion energy of a cluster is proportional to its dipole moment, there may exist a critical field H_c above which the curvature is positive and the Lehmann cluster would be stable.

At non-zero fields, an analytic expression for the total energy is not available; numerical calculations are necessary. As we have mentioned repeatedly, the applied field orients the director at long range. Therefore it is profitable to discuss the long range energetics of a cluster of disclinations. The long range distortion of a cluster (at H = 0) may be calculated most simply by taking a multipole expansion analogous to electrostatics.

$$\phi = 1/r\,[\sin\theta \Sigma s_i x_i - \cos\theta \Sigma s_i y_i] + 1/r^2[\text{quadrupole terms}] + \ldots, \tag{6.20}$$

where r and θ are polar coordinates and $\Sigma s_i x_i$ is the x component of the dipole moment. The dominant term far from the cluster is due to its dipole moment. The free energy density becomes:

$$g = k/2r^4\,[\Sigma s_i x_i(\sin\theta - \cos\theta) + \Sigma s_i y_i(\sin\theta + \cos\theta)]^2 \tag{6.21}$$

Integrating this from some distance, R, outside the cluster to infinity, the distortional free energy is:

$$G = k\pi/8R^2\ m^2 \quad , \tag{6.22}$$

where m is the dipole moment. Since the long range distortional energy is proportional to the square of the dipole moment, it is easy to understand that the applied field will tend to reduce the dipole moment of a cluster of disclinations.

Figure 6.11(a) clearly shows the reduction of the long range distortion of the director field due to the special structure of the Lehmann cluster. Outside of the circle enclosing the cluster, the director is fully aligned with the flow direction. However, at the same radius about the lone $\pm\pi$ disclination dipole in the upper part of the figure, the director is at a measurable angle to the flow direction, the area of material which is misaligned with respect to the flow is larger, and this increases the long range energy.

To test the importance of the idea that an applied field tends to reduce the dipole moment of a cluster of disclinations, the energy of the cluster is examined for two types of tangential fluctuations--those that preserve the zero dipole moment of the Lehmann cluster and those that cause the dipole moment to increase. These fluctuation modes are shown in figure 6.13(a). Using the finite element method, the director field and its energy were calculated as a function of field strength. Results of the curvature of the energy for each of the two modes is shown in figure 6.13(b). The dipole fluctuation tends to be suppressed at intermediate fields. The zero dipole fluctuation, however, is always enhanced even for very weak fields. Results are also listed in table 6.1. Unfortunately, these results are only qualitatively correct. The linear interpolation used in the finite element program incorrectly calculates the Laplacian of the director field. Consequently, the calculated distortion due

Table 6.1 Finite element calculations of the curvature of the total cluster energy as a function of field strength and fluctuation mode.

	$\partial^2 G/\partial x^2$ (k/d)	
H ($[k/\chi_a]^{1/2}/d$)	m ~ x	m = 0
0.000	-0.56400	-0.55849
0.014	-0.56362	-0.55854
0.141	-0.53855	-0.56313
0.283	-0.50168	-0.57792
0.467	-0.46112	-0.61725
0.707	-0.44603	-0.70813
1.010	-0.52815	-0.92439
1.414	-0.94980	-1.51027
1.768	-1.89686	-2.58272
2.020	-3.29496	-4.05869

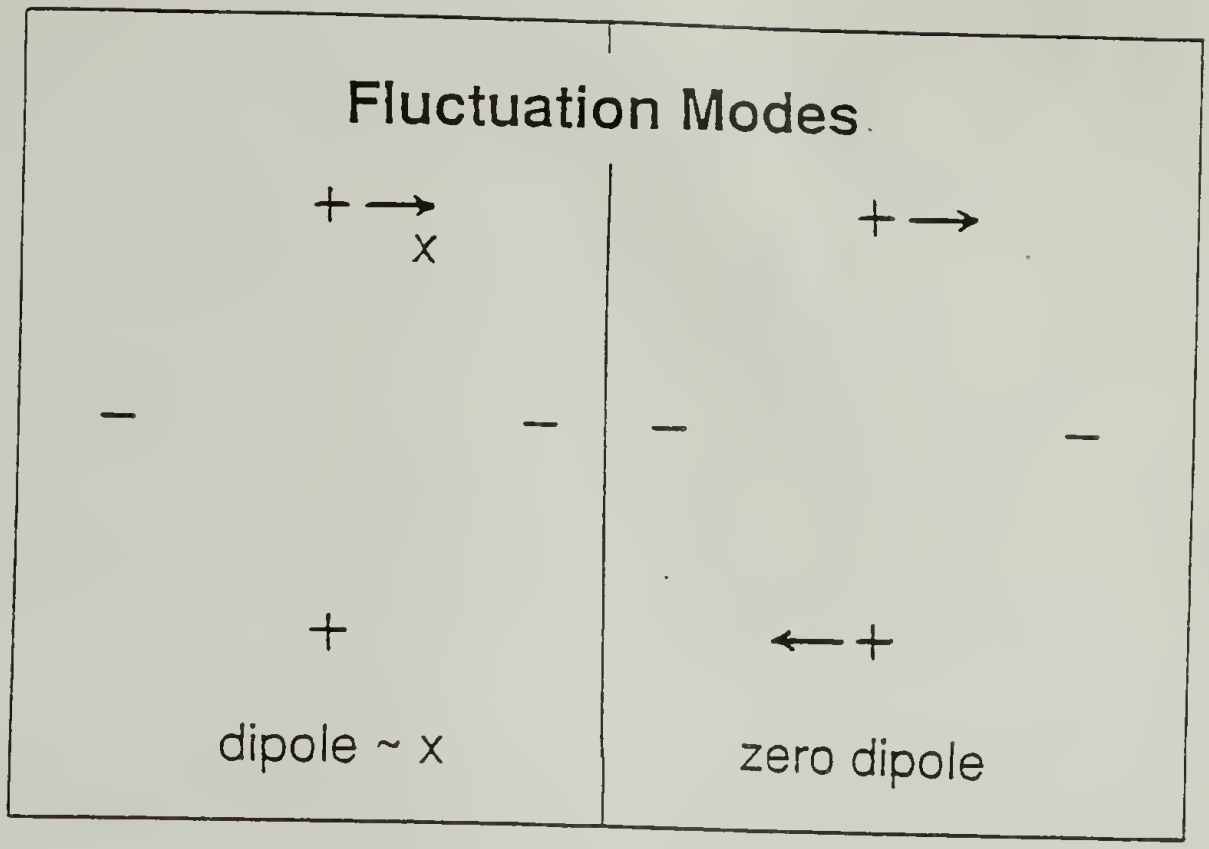

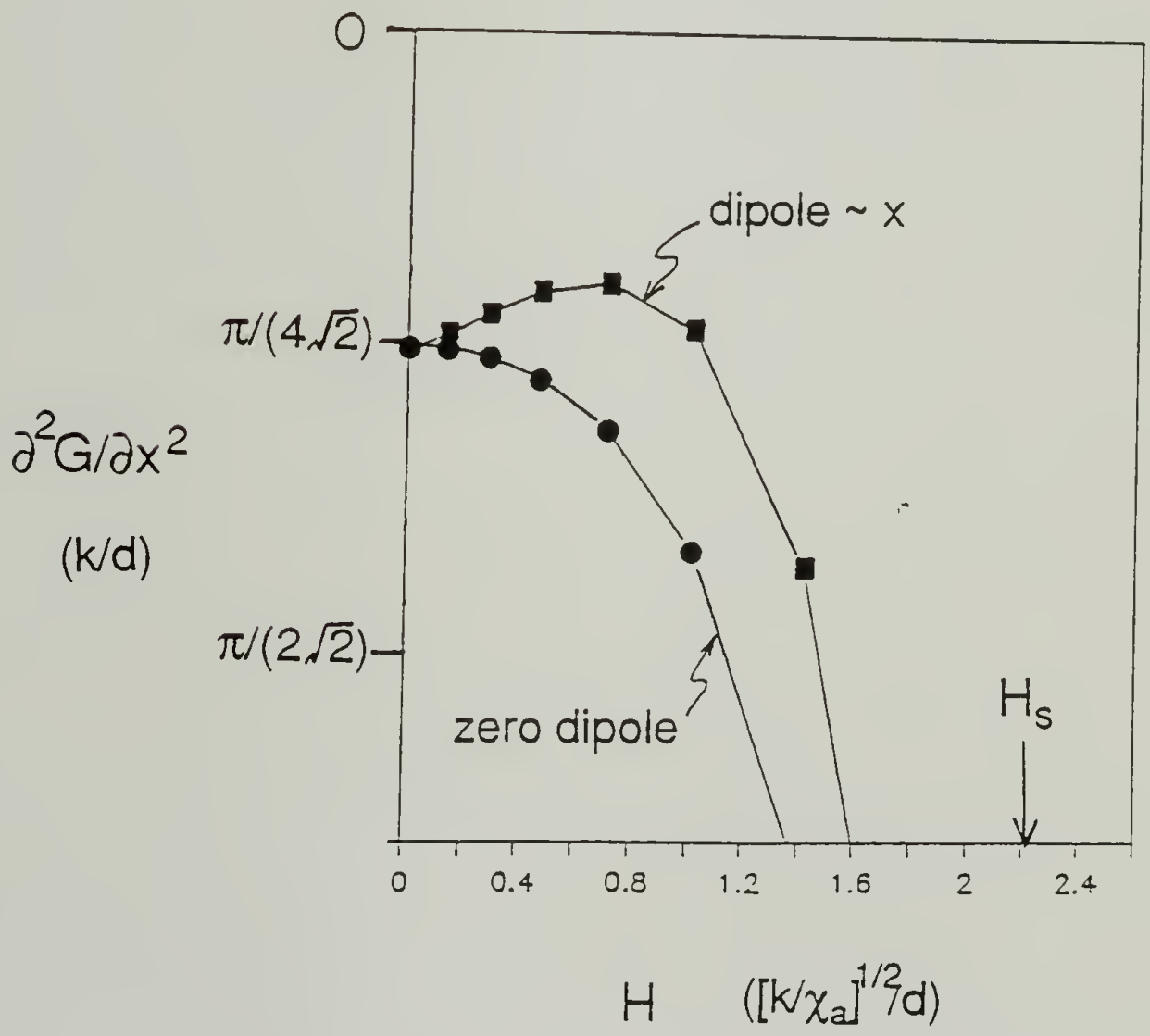

Figure 6.13 Stability of the Lehmann cluster to fluctuations in disclination postion. (a) Dipole and zero-dipole modes of fluctuation. (b) Finite element results of $\partial^2 G/\partial x_d^2$ v. H.

to magnetic field is too large near the disclination cores. The general trend of the two curves for the curvature should not be effected by this scaling. Therefore it is safe to conclude that the magnetic field suppresses fluctuations which increase the dipole moment and promotes zero dipole fluctuations. The dipole fluctuations are supressed more strongly until, at higher fields, fluctuation induced symmetry breaking occurs.

After the symmetry breaks (at high fields), inversion walls begin to form between the disclinations as shown in figure 14. Both the symmetric and the asymmetric structures have a two-fold axis at the origin, but the symmetric structure is also anti symmetric about both the x and y axes. The transition to the asymmetric structure at large field is similar to the Freedericksz transition familiar in liquid crystals.

An order parameter that is useful to describe this transition is the orientation of the director at the center of the cluster, ϕ_o. We define the deviation from the symmetrical phase as:

$$\eta = 2\phi_m/\pi \qquad (6.23)$$

where $\phi_m = \pi/2 - \phi_o$. This order parameter is zero until the symmetry breaks; it then grows to 1 when $d >> \xi$. Figure 6.14 shows the cluster at an intermediate order parameter.

The strength of the critical field may be calculated by considering the cluster at a field infinitesimally greater than the critical field. The director field again must satisfy the Euler-Lagrange differential equation (6.14). Consider the director field on the y axis between the two positive disclinations. The curvature of the director in the x direction, which is zero below the critical field, is expected to be negligible infinitesimally above the critical field. The director along the y axis can then be described as [Stephen and Straley, 1974]:

$$\phi(0,y) = \pi/2 - \phi_m \cos(y/\xi_s) \; . \qquad (26)$$

ξ_s is defined by the disclination positions: $\xi_s = 2y_1/\pi = 0.45d$, where d, as before, is the distance between opposite signed disclinations. Alternatively, $d_s = 2.22\xi$. Note that the

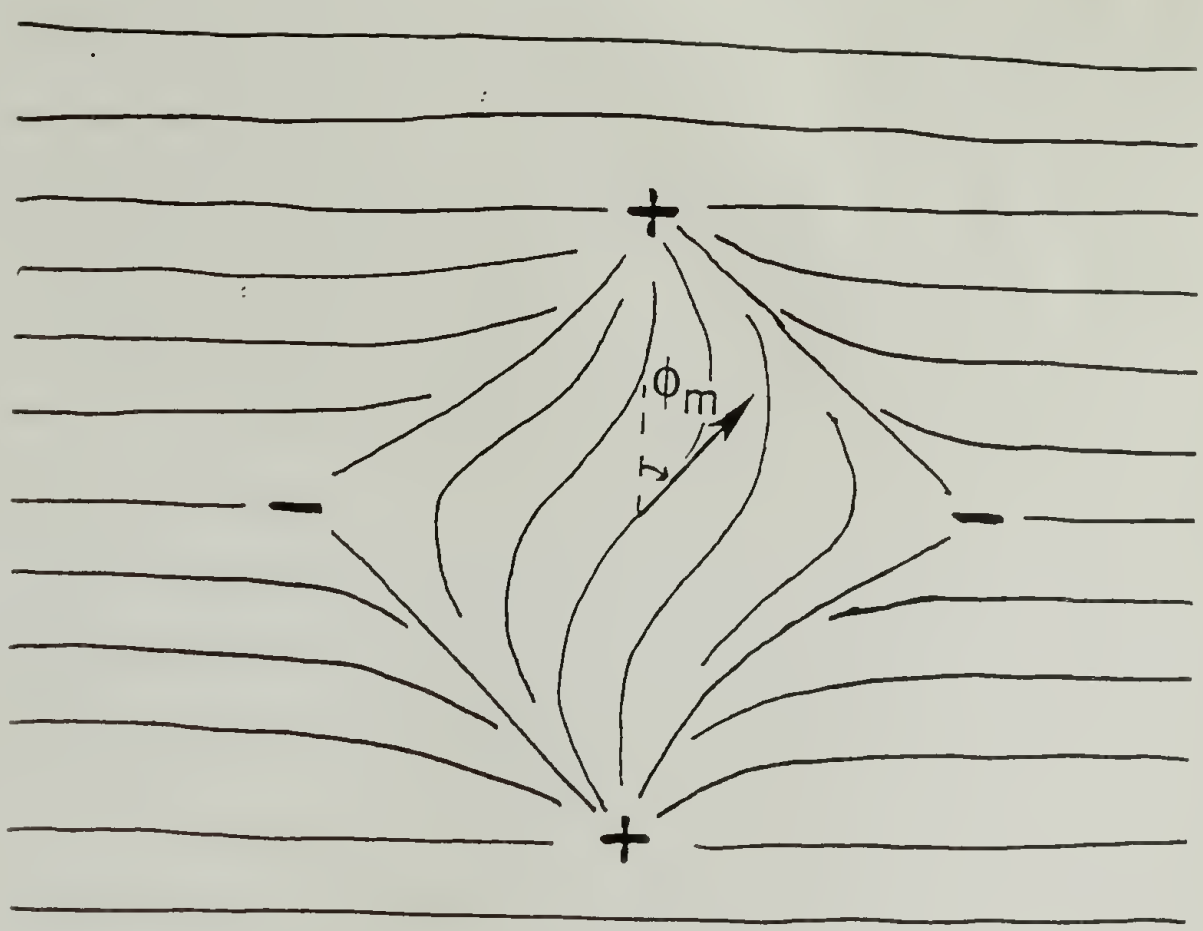

Figure 6.14 The Lehmann cluster at field strengths where the symmetry has broken. The order parameter angle, ϕ_m, is shown. Inversion walls are beginning to form: one between the top and the right disclination; the other between the bottom and the left disclination.

numerical calculations are in accord with this result. The curvature of the energy dives as the applied field approaches the symmetry breaking field, $H_s = 2.22\, d(k/\chi_a)^{1/2}$.

The above is true for exactly symmetric disclination positions. Fluctuations in the disclination positions, however, will make the transition be first instead of second order. The fluctuations of disclination position induce asymmetric fluctuations in the director field.

Measurement of the characteristic length for distortions in flow allows further characterization of the Lehmann cluster. The Lehmann cluster is observed in both the flow and magnetic alignment cases, to occur when the disclination separation is 0.7 - 3.2 ξ. The disclination separation is generally smaller in Lehmann clusters observed in magnetically

aligned samples. The maximum disclination separation observed is shown in figure 6.11(a) where the disclinations are at 3.2ξ (and the director field is symmetrical). According to the argument above, the maximum separation should be 2.22ξ. At greater separations, the director field is presumed to break its symmetry. Some suggestions explaining the observation of a symmetric Lehamnn cluster having larger disclination separation are discussed next.

6.4.3 Additional effects

In magnetic alignment, the field strength is uniform. However, in flow, experiments by Cladis et al. [1987] indicate that as a disclination moves rapidly, it drags surrounding material with it. If the deformation rate is reduced near the disclination, the Lehmann cluster would be further stabilized. Not only are the individual disclinations expected to behave like particles, but the interactions between disclinations will cause the whole cluster to also have particle character. Both of these effects will reduce the deformation rate and stabilize the cluster at higher field strengths.

An additional effect is elastic anisotropy. Elastic anisotropy introduces orientational dependence as depicted in figure 6.15. Both in this work (using TQT10-M) and in Wood's [1985] (using TQT10-H), the orientation of the Lehmann cluster consistent with positive elastic anisotropy is almost exclusively observed. The value of ε for TQT10-H, however, has

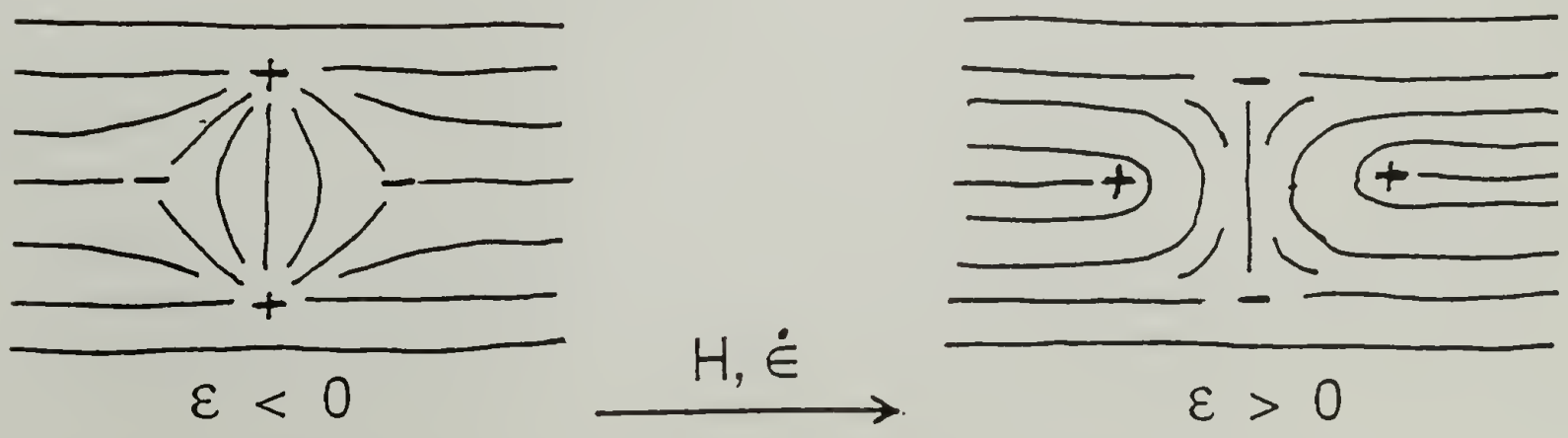

Figure 6.15 Orientation of the Lehmann cluster as a function of elastic anisotropy.

been measured in the previous chapter to be -0.13. This inconsistancy may be resolved by noting that the disclination separation of the observed Lehmann clusters is a few hundred nanometers. At this distance, the apparent elastic anisotropy was found to be positive. When the disclination cores overlap, the apparent elastic anisotropy of the cores may determine the most favorable orientation of the cluster. Disclination interaction is therefore expected to vary with separation. Additionally, the core of the disclination may vary with the nature and the strength of the applied field.

Elastic anisotropy should also stabilize the cluster because it is expected that the largest of the elastic constants will determine the critical field for symmetry breaking.

In this chapter, it is shown that the Lehmann cluster is very prominent in two dimensions in the presence of extensional flow (or magnetic field). However, it remains to be seen if such phenomena would exist in either shear flow or in three dimensions. First consider three dimensions.

The Lehmann cluster in three dimensions corresponds to the simplest zero dipole structure--two circular disclination loops parallel to each other but with opposite sense to the line direction. (A cross section of this Lehmann cluster is the Lehmann cluster in 2D.) I expect that such a cluster should be stabilized in magnetic fields or extensional flow.

Because shear flow involves molecular rotation, it does not align the director in the same way as a magnetic field. As described in chapter 1, shear flow may simultaneously produce two effects: one which is completely analogous to magnetic fields and another which tends to rotate the director. The alignment effect is global, whereas the rotation effect is a result of local rotation. These two effects in competition are just the ingredients for disclination creation. This explains the motivation for the observed production of disclinations in shear flow [Mackley, 1987]. If the alignment effect is strong compared to the rotation, the Lehmann cluster may be stabilized in shear as well as extensional flow.

CHAPTER 7

SUMMARY

This work includes unique advancement in the understanding of disclination interaction in nematic liquid crystals in general. Although the physics of nematic materials has been well studied for decades, it remains a subject with great potential for fruitful work. Throughout the text I have included sections proposing future work. The interaction of disclinations in the presence of an applied field which tends to align the director has not been studied before. At intermediate field strengths, where the characteristic length for distortions is approximately equal to the disclination separation, pairwise interaction no longer dominates, but clusters of disclinations are observed to form. Borrowing from the analogy to electrostatics, a cluster of disclinations may be characterized by its dipole moment. The applied field suppresses fluctuations of the disclination positions which increase the dipole moment of a cluster while enhancing those that preserve zero dipole. The applied field tends to minimize the long range distortional energy which is proportional to the square of the dipole moment. As a result, quadrupolar (Lehmann) clusters of disclinations are commonly observed in either magnetically or extensionally flow aligned samples.

The prominence of the Lehmann cluster has in this work been well established in two dimensional samples. The existence of a Lehmann cluster in three dimensions has yet to be examined. In this case, the Lehmann cluster would exist as two parallel but oppositely sensed disclination loops.

Even in the absence of an applied field, complexities of many-bodied disclination interaction are not understood. The pairwise interaction of disclinations has been well understood for more than a decade, and I have used this basic understanding to numerically simulate the annealing process. The calculated asymptotic time dependence for disclination

annihilation agrees favorably with recent experimental studies. An advantage of the simulation, which needs to be better exploited, is its ability to calculate the interdisclination structure.

The high resolution of the lamellar decoration technique to image thermotropic liquid crystalline polymers (TLCP's) also allows a unique investigation of disclination core structure. The results of this part of the work are specific to polymer liquid crystals. The core size is on the order of the molecular length, and its structure depends upon polymer architecture. A rigid polymer splays more within the core of a π disclination, while a semi-flexible polymer bends more. An excess of chain ends aggregates at the core of π disclinations in the rigid material. Hairpins are not expected to be abundant in the core of the semi-flexible TLCP. The core structure of - π disclinations is expected to be quite different. Interesting experiments are possible with blending miscible or immiscible components to see if segregation occurs at the disclination core.

The utility of the lamellar decoration technique has also been greatly extended by using an etch technique to image the director in sections of a bulk sample. This technique has been used to image the director field of magnetically aligned films. The resultant director field texture has been characterized not only by the disclination density but also the characteristic length for distortion and the inversion wall density. All of these parameters may be measured via microscopy. The etch technique also opens the door to investigate the morphology of flowing liquid crystal polymers if samples may be quenched rapidly enough.

The main emphasis of the thesis was to understand nematic liquid crystal and nematic liquid crystal polymer physics from microscopic observation. The semi-crystalline phase having the lamellar decoration morphology was used as a tool to observe the director in the precursor nematic. More traditional microscopy of the TLCP crystal morphology in general has also been started. The morphology is observed to depend upon the relative primary crystal nucleation and crystal growth rates. The lamellar decoration morphology, where the crystalline lamellae are everywhere perpendicular to the director of the precursor

nematic, is favored by rapid nucleation and slow growth. This morphology is unique to TLCP's, but other morphologies are possible. Spherulites have also been grown from the nematic melt. Their growth is favored by slow nucleation and rapid growth. Further characterization of the factors leading to spherulitic growth is planned.

BIBLIOGRAPHY

Atkins, E.D.T., Thomas, E.L., and Lenz, R.W., X-ray Diffraction Studies on Oriented Semi-Rigid Liquid Crystalline Polyesters, *Mol.Cryst.Liq.Cryst.* **155**, 271-279 (1988).

Baur, G., Liquid Crystal Display Devices, Polymer Liquid Crystals, ed. A.Ciferri, W.R.Krigbaum, and R.B.Meyer, p. 309-327, Acedemic Press, New York, 1982.

Biswas, A., and Blackwell, J., Three Dimensional Structure of Main-Chain Liquid-Crystalline Copolymers. 3. Chain Packing in the Solid State, *Macromolecules* **21**(11), 3158-3164 (1988).

Bosch, A.Ten, and Sixou, P., Elastic Constants of Semirigid Liquid -Crystal Polymers, *J.Chem.Phys.* **86**(11), 6556-6559 (1987).

Bramson, M., and Lebowitz, J.L., Asymptotic Behavior of Densities in Diffusion-Dominated Annihilation Reactions, *Phys.Rev.Lett.* **61**(21), 2397-2400 (1988).

Brinkman, W.F., and Cladis, P.E., Defects in Liquid Crystals, *Physics Today* **35**(5), 48-54 (1982).

Brock, J.D., Birgeneau, R.J., Litster, J.D., and Aharony, A., Liquids, Crystals, and Liquid Crystals, *Phys.Today* **42**(7), 52-59 (1989).

Carlsson, T., and Skarp, K., Observation of the Tumbling Instability in Torsional Shear Flow of a Nematic Liquid Crystal with $\alpha_3 > 0$, *Liq.Cryst.* **1**(5), 455-471 (1986).

Caroli, C., and Dubois-Violette, E., Energy of a Disclination Line in an Anisotropic Cholesteric Liquid Crystal, *Sol. St.Commun.*, **7**(11), 799-802 (1969).

Chandrasekhar, S., and Ranganath, G.S., The Structure and Energetics of Defects in Liquid Crystals, *Adv. Phys.* **35**, 507-596 (1986).

Chandrasekhar, S., Liquid Crystals, Cambridge Univ. Press, Cambridge, 1977.

Chrandrasekhar, S., and Kini, U.D., Instabilities in Low Molecular Weight Nematic and Cholesteric Liquid Crystals, Polymer Liquid Crystals, ed. A.Ciferri, W.R.Krigbaum, and R.B.Meyer, p.201-245, Acedemic Press, New York, 1982.

Cladis, P.E., and Torza, S., Flow Instabilities in Couette Flow in Nematic Liquid Crystals, *Colloid.Int.Sci.* **4**, 487-498 (1976).

Cladis, P.E., Saarloos, W. van, Finn, P.L., and Kortan, A.R., Dynamics of Line Defects in Nematic Liquid Crystals, *Phys.Rev.Lett.* **58**(3), 222-225 (1987).

Dafermos, C.M., Disclinations in Liquid Crystals, *Quart.J.Mech.Appl.Math.* **23**, s49-s64 (1970).

Das, E.S.P., deWit, R., Armstrong, R.W., and Marcinkowski, M.J., Kinks, Jogs, and a Regeneration Mechanism for Volterra Disclinations, *J.Appl.Phys.* **44**(11), 4804-4806 (1973).

Demus, D., and Richter, L., Textures of Liquid Crystals, Verlag-Chemie, New York, 1978.

Dicke, H-R., and Lenz, R.W., Liquid Crystal Polymers. 14. Synthesis and Properties of Thermotropic Poly(1,4-Alkylphenylene Terephthalates), *J.Polym.Sci.PC* **21**, 2581-2588 (1983).

Dreizen, Y.A., and Dykhne, A.M., Plane Problems in Elasticity Theory of Nematic Liquid Crystals, *Sov.Phys.JETP* **34**(5), 1140-1143 (1972).

DuPre, D.B., Techniques for the Evaluation of Material Constants in Lyotropic Systems and the study of Pretransitional Phenomena in Polymeric Liquid Crystals, Polymer Liquid Crystals, ed. A.Ciferri, W.R.Krigbaum, and R.B.Meyer, p.165-200, Acedemic Press, New York, 1982.

Dutton, R.N., Bassett, D.C., and Mitchell, G.R., The Structure and Solid State Morphology of a Series of Main-Chain Thermotropic Polyesters, (1990).

Dzyaloshinskii, I.E., Theory of Disclinations in Liquid Crystals, *Sov.Phys.JETP* **31**(4), 773-777 (1970).

Ericksen, J.L., Singular Solutions in Liquid Crystal Theory, Liquid Crystals and Ordered Fluids, ed. J.F.Johnson and R.S.Porter, p.181-193, Plenum, 1970.

Ericksen, J.L., Equilibrium theory of liquid crystals, Advances in Liquid Crystals, ed. G.H.Brown, **2**, 233-298 (1976).

Ericksen, J.L., and Kinderleher, D., Theory and Applications of Liquid Crystals, IMA **5**, Springer-Verlag, Berlin, 1987.

Fincher Jr., C.R., Field-Induced Textures and Elastic Constants of Nematic Polymers, *Macromolecules* **19**, 2431-2435 (1986).

Folda, T., Hoffman, H., Chanzy, H., and Smith, P., Liquid Crystalline Suspensions of Poly(tetrafluoroethylene) 'Whiskers', *Nature* **333**, 55-56 (1988).

Frank, F.C., On the Theory of Liquid Crystals, *Disc. Faraday Soc.* **25**, 19-28 (1958).

Freedman, A.M., Bassett, D.C., Vaughan, A.S., and Olley, R.H., On Quantitative Permanganic Etching, *Polymer* **27**, 1163-1169 (1986).

Friedel, G., Les Etats Mesomorphes de la Matiere, *Ann. Physique* **18**, 273-474 (1922).

Friedel, J., Dislocations and Disclinations Past and Present: Some Personal Views and Reminiscences, *Ann.Rev.Mater.Sci.* **18**, 1-24 (1988).

Gahwiller, Ch., Direct Determination of the Five Independent Viscosity Coefficients of Nematic Liquid Crystals, *Mol. Cryst.Liq. Cryst.* **20**, 301-318 (1973).

Galerne, Y., Itoua, J., and Liebert, L., Zigzag Disclinations in Uniaxial Nematic Liquid Crystals, *J.Physique* **49**, 681-687 (1988).

Gennes, P.G. de, Calcul de la distorsion d'une struture cholesterique par un champ magnetique, *Sol.St.Commun.* **6**, 163-165 (1968).

Gennes, P.G. de, Mouvements de Parois dans un Nematique sous Champ Tournant, *J.Physique* **32**, 789-792 (1971).

Gennes, P.G. de, The Physics of Liquid Crystals, Clarendon Press, Oxford, 1974.

Gennes, P.G. de, Polymeric liquid crystals: Frank elasticity and light scattering, *Mol.Cryst.Liq.Cryst.Lett.* **34**, 177-182 (1977).

Gennes, P.G. de, Mechanical Properties of Nematic Polymers, Polymer Liquid Crystals, ed. A.Ciferri, W.R.Krigbaum, and R.B.Meyer, p.115-131, Acedemic Press, New York, 1982.

Gennes, P.G. de, "Flexible" Nematic polymers: stiffening near the clearing point, *Mol.Cryst.Liq.Cryst.Lett.* **102**, 95-104 (1984).

Gray, G.W., Relationship between Chemical Structure and Properties for Low Molecular Weight Liquid Crystals, Polymer Liquid Crystals, ed. A.Ciferri, W.R.Krigbaum, and R.B.Meyer, Acedemic Press, New York, 1982, chapter 1.

Graziano, D.J., and Mackley, M.R., Disclinations Observed During the Shear of MBBA, *Mol.Cryst.Liq.Cryst.* **106**, 103-119 (1984).

Guyon, E., Meyer, R.B., Salan, J., Domain Structure in the Nematic Freedericksz Transition, *Mol.Cryst.Liq.Cryst.* **54**, 261-273 (1979).

Hahn, P.E., Light and X-ray Scattering Studies of the Mesophase of Main-Chain Thermotropic Polymeric Liquid Crystals, Ph.D. Thesis, University of Massachusetts, Amherst, 1987.

Hardouin, F., Achard, M.F., Gasparoux, H., Leibert, L., Strzelecki, L., Magnetic Effects and Viscosity in the Nematic Phase of a Polymer Series, *J.Polym.Sci.PP* **20**, 975-980 (1982).

Harris, W.F., Disclinations, *Sci.American* **237**, 130-145 (1977).

Hedmark, P.G., et al., Selective Etching of Thermotropic Liquid Crystalline Polyesters, *J. Appl. Polym. Sci.* **34**(2), 743-762 (1987).

Helfrich, W., Alignment-Inversion Walls in Nematic Liquid Crystals in the Presence of a Magnetic Field, *Phys.Rev.Lett.* **21**(22), 1518-1521 (1968).

Hermann, C., The Symmetry Groups of the Amorphous and Mesomorphic Phases, *Zeit.Kristallographie* **79**, 186-221 (1931).

Hudson, S.D., Thomas, E.L., and Lenz, R.W., Imaging of Textures and Defects of Thermotropic Liquid Crystalline Polyesters by Electron Microscopy, *Mol.Cryst.Liq.Cryst.* **153**, 63 (1987).

Hudson, S.D., and Thomas, E.L., Frank Elastic-Constant Anisotropy Measured from Transmission-Electron-Microscope Images of Disclinations, *Phys.Rev.Lett.* **62**, 1993-1996 (1989).

Hudson, S.D., and Thomas, E.L., Microscopic Observation of Director Field Textures in Magneticaly Oriented TLCP Thin Flims, *Polym.Preprints* **31**(1), 379-380 (1990).

Hudson, S.D., Vezie, D.L., and Thomas, E.L., Director Textures in Bulk Samples of Liquid Crystal Polymers, *Makromol.Chem.,Rap.Comm.*, in press (1990).

Hudson, S.D., Fleming, J.W., and Thomas, E.L., Disclination Core Structure in Rigid and Semi-flexible Main Chain Polymer Nematic Liquid Crystals, submitted to *J.Physique* (1990).

Jonsson, H., Werner, P.-E., Gedde, U.W., and Anders H., Synthesis and Structure of Thermotropic Main-Chain Polyethers Based on Bis(4-hydroxyphenoxy)-p-xylene, *Macromolecules* **22**, 1683-1689 (1989).

Keith, H.D., and Padden, Jr., F.J., A Phenomenological Theory of Spherulitic Crystallization, *J.Appl.Phys.* **34**(8), 2409-2421 (1963).

Keith, H.D., and Padden, Jr., F.J., Spherulitic Crystallization from the Melt. I. Fractionation and Impurity Segregation and Their Influence on Crystalline Morphology, *J.Appl.Phys.* **35**(4), 1270-1285 (1964).

Keith, H.D., and Padden, Jr., F.J., Spherulitic Crystallization from the Melt. II. Influence of Fractionation and Impurity Segregation on the Kinetics of Crystallization, *J.Appl.Phys.* **35**(4), 1286-1296 (1964).

Keller, A., Polymer Crystals, *Rep.Prog.Phys.* **31**(2), 623-704 (1968).

Kini, U.D., and Ranganath, G.S., Singularities in Nematics: The Effect of Elastic Constant Variations, *Mol.Cryst.Liq.Cryst.* **38**, 311-317 (1977).

Kirkpatrick, R.C., Nearest Neighbor Algorithm, The Free Lagrange Method, ed. M.J.Fritts et al., p.302-309, Springer-Verlag, Berlin, 1985.

Kleman, M., Liebert, L. and Strzelecki, L., Preliminary Observations of Defects in a Polymeric Nematic Phase, *Polymer* **25**, 295 (1983).

Kleman, M., Points, Lines, and Walls, Wiley, Chichester, 1983.

Kleman, M., Defects in Liquid Crystals, *Rep.Prog.Phys.* **52**, 555-654 (1989).

Krigbaum, W.R., The Effects of External Fields on Polymeric Nematic and Cholesteric Mesophases, Polymer Liquid Crystals, ed. A.Ciferri, W.R.Krigbaum, and R.B.Meyer, p.275-308, Acedemic Press, New York, 1982.

Landau, L.D., and Lifshitz, E.M., Theory of Elasticity, 3rd ed., Pergamon Press, Oxford, 1986.

Lee, S-D., and Meyer, R.B., Computations of the Phase Equilibrium, Elastic Constants, and Viscosities of a Hard-Rod Nematic Liquid Crystal, *J.Chem.Phys.* **84**(6), 3443-3448 (1986).

Lee, S-D., and Meyer, R.B., Crossover Behavior of the Elastic Coefficients and Viscosities of a Polymer Nematic Liquid Crystal, *Phys.Rev.Lett.* **61**(19), 2217-2220 (1986).

Lehmann, O., Flussigen Krystallen, Verlag, Wiesbaden, 1918.

Leibbrandt, G., Exact Solutions of the Elliptic Sine Equation in Two Space Dimensions with Application to the Josephson Effect, *Phys.Rev.B* **15**(7), 3353-3361 (1977).

Lenz, R.W., Furukawa, F., Bhowmik, P., Garay, R.O., and Majnusz, J., Synthesis and Characterization of Rigid Rod Thermotropic Polyesters with Polyoxyethelene Pendant Substituents, *Polymer*, in press (1990).

Leslie, F.M., Some Constitutive Equations for Liquid Crystals; *Arch R Mech* **28**, 265-283 (1968).

Leslie, F.M., Theory of Flow Phenomena in Liquid Crystals, Advances in Liquid Crystals (ed. G.H.Brown) **4**, 1-81 (1979).

Lonberg, F., Fraden, S., Hurd, A.J., and Meyer, R.B., Field-Induced Transient Periodic Structures in Nematic Liquid Crystals: The Twist-Freedericksz Transition, *Phys.Rev.Lett.* **52**(21), 1903-1906 (1984).

Lotz, B., Fraser Price Award lecture, University of Massachusetts, Amherst, 1989.

Mabis, A.J., Structure of Mesomorphic Phases, *Acta.Cryst.* **15**, 1152-1157 (1962).

Mackley, M.R., Opitcal textures observed during shearing of thermotropic liquid-crystal polymers, *Faraday Disc. Chem.Soc.* **79**, 149-160 (1985).

Mackley, M.R., The Rheology and Micro-Structure of Flowing Thermotropic Liquid Crystal Polymers, *Mol.Cryst.Liq.Cryst.* **153**, 249-261 (1987).

Marrucci, G., Prediction of Leslie Coefficients for Rodlike Polymer Nematics, *Mol.Cryst.Liq.Cryst.* **72**, 153-161 (1982).

Marrucci, G., Remarks on the Viscosity of Polymeric Liquid Crystals, Proc. IX Intl. Congress on Rheology, Mexico, 441-448 (1984).

Marrucci, G., and Maffettone, P.L., Description of the Liquid-Crystalline Phase of Rodlike Polymers at High Shear Rates, *Macromolecules* **22**, 4076-4082 (1989).

Martin, P.G., and Stupp, S.I., The Contrasting Behavior of Chemically Ordered versus Chemically Disordered Liquid Crystal Polymers, *Macromolecules* **21**, 1222-1227 (1988).

Mazelet, G., and Kleman, M., Electron Microscopy Observations of a Nematic Polyester, *J.Mater.Sci.* **23**, 3055-3060 (1988).

Mazelet, G., and Kleman, M., Observation of defects in a polyester nematic phase: 2., *Polymer* **27**(5), 714-720 (1986).

Mermin, N.D., The Topological Theory of Defects in Ordered Media, *Rev.Mod.Phys.* **51**, 591-648 (1979).

Meyer, R.B., On the Existence of Even Indexed Disclinations in Nematic Liquid Crystals, *Phil.Mag.* **27**, 405-424 (1972).

Meyer, R.B., The Interaction Between a Disclination in a Nematic Liquid Crystal and a Rubbed Surface, *Sol.St.Comm.* **12**, 585-588 (1973).

Meyer, R.B., Macroscopic Phenomena in Nematic Polymers, Polymer Liquid Crystals, ed. A.Ciferri, W.R.Krigbaum, and R.B.Meyer, p.133-163, Acedemic Press, New York, 1982.

Milne-Thomson, L.M., Theoretical Hydrodynamics, 5th ed., MacMillan Press, London, 1968.

Mineyev, V.P., and Volovik, G.E., Planar and linear solitons in superfluid ^{3}He, *Phys.Rev.B* **18**(7), 3197-3203 (1978).

Moon, P., and Spencer, D.E., Field Theory Handbook, Springer-Verlag, Berlin, 1961.

Moore, J.S., and Stupp, S.I., Orientation Dynamics of Main-Chain Liquid Crystal Polymers. 1. Synthesis and Characterization of the Mesogen, *Macromolecules* **20**, 273-281 (1987).

Moore, J.S., and Stupp, S.I., Orientation Dynamics of Main-Chain Liquid Crystal Polymers. 2. Structure and Kinetics in a Magnetic Field, *Macromolecules* **20**, 282-293 (1987).

Moore, J.S., and Stupp, S.I., Synthesis of a Chemically Ordered Liquid Crystal Polymer, *Macromolecules* **21**, 1217-1221 (1988).

Nabarro, F.R.N., Theory of Crystal Dislocations, Oxford University Press, London, 1967.

Nehring, J., and Saupe, A., On the Schlieren Texture in Nematic and Smectic Liquid Crystals, *J. Chem. Soc. Faraday Trans. II* **68**, 1-15 (1972).

Nelson, D.R., Defect-Mediated Phase Transitions, Phase Transitions **7**, 1-99, Academic Press, London, 1983.

Nivard, P., seminar, University of Massachusetts, Amherst, 1989.

O'Neill, G.J., The Determination of the Viscosity Coefficients of Nematic Liquid Crystals, *Liq.Cryst.* **1**(3), 271-280 (1986).

Ober, C., Lin, J-I., and Lenz, R.W., Liquid Crystal Polymers. V. Thermotropic Polyesters with Either Dyad or Triad Aromatic Ester Mesogenic Units and Flexible Polymethylene Spacers in the Main Chain, *Polymer J.* **14**(1), 9-17 (1982).

Odijk, T., Elastic Constants of Nematic Solutions of Rod-Like and Semi-Flexible Polymers, *Liq.Cryst.* 1(6), 553-559 (1986).

Olley, R.H., Bassett, D.C., and Blundell, D.J., Permanganic etching of PEEK, *Polymer* **27**(3), 344-348 (1986).

Organ, S.J., and Barham, P.J., Electron microscopic investigations of the structure and nucleation of polyalkanoate copolymers and blends, *Polymer Preprints* **29**(1), 602 (1988).

Oseen, C.W., The Theory of Liquid Crystals, *Trans. Faraday Soc.* **29**, 883-899 (1933).

Poenaru, V. and Toulouse, G., The Crossing of Defects in Ordered Media and the Topology of 3-Manifolds, *J.Physique* **38**(8), 887-895 (1977).

Ranganath, G.S., Twist Disclinations in Elastically Anisotropic Nematic Liquid Crystals, *Mol.Cryst.Liq.Cryst.* **87**, 187-195 (1982).

Robinson, C., Liquid-Crystalline Structures in Solutions of a Polypeptide, *Trans.Farad.Soc.* **52**, 571-592 (1956).

Rojstaczer, S., and Stein, R.S., Domain Growth in Thermotropic Liquid Crystalline Polymers by Small Angle Light Scattering, *Mol.Cryst.Liq.Cryst.* **157**, 293-301 (1988).

Rojstaczer, S., Hsiao, B.S., and Stein, R.S., Texture Formation in Liquid Crystalline Polymers, *Polymer Preprints* (1988).

Schopohl, N., and Sluckin, T.J., Defect Core Structure in Nematic Liquid Crystals, *Phys.Rev.Lett.* **59**(22), 2582-2584 (1987).

Se, K., and Berry, G., Frank Elastic Constants and Leslie-Ericksen Viscosity Coefficients of Nematic Solutions of a Rodlike Polymer, *Mol.Cryst.Liq.Cryst.Lett.* **153**, 133-142 (1987).

Shiwaku, T., Nakai, A., Hasegawa, H., and Hashimoto, T., Ordered Structure of Thermotropic Liquid-Crystal Polymers. I. Characterization of Liquid-Crystal Domain Texture, *Macromolecules* **23**, 1590-1599 (1990).

Shiwaku, T., Nakai, A., Hasegawa, H., and Hashimoto, T., Novel Method to Characterize Dynamics of Disclination Lines in Thermotropic Liquid Crystalline Polymers, *Polymer Comm.* **28**, 174-178 (1987).

Smythe, W.R., Static and Dynamic Electricity, McGraw-Hill, New York, 1968.

Sonin, A.S., Chuvyrov, A.N., Sobachkin, A.A., and Ovchinnikov, V.L., Annihilation of Disclinations with the Frank Index m = +2 in Nematic Liquid Crystals, *Sov.Phys.Sol.St.* **18**(10), 1805-1807 (1977).

Stephen, M.J., and Straley, J.P., Physics of Liquid Crystals, *Rev. Mod. Phys.* **46**(4), 617-704 (1974).

Straley, J.P., Frank Elastic Constants of the Hard-Rod Liquid Crystal, *Phys.Rev.A* **8**(4), 2181-2183 (1973).

Strzecka, T.E., Davidson, M.W., and Rill, R.L., Multiple Liquid Crystal Phases of DNA at High Concentrations, *Nature* **331**, 457-460 (1988).

Stupp, S.I., Moore, J.S., and Martin, P.G., Chemical Disorder and Phase Separation: A Study of Two Liquid Crystal Polymers, *Macromolecules* **21**, 1228-1234 (1988).

Taratuta, V.G., Lonberg, F., and Meyer, R.B., Anisotropic Mechanical Properties of a Polymer Nematic Liquid Crystal, *Phys.Rev.A* **37**(5), 1831-1834 (1988).

Thomas, E.L., and Wood, B.A., Mesophase Texture and Defects in Thermotropic Liquid-crystalline Polymers, *Faraday Discuss. Chem. Soc.* **79**, 229-239 (1985).

Tseng, H.C., Silver, D.L., and Finlayson, B.A., Application of the Continuum Theory to Nematic Liquid Crystals, *Phys.Fluids* **15**(7), 1213-1222 (1972).

Vanderheyden, W.B., and Ryskin, G., Computer Simulation of Flow and Molecular Orientation in Liquid Crystal Polymers, *J.Non-Newt.Fluid Mech.* **23**, 383-414 (1987).

Viney, C., Light Microscopy of Liquid Crystalline Polymers, submitted for publication.

Viola, G.G., and Baird, D.G., Studies on the Transient Flow Behavior of Liquid Crystal Polymers, *J. Rheol.* **30**(3), 601-628 (1986).

Voigt-Martin, I.G., and Durst, H., Direct Observation of Smectic Layers in Side Chain Liquid Crystal Polymer Films, *Liq.Cryst.* **2**(5), 601-610 (1987).

Wahl, J., and Fischer, F., Elastic and Viscosity Constants of Nematic Liquid Crystals from a New Optical Method, *Mol.Cryst.Liq.Cryst.* **22**, 359-373 (1973).

Windle, A., *MRS Bulletin*, Jan. 1988.

Windle, A.H., Viney, C., Gulombok, R., Donald, A.M., and Mitchell, G.R., Molecular Correlation in Thermotropic Copolesters, *Faraday Disc.Chem.Soc.* **79**, 55-72 (1985).

Wissbrun K.F., Orienting Polymers, Springer Lecture Notes **1063**, ed. J.L.Ericksen, 1-26, 1984.

Wissbrun, K.F., A model for domain flow of liquid-crystal polymers, *Faraday Disc.Chem.Soc.* **79**, 161 (1985).

Wood, A.S., Why the Build-up in Supply of Liquid Crystal Polymers?, *Mod. Plastics*, 99-102, Nov. 1987.

Wood, B.A., Ultrastructural Studies of Thermotropic Liquid Crystalline Polymers, Ph.D. Thesis, University of Massachusetts, Amherst, 1985.

Wood, B.A., and Thomas, E.L., Are Domains of Liquid Crystalline Polymers Arrays of Disclinations?, *Nature* **324**, 655-657 (1986).

Wright, D.C., and Mermin, N.D., Crystalline Liquids: the Blue Phases, *Rev.Mod.Phys.* **61**(2), 385-432 (1989).

Zheng-Min, S. and Kleman, M., Measurement of the Three Elastic Constants and the Shear Viscosity γ_1 in a Main-Chain Nematic Polymer, *Mol.Cryst.Liq.Cryst.* **111**, 321-328 (1984).

Zhou, Q-F., and Lenz, R.W., Liquid Crystal Polymers. 15. Synthesis and Liquid Crystalline Properties of Alkyl Substituted Polyesters, *J.Polym.Sci.PC* **21**, 3313-3320 (1983).